NANOHOOPS AS NEW BUILDING BLOCKS FOR SUPRAMOLECULAR CHEMISTRY

by

JEFF M. VAN RADEN

A DISSERTATION

Presented to the Department of Chemistry and Biochemistry
and the Graduate School of the University of Oregon
in partial fulfillment of the requirements
for the degree of
Doctor of Philosophy

September 2019

DISSERTATION APPROVAL PAGE

Student: Jeff M. Van Raden

Title: Nanohoops as New Building Blocks for Supramolecular Chemistry

This dissertation has been accepted and approved in partial fulfillment of the requirements for the Doctor of Philosophy degree in the Department of Chemistry and Biochemistry by:

Mike Haley	Chairperson
Ramesh Jasti	Advisor
Mike Pluth	Core Member
Gregory Bothun	Institutional Representative

and

Janet Woodruff-Borden	Dean of the Graduate School

Original approval signatures are on file with the University of Oregon Graduate School.

Degree awarded September 2019

DISSERTATION ABSTRACT

Jeff M. Van Raden

Doctor of Philosophy

Department of Chemistry and Biochemistry

September 2019

Title: Nanohoops as New Building Blocks for Supramolecular Chemistry

The delocalization of pi-electrons through extended carbon networks is a key design strategy to modulate the chemical and physical properties of organic molecules and materials. In addition to the extent of delocalization, the overall topology or three-dimensional geometry of the resulting molecule can have a profound impact on the resulting properties. Cycloparaphenylenes, also known as nanohoops, are a particularly illustrative example, where the fully conjugated cyclic structure results in properties that are often times in stark contrast to their linear counter parts. These electronic differences as well as their macrocyclic shape renders them as fascinating candidates for various applications in supramolecular and materials chemistry.

Chapter **I** provides a brief overview of the importance of template-directed synthesis in preparing complex architectures. Examples of common synthetic macrocycles will first be discussed which will then be followed with a more in-depth presentation of how the radial, yet fully conjugated cylindrical geometry of nanohoops make them distinguished building blocks for supramolecular applications. Chapter **II** provides a more detailed understanding of the synthetic and electronic considerations of nanohoop macrocycles. A scalable and mild synthetic approach is disclosed that allows for the preparation of a highly strained nitrogen-doped nanohoop. Using the nitrogen atom, the

electronic structure is then fined tuned via alkylation. Chapter **III** describes the synthesis of cycloparaphenylenes that contain a metal-coordination site, a 2,2'-bipyridine, which acts as versatile handle for a variety of metal centers. Chapter **IV** expands on the coordination chemistry of these macrocycles; however, the ligand geometry is engineered to direct a metal to the inside of the macrocyclic cavity, which is then used to construct a new type of mechanically interlocked nanohoop structure. Chapter **V** discusses how other non-covalent interactions can be leveraged to construct supramolecular cylindrical assemblies, where weak arene-perfluoroarene interactions guide nanohoops into perfect cylinders. In summary, the findings discussed in this dissertation provide synthetic strategies for the selective functionalization of nanohoops and highlight this class of molecules as a novel scaffold for the design of new types of carbon nanomaterials.

This dissertation includes previously published and unpublished co-authored material.

CURRICULUM VITAE

NAME OF AUTHOR: Jeff Van Raden

GRADUATE AND UNDERGRADUATE SCHOOLS ATTENDED:

University of Oregon, Eugene
Northern Michigan University, Marquette

DEGREES AWARDED:

Doctor of Philosophy, Chemistry, 2019, University of Oregon
Bachelor of Science, Chemistry, 2014, Northern Michigan University

AREAS OF SPECIAL INTEREST:

Synthetic Organic Chemistry
Physical Organic Chemistry

PROFESSIONAL EXPERIENCE:

Teaching Fellow, University of Oregon, 2014-2019

GRANTS, AWARDS, AND HONORS:

Poster Prize at Gordon Research Symposium – Artificial Molecular Motors and Switches 2019
Holderness, New Hampshire

Lucian Hunt Award, Northern Michigan University, Department of Chemistry, 2014

PUBLICATIONS:

Van Raden, J. M.; Leonhardt, E. J.; Zakharov, L. N.; Pérez-Guardiola, A.; Pérez-Jiménez, A. J.; Marshall, C. R.; Brozek, C. K.; Sancho-García, J. C.; Jasti, R. Precision Nanotube Mimics via Self-Assembly of Programmed Carbon Nanohoops. *ChemRxiv*, **2019**. DOI:10.26434/chemrxiv.8079776.v1

Van Raden, J. M.; Jasti, R. How to make interlocked nanocarbons. *Science,* **2019**, *365*, 216-217.

Van Raden, J. M.; White, B. W.; Zakharov, L. N.; Jasti, R. Nanohoop Rotaxanes via Active Metal Template Syntheses and their Potential in Sensing Applications. *Angew. Chem. Int. Ed.* **2019**, *58*, 7341-7345.

Leonhardt, E. J.; Van Raden, J. M.; White, B. W.; Zakharov, L. N.; Jasti, R. Nanohoop Rotaxanes via Active Metal Template Syntheses and their Potential in Sensing Applications. *Nano Lett.* **2018**, *18*, 7991-7997.

Van Raden, J. M.; Louie, S.; Zakharov, L. N.; Jasti, R. 2,2'-Bipyridyl-embedded Cycloparaphenylenes as a General Strategy to Investigate Nanohoop Based Coordination Complexes. *J. Am. Chem. Soc.* **2017**, *139*, 2936-2939.

Van Raden, J. M.; Darzi, E. D.; Zakharov, L. N.; Jasti, R. Synthesis and Characaterization of a Highly Strained Donor-Acceptor Nanohoop. *Org. Biomol. Chem.* **2016**, *14*, 5721-5727.

ACKNOWLEDGMENTS

First, I would like to thank Professor Ramesh Jasti, my advisor, for his constant guidance and support over the years. He has provided an incredibly clear picture of different pathways one can take through life and this has helped me tremendously in deciding where to go next on so many different occasions. As a mentor, he demonstrates on a daily basis how one should carry themselves, both in and out of a research setting. This trait has been adopted by each graduate student he mentored, all of which has helped to build the Jasti lab into a special environment that encourages curiosity, discovery, and growth.

I would like to express my appreciation for each of these members. Specifically, Dr. Tom Sisto, Dr. Matt Golder, Dr. Penghao Li, Dr. Paul Evans, Dr. Evan Darzi, and Dr. Brittany White. Beyond the science, each of these individuals made transitioning from Michigan to Oregon far easier than I could have imagined. I would like to add a special thanks to Dr. Evan Darzi for being an excellent mentor during my first, second, and ultimately final years of graduate school. Additionally, I would thank Dr. Brittany White for being a constant source of help both in and out of lab during my early and final years of graduate school.

Jon Marshall, Gabe Rudebusch, and the rest of the Haley lab also deserve a large thank you as well as each Professor and Staff member in the Chemistry department at the University of Oregon. Professor Mike Haley in particular for helping to provide very enjoyable, entertaining, and insightful group meetings. Also, I would like to thank Professor Haley for being an easily approachable committee chair and for helping me identify a promising post-graduate school career pathway. Professor Mike Pluth I am also

very grateful for as both a committee member and source of help. Over the years, he has provided many suggestions that have lead to a number of exciting results. I sincerely appreciate the help that each of you have provided.

Working with undergraduate student Shayan Louie was also an incredible opportunity and I hope he understands that I am very grateful to have had the pleasure to work with him on so many projects. I would like to extend a large thank you to Erik Leonhardt, Justin Dressler, Josh Barker, Matt Cerda, Turner Newton, and Ruth Maust for being such excellent friends over the years. Our friendship has created a positive and enjoyable work atmosphere and it has helped generate a number of ideas, concepts, and jokes. Outside of research, the friendship we have built has helped take me through the most challenging times of graduate school. I would like to extend a special thank you to Ruth Maust for being my best friend, despite many disagreements and arguments. You have all been exceptionally fun to work with and again, I thank you all. Additionally, I would like to thank Dr. Evan Jackson, Dr. Tobias Schaub, Terri Lovell, Curtis Colwell, Claire Otteson, James May, Tavis Price, and Julia Fehr for all the help they have provided.

Finally, I would like to thank my family for pushing me to pursue what I find interesting and enjoyable, regardless of potential pitfalls. My mother, Joanna Van Raden, and my father, Mike Van Raden, have been so supportive and helpful and I absolutely would not be here without their assistance. My brother, Scott Van Raden, I would like to thank for being available to talk at all times, especially during the hardest times of graduate school. My sister, Sarah Van Raden, I would like to thank for constantly reminding me that my choice to pursue graduate school was a worthwhile investment. They are an incredible family, I am lucky to have them and the support they provide.

Dedicated to my dog, Moose; my closest friend, my adventure buddy, my hero, and my favorite pitbull.

TABLE OF CONTENTS

Chapter Page

Chapter Page

LIST OF FIGURES

Figure Page

Figure Page

Figure Page

Figure Page

Figure Page

Figure Page

Figure Page

LIST OF SCHEMES

Scheme Page

CHAPTER I

MERGING CARBON NANOSCIENCE WITH SUPRAMOLECULAR CHEMISTRY

Chapter **I** was written by myself and edited by Professor Ramesh Jasti.

Chapter **II** is based on published work in *Organic and Biomolecular Chemistry*. The manuscript was written by myself with editorial assistance from Professor Ramesh Jasti. Experimental work included in this chapter was carried out by myself or Dr. Evan Darzi. Lev N. Zakharov provided crystal structure analysis discussed in the manuscript.

Chapter **III** is based on published work in the *Journal of the American Chemical Society* and the manuscript was written by myself with editorial assistance from Professor Ramesh Jasti. The experimental work was carried out by myself or with assistance from Shayan Louie under my direction. Lev N. Zakharov provided crystal structure analysis of each of the reported complexes in the manuscript.

Chapter **IV** is based on published work in *Angewandte Chemie International Edition*. The manuscript was written by myself with editorial assistance from Professor Ramesh Jasti. The experimental work was carried out by myself or with assistance from Brittany M. White. Lev N. Zakharov provided all crystal structure analyses throughout the manuscript.

Chapter V is based on published work in *Nano Letters* as well as unpublished co-authored work. Experimental work was performed by myself, Erik J. Leonhardt, David J. Miller, and Lev N. Zakharov. The excerpt was written by myself with assistance from Erik J. Leonhardt and editorial assistance from Professor Ramesh Jasti.

1.1. Introduction

A primary goal of contemporary synthetic chemistry is to design, construct, and build molecular frameworks which can address health-, energy-, and technology-related problems. For example, the development of pharmaceuticals with improved bioactivity is heavily dependent on organic synthesis.[1] On the other hand, through the preparation of synthetic molecular machines, we can now access new forms of nanotechnology.[2] Bearing this in mind, a major objective is to develop new synthetic strategies to overcome limitations that prevent new molecular architectures from being realized. Inspiration for these methods can come from a variety places, however, nature has provided a number of elegant strategies that have allowed for the formation of some of the largest, most complex molecular systems known. Therefore, as a guide, nature has provided synthetic chemists with invaluable blueprints for addressing unexpected limitations in complex synthesis.

A key design concept encountered in natural systems is the ability to carefully balance covalent and non-covalent linkage—a design principle which gives rise to many of the high-functioning biological molecular machines. Over the past several decades, synthetic chemists have worked toward to uncovering the underlying principles that can allow this balance to be harnessed in the lab, ultimately giving rise to the field of supramolecular chemistry. This work was pioneered early on by Pederson, Cram and Lehn, typically regarded as the fathers of supramolecular chemistry. This lead to numerous design considerations and has significantly contributed to our current understanding of the fundamentals of physical organic chemistry resulting in the Nobel Prize in Chemistry being in 1987.[3-5]

The successful application of supramolecular chemistry to new types of functional materials and molecules relies on the ability to design and synthesize small molecule building blocks that have been programmed to engage in multiple non-covalent interactions. Under the correct conditions, these building blocks can then act in concert to form large, complex, yet well-defined structures that would be other inaccessible through pure covalent approach. Therefore, molecular design is a primary consideration in the preparation of supramolecular systems with two major structural features—three-dimensional molecular shape and electronic structure—ultimately dictating the resulting functionality of the supramolecular system.

Carbon-rich materials such as fullerenes, graphene, and carbon nanotubes have a wide range of unusual physical properties resulting from their unique topography and extensive delocalized circuits of pi-electrons.[6-11] For example, graphene, a two-dimensional sheet material consisting solely of carbon atoms, is a zero-gap semiconductor.[12] When this same material is rolled into a cylindrical topology—a carbon nanotube—the resulting material can be either metallic or semiconducting, depending on the specific atom connectivity. These features have contributed to an intense interest in the generation of molecular-scale graphitic structures, earning the title of the so-called nanocarbons.[13] Indeed, many other molecular entities can be synthesized primarily from carbon, with limitations being only creativity and current synthetic methods. Thus, as new fragments or building blocks for supramolecular applications, these nanocarbons hold great potential for exploring new complex architectures and are expected to deliver unusual properties.

Through the presentation of recent literature examples, this chapter aims to demonstrate how molecular properties are intrinsically tied to the molecular topology.

From this discussion, the ability to leverage supramolecular chemistry to access these unusual topologies will be highlighted as specific attention will be paid to literature examples that possess extensive pi-conjugation. This is intended to illustrate how pi-conjugation ultimately contributes to unique chemical and physical properties that otherwise would not be observed in the absence of such electronic delocalization.

First, in **Chapter 1.2**, examples will be provided that show how metal-coordination can be leveraged in the template-directed synthesis of complex molecules. Emphasis will be placed on how metal ions can pre-organize molecular fragments in either a passive or active manner prior to a covalent capture event to ultimately provide access to various topological landscapes. Next, in **Chapters 1.3** and **1.4**, a discussion on several selected macrocyclic architectures will be provided which will highlight desirable features or structural considerations when designing new building blocks for supramolecular applications. Additionally, where applicable, examples of these macrocyclic architectures participating in non-metal mediated template-directed syntheses will be discussed. Finally, in **Chapter 1.5**, macrocycles with fully conjugated radial pi-conjugation will be introduced in order to highlight their emerging potential in supramolecular and materials chemistry. Again, a major focus will be on how these macrocyclic architectures differ from typical macrocycles such as those in **Chapter 1.3** and **1.4** and how, as a result, new template strategies have been developed to construct new architectures. The ultimate goal will be to establish an understanding of how nanocarbon research is beginning to merge with the powerful concepts of supramolecular chemistry and as a result, a variety of new challenges are emerging that are poised to lead to an exciting new era in carbon nanoscience.

1.2. Metal-Mediated Template-Directed Synthesis of Organic Molecules

Template-directed synthesis is a powerful method to create complex molecular architectures.[14-16] This concept allows for molecular fragments to be positioned or pre-organized in solution prior to a covalent capture event which can result in a significant improvement in yield or unique reaction outcomes. Typically, the molecular fragments are held in place via a reversible interaction such that after the desired architecture is captured, the template can be removed to release the final product. A variety of templating strategies have been developed such as metal coordination, donor-acceptor interactions, and anion binding. As shown below, template-directed syntheses enable the preparation of a range of highly complex structures, often times possessing various interlocked componentry or high molecular weights that would be otherwise inaccessible in the absence of a template agent.

A especially noteworthy example of how the power of template-directed synthesis can dramatically improve access to particular molecular architecture was reported by Sauvage in 1983[17] in the preparation of a [2]Catenane: a structural motif consisting of two macrocycles that have been linked/threaded together via a non-covalent bond. In this case, two phenol-functionalized 1,10-phenanthroline units **I.1** were bound together **I.2** via a tetrahedral Cu(I) metal (**Figure 1.1**), producing a point at which each ligand crosses over the other. Importantly, by functionalizing the phenanthroline at the 1,10-positions with aryl groups, the otherwise highly sensitive Cu(I) metal center is protected such that a Williamson ether macrocyclization strategy can be used to form the key macrocyclic bonds forming the desired [2]catenane **I.3** in 27% yield (**Figure 1.1**). This was also expanded on via the formation of a macrocycle containing an 1,10-diaryl substituted phenanthroline **I.4**. In the presence of 1 equivalent of $Cu(MeCN)_4PF_6$ and linear strand **I.1**, the formation of a

thread structure (**I.5**) was observed, which, under Williamson ether conditions allowed the [2]catenane **I.3** to be formed in an improved 42% yield. The improved yield can be attributed to the fact that only one macrocyclization event is needed to capture to targeted [2]Catenane. Additionally, by reacting **I.3** with KCN, the Cu(I) metal center could removed to give the unmetallated [2]Catenane. This particular report[17] was a pivotal point in the early stages of mechanically interlocked molecules given that the previous synthetic approaches by Wasserman delivered the first example of a catenane in less than 1% yield.[18]

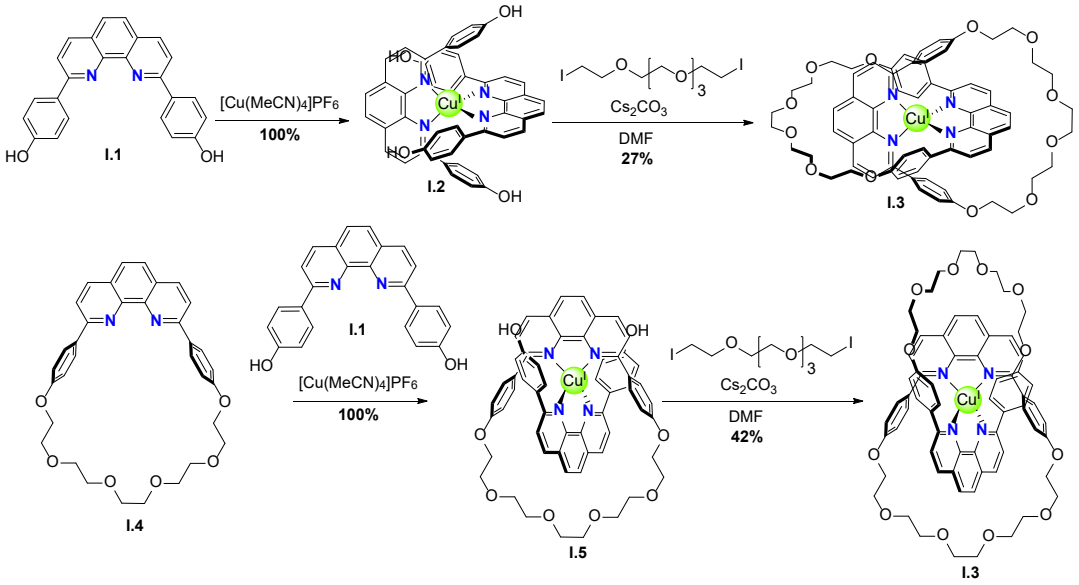

Figure 1.1. Early example of template-directed synthesis of a [2]Catenane **I.3** by Sauvage showing templation followed by covalent capture. In the top example, two macrocyclization events are needed to form the [2]Catenane. In the lower example, only a single macrocyclization event is needed, resulting in an overall higher yield.

This phenanthroline-based templation strategy was recently applied in two separate reports by the Bäurle[19] and Cong[20] groups in the preparation of two unprecedented fully conjugated [2]Catenanes (**Figure 1.2**). Unlike typical mechanically interlocked molecules,

both of these molecules represent rare cases of interlocked fully sp^2-hybridized macrocycles. The effects of catenation were readily apparent in both cases. For example, in the case of the oligothiophene catenane **I.7**, it was found that that the molar extinction coefficient was doubled relative to the free macrocycle. Additionally, the quantum yield of catenane **I.7** was reduced relative to free macocycle, indicating charge-transfer through the mechanical bond. On the other hand, the oligophenylene catenane **I.9** by Cong et al. demonstrated a rare case of solid-state stabilized Mobius topology which the authors attribute to the mechanically interlocked topology. It should be noted that in both cases, each [2]Catenane prepared using Sauvage's metal templation concept was isolated in a reasonable yield (22% (**I.7**) and 28% (**I.9**)) from the linear precursors which highlight the effectiveness of a metal-templated approach. Ultimately, Sauvage's templation strategy[17] has been applied in the preparation of a range of small molecules as well as materials and the seminal report established a foundation for many template-directed syntheses of mechanically interlocked molecules. It should be noted that metals known to adopt geometries such as octahedral, square planar, and linear arrangements have also been used in template-directed syntheses, which highlights the generality of this approach.[15]

The work by Sauvage leveraged the metal ions coordination geometry in a passive way, where the metal acts solely to pre-organize two molecular strands that are then coupled using an orthogonal reaction. In a conceptually different approach, Leigh demonstrated in 2006[21] that a metal ion can both pre-organize components and form a mechanical bond. This strategy, referred to as an active metal template synthesis, is fundamentally different from a passive template strategy in that the requirement for

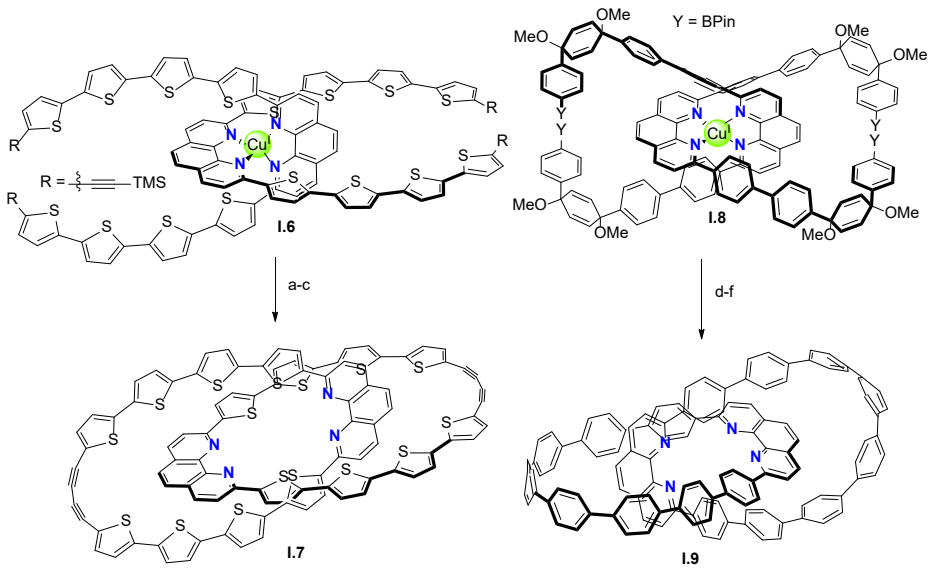

Figure 1.2. Application of Sauvage's templation strategy in the synthesis of conjugated [2]Catenanes by Bäurle (left) and Cong (right). Conditions: a) CsF/[Pt(dppp)Cl_2], 34%; b) I_2, 74%; c) KCN 44%; d) Pd(PPh_3)$_2Cl_2$, KF, air; e) TMSCN, KF (28%, two steps); f) Sodium naphthalenide, 78%.

complimentary recognition motifs between each strand are no longer needed. In the initial 2006 report, they reported that a macrocycle **I.10** containing an endocyclic pyridine unit was capable of binding copper(I) within the macrocyclic pocket (**Figure 1.3**). Next, under Cu(I)-catalyzed azide-alykne cycloaddition reaction conditions with a terminal alkyne **I.11** and terminal azide **I.12**, a [2]Rotaxane **I.13** could be generated by directing the key bond-formation event to occur within the macrocyclic pocket. Again, this was a natural consequence of the macrocycle geometry, where the endocyclic pyridyl unit allowed for the reaction to take place within the macrocycle cavity.

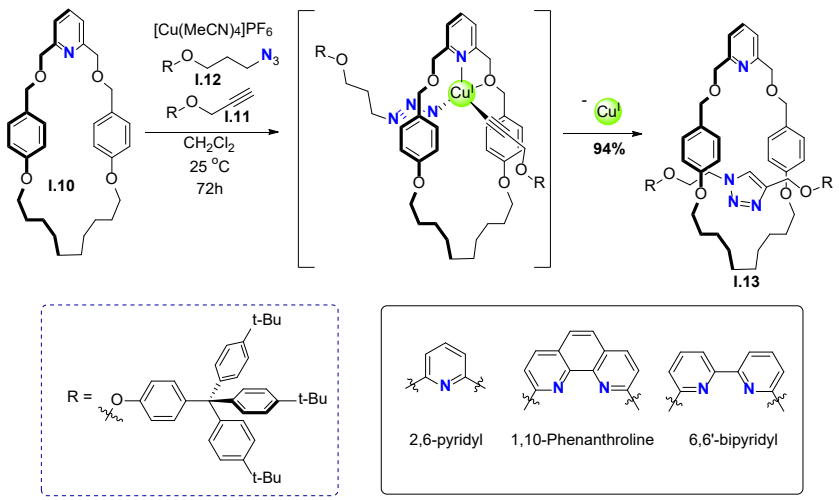

Figure 1.3. First example of an active metal template synthesis of a [2]Rotaxane by Leigh. The mechanical bond is formed via Cu(I) catalyzed azide-alkyne cycloaddition, resulting in [2]Rotaxane **I.13** bearing a triazole moiety.

Since this initial report, a number of reactions[22] have been shown to participate in active metal template method such as the Cadiot-Chodkiewicz coupling as well palladium-free Sonogashira reactions. An excellent illustration of the power of this strategy was shown by the Anderson and Tykwinski groups[23] where [2]Rotaxane formation allowed for the stabilization of long polyynes (**I.14-I.17**) (**Figure 1.4**)—a structural motif known for being highly reactive. The impact of encapsulation was particularly noteworthy in the case of [2]Rotaxane **I.17**, where decomposition occurred at 60 °C higher in the [2]Rotaxane versus a polyyne of same length with no macrocycle for protection (**Figure 1.4**). This synthetic strategy was also applied to the formation of a large 6-porphryin nanoring bearing 3 additional macrocycles **I.18**, i.e. a [4]Catenane.[24] While not tested for thermal stability, this example highlights a rare example of both passive and active metal template strategies

being used in concert to construct complex architectures. A similar approach toward molecular trefoil knot was also recently reported by the Leigh group.[25]

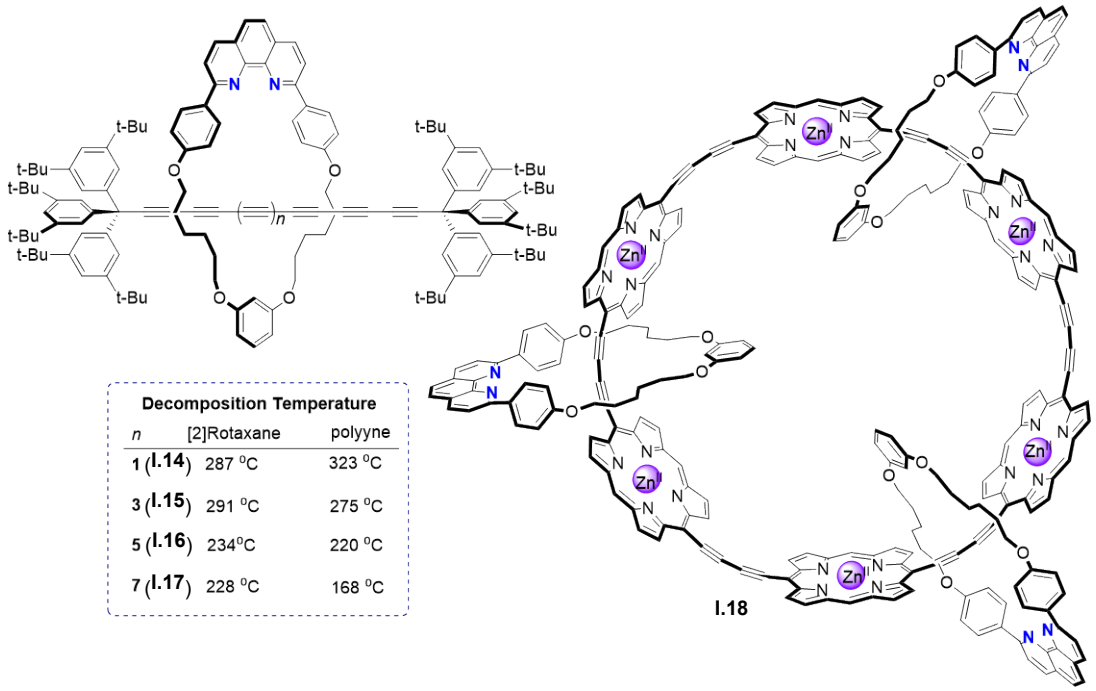

Figure 1.4. Selected examples of a [2]Rotaxane (left) and [4]Catenane (right) prepared via an active metal template synthesis. The inserted table showing decomposition temperatures refers to the difference between polyynes that are encapsulated by a macrocycle or those that are unencapsulated.

Template-directed syntheses are often performed on structures that are in a relatively small size regime (<1 nm), with traditional methods being less reliable for the formation of structures on the multi-nanometer scale. In 2011, the Anderson group reported the synthesis (**Figure 1.5**) of a 12-porphryin nanoring **I.19** bearing a diameter of 4.7 nm.[26] This is a rather large improvement over their previous reports of an 8- and 6-porphyrin nanoring.[27, 28] The key difference between these reports is the templation method used to prepare each nanoring. In the case of the smaller nanorings, a single linear chain of 8 or 6

diyne-linked porhphyrins was combined with a circular pyridine based template containing exactly 8 or 6 binding sites to form 1:1 complexes. After an oxidative palladium alkyne homocoupling reaction, the 8-porphyrin nanoring was formed in 14% isolated yield. In contrast, the 12-porphyrin nanoring was assembled by using two templates bearing 6 binding sites with three individual tetrameric porphyrin chains (**Figure 1.5**, left), i.e. a 2:3 complex. Again, capture of the final nanoring was accomplished using an oxidative palladium catalyzed alkyne homocoupling reaction to give the final product in 39% yield. Attempts to prepare the same 12-porhpyrin nanoring via the classical template strategy were successful (**Figure 1.5**, right), however, the required template molecule required ten steps to synthesize and was reportedly accessible only in small quantities. In contrast, the Vernier approach leveraged a template that was easily accessible, ultimately highlighting the benefits of using a Vernier approach to access large nanostructures. Importantly, it was found that without the added template, macrocyclization attempts all failed to generate any cyclic **I.19** and instead give linear polymers.

With access to these large fully conjugated structures, fundamental concepts in aromaticity and antiaromaticity have recently been investigated. In a recent report by the Anderson group,[29] they demonstrated that a macrocycle consisting of 6 porphyrin rings (**I.20**) with diameter 2.4 nm showed antiaromatic or aromatic ring currents (**Figure 1.6**) in either a 4+ or 6+ oxidation state, respectively. This work showed that global ring currents begin to dominate on suppression of local ring currents via changes in oxidation state. Additionally, the authors found it was essential for the template to be present in order to observe the well-defined antiaromatic currents, but, interestingly, was not needed for the

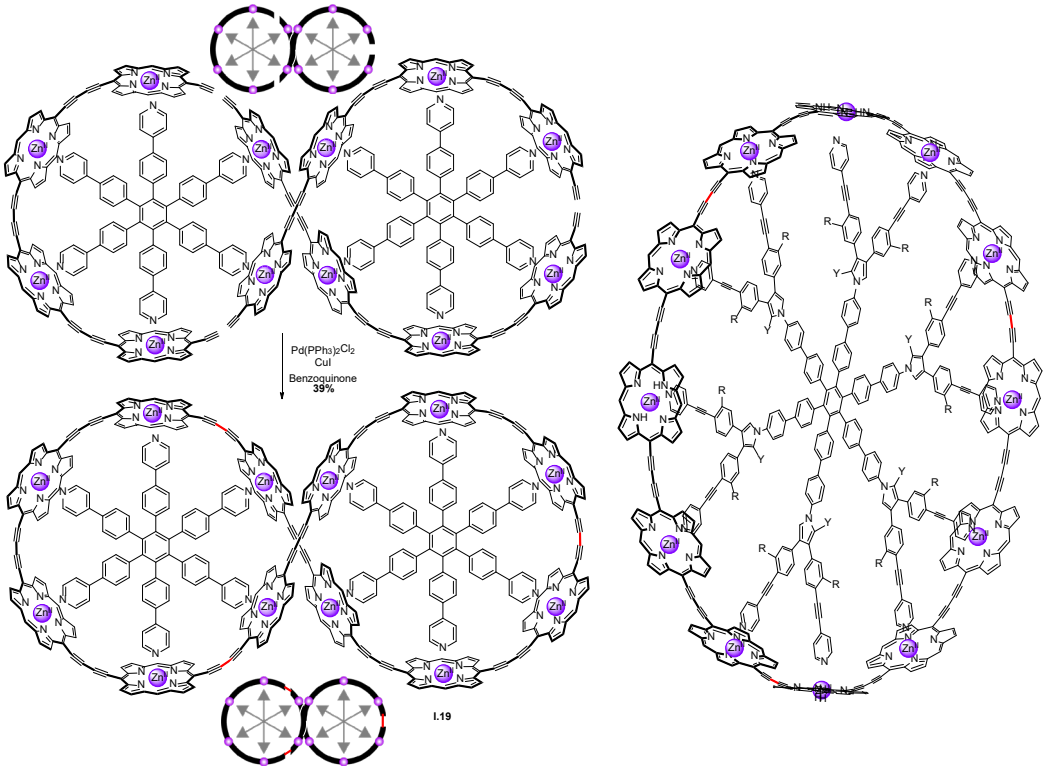

Figure 1.5. Vernier-templated synthesis of 12-porphyrin nanoring **I.19** using two small templates (left) or a single large template (right). Bonds colored in red highlight the key bonds that are formed during the macrocyclization step. Cartoons represent templated structure before (top) and after (bottom) macrocyclization.

aromatic currents in 6+ state. Prior to this work, the largest known aromatic molecule that demonstrated global aromaticity was around 1.3 nm (50 pi electrons)[30] and studies to investigate this further were hindered by synthetic access to larger fully conjugated systems. Thus, the ability to leverage template-directed syntheses in the preparation of large systems becomes a powerful tool for studying fundamental concepts.

As previously mentioned, the macrocyclic architecture plays a pivotal role in supramolecular chemistry. In general, this stems from the ability of macrocycles to act as

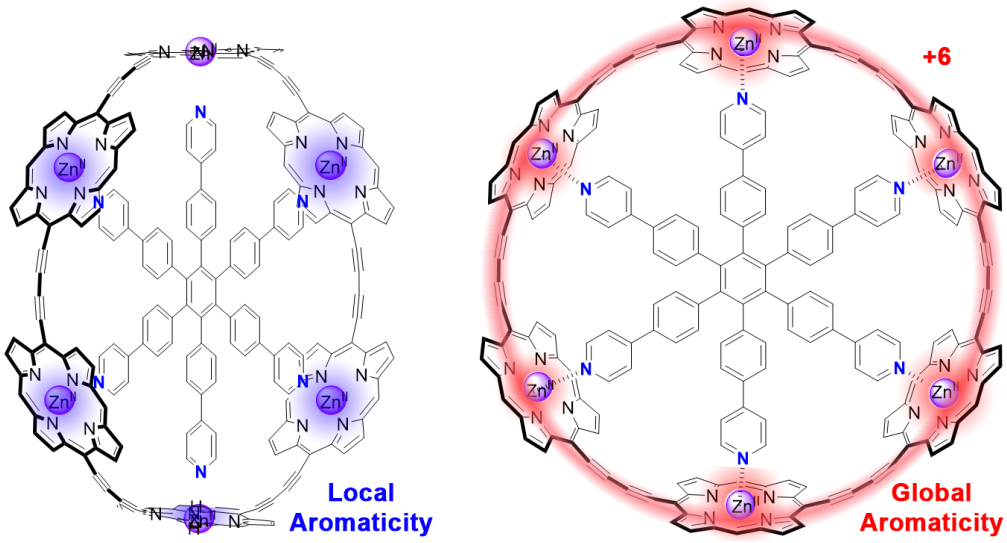

Figure 1.6. Recent example of a large 6-porphryin nanoring **I.20** prepared via template-directed synthesis that demonstrates local aromaticity in a charge neutral state (left) or global aromaticity in a 6+ oxidation state (right).

molecular hosts for a range of guest molecules. This observation and concept was proposed by Pederson and Cram and has since become the foundation for modern supramolecular chemistry. As a result, naturally occurring macrocycles such as cyclodextrins as well countless synthetic macrocycles have been explored extensively in the area of host-guest chemistry for the last several decades. The chemistry of these systems has been covered in numerous reviews and as such, the following discussions in this chapter are focused primarily on strained macrocycles such as cyclophanes as well as macrocycles that exhibit extended conjugation.

1.3. Importance of Electronic Structure in Molecular Recognition

The ability to tune the electronic structure of a macrocyclic host will ultimately determine which guest molecules can be recognized. A class of macrocycles known as the cyclophanes have a rich history in this regard. Cyclophane macrocycles typically consist of an aromatic unit linked by sp^3-hybridized bridge. In general, these particular macrocycles display large deviations in the planarity of each aryl ring, resulting in a significant build up of molecular strain (**Figure 1.7**). Given this high strain, cyclophane type macrocycles are remarkably rigid and therefore possess a well-defined molecular pocket that is well suited for host-guest interactions.

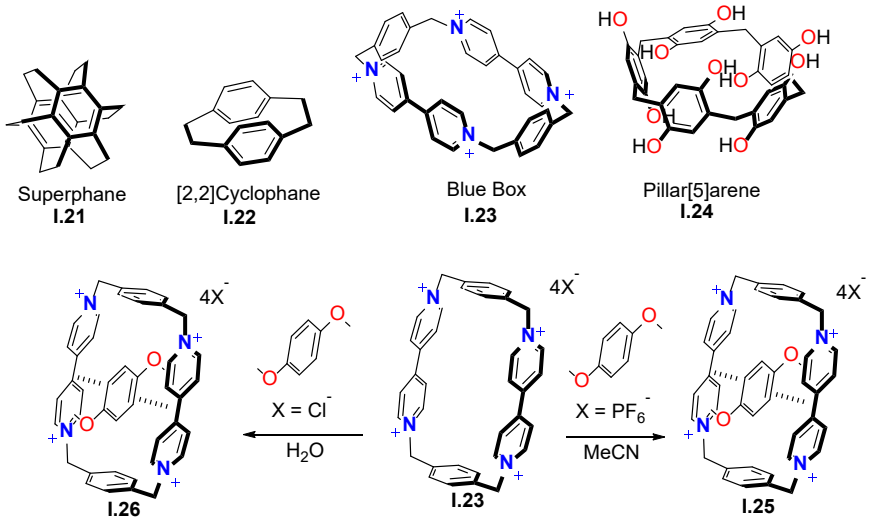

Figure 1.7. Representative examples of common cyclophane macrocycles. First reported host-guest chemistry of **I.23** showing binding to electron rich guests.

As an early example of host-guest complexation with a cyclophane host, the Stoddart group sought to prepare a new electron-poor cyclophane macrocycle that they anticipated would bind electron-rich guests. In their first investigation in 1988, the Stoddart group reported the tetracationic cyclobis(paraquat-*p*-phenylene) cyclophane (**I.23**,

"blue box").[31] This particular macrocycle possesses a well-defined box-like cavity size of 10.3 x 6.8 A. Importantly, through electrostatic potential surface analysis, the interior of the macrocycle was shown to be highly electron-poor owing to the cationic pyridinium units. In this first report, they demonstrated that the cationic host binds electron-rich dimethoxy guests (**Figure 1.7**) in a 1:1 charge-transfer complexation **I.25**—an observation that was confirmed via UV-Vis and NMR spectroscopy. Additionally, the authors also show that by exchanging the counterion from PF_6 to Cl-, **I.23** becomes water soluble which allowed for an investigation in the aqueous host-guest complexation **I.26** ability of this macrocycle.

The initial 1988 report effectively established **I.23** as general receptor for electron rich guests, which, depending on the connectivity of the pyridyl unit, could be readily tailored to a variety of guest sizes and shapes.[32] Shortly after this report, the Stoddart group demonstrated (**Figure 1.8**) that this receptor could be leveraged in a template-directed manner to construct mechanically interlocked molecules with a report of a [2]Catenane **I.27** and [2]Rotaxane **I.28** following in 1989[33] and 1991,[34] respectively. Importantly, these reports deviated from that of Sauvage in that it successfully demonstrated that a metal ion was, in some cases, no longer necessary. In the first case, **I.29** was combined with a 2.5 fold excess of **I.30** in the presence of **I.31** to give the targeted [2]Catenane **I.27** in a exceedingly high 70% yield. This high yield can be explain via the mechanism of formation, where complexation of **I.29** with **I.30** occurs followed by covalent capture via SN2 to give the desired [2]Catenane **I.27**. This is consistent with their previous report on the complexation of paraquat with a hyodrquinone cyclophane-like receptor.[31] While [2]Catenanes had been prepared prior to this report, the fact that **I.27** still possessed the

templating interaction in the final product differentiated this structure from all previous reports which would be expected to impart unsual dynamics into the system. Additionally, the effect of catenation on the electrochemical properties of **I.27** were readily apparent in the cyclic voltammograms, where on single electron reduction of **I.27**, it was reported that the inner paraquat unit is stabilized stronger by the proximity of two hydroquinone units, resulting in a selective reduction of the outer paraquat unit. On second reduction, the difference between each paraquat unit is likely diminished given that single electron reduction attenuates the interaction between each hydroquinone unit. This work ultimately established donor-acceptor interactions as a foundation for preparing a wide range of MIMs, with a report of a [2]Rotaxane **I.32** following in 1992.[34] This particular report demonstrated the unique dynamics in these systems, where it was revealed that these donor-acceptor interactions could be leveraged to initiate a shuttling type motion.

In 2008, a similar class of macrocycles was introduced by Ogoshi and coworkers known as the pillar[n]arenes.[35] These macrocycles are composed entirely of electron-rich hydroquinone units linked together through methylene bridges (**Figure 1.9**), rendering the macrocyclic unit a host for electron-poor guests despite an overall neutral charge. In this report they demonstrated the ability of **I.24** to host pyridinium salts, a feature that can be attributed to a combination of an electron rich pore as well as ionophores on both faces of the macrocycle. In a follow up report[36] on the synthesis of pillar[5]arene **I.24**, the macrocycle was obtained in 71% yield through a single lewis acid-catylzed step via commercially available starting materials (**Figure 1.9**). Particularly noteworthy is that this reaction was completed in only 3 minutes. The ability to host electron poor guests is a

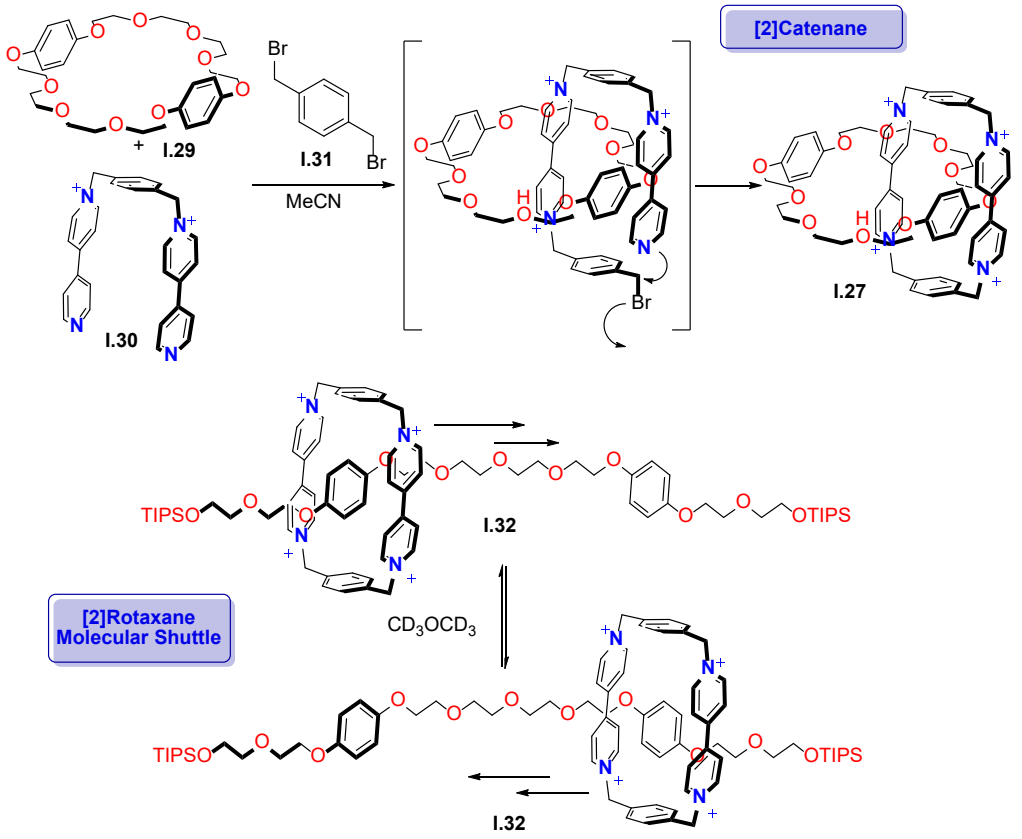

Figure 1.8. Examples of mechanically interlocked molecules prepared by the Stoddart group using donor-acceptor interactions to template the formation.

feature that is opposite to that observed in the cationic cyclophanes which highlights the importance of controlling electronic structure. Since the initial report of this class of macrocycle, the supramolecular capabilities have been well-established, both in solution and the solid-state.

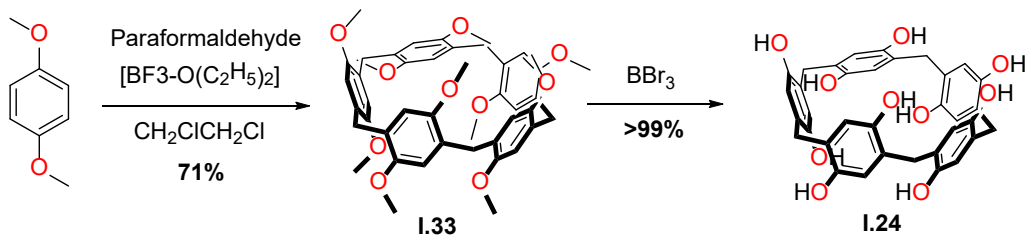

Figure 1.9. Optimized synthesis of pillar[5]arene **I.24**.

1.4. Shape-Persistence in Molecular Recognition

The key structural features that enable macrocycles to engage in molecular recognition stem primarily from the molecular composition within the macrocyclic pocket. Additionally, the tendency for this macrocyclic pocket to retain its shape and avoid conformations that may prohibit molecular recognition capabilities is crucial. The development of macrocycles with a shape-persistent structure are therefore highly desirable as supramolecular building blocks with a major design strategy being the inclusion of extensive conjugation. Conjugation of a molecular fragment can provide necessary structural rigidity which ultimately allows for a macrocycle to maintain a specific three-dimensional geometry under a wide range of conditions which can greatly enhance the binding ability of the host.

Work by the Flood group in 2008 demonstrated this concept, where a fully conjugated macrocycle **I.34** bearing four 1,2,3-triazoles units enabled strong binding to chloride anions.[37] This report is an unusual case where a negatively charged chloride anion can be hosted in an overall neutral host through only C-H interactions—interactions that typically regarded as additional binding sites rather than primary sites. The key macrocycle **I.34** was prepared in 27% yield over seven steps (**Figure 1.10**) using a combination of Sonogashira cross-couplings and Cu(I) catalyzed azide-alkyne cycloaddition reactions. Importantly, by including 1,2,3-triazole units, two important structural features are provided: 1) the macrocycle adopts a shape-persistent coplanar arrangement with a total of eight C-H interactions facing the interior of the macrocycle and 2) the highly polarized C-H bonds of the triazole units enhance the ability to bind the negatively charged chloride anion. To illustrate the advantage of shape-persistence, macrocycle **I.34** was compared

against a linear analogue in a titration with TBACl. It was found that in the case of **I.34** a K_a of 1.3 x 10^5 M^{-1} was calculated versus a K_a of 7 M^{-1} for the linear analogue. Again, this large difference can be attributed to the preorganized shape of **I.34**. Very recently, a similar cage-like structure **I.35** using 1,2,3-triazole moieties was prepared which resulted in attomolar affinity (K_a 1 x 10^{17} M^{-1}).[38] This further illustrates the importance of preorganization and rigidity in molecular recognition.

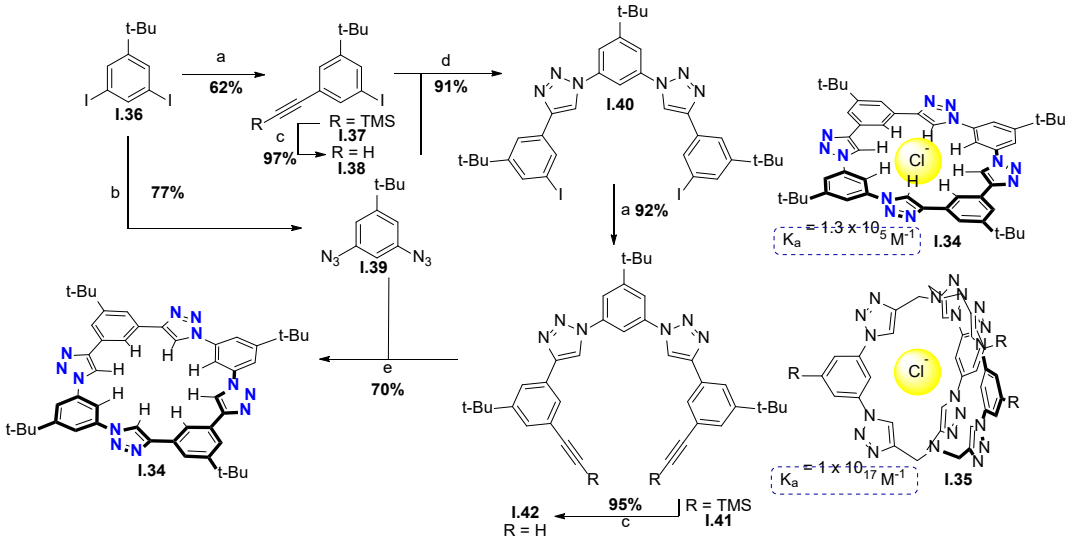

Figure 1.10. Synthetic strategy used to access triazole macrocycle **I.34**. Conditions: (a) TMSA, [$PdCl_2(PPh_3)_2$], CuI, *i*Pr_2NH, THF, 8h. (b) NaN_3, CuI, DMEA, Sodium Ascorbate, EtOH/H_2O/Toluene. (c) KF, MeOH, THF, 8h. (d) $CuSO_4$, sodium ascorbate, EtOH/H_2O/Toluene. (e) CuI, DBU, Toluene, 4h. Reported binding affinities with chloride using macrocycle **I.34** and cage **I.35**.

As another example, in 2013 the Flood group reported a new type of fully conjugated shape-persistent macrocycle **I.43** comprised of cyanostillbene units (**Figure 1.11**).[39] Similar to the polarized C-H bonds (5.0 D) in the 1,2,3-triazole moieties, the C-H bond of cyanstillbene units are highly polarized (3.70 D) which was anticipated to assist in

anion binding. In this first report, the targeted macrocycle (**I.43**) was prepared in a one-pot synthesis delivering **I.43** in exceptional 81% yield. Characterization of this macrocycle revealed a bowl-shaped coplanar arrangement of each aryl unit, similar to that in the case of **I.34**. Encouraged by a relatively large cavity size (5.2 Å), the authors then explored the ability to bind anions, which resulted in the observation that the host macrocycle binds rather strongly in a 2:1 fashion with larger anions (BF_4, ClO, PF_6). This enhanced binding affinity can be attributed to the resulting electropositive cavity from each polarized C-H bond as well the rigid and shape-persistent nature of the host. Encouraged by the 2:1 complexation and the ability to bind large anions, the authors then constructed an unprescendented [3]rotaxane **I.44**—a mechanically interlocked structure bearing 2 macrocycles of **I.43** threaded over a dialkyl-substituted phosphate.

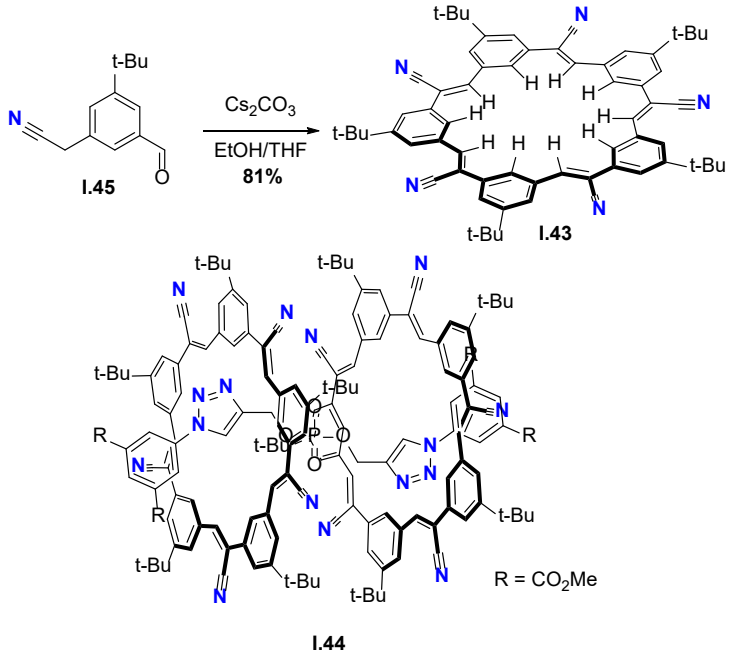

Figure 1.11. Synthetic strategy used to access cyanostar macrocycle **I.43** from **I.45** and reported phosphate [3]Rotaxane **I.44**.

Ultimately, these studies as well others highlight the importance of structural rigidity in molecular recognition. In these cases, the structural rigidity improves the affinity for anionic guests owing to improved preorganization for the targeted anion. Again, this is in line with Cram's early idea that a preorganized rigid host should show the strongest binding to a guest. In addition to providing structural rigidity, these pi-rich macrocycles also tend to display unusual electronic properties relative to their linear counterparts as in the cause of cyclic thiophenes. These properties will be expanded on in following chapter with an overview of macrocycles that possess radial conjugation.

1.5. Macrocycles with Radially Oriented Pi-Systems

The molecular shape of the macrocycles presented in **Chapter 1.3** can be characterized by a radial orientation of each aryl ring owing to a combination of strain and *para*-connectivity of each ring. Additionally, the electronic structure can be viewed generally as either electron deficient as in the case of **I.23** or electron rich in the case of pillar[5]arene **I.24**. In contrast, the molecular shape of the macrocycles discussed in **Chapter 1.4** are non-radially oriented, but instead are flat fully conjugated structures with an electronic structure dictated by the extent of conjugation. As previously mentioned, the combination of electronic structure and three-dimensional shape are key parameters that govern functionality in supramolecular structures and these examples illustrate this importance. In the following chapter, a type of macrocycle that shares features (**Figure 1.12**) similar to those discussed in **Chapter 1.3** and **1.4**, the [n]Cycloparaphenylene ([n]CPP) or carbon nanohoop, is introduced. Specifically, these macrocycles are fully conjugated, but, due molecular strain, are oriented in a radial geometry. Throughout this

chapter a large emphasis will be placed on the emerging supramolecular reports of this unique macrocycle and, where applicable, prospects and potential research directions will be discussed.

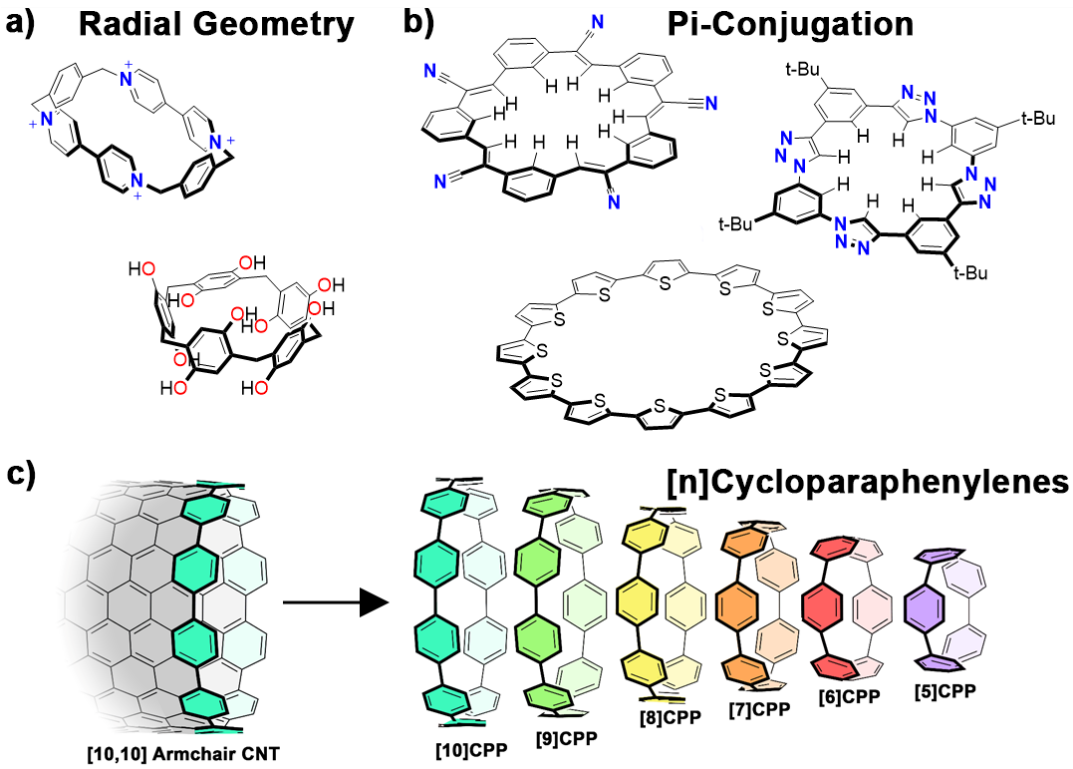

Figure 1.12. a) Selected examples of macrocycles with radial geometry. b) Selected examples of macrocycles with full pi-conjugation. c) Relationship of the [n]CPPs to other macrocycles and carbon nanotubes. These macrocycles possess properties from both a) and b).

The [n]CPPs have been a longstanding molecular target of numerous synthetic groups since 1934.[40] The synthetic challenge of these unusual macrocycles can be understood by the realization that in some cases, such as [5]CPP for example, an

astounding 120 kcal/mol of strain energy must be overcome during the synthetic route.[41] This is sharp contrast to each of the examples discussed prior. The first synthesis of [n]CPPs was shown by Jasti and Bertozzi in 2008 (**Figure 1.13**) using a "shot-gun" type macrocyclization.[42] In this report, diboronate **I.45** was first prepared and then subjected to dilute Suzuki-Miyaura coupling conditions with diiodide **I.46** to give a statistical mixture of macrocycles **I.47-I.49** in 2%, 10%, and 10% yield, respectively. Importantly, by using a cyclohexadiene moiety, the macrocyclic precursors adopted a "bent" geometry which provided curvature, ultimately enabling the formation of cyclic products which are relatively unstrained in comparison to the fully conjugated counterpart. To build in the remaining strain, reductive aromatization of each cyclohexadiene moiety with sodium napthalenide transformed the intermediate macrocycle into fully conjugated variants, i.e. the [n]CPPs **I.50-I.52**. Since the initial report, this strategy has been greatly expanded upon in our group, which has ultimately lead to the preparation of [5]-[12]CPP.[43] Work by the Itami group has shown that cyclohexane units can also provide the necessary curvature for macrocycle formation (**I.53**) which can then be oxidatively aromatized using an acid catalyzed dehydration to give macrocycle **I.54** in 62%.[44] Lastly, another key strategy for these strained targets was shown by the Yamago[43] and Isobe groups,[13] where cyclometalated Pt(II) units (**I.55**) act as bent functional groups which can then reductively eliminated to give the final conjugated macrocycle **I.56**. In should be noted that in general, these strategies are amenable to a wide range of different functional groups[13] and that these techniques have allowed for the preparation of numerous CPP derivatives.

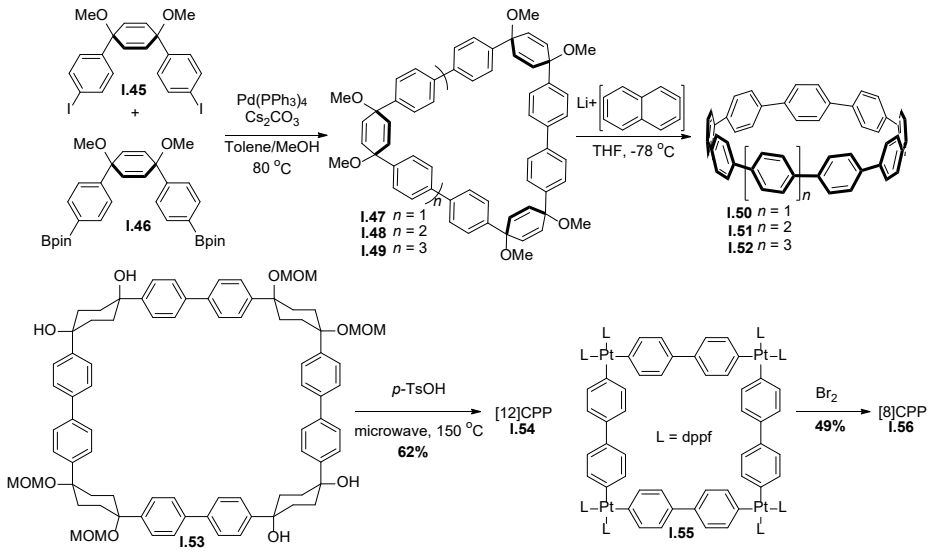

Figure 1.13. Synthetic approaches toward making strained carbon nanohoops by Jasti (top), Itami (bottom left), and Yamago (bottom right).

One of the more striking features of this class of macrocycles lies in the photophysical and overall electronic structure.[43] In many cases, the properties observed in macrocycles with radial pi-conjugation are in stark contrast with their linear counterparts. For example, when *n* is greater than 6, the [n]CPPs are fluorescent. More interestingly, however, is that as conjugation increases, the emission begins to blue shift—again, a trend that is in stark contrast with typical fluorescent molecules. This trait is also reflected in the frontier molecular orbital energies, where the difference between highest occupied molecular orbital (HOMO) energy and lowest unoccupied moileccular orbital (LUMO) energy increases with extending conjugation. While the underlying electronics that give rise to these properties are of fundamental interest, these properties have practical applications given that redox-active molecules play a pivotal role in molecular electronics. For example, the redox chemistry of [8]CPP (**I.56**) has been the subject of several

reports.[46-48] Recent work by Yamago and coworkers showed that oxidation of [8]CPP (**I.56**) to the dication allows the macrocycle to exhibit global aromaticity.[48] On the other hand, the charge neutral macrocycle shows only local aromaticity. Moreover, it was recently shown that [10]CPP (**I.57**) and its alkoxy derivates[49] are capable of transporting charge suggesting materials applications. Bearing these properties in mind, these macrocycles hold potential for new molecular building blocks in a variety of avenues.

One of the first reports of [n]CPPs engaging in supramolecular chemistry was shown by Yamago,[50] where complexation between [10]CPP (**I.57**) and spherical fullerene C_{60} was observed to occur with a K_a of 2.79 x 10^6 M^{-1}. Similar complexation was reported by Oda[51] as well as Lee[52] in acetylene functionalized nanohoops, however, in work by Yang and Du, a consistent increase in binding affinity was reported through extension (**I.58**, **I.59**) of the nanohoop backbone (**Figure 1.14**).[53] Additionally, these fullerene nanohoop complexes were shown to act as photoconductive heterojunctions. The selectivity of the complexation between [10]CPP (**I.57**) and C_{60} was also reported, where addition of excess C_{60} to an equimolar mixture of [8]-[12]CPP resulted in characteristic ^{1}H-NMR shift changes only in [10]CPP (**I.57**).[50] Taken together, the size-complementarity and pre-organized shape between [10]CPP (**I.57**) and C_{60} render this complexation both strong and selective amongst reported fullerene hosts. In addition to this report, a variety of [10]CPP derivatives are known for their ability to host fullerenes.[54]

A particularly noteworthy example of how this complexation can be applied as a template was shown in work by the von Delius group, where [2]Rotaxane formation was accomplished using a functionalized fullerene C_{60}.[55] The synthesis was performed as

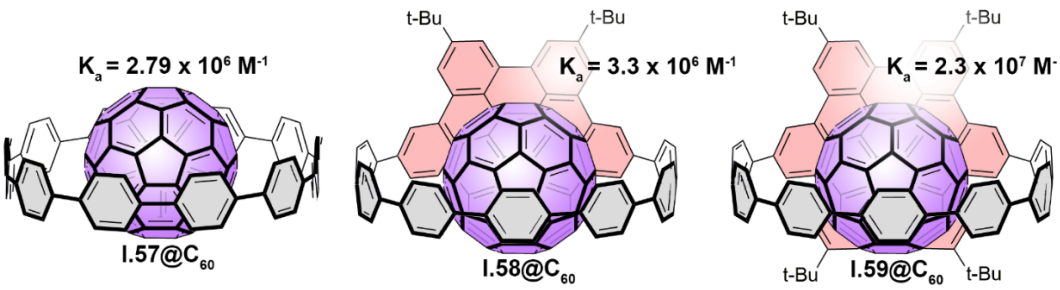

Figure 1.14. Selected examples of fullerene [10]CPP host-guest complexes showing increase in binding affinity via extension of the nanohoop backbone.

shown in **Figure 1.15**. First, formation of a pseudorotaxane **I.60** was carried out using a diethyl malonate pentakis-fullerene. Importantly, the diethyl malonate pentakis functionalization was necessary in order to prevent the [10]CPP macrocycle from sliding over the terminal fullerene groups. In the presence of a slight excess of brominated stopper **I.61** under Bingel reaction conditions, the targeted [2]Rotaxane **I.62** was then accessed in 40% yield which consisted of two different isomers. It should be noted that the formation of only two isomers is rather unusual given that a typical bingel reaction would be expected to provide a more complicated mixture of isomers. This result suggested that [10]CPP provides steric protection to a variety of locations on the central C_{60}. Indeed, the authors then investigated the ability of [10]CPP to act as a supramolecular protecting group for fullerene C_{60}, which revealed that in the absence of [10]CPP, addition of a brominated malonate derivative to malonate functionalized C_{60} resulted in the formation of roughly 7 different isomers. However, in the presence of [10]CPP, the formation of four of these isomers were suppressed which highlight the ability of [10]CPP to act as a supramolecular protecting group. This work ultimately established concave-convex pi-pi type templation as a new strategy to form mechanically interlocked molecules that bear nanohoop

macrocycles and also demonsrated that nanohoop macrocycles can impact reaction outcomes. While fullerene guests have been the most heavily investigated with nanohoop macrocycles, reports of other guests such as pyridiniums, [n]CPPs themselves, corannulene, and cations are beginning to emerge.[54]

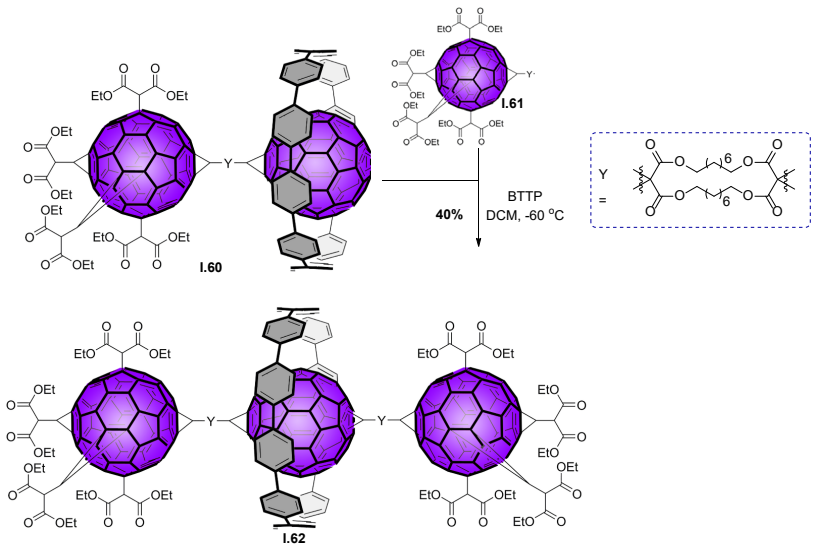

Figure 1.15. Von Delius's synthetic fullerene-templated approach toward [10]CPP [2]Rotaxane **I.62**.

While reports on the supramolecular chemistry this class of macrocycle are only beginning to emerge, the current examples suggest they hold great potential. The ability to impart regioselectivity in fullerene chemistry for example may enable more facile synthesis of fullerene derivatives. On the other hand, the seemingly frictionless motion observed in the mechanically interlocked variants may lead to unusual dynamics in molecular machines. Since the initial report in 2008, there has been a tremendous advance in the ability to functionalize the nanohoop backbone which has ultimately allowed for these

reports to emerge. The features ultimately render these macrocycles as fascinating candidates as new building blocks in supramolecular chemistry.

1.6. Conclusion

By perfecting the balance between covalent and non-covalent interactions, synthetic chemists have gained access to molecular architectures that would be otherwise inaccessible. These structures have displayed unusual chemical and physical properties which have in turn been leveraged to study phenonema such as aromaticity and antiaromaticty at the nanometer scale. While the reports concerning the supramolecular chemistry of nanohoops are just beginning to emerge, the current examples strongly suggest unusual chemical properties exist within these fascinating targets. It should also be noted that a majority of the reports concerning the supramolecular chemistry of nanohoops involve complexation with fullerene-type guests and those that involve metal-templation are limited, despite the demonstrated power in template-directed synthesis. With this in mind, exploring how metal-coordination can be leveraged with nanohoop macrocycles is a primary focus of this dissertation.

1.7. Bridge to Chapter II

This chapter highlights how weak interactions can be used to construct a variety of complex molecules that would otherwise be inaccessible. In many cases, access to these structures enables investigations into interesting phenomena, such as aromaticity and antiaromaticity on nanometer sized assemblies. Our ability to investigate these types of structures as well as new architectures depends on the molecular components and synthetic

methods available to prepare them. Given that the underlying electronic structure gives rise to the many of the observed properties, the next chapter provides a more detailed discussion of how to design the energy levels of frontier molecular orbitals in [n]CPPs and their derivatives.

CHAPTER II

SYNTHESIS AND CHARACTERIZATION OF A HIGHLY STRAINED DONOR-ACCEPTOR NANOHOOP

From Van Raden, J. M.; Darzi, E. D.; Zakharov, L. N.; Jasti, R. *Org. Biomol. Chem.* **2016**, *14*, 5721-5727. Further permissions related to the use of the material excerpted in this chapter should be directed to the RSC. This manuscript was written by myself with editorial assistance from Professor Ramesh Jasti and Dr. Evan Darzi. Experimental work in this chapter was performed by myself or Dr. Evan Darzi.

A highly-strained, nitrogen-doped cycloparaphenylene (CPP), aza[6]CPP, was synthesized and then converted to a donor–acceptor nanohoop, *N*-methylaza[6]CPP, via alkylation of the nitrogen center. The energy levels of the lowest unoccupied molecular orbital (LUMO) and the highest occupied molecular orbital (HOMO) for both molecules were then probed by cyclic voltammetry (CV), which revealed that the donor–acceptor nanohoop had a significantly lower LUMO energy relative to [6]CPP and aza[6]CPP. Density functional theory (DFT) revealed that the donor–acceptor nanohoop underwent a redistribution of the frontier molecular orbital (FMO) density such that a significant portion of the LUMO density resided upon the electron-deficient nitrogen-containing ring. This localization of LUMO density caused a large lowering in the LUMO energy of nearly a full electron volt, while the HOMO energy was less affected due to a large centralization of the FMO on the electron-rich phenylene backbone. This ultimately resulted in a net lowering of the HOMO–LUMO energy gap which was observed both experimentally and computationally. In addition, *N*-methylaza[6]CPP has a significantly

lower energy LUMO than N-methylaza[8]CPP, illustrating that the FMO levels of donor–acceptor nanohoops can be tuned by adjusting the hoop size.

2.1. Introduction

Organic small molecules and polymers have been heralded as attractive materials for use in electronic devices such as organic field-effect transistors (OFETs) and organic photovoltaics (OPVs) due to their mechanical flexibility, ease of design, and potential for low-cost production methods.[1-3] The advent of new molecular architectures with unique optoelectronic properties is essential for the further development of these technologies. CPPs, or nanohoops, are cyclic arrays of [*n*]*para*-linked benzene rings, where *n* denotes the number of benzene rings that comprise the hoop.[4-7] With decreasing *n*, the nanohoops begin to adopt highly strained conformations that force the adjacent phenyl rings to have reduced dihedral angles. The reduced dihedral angles of the smaller CPPs along with the distortion of the aromatic units ultimately result in a decreased HOMO–LUMO energy gap. This trend is in direct contrast to that of flat aromatics, where an extension of the π-system results in a decreased HOMO–LUMO energy gap.[8] Moreover, the curved architecture of CPPs decreases intermolecular aggregation, increasing their solubility in organic solvents. Due to the increased solubility, as well as the ability to tune the HOMO–LUMO energy levels, fluorescence emission, redox potential, and solid-state morphology via adjustments in the nanohoop diameter, CPPs are emerging as attractive materials for use in organic electronics.

Our group[9] and others[10,11] have demonstrated that cyclic systems such as CPPs and conjugated corrals can act as new donor–acceptor scaffolds (**Figure 2.1**). Our approach

relied on the common strategy of hetereoatom-doping[12-14], where nitrogen atoms were incorporated into the backbone of [8]CPP. In our previous study, two new nanohoops, aza[8]CPP and 1,15-diaza [8]CPP as well as their alkylated analogues, *N*-methylaza[8]CPP and *N,N*-dimethylaza[8]CPP, were prepared and characterized. Alkylation of the nitrogen center caused the LUMO energy level to lower, but left the HOMO energy levels essentially unaffected, resulting in a dramatically decreased HOMO– LUMO energy gap. Through DFT calculations, it was discovered that a majority of the LUMO density was localized around the pyridinium center (acceptor) while the HOMO density was evenly distributed over the phenylene backbone (donor). The large decrease in LUMO energy was then attributed to the increased orbital density around the nitrogen atom.

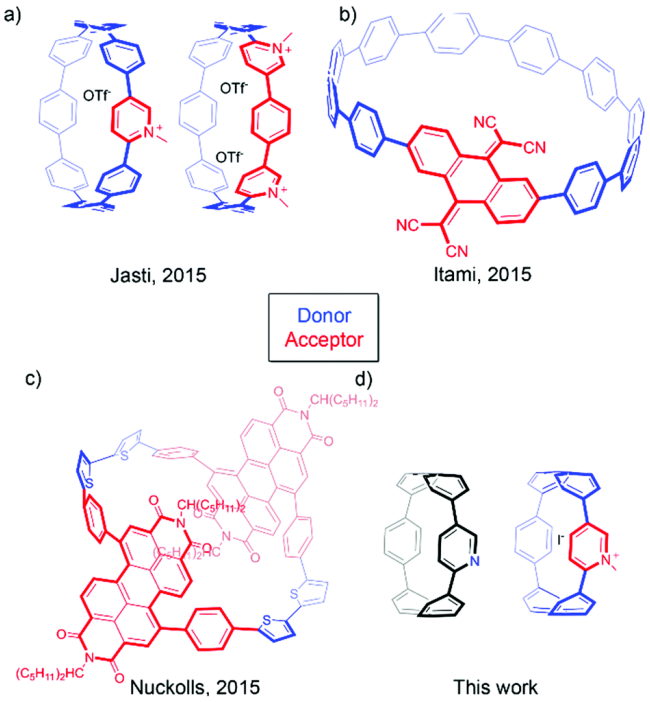

Figure 2.1 Donor–acceptor nanohoops with the donor highlighted in blue and the acceptor highlighted in red (a) N-methylaza[8]CPP and N,N-dimethyl-1,15-diaza[8]CPP (b) cyclo[10]paraphenylene-2,6-tetracyanoanthraquino-dimethylene (c) acceptor–donor–acceptor–donor conjugated corral (d) Aza[6]CPP and N-methylaza[6]CPP (this work).

In all carbon CPPs, a reduction in nanohoop diameter leads to a higher HOMO energy and lower LUMO energy.[8] To explore how the HOMO and LUMO energies can be further tuned in donor–acceptor CPPs, we wanted to investigate a smaller nitrogen-doped CPP. Herein, we report the synthesis, characterization, and computational studies of nitrogendoped, aza[6]CPP as well the donor–acceptor nanohoop, *N*-methylaza[6]CPP. Our studies illustrate how the macrocycle size can be used to tune the HOMO–LUMO properties in donor–acceptor nanohoops.

2.2. Results and Discussion

CPPs are highly strained molecules, with the magnitude of strain becoming larger as the diameter is decreased.[8] Using homodesmotic reactions, aza[6]CPP was determined to have 98.3 kcal mol^{-1} of strain energy, similar to that of [6]CPP at 97.0 kcal mol^{-1}.[15] The synthetic strategy used to prepare this challenging target is illustrated in **Figure 2.2**. The route utilizes the increased reactivity of aryl bromides relative to aryl chlorides in both lithium–halogen exchange and Suzuki–Miyaura cross-coupling reactions. The synthesis was begun by preparing quinol **II.1**, as previously reported.[9] Addition of 4-bromophenyllithium to deprotonated quinol **II.1**, followed by methylation delivered tetramethyl ether **II.2** as a single diastereomer in 55% yield over two steps. Conversion of **II.2** to dihalide **II.3** was accomplished under Suzuki–Miyaura conditions. The macrocycle is then accessed after sequential Miyaura borylation and an oxidative homocoupling reaction as we have described previously.[16] Its noteworthy that the initial report for the synthesis of [6]CPP relied on intermolecular Suzuki–Miyaura cross-coupling for macrocyclization and yielded the desired macrocycle in only 12%. By employing our

oxidative homocoupling strategy, we have dramatically improved access to the strained macrocycle **II.5** (51% yield) and have accomplished the key reaction at much lower temperatures (50 °C versus 130 °C). Moreover, the calculated strain of the macrocyclic precursor to [6]CPP is 37.5 kcal mol^{-1}, suggesting that the boronate homocoupling strategy presented here could potentially be used for a more efficient route to [6]CPP. Subjecting **II.5** to a sodium naphthalenide reduction at −94 °C provided highly strained aza[6]CPP **II.6**) as a red/orange solid in 45% yield. Previous work to generate donor–acceptor pyridinium nanohoops relied on methyl triflate for alkylation, which often yielded the undesired protonated product due to trace amounts of triflic acid. Aza[6]CPP was readily converted to donor–acceptor nanohoop **II.7** in 83% yield using methyl iodide in a microwave reactor as an operationally simpler alternative.

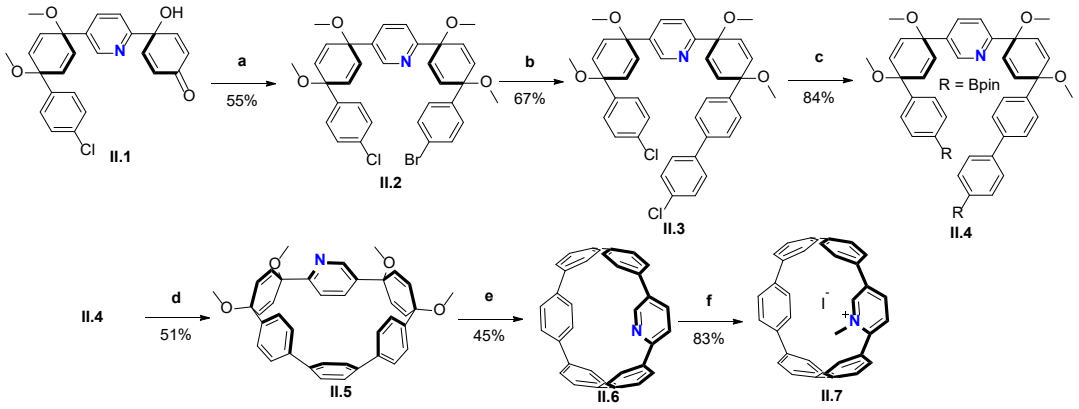

Figure 2.2. Reagents and conditions: (a) i. NaH, THF, −78 °C, 2 h; ii. 4-bromophenyllithium, THF, −78 °C, 2.5 h, iii. MeI, DMF, −78 °C → rt; (b) $Pd(dppf)Cl_2$, K_3PO_4, 4-chlorophenylboronic acid, 1,4-dioxane, 80 °C; (c) $Pd(OAc)_2$, SPhos, bis(pinacolato)diboron, K_3PO_4, 1,4-dioxane, 80 °C; (d) $Pd(PPh_3)_2Cl_2$, KF, $B(OH)_3$, O_2, THF/H_2O (10 : 1), 40 °C; (e) i. sodium naphthalenide, THF, −94 °C; ii. I_2, THF; (f) methyl iodide, dichloromethane, 100 °C, μW

In order to assess the electronic effects of doping [6]CPP with nitrogen, cyclic voltammetry was performed on **II.6** and **II.7** (all potentials are versus the ferrocene/ferrocenium couple). Previous work has shown that aza[8]CPP exhibits a pseudoreversible reduction event with a potential of −2.39 V.[9] The cyclic voltammogram (**Figure 2.8**) of aza[6]CPP (**II.6**) exhibited a single pseudo-reversible reduction potential of −2.18 V, confirming that a reduction in nanohoop diameter leads to a lowering of the LUMO energy, as was expected. Similarly, the oxidation potential of aza[6]CPP **II.7** was 0.670 V, whereas in the case of aza[8]CPP this oxidation falls outside of the solvent window and we were not able to obtain a value. Again, as expected, this illustrates that smaller nanohoops have higher HOMO energy levels than larger nanohoops. To ascertain how the HOMO and LUMO energies are modulated by nitrogen incorporation in the smaller nanohoop series, the reduction and oxidation potentials of **II.6** and **II.7** can be compared to those of all-carbon [6]CPP. The reduction potential of **II.6** (−2.18 V) is very similar to the value obtained for [6]CPP (−2.13 V). [6]CPP has a reversible oxidation at 0.440 V (ref. 17) while **II.6** has a non-reversible oxidation peak with an onset potential at 0.670 V. This suggests that the LUMO energy is not strongly altered by the inclusion of nitrogen and the HOMO energy is marginally lowered. Taken together, this data demonstrates that the simple inclusion of one nitrogen atom into [6]CPP does not significantly alter the HOMO and LUMO energies. Once converted to the donor–acceptor nanohoop (**II.7**), however, a pronounced non-reversible reduction event occurs (**Figure 2.9**) with an onset potential of −1.42 V, providing evidence for the markedly lowered LUMO energy compared to both [6]CPP and aza[6]CPP (**II.6**). The previously reported larger donor–acceptor nanohoop, N-methylaza[8]CPP, exhibited a non-reversible reduction

with an onset potential of −1.49 V, which suggests that the LUMO in **II.7** is lowered due to the decreased ring size. Two additional non-reversible reduction events were also observed, with the second at −2.47 V, and the third at −2.72 V. The oxidation of **II.7** showed a single non-reversible event with an onset potential of 0.660 V. The proximity of this oxidation potential to that of **II.7** (0.670 V) shows that the HOMO energy is largely unaffected upon alkylation and that alkylation primarily affects the LUMO energy resulting in a narrower HOMO– LUMO gap.

To understand the origin of these trends, we chose to study both **II.6** and **II.7** using DFT calculations at the B3LYP/6-31g* level of theory using Gaussian 09.[18] Ground state geometries were first minimized in the gas phase, followed by a solvated (acetonitrile) single point energy calculation using the conductor-like polarization continuum model (CPCM). This has been shown to give higher correlations between the computed FMOs and experimental reduction and oxidation potentials for both charged and neutral aromatic species.[19] Shown in **Figure 2.3** are the calculated frontier molecular orbitals (FMOs) and the energy levels for [6]CPP, **II.6**, and **II.7**. Comparing **II.7** with [6]CPP, the LUMO and HOMO energies are lowered by 0.35 eV and 0.07 eV, respectively, which give an energy gap of 2.84 eV (0.29 eV narrowing compared to [6]CPP). Interestingly, when making a similar comparison of [8]CPP to nitrogen-doped, aza[8]CPP, the LUMO energy is reduced by only 0.11 eV.[9] This suggests that the smaller nanohoop, **II.6**, is more sensitive to the addition of nitrogen. As is shown experimentally, incorporation of the pyridinium unit has a much more powerful effect on the orbital energies than the simple neutral pyridine, specifically upon the LUMO energy. In **II.7**, the LUMO energy is lowered by 1.08 eV, while the HOMO energy is only lowered by 0.479 eV. This selective LUMO energy

lowering results in a decreased energy gap to 2.53 eV (0.60 eV lower than [6]CPP). Localization of the FMOs provides a good rationale for the observed behavior. In **II.6**, the HOMO and LUMO orbital density is symmetrically distributed while in **II.7** the positively charged pyridinium moiety contributes significantly more to the LUMO than the HOMO, and therefore the energy level of the LUMO is lowered more dramatically than in the case of the HOMO. Interestingly, the HOMO energy in **II.6** is slightly less (0.03 eV) than the HOMO energy observed in *N*-methylaza[8]CPP, although a priori one would expect the smaller hoop to have the higher HOMO.[9] Due to the smaller size of **II.6**, however, the orbital coefficient of the HOMO resides slightly more on the nitrogen containing ring than in the larger hoop, which leads to this counterintuitive result. Importantly, the HOMO–LUMO energy levels can be fine-tuned by both heteroatom/acceptor incorporation as well as by the nanohoop size in a predictable manner.

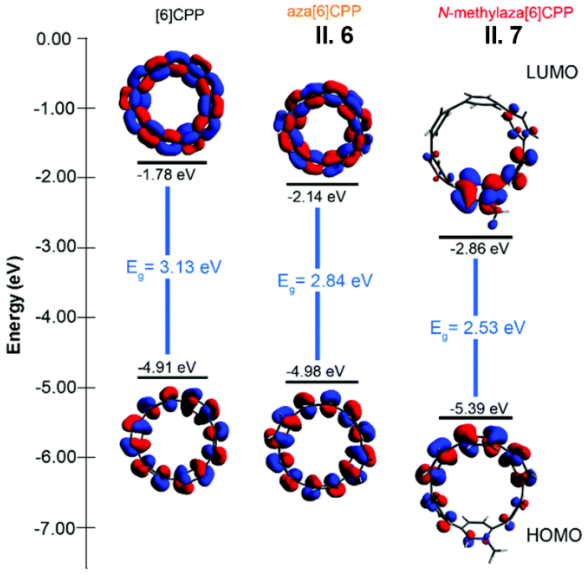

Figure 2.3. DFT calculated frontier molecular orbitals of (from left to right) [6]CPP, aza[6]CPP **II.6**, and *N*-methylaza[6]CPP **II.7**.

To explore the impact of nitrogen incorporation on the photophysical properties of the smaller nitrogen-doped nanohoops, UV-Visible spectroscopy was carried out on both **II.6** and **II.7**. The UV-Vis spectra of [6]CPP, aza[6]CPP, and *N*-methylaza[6] CPP in dichloromethane are shown in **Figure 2.4**. The all carbon nanohoop, [6]CPP, has a maximum absorption at 338 nm.[17] Nitrogen-doped nanohoop, **II.6**, shares a similar absorption maximum of 342 nm ($\varepsilon = 5.50 \times 10^4$ M^{-1} cm^{-1}) and its methylated analogue, **II.7**, also has a similar absorption maximum centered at 343 nm ($\varepsilon = 2.30 \times 10^4$ M^{-1} cm^{-1}). All three CPPs ([6]CPP, **II.6**, and **II.7**) also show minor absorptions in the 350–600 nm range. Lastly, there was pronounced broadening of the absorption of **II.7** that extended its absorption into the visible region. The absorption maximum of CPPs is typically size-independent, with all CPPs sharing a common absorbance maximum of approximately 340 nm.[6] Through TD-DFT, the Yamago group has assigned this shared maximum to a combination of HOMO−1 to LUMO, HOMO−2 to LUMO, HOMO to LUMO+1, and HOMO to LUMO+2 transitions.[20] Likewise, we used TD-DFT to assign the observed transitions in **II.6** and **II.7** (**Figure 2.10**). Given the high symmetry of their molecular orbitals, the HOMO–LUMO transitions in the all carbon CPPs are Laporte forbidden and do not contribute to the absorption maximum.[21] Interestingly, despite being forbidden, the HOMO–LUMO transitions are observed experimentally (minor absorptions in the 350–600 nm range), albeit with low extinction coefficients. This was corroborated with TD-DFT, where the calculated oscillator strengths, *f*, for the HOMO–LUMO transition are at or near 0, illustrating the high symmetry of their molecular orbitals. While [6]CPP has $f = 0$, the nitrogen doped **II.6** and **II.7** are non-zero, with $f = 0.003$ and $f = 0.022$, respectively. Addition of nitrogen into these systems causes a minor breakage of molecular orbital

symmetry rendering the HOMO–LUMO transition allowed (albeit weak), with the effect being stronger in the case of **II.6** due to the addition of the methyl group. Computationally, the HOMO–LUMO absorption also red-shifts from **II.6** (551 nm) to **II.7** (619 nm), as would be expected given the narrowing of the HOMO–LUMO energy gap. Experimentally, this was also observed, with **II.6** at 463 nm and **II.7** at 560 nm. Through TD-DFT, the broadened absorption of **II.6** was assigned to HOMO−1 to LUMO and HOMO to LUMO+1 transitions (412 nm, f = 0.278). This has been observed in previous work with the larger donor–acceptor nanohoops.[9,22] Similar to [6]CPP, no fluorescence was observed for either **II.6** or **II.7**.[17,23] All reports thus far have revealed that, with the exception of [6]CPP, the solid-state packing of CPPs is dominated by a herringbone-type motif.[8, 24, 25] Anomalously, [6]CPP adopts a unique columnar-like packing style, with the nanohoops arranging into long tube-like channels.

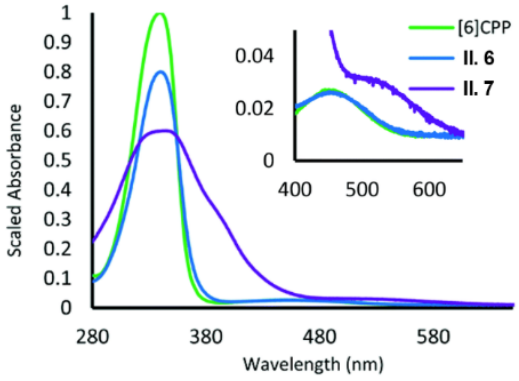

Figure 2.4. Scaled (for clarity) absorption spectrum of [6]CPP (green), aza[6]CPP **II.6** (blue), and *N*-methylaza[6]CPP **II.7** (purple) in dicholoromethane. Expanded plot shows HOMO–LUMO transitions.

To explore the impact of nitrogen on the solid-state morphology of [6]CPP, attempts were made to obtain X-ray quality crystals of both **II.6** and **II.7**. Despite

numerous attempts, suitable crystals of **II.7** have been elusive thus far, however single-crystals of **II.6** were readily collected through slow evaporation. Illustrated in **Figure 2.5** are the intermolecular contacts observed in the packing motif, torsional angles, as well nanohoop diameter in the ORTEP. The nitrogen atom in **II.6** was found to be disordered over all 24 possible locations. Similar to [6]CPP, **II.6** packs into long columnar-like channels, with carbons of neighboring channels separated by 3.49 Å. Both the diameter of the hoop (7.85 Å) and torsional angles (24.2° and 24.4°) were found to be slightly smaller than that of [6]CPP, likely due to the distribution of the nitrogen over the 24 carbon positions.17 This suggests that the 6-ring sized nanohoops all favor the columnar packing. More studies in regard to this unique solid-state packing are warranted.

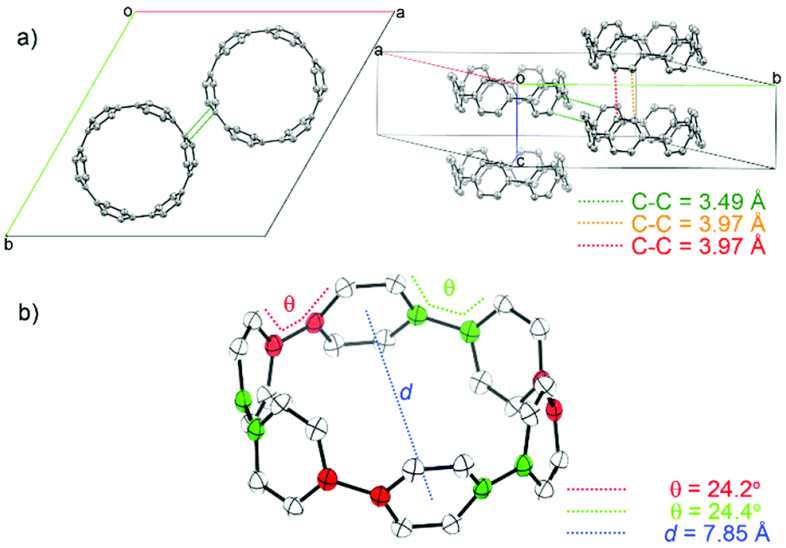

Figure 2.5. (a) View of packing arrangement of **II.6** in *c* axial direction (left) and *cb* plane (right) and (**b**) ORTEP (50% probability) of **II.6** showing torsional angles (Θ) and nanohoop diameter (*d*). Hydrogens omitted for clarity.

2.3. Conclusions

In summary, two new nitrogen-doped cycloparaphenylenes have been successfully

synthesized and characterized. The optoelectronic properties of aza[6]CPP (**II.6**) showed a strong resemblance to [6]CPP whereas the N-methylaza[6]CPP (**II.7**) showed a broadened absorption into the visible range. Electrochemistry provided evidence for a decreased LUMO in N-methylaza[6]CPP relative to [6]CPP and aza[6]CPP, while the HOMO energy remained fairly constant resulting in a decreased HOMO–LUMO gap. The lowering of the LUMO in donor–acceptor nanohoops can be enhanced by decreasing the size (N-methylaza[8]CPP versus N-methylaza[6]CPP). All of these properties were investigated and rationalized through DFT and TD-DFT calculations. The solid-state morphology of aza[6]CPP displayed virtually no difference from [6]CPP demonstrating that incorporation of the nitrogen heteroatom does not disrupt the unique columnar packing motif observed.

2.4. Experimental Sections

2.4.1. General Experimental Details

^{1}H NMR spectra were recorded at 500 MHz on a Varian VNMR spectrometer or on a Bruker 500 MHz. All ^{1}H NMR spectra are referenced to TMS (δ 0.00 ppm) or CH_2Cl_2 (δ 54.0 ppm). All ^{13}C NMR spectra are referenced to a residual $CHCl_3$ (δ 77.0 ppm). All reagents were obtained commercially. All glassware was flame-dried and cooled under an inert atmosphere of nitrogen unless otherwise noted. Moisture sensitive reactions were carried out under an inert atmosphere of nitrogen using the standard syringe/septa technique. Absorbance spectra for 8 and 9 were collected in dichloromethane in a 1 cm quartz cuvette on an Agilent Cary 60 UV-Vis spectrophotometer. Cyclic voltammetry experiments (scan rate = 100 mV s^{-1}) were performed using a CH Instruments 1200B potentiostat running CH Instruments software. Measurements were conducted in degassed

0.100 M nBu$_4$PF$_6$ (recrystallized 3× from methanol) in tetrahydrofuran under an N_2 atmosphere with a glassy carbon working electrode, platinum counter electrode, and an Ag reference electrode. The ferrocene/ferrocenium couple was used as an internal reference. Compounds 1, 2, 3, and 4 were prepared according to Jasti *et al.*[9]

2.4.2. Synthetic Details

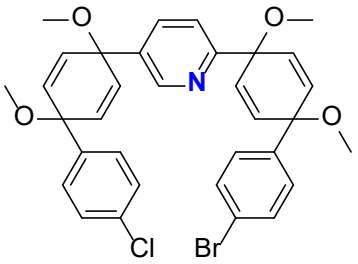

II.2

A flame-dried 1 L flask was charged with **II.1** (30.0 g, 68.9 mmol, 1.00 equiv.) and 500 mL THF and was then cooled to −78 °C for 1 h. To this flask was added NaH (3.30 g, 60% suspension in mineral oil, 82.8 mmol, 1.20 equiv.), which resulted in a slurry. This reaction was allowed to proceed for 2 h. In a separate flame-dried 2 L flask was added 1,4-dibromobenzene (35.8 g, 151.7 mmol, 2.20 equiv.) followed by 1 L THF. After cooling at −78 °C for 1 h, *n*-BuLi (2.5 M in hexanes, 60.7 mL, 151.7 mmol, 2.20 equiv.) was added dropwise over 45 minutes which, after stirring for an additional 15 minutes, resulted in a cloudy-white slurry. After generating the lithiate for 15 minutes, the slurry containing **II.1** was rapidly transferred *via* a cannula to the 2 L flask containing the lithiate. After 1 hour of stirring, MeI (42.9 mL, 689.7 mmol, 10.0 equiv.) was added, followed by DMF (150 mL) to the 2 L flask. After 18 h of stirring, the reaction was quenched with H_2O (150 mL) and allowed to warm to room temperature. THF was then removed *via* rotary evaporation and the remaining aqueous phase was extracted with DCM (3 × 200 mL). The

combined organic phases were washed using 5% LiCl (3 × 100 mL), H_2O (100 mL), and brine (100 mL), and dried over sodium sulfate. The solvent was removed under reduced pressure to afford crude **II.2** as a red-orange oil. Addition of ethanol to the crude oil precipitated **II.2** as a tan solid, which was the collected *via* vacuum filtration and washed with cold ethanol (50.0 mL) (23.6 g, 55%). ^{1}H NMR (500 MHz, $CDCl_3$) δ(ppm) 8.60 (d, J = 1.2 Hz, 1H), 7.64 (dd, J = 8.1, 1.9 Hz, 1H), 7.51 (d, J = 8.6 Hz, 3H), 7.39 (d, J = 8.6 Hz, 2H), 7.35–7.27 (m, 4H), 6.16–6.02 (m, 8H), 3.48–3.40 (m, 12H). ^{13}C NMR (126 MHz, $CDCl_3$) δ(ppm) 148.34, 141.35, 141.25, 138.48, 136.37, 134.73, 134.73, 133.80, 132.89, 132.50, 128.79, 128.63, 127.66, 127.42, 127.21, 74.09, 73.23, 52.10, 51.98. IR (neat): 3070, 2941, 2822, 1590, 1560, 1471, 1401, 1368, 1228, 1177, 1080, 1066, 1012, 984, 951, 855, 824 cm^{-1}. δ HRMS (TOF, ES+) (m/z): $[M + Na]^+$ calculated for $C_{33}H_{31}NO_4ClBrNa$, 642.1023; found, 642.1028.

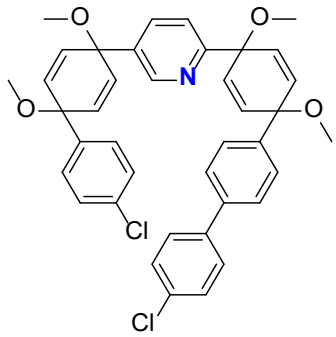

II.3

To a 1 L flame-dried flask were added $Pd(dppf)Cl_2$ (0.835 g, 1.14 mmol, 0.04 equiv.), 4-chlorophenylboronic acid (18.87 g, 114.1 mmol, 4.00 equiv.), and **II.2** (17.7 g, 28.5 mmol, 1.00 equiv.). The flask was evacuated and then back-filled with nitrogen. This was repeated 5 times, at which point dioxane (250 mL) and vigorously nitrogen-spared 2 M K_3PO_4 (25.0 mL, 50.0 mmol, 1.75 equiv.) were added *via* a syringe to the flask resulting in a yellow

transparent solution. The reaction was then placed into an 80 °C oil bath, at which point the solution turned dark red over a period of 10 minutes. After stirring for 18 h, the black solution was brought to room temperature and the dioxane was removed under reduced pressure to afford a black oil. The oil was dissolved in DCM (250 mL) and filtered through Celite/carbon. The resulting red/yellow filtrate was then added to a separatory funnel, washed with water (3 × 100 mL), brine (1 × 50 mL), and then dried over sodium sulfate. The solvent was then removed under reduced pressure to afford an orange oil, which was chromatographed on silica (ethyl acetate/hexanes = 3 : 7). The combined fractions were then washed with ethanol and filtered to give **II.3** as a white solid (12.1 g, 67%). ^{1}H NMR (500 MHz, $CDCl_3$) δ(ppm) 8.65 (d, J = 1.2 Hz, 1H), 7.68–7.64 (m, 3H), 7.54–7.45 (m, 5H), 7.38 (d, J = 8.5 Hz, 2H), 7.33–7.25 (m, 4H), 6.19–6.07 (m, 8H), 3.49 (s, 6H), 3.43 (s, 3H), 3.41 (s, 3H). ^{13}C NMR (126 MHz, $CDCl_3$)δ(ppm) 161.23, 147.21, 142.81, 141.63, 139.41, 138.95, 137.83, 134.74, 134.56, 134.41, 133.80, 133.56, 132.82, 132.02, 128.33, 127.28, 126.77, 126.71, 120.42, 75.90, 74.90, 74.14, 73.41, 52.03, 51.95. IR (neat): 3068, 2943, 2823, 1595, 1564, 1487, 1471, 1451, 1393, 1262, 1226, 1178, 1073, 1019, 1011, 1005, 987, 950, 853, 840, 827, 821, 771, 753, 729 cm^{-1}. δ HRMS (TOF, ES+) (m/z): [M + Na]$^{+}$ calculated for $C_{39}H_{35}NO_4Cl_2Na$, 674.1841; found, 674.1856.

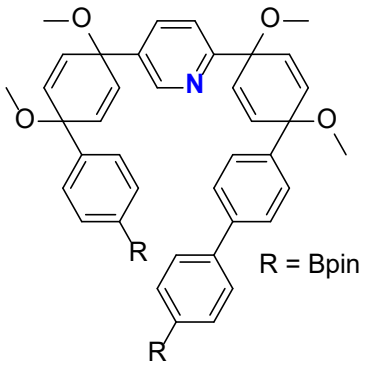

II.4

To a 1 L flame-dried flask was added $Pd(OAc)_2$ (0.390 g, 1.76 mmol, 0.100 equiv.), 2-dicyclohexylphosphino-2′,6′dimethoxybiphenyl (1.80 g, 4.40 mmol, 0.250 equiv.), bis(pinacolato)diboron (22.3 g, 8.80 mmol, 5.00 equiv.), **II.3** (11.5 g, 17.6 mmol, 1.00 equiv.), and K_3PO_4(22.4 g, 106 mmol, 6.00 equiv.). After the solids were added, the flask was evacuated and backfilled with nitrogen 5 times. Dioxane (300 mL) was then added to the flask resulting in an orange solution, which was then placed into an 80 °C oil bath, at which point the solution gradually became green. After 18 h, the resulting black solution was brought to room temperature and the solvent was removed under reduced pressure. The resulting black solid was then dissolved in DCM (300 mL) and filtered through celite/activated carbon. The resulting yellow filtrate was then added to a separatory funnel, washed with water (3 × 150 mL), brine (1 × 100 mL), and then dried over sodium sulfate. After removing the organic solvent *via* rotary evaporation, the resulting orange solid was filtered through a short silica plug (wet loaded with DCM, eluted with 3 : 7 ethyl acetate : hexanes), followed by removal of the organic solvent *via* rotary evaporation. The resulting white solid was then washed with hot ethanol (100 mL) to give **II.4** as a white solid. The solid was collected *via* vacuum filtration and washed with cold ethanol (50 mL) (2.82 g, 84%). ^{1}H NMR (500 MHz, $CDCl_3$) δ(ppm) 8.72 (d, J = 1.2 Hz, 1H), 7.86 (d, J = 7.7 Hz, 2H), 7.78 (d, J = 7.8 Hz, 2H), 7.65 (d, J = 8.1 Hz, 2H), 7.59–7.53 (m, 5H), 7.46 (d, J = 8.0 Hz, 1H), 7.39 (d, J = 7.8 Hz, 2H), 6.21–6.13 (m, 6H), 6.06 (d, J = 10.0 Hz, 2H), 3.49 (s, 3H), 3.48 (s, 3H), 3.44 (s, 3H), 3.42 (s, 3H), 1.36 (s, 12H), 1.31 (s, 12H). ^{13}C NMR (126 MHz, $CDCl_3$) δ(ppm) 161.01, 147.38, 145.94, 143.63, 142.74, 139.89, 137.89, 135.16, 135.05, 134.69, 134.39, 134.14, 133.98, 132.53, 132.03, 127.01, 126.59, 126.38, 125.13, 120.25, 83.74, 75.88, 74.95, 74.63, 73.62, 52.03, 51.98, 24.84, 24.80. IR (neat):

3053, 2977, 2935, 2823, 1609, 1560, 1525, 1470, 1448, 1390, 1356, 1318, 1273, 1213, 1166, 1142, 1125, 1081, 1034, 1015, 962, 949, 858, 821, 760, 755, 731 cm^{-1}. HRMS (TOF, ES+) (*m*/*z*): $[M + Na]^+$ calculated for $C_{51}H_{59}NO_8B_2Na$, 858.4341; found, 858.4315.

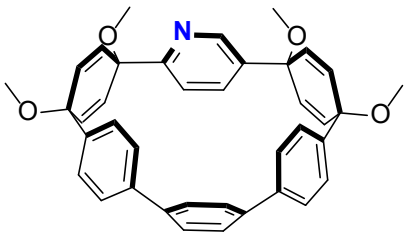

II.5

To a 2 L flask were added **II.4** (1.00 g, 1.20 mmol, 1.00 equiv.), $Pd(PPh_3)_2Cl_2$ (252 mg, 0.359 mmol, 0.300 equiv.), boric acid (370 mg, 5.99 mmol, 5.00 equiv.), and 1 L of THF. This was then placed in an oil bath at 40 °C. The bright yellow solution was then vigorously sparged with O_2 for 1 h. In a separate 250 mL flask was added KF (138 mg, 2.39 mmol, 2.00 equiv.), and 100 mL of H_2O, which was then sparged with O_2 for 1 h. The KF solution was then transferred to the 2 L flask resulting in a bright orange solution. After 2 h of stirring at 40 °C, the THF was removed under reduced pressure. The aqueous phase was then extracted with DCM (3 × 100 ml), followed by a washing of the combined bright orange organic phases with H_2O (3 × 50 mL), brine (1 × 50 mL), and dried over sodium sulfate. After removal of solvent under reduced pressure, the resulting orange oil was purified by column chromatography (THF/DCM = 1 : 5) to give **II.5** as a tan/yellow solid (357 mg, 51%). ^{1}H NMR (500 MHz, $CDCl_3$) δ(ppm) 8.76 (d, J = 1.6 Hz, 1H), 7.46 (d, J = 2.3 Hz, 4H), 7.35–7.27 (m, 4H), 7.24–7.15 (m, 4H), 6.43 (dd, J = 8.2, 2.4 Hz, 1H), 6.31 (dd, J = 12.0, 10.3 Hz, 4H), 6.10 (dd, J = 8.3, 0.9 Hz, 1H), 5.94 (d, J = 10.4 Hz, 2H), 5.73 (d, J = 10.3 Hz, 2H), 3.45 (s, 3H), 3.44 (s, 3H), 3.35 (s, 3H), 3.30 (s, 3H). ^{13}C NMR (126

MHz, $CDCl_3$) δ(ppm) 159.38, 147.82, 141.71, 141.60, 139.87, 139.53, 137.88, 134.73, 134.44, 133.89, 132.05, 131.41, 128.96, 128.45, 128.34, 126.64, 119.86, 75.27, 74.25, 73.90, 73.24, 52.67, 52.64, 51.59, 51.24. IR (neat): 3053, 3025, 2978, 2934, 2894, 2820, 1589, 1580, 1449, 1394, 1370, 1318, 1263, 1230, 1173, 1119, 1070, 1004, 943, 815, 758, 720 cm^{-1}. MALDI-TOF (*m*/*z*): $[M + Ag]^+$calculated for $C_{39}H_{35}AgNO_4$ 689.58; found, 689.33.

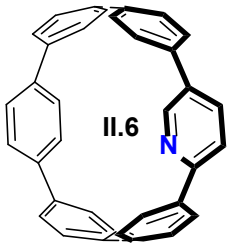

To a flame-dried 250 mL flask were added **II.5** (599 mg, 1.03 mmol, 1.00 equiv.) and THF (50 mL), which was then cooled to −94 °C for 1 h under N_2. Freshly prepared 0.5 M (in THF) sodium naphthalanide (42.0 mL, 21.0 mmol, 21.0 equiv.) was then added dropwise resulting in a dark purple solution to which, after 30 minutes of vigorous stirring, 1 M (in THF) I_2 (25.0 mL, 25.0 mmol, 25.0 equiv.) was added dropwise to afford an orange solution. The excess I_2 was then quenched with excess saturated sodium thiosulfate and the solution was allowed to warm to room temperature, which resulted in a bright red liquid. The THF was removed under reduced pressure and the resulting aqueous phase was extracted with DCM (3 × 50 mL), followed by a washing of the organic phases with H_2O (3 × 50 mL), brine (1 × 50 ml), and dried over sodium sulfate. The resulting bright red solid was chromatographed on silica (DCM/ethyl acetate/hexanes = 2 : 1 : 7) to afford **II.6** as red solid (201 mg, 43%). ^{1}H NMR (500 MHz, $CDCl_3$): δ(ppm) 8.95 (s, 1H), 8.35 (d, J = 9.1 Hz, 1H), 7.87–7.49 (m, 21H).^{13}C NMR (126 MHz, $CDCl_3$): δ(ppm) 152.27, 146.31,

136.77, 135.73, 135.71, 135.52, 135.46, 135.12, 135.02, 134.88, 134.24, 132.34, 130.82, 129.03, 129.01, 128.50, 128.45, 127.96, 127.89, 127.68, 127.47, 127.38, 127.34, 127.31, 127.23, 127.21, 127.19, 127.11, 126.76, 126.72, 126.38, 126.29, 126.04, 117.54.|| IR (neat): 3040, 2927, 2822, 1589, 1473, 1456, 1419, 1400, 1228, 1174, 1080, 1012, 950, 816, 755 cm^{-1}. δHRMS (TOF, ES+) (*m*/*z*): $[M + Na]^+$ calculated for $C_{35}H_{23}NNa$, 480.1728; found, 480.1746.

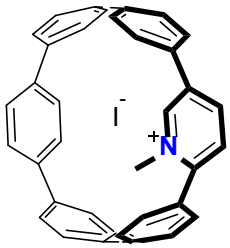

II.7

To a flame-dried 5 mL microwave tube equipped with a stir bar were added **II.6** (10.0 mg, 0.0219 mmol, 1.00 equiv.), 2.5 mL DCM, and MeI (1.50 mL, 24.1 mmol, 1.10 × 103 equiv.). The reaction vessel was heated to 100 °C for 11 h, at which point the vessel was allowed to cool to room temperature, followed by the removal of DCM and MeI *via* high vacuum equipped with a cold trap. The resulting black/brown solid was washed with ether (5 × 1 mL) and the remaining solid was filtered to afford **II.7** (11.4 mg, 83%) as a dark red solid.^{1}H NMR (500 MHz, CD_2Cl_2): δ(ppm) 9.72 (s, 1H), 8.34 (d, J = 8.4 Hz, 1H), 8.04 (d, J = 8.6 Hz, 1H), 7.90–7.43 (m, 19H), 7.37 (d, J = 9.4 Hz, 1H), 4.93 (s, 3H). ^{13}C NMR (126 MHz, CD_2Cl_2) δ(ppm) 149.19, 144.63, 141.49, 141.08, 139.79, 138.11, 136.78, 136.26, 135.97, 135.74, 135.33, 135.31, 135.20, 134.87, 132.85, 132.62, 132.27, 131.88, 131.16, 131.12, 130.83, 130.48, 130.16, 130.06, 128.55, 127.46, 126.48, 126.23, 126.14, 125.91, 125.72, 125.71, 125.63, 125.57, 49.00.|| IR (neat): 3025, 2981, 2937, 2897, 2821,

1658, 1651, 1473, 1449, 1394, 1262, 1175, 1119, 1077, 1017, 952, 823 cm^{-1}. HRMS (TOF, ES+) (*m*/*z*): $[M]^+$ calculated for $C_{36}H_{26}N$, 472.2065; found, 472.2082.

2.4.3. Optical Data

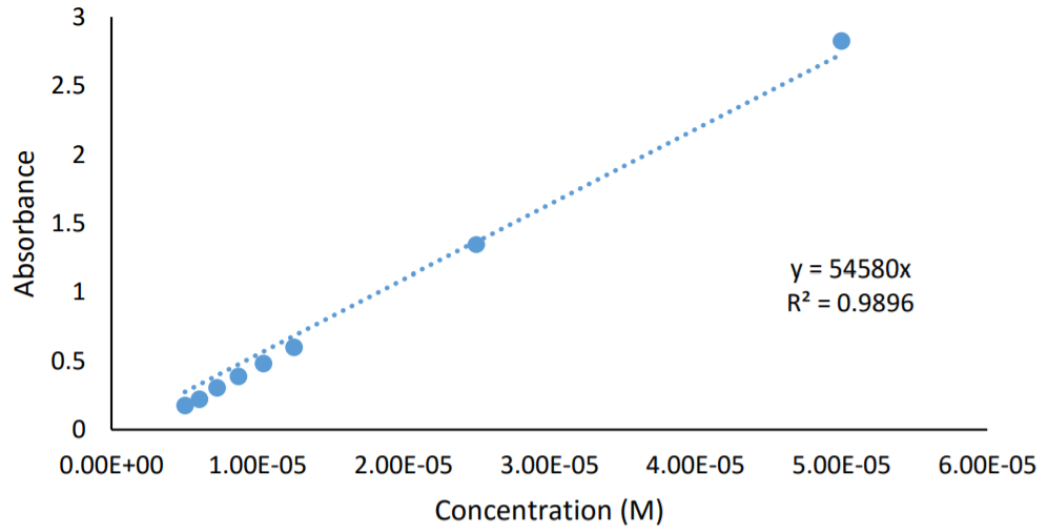

Figure 2.6. Beer-Lambert Plot of **II.6** at 342 nm ($\varepsilon = 5.5 \times 10^4\ M^{-1}\ cm^{-1}$)

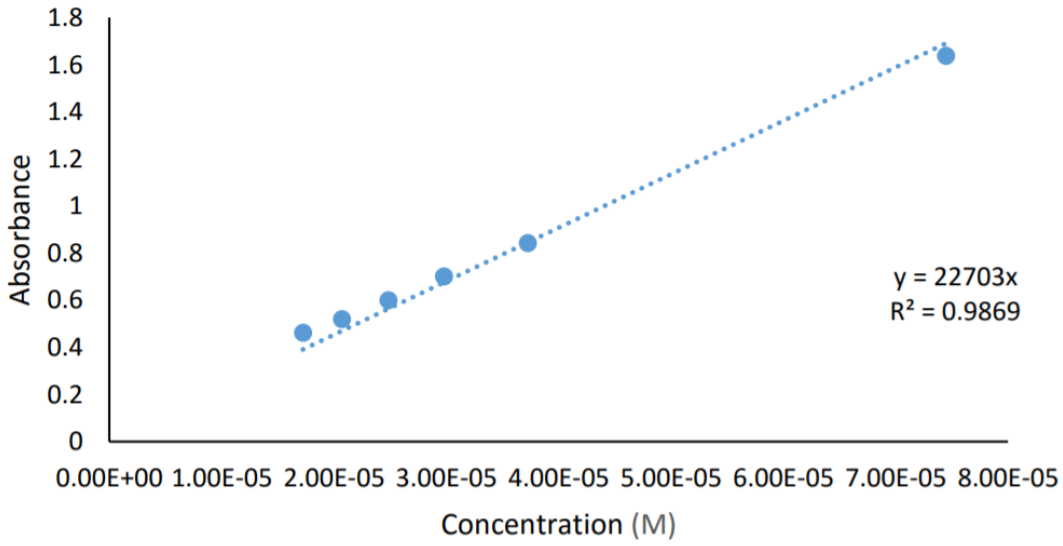

Figure 2.7. Beer-Lambert Plot of **II.7** at 342 nm ($\varepsilon = 5.5 \times 10^4\ M^{-1}\ cm^{-1}$)

2.4.4. Electrochemical Data

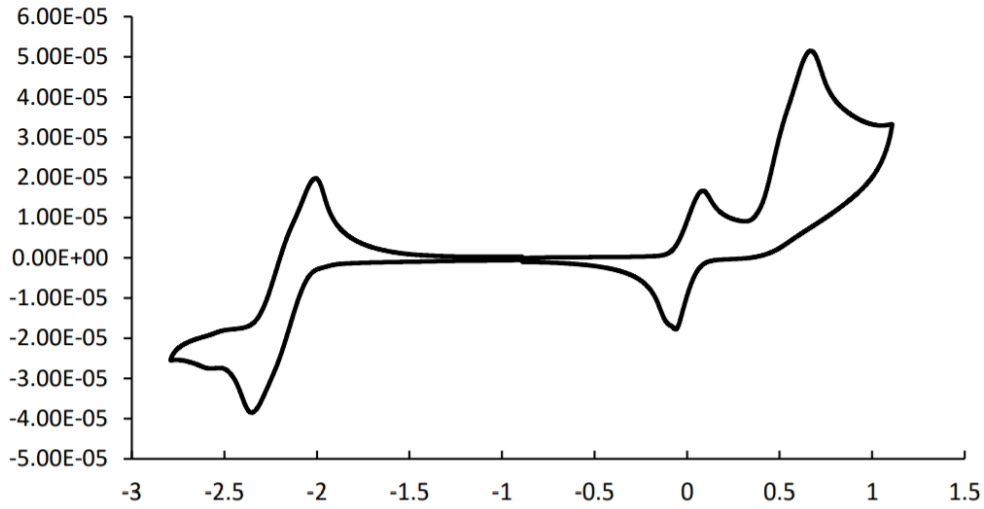

Figure 2.8. Cyclic voltammogram of **II.6** in THF (0.1 M tetrabutylammonium hexfluorophoshate) with ferrocene/ferrocenium added as internal standard.

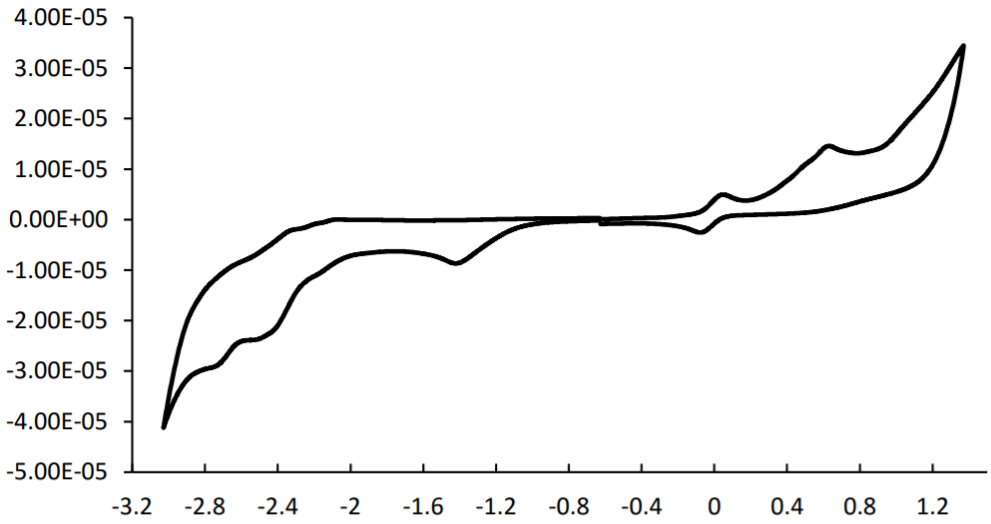

Figure 2.9. Cyclic voltammogram of **II.7** in THF (0.1 M tetrabutylammonium hexfluorophoshate) with ferrocene/ferrocenium added as internal standard.

2.4.5. Computational Data

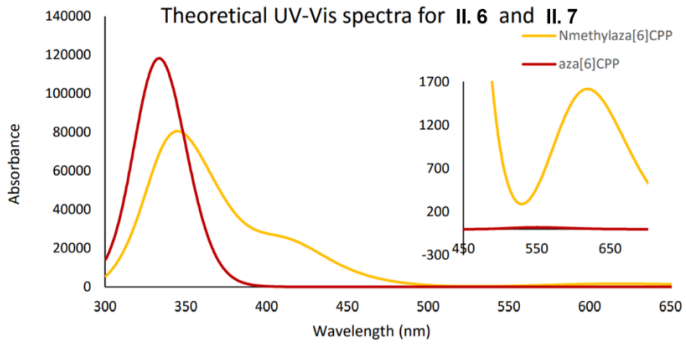

Figure 2.10. TD-DFT (B3LYP/6-31g*) plot for **II.6** and **II.7**.

Energy (cm^{-1})	Wavelength (nm)	Osc. Strength	Major contribs
18166.96	550.4499	0.0003	HOMO->LUMO (99%)
26780.21	373.41	0.0023	H-1->LUMO (45%), HOMO->L+1 (53%)
27754.54	360.3015	0.0093	H-2->LUMO (56%), HOMO->L+2 (41%)
28894.21	346.0902	0.0523	HOMO->L+3 (80%)
29428.95	339.8014	0.7775	H-1->LUMO (40%), HOMO->L+1 (40%)
30469.42	328.1979	0.878	H-2->LUMO (34%), HOMO->L+2 (53%)
30846.89	324.1818	0.061	HOMO->L+4 (73%)
31771.2	314.7504	0.0202	H-4->LUMO (10%), HOMO->L+5 (65%)
32549.54	307.224	0.1062	H-6->LUMO (16%), H-5->LUMO (38%), H-4->LUMO (19%)
33802.93	295.8323	0.0033	H-6->LUMO (20%), H-3->LUMO (57%)
34111.84	293.1533	0.0058	H-2->L+1 (46%), H-1->L+1 (15%), H-1->L+2 (28%)
34239.28	292.0622	0.0061	H-6->LUMO (18%), H-4->LUMO (19%), HOMO->L+4 (11%), HOMO->L+6 (17%)

Figure 2.11. Major transitions for **II.6** determined by TD-DFT using B3LYP/6-31g*

Energy (cm^{-1})	Wavelength (nm)	Osc. Strength	Major contribs
16154.59	619.0191	0.0223	HOMO->LUMO (97%)
22190.89	450.6355	0.0498	HOMO->L+1 (89%)
24221.8	412.8512	0.278	H-1->LUMO (91%)
26165.61	382.181	0.1353	H-2->LUMO (79%), HOMO->L+2 (16%)
27646.46	361.71	0.4701	H-2->LUMO (14%), H-1->L+1 (11%), HOMO->L+2 (72%)
29062.78	344.0827	0.2255	H-3->LUMO (10%), H-1->L+1 (30%), HOMO->L+3 (47%)
29405.56	340.0717	0.2205	H-3->LUMO (49%), H-1->L+1 (35%)
29635.43	337.4339	0.3963	H-3->LUMO (30%), H-1->L+1 (21%), HOMO->L+3 (43%)
30383.92	329.1214	0.0524	H-4->LUMO (79%)
31036.43	322.202	0.009	H-6->LUMO (19%), H-5->LUMO (57%)
31584.08	316.6152	0.0883	H-6->LUMO (15%), H-5->LUMO (18%), H-2->L+1 (58%)
31765.56	314.8064	0.0599	H-7->LUMO (25%), H-6->LUMO (41%), H-2->L+1 (18%)

Figure 2.12. Major transitions for **II.7** determined by TD-DFT using B3LYP/6-31g*

2.5. Bridge to Chapter III

This chapter highlights how the electronic structure of [n]CPPs differs from typical flat conjugated molecules. To fine-tune this electronic structure, we have shown that nitrogen incorporation can be leveraged to selectively reduce the LUMO energy levels, with the most pronounced effect coming from alkylation of the nitrogen center. Therefore, the nitrogen heteroatom can be viewed as an entry point for post-synthetic modification of the nanohoop framework. Encouraged by this observation as well the countless example of nitrogen-based coordination complexes, the next chapter focuses on how nitrogen-doped nanohoops can be used to construct new cylindrical coordination complexes.

CHAPTER III

2,2'-BIPYRIDYL-EMBEDDED CYCLOPARAPHENYLENES AS A GENERAL STRATEGY TO INVESTIGATE NANOHOOP-BASED COORDINATION COMPLEXES

From Van Raden, J. M.; Louie, S.; Zakharov, L. N.; Jasti, R. *J. Am. Chem. Soc.* **2018**, *139*, 2936-2939. Further permissions related to the use of the material excerpted in this chapter should be directed to the American Chemical Society. This manuscript was written by myself with editorial assistance from Professor Ramesh Jasti. Experimental work in this chapter was performed by myself, Shayan Louie, or Lev Zakharov.

Because of their unique cyclic architectures, tunable electronic properties, and supramolecular chemistries, cycloparaphenylenes (CPPs) have the potential to act as a new class of ligands for coordination cages, metal− organic frameworks, and small-molecule transition-metal complexes. However, currently there is no general strategy to coordinate the cyclic framework to a variety of metal centers. We report here a general and scalable synthetic strategy to embed 2,2′-bipyridine units into the backbone of CPPs. We use this approach to synthesize a 2,2′- bipyridine-embedded [8]CPP, which we show can successfully coordinate to both Pd(II) and Ru(II) metal centers. The resulting coordination complexes, a Pd(II)− nanohoop dimer and a bis(bipyridyl)ruthenium(II)-functionalized nanohoop, show unique solid-state and photophysical properties. This work provides a proof of concept for a general strategy to use nanohoops and their derivatives as a new class of ligands.

3.1. Introduction

The development of ligands with tunable electronic structures and unique three-dimensional molecular shapes has provided access to an abundance of metal coordination complexes with desirable properties for a wide range of applications. For example, the development of new redox-active ligands is a central driver in the fields of photocatalysis and photovoltaics.[1-3] In addition, the increase in functionalization of organic linker ligands[4,5] in metal−organic frameworks (MOFs) and coordination cages has enabled advanced functionality such as catalysis,[6,7] chemical sensing,[8] molecular recognition,[9,10] and energy transfer.[11] As many of the currently available ligands are centralized around a linear, flat aromatic framework,[5] the introduction of new cyclic ligand scaffolds—in particular those with radially oriented π systems—
would provide new metal− ligand architectures that would offer unique features, thereby furthering the development and application of large metal− ligand assemblies as well as small-molecule transition-metal complexes.

The [n]cycloparaphenylenes (CPPs),[12] or nanohoops, are composed of n benzene rings linked at the para positions, resulting in a rigid, three-dimensional, fully sp^2 -hybridized cylindrical architecture with a radially oriented π system. The unique geometry of CPPs provides novel electronic properties such as narrowing HOMO−LUMO energy gaps and red shifting fluorescence with decreasing size—a trend exactly opposite to that of linear analogues.[13] In addition, the radially oriented π systems provide a hydrophobic, electron-rich cavity that acts as a strong host for electron-poor guests such as C_{60}.[18-21] These diameter-dependent optoelectronic properties, coupled with the molecular recognition capabilities, position CPPs and related cyclic derivatives[22-25] as a new class of inherently

porous, cylindrical ligands with numerous potential applications. Using CPPs as ligands, however, is currently restricted to η-type coordination complexes[26,27] (**Figure 3.1**), which limits their use and potential as a general ligand class. An early report by the Itami group[28] suggested that embedding 2,2′-biypridyl units into the nanohoop framework is possible, but the reported synthetic route was not amenable to CPPs of different diameters and the reported nanohoop was only accessed in small quantities. Herein we illustrate a general synthetic method to access 2,2′-bipyridyl-embedded nanohoops in a size-selective[29] and scalable manner. By constructing a Pd(II) nanohoop dimer and a photosensitized Ru(II) nanohoop, we demonstrate that nanohoops can be used as ligands toward the construction of new cylindrical coordination cages as well as a novel photoactive transition-metal complexes with supramolecular capabilities.

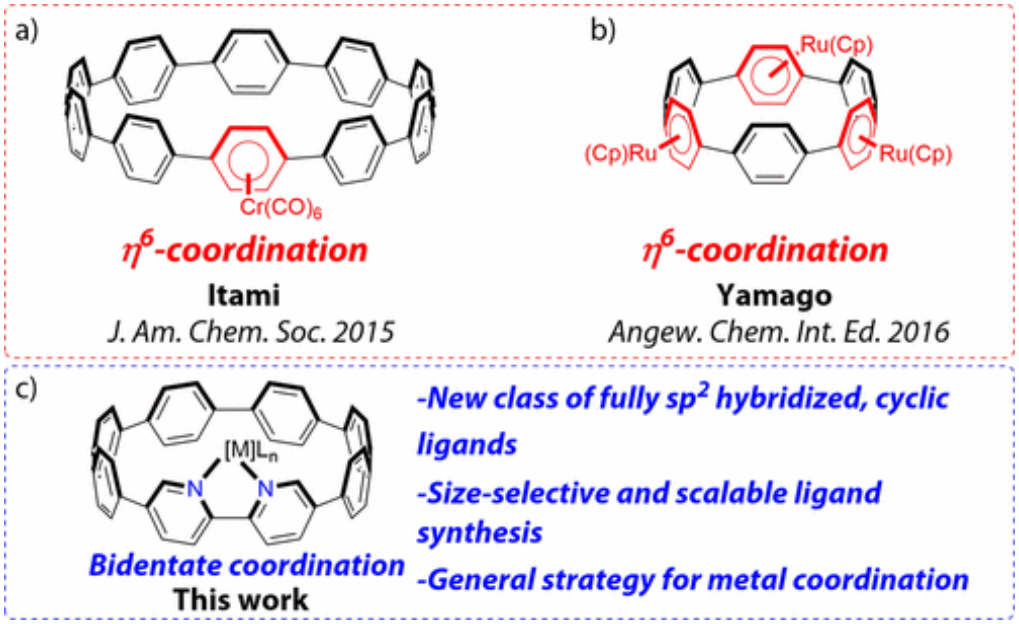

Figure 3.1. Current examples of metal–nanohoop coordination complexes.

3.2. Results and Discussion

Our investigations began by developing synthetic methodology that would allow 2,2′-bipyridyl-embedded CPPs to be accessed in a size-selective and scalable manner. Previous work by our group[12] and others[15] has shown that CPPs and related derivatives are readily accessed by the reductive aromatization of macrocycles containing cyclohexadienes as "masked" aromatic rings (e.g., structure **III.7** in **Scheme 3.1**). These relatively unstrained macrocycles can be prepared in a variety of sizes via aryl−aryl coupling reactions. We surmised that the most general synthetic strategy leading to the 2,2′-bipyridylembedded nanohoops would be one that formed the pyridine−pyridine linkage in the macrocyclization step. Because of the instability of 2-pyridylboranes,[30, 31] we targeted reductive couplings of pyridyl halides as the key cyclization step.[32-35] Yamago recently demonstrated that reductive homocoupling of aryl bromides can be used to prepare a precursor to [5]CPP.[15] In order to leverage previous methods relying on the orthogonal reactivity of aryl chlorides and bromides, we envisioned the reductive homocoupling of pyridyl chlorides as the key development for general access to the 2,2′-bipyridylembedded nanohoops. Guided by these thoughts as well as the work by Goldup[34] and Drew,[35] we prepared intermediate **III.6** with terminal pyridyl chloride units (**Scheme 3.1**) via Suzuki−Miyaura cross-coupling of bromide **III.5** and boronic ester **III.4** in good yield. Precursor **III.6** can be easily prepared on a multigram scale. After significant optimization of reductive nickel homocoupling conditions, we were then able to access macrocycle **III.7** in 57% yield. With macrocycle **III.7** in hand, we explored the reductive aromatization step and found that the mild H_2SnCl_4 strategy reported by Yamago[15] afforded the desired bipy-CPP ligand **III.8** in 61% yield over two steps. Noteworthy is the use of pseudodilution conditions for the macrocyclization step, which allows the ligand synthesis to be highly

scalable. Additionally, the use of pyridyl chlorides over bromides allows for orthogonal lithium−halogen exchange and Suzuki−Miyaura coupling for rapid access to the macrocyclic precursor. Moreover, this strategy can be expanded to a variety of 2,2′-bipyridylembedded nanohoops with different diameters using strategies we have developed for cycloparaphenylene synthesis.[17]

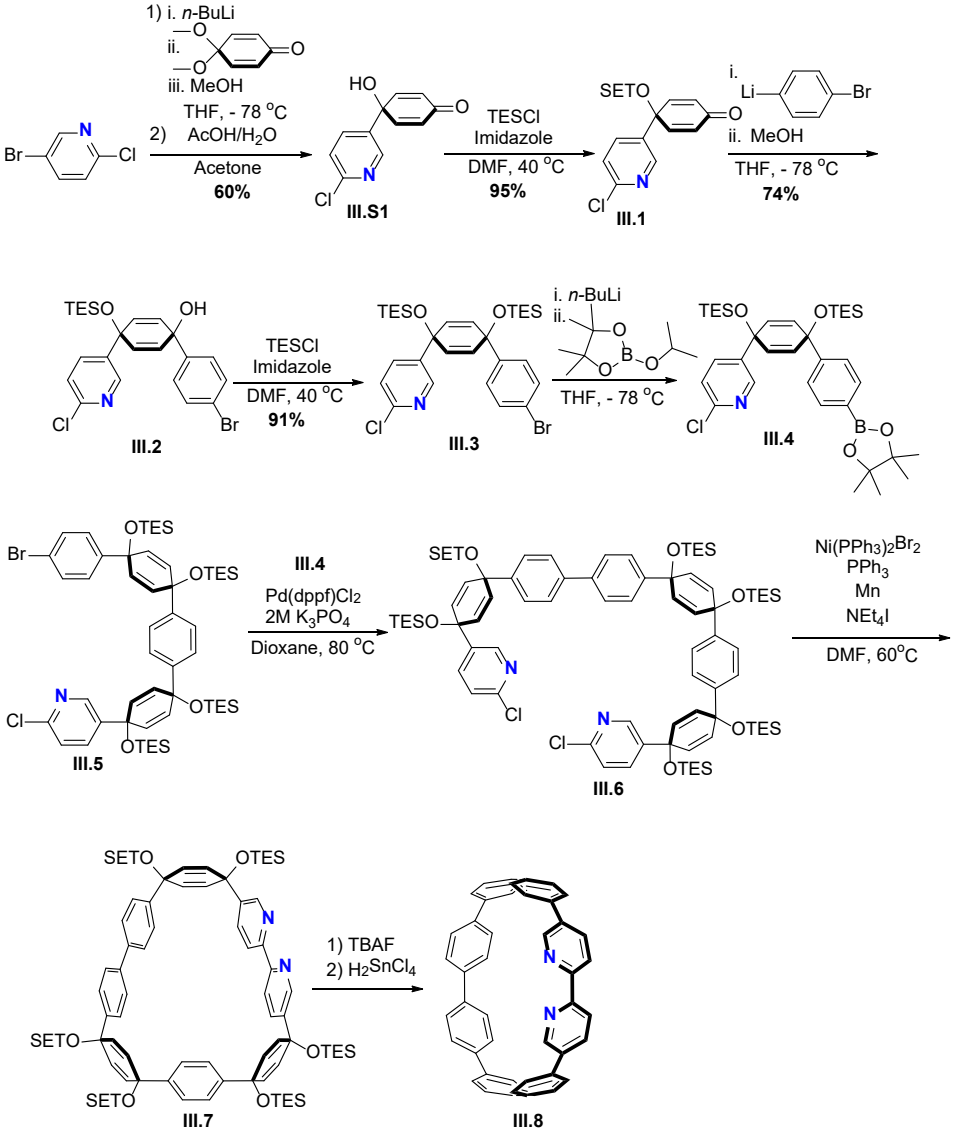

Scheme 3.1. Synthetic Route toward CPP Ligand **III.8**

As a first pass at exploring the coordination chemistry of these new ligands, we probed the feasibility of constructing a nanotube-inspired coordination cage from these systems. We began by first preparing intermediate **III.9** (**Figure 3.2**) via the reaction of $PdCl_2$ with bipy-CPP **III.8** in acetonitrile. Pd−CPP **III.9** was then combined with another equivalent of bipy-CPP **III.8** in the presence of 2 equiv of $AgBF_4$ for 2h in dichloromethane, providing nanohoop dimer **III.10** in quantitative yield. In the ^{1}H NMR spectrum of dimer **III.10**, only three 3-pyridyl centered protons were observed, suggesting high symmetry. However, this spectrum could result from a dimeric structure that possessed either of two geometries (*trans* or *cis*) about the Pd(II) metal center. In order to elucidate the exact geometry, dark-red crystals suitable for X-ray crystallography were obtained after slow vapor diffusion of pentane into a concentrated solution of **III.10** in acetone. Crystallographic analysis not only confirmed the formation of **III.10** but also provided direct solid-state evidence for a *trans* preference about the Pd(II) center. Bis(bipyridyl)palladium(II) complexes often show a distorted square-planar geometry because of steric repulsions between hydrogens of the coordinated biypyridine ligands.[36] Thus, the observed preference for a *trans* conformation about the Pd(II) center in dimer **III.10** can be explained on the basis that similar steric repulsions that exist upon formation of complex **III.10**.

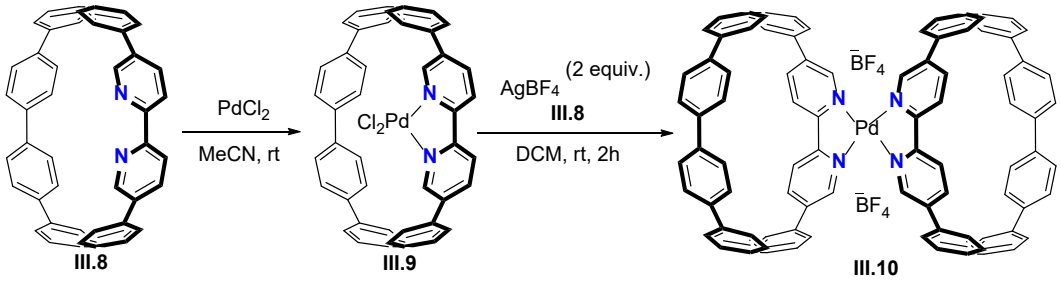

Figure 3.2. Synthetic route for nanohoop dimer **III.10**.

We then investigated how the Pd(II) metal center impacted the nanohoop structure and solid-state packing. Detailed analysis of the crystal structure of **III.10** revealed that two different dimeric units are present, each of which shows subtle changes in their corresponding torsional (θ) and displacement angles (α°). In both dimers, the torsional angle between adjacent pyridyl rings, θ (**Figure 3.3**), is approximately 6°, which is decreased significantly from that of the all-carbon nanohoops (average of approximately 31° for [8]CPP). The torsional angles of the remaining aryl rings spanned from 0° up to nearly 38°. Additionally, the displacement angles of the pyridyl units, α° (**Figure 3.3a**), varied from 6.0° to 12.7°, similar to those in the parent all-carbon nanohoop [8]CPP.[13] Taken together, these data suggest that while ligation to a Pd(II) metal center does reduce the dihedral angle of the embedded bipyridyl unit, this does not strongly affect the remaining aryl rings. Interestingly, these two dimeric units contributed to an unusual multilayer packing motif (**Figure 3.3b**) in which each layer possesses a unique microstructure. In one case (**Figure 3.3c**), the dimeric units pack into flat, sheet-like arrangements. In the other case, the dimeric units arrange into a herringbone-type motif, which is commonly observed in the parent all-carbon CPPs. While the reasoning for this packing arrangement is less clear, we anticipate that nanohoop ligands with different diameters will strongly affect both the packing motif and observed angle distortions. Moreover, through our synthetic methods, we can incorporate multiple pyridyl units such that the nanohoops can be extended into trimeric, oligomeric, or polymeric networks, which will enable new pathways toward novel porous materials.

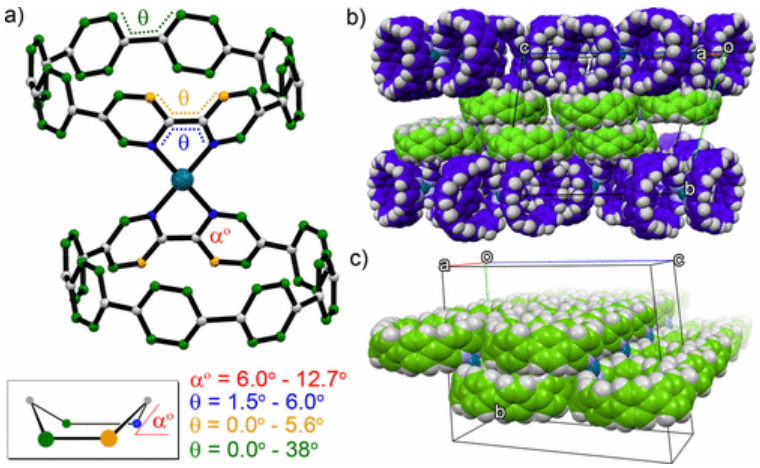

Figure 3.3. (a) Crystal structure of Pd dimer **III.10** showing torsional angles and pyridyl displacement angles. (b) Observed packing motif showing the multilayered structure. (c) View of the flat layer. Counterions and solvent have been omitted for clarity.

In addition to the nanohoops' unique structural features, we were curious whether the tunable optoelectronic properties of the nanohoops could be leveraged in new coordination complexes as well. With this in mind, we found that refluxing bipy-CPP **III.8** with $Ru(bipy)_2Cl_2$ in ethanol (**Figure 4.4**) provided Ru(II)–nanohoop complex **III.11** in 83% yield as the racemate. Red plate-like crystals suitable for X-ray crystallography were obtained by diffusion of diethyl ether into a dilute solution of **III.11** in acetone, and crystallographic analysis unambiguously confirmed both the structure of **III.11** and the racemic solid-state morphology.

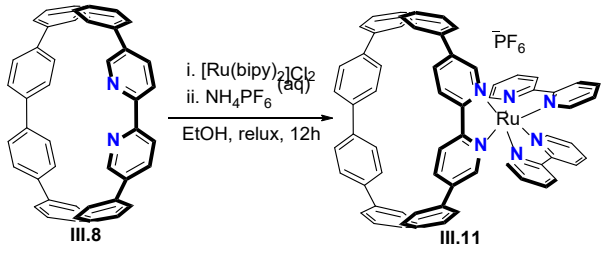

Figure 3.4. Synthetic route for Ru(II)–nanohoop complex **III.11**.

The electronic structures of **III.8** and **III.11** were then studied using UV−vis spectroscopy and compared with the parent system, [Ru- (bipy)$_3$](PF$_6$)$_2$ (**Figure 3.5**). Bipy-CPP **III.8** has a λ_{max} of 345 nm ($\varepsilon = 1.2 \times 10^5$ M^{-1} cm^{-1}), which is similar to that of the parent all-carbon nanohoop [8]CPP (λmax = 340 nm, $\varepsilon = 1.0 \times 10^5$ M^{-1} cm^{-1}),[13] suggesting that the nitrogen atoms have little impact on the electronic structure—a common observation in other nitrogen-doped CPPs.[14,28] On the other hand, the absorption spectrum of Ru(II)−nanohoop complex **III.11** showed a dramatic difference relative to those of **III.8** and [Ru(bipy)$_3$](PF$_6$)$_2$. The first absorption of complex **III.11** is centered at 290 nm and is due to bipyridine π to π^* transitions,[36] while the absorption at 357 nm originates from the nanohoop; both are broadened and red-shifted relative to those of **III.8** and [Ru(bipy)$_3$](PF$_6$)$_2$. The broad absorption from approximately 425 to 575 nm is due to metal-to-ligand charge transfer (MLCT)—a hallmark of Ru(II)−polypyridyl complexes.[36]

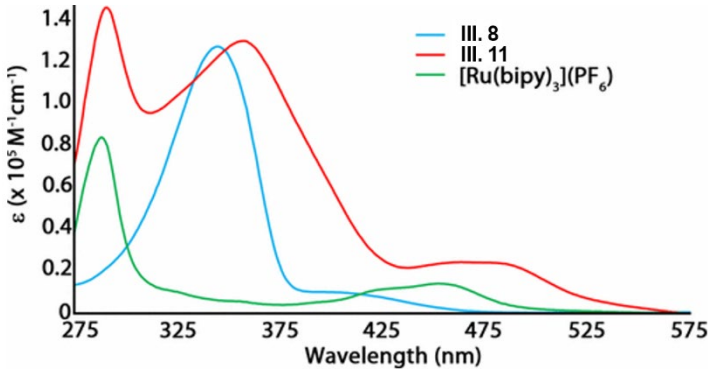

Figure 3.5. Absorption spectra of CPP **III.8**, Ru(II)–nanohoop complex **III.11**, and [Ru(bipy)$_3$](PF$_6$)$_2$ in dichloromethane.

In homoleptic $[Ru(bipy)_3](PF_6)_2$, irradiation with visible light creates an excited state that resides on one of three bipyridine ligands.[36] However, in the case of heteroleptic complex **III.11**, the destination of the charge is less obvious because of the presence of the nanohoop ligand. In order to further investigate the MLCT absorptions, we turned to density functional theory (DFT) and time-dependent DFT (TDDFT). From TD-DFT studies, we found that five major transitions (**Figure 3.6**) are responsible for the absorptions between 440 and 490 nm. In all cases, it was found that the filled molecular orbital was centralized around the Ru(II) metal center and the unfilled orbital was predominately localized on the nanohoop. This supports our expectations that the experimentally observed absorptions in the 430 to 500 nm range result from MLCT transitions. Additionally, this further suggests that there is a significant amount of electron transfer between the Ru(II) metal center and the nanohoop ligand, with apparently very minimal transfer to the bipyridine ligands. Taken together, these results indicate that the excited state of the Ru(II)−nanohoop complex is primarily localized on the nanohoop backbone. Given that the redox potential of nanohoops can be easily tuned,[14] we expect that this excited-state localization can be leveraged via supramolecular interactions to provide new functionality for catalysis and energy transfer with electron-deficient guests.

3.3. Conclusions

In conclusion, this work illustrates a general strategy for coordinating the nanohoop framework to common metal centers. We have shown that the ligand is readily accessible using straightforward methodology and can be obtained in sufficient quantity and good yield. The resulting coordination complexes, a homoleptic Pd(II) dimer and a

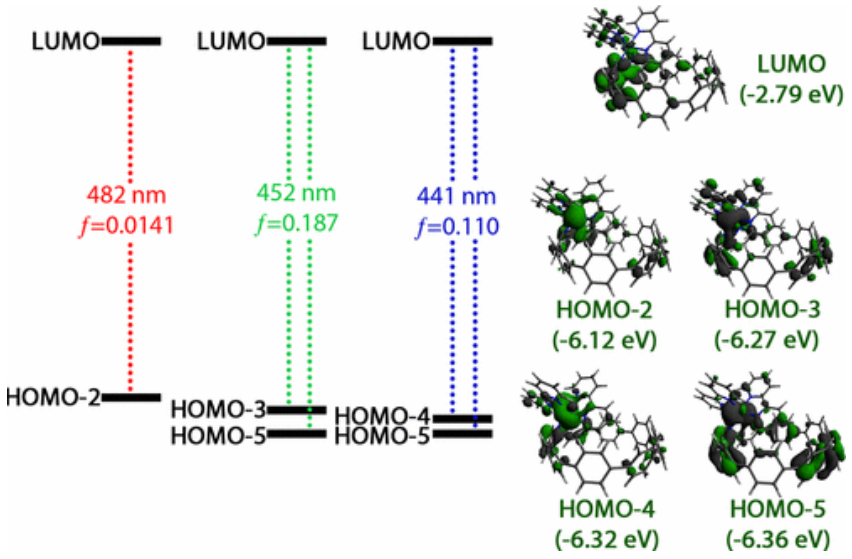

Figure 3.6. Major electronic transitions (TD-DFT) contributing to MLCT absorptions and representative frontier molecular orbitals for Ru(II)–nanohoop complex **III.11**, calculated at the B3LYP/6-31G(d,p) (C, H, N) and LANL2DZ (Ru) level of theory.

Ru(II)−nanohoop complex, show excellent stability and unique solid-state and photophysical properties, suggesting that CPPs show promise as a new class of ligands. While this work centralized around a 2,2′-bipyridyl-embedded[8]CPP, we argue that the synthetic methodology is readily applicable to [n]CPPs with different diameters, and work is currently underway to prepare both reduced- and expanded-diameter nanohoop ligands in order to explore new cylindrical metal−ligand assemblies with interesting supramolecular and solid-state properties.

3.4. Experimental Sections

3.4.1. General Experimental Details

^{1}H NMR spectra were recorded at 500 MHz on a Varian VNMR spectrometer, 500 MHz on a Bruker, or 600 MHz on a Bruker Avance-III-HD NMR spectrometer. 13C NMR spectra were recorded at 125 MHz on a Varian VNMR spectrometer or 150 MHz on a

Bruker Avance-III-HD NMR spectrometer. All 1H NMR spectra are referenced to TMS (δ 0.00 ppm), residual CH2Cl2 (δ 5.32 ppm), or (CH3)3CO (δ 2.05 ppm). All 13C NMR spectra are references to a residual CHCl3 (δ 77.16 ppm), CH2Cl2 (54.00 ppm), or (CH3)3CO (δ 29.84 ppm). All reagents were obtained commercially. All glassware was flame-dried and cooled under an inert atmosphere of nitrogen unless otherwise noted. Moisture sensitive reactions were carried out under an inert atmosphere of nitrogen using standard syringe/septa technique. Absorbance spectra for **III.8** and **III.11** were collected in dichloromethane in a 1 cm quartz cuvette on an Agilent Cary 60 UV-Vis spectrophotometer. Silica column chromatography was conducted with Zeochem Zeoprep 60 Eco 40-63 uM silica gel while alumina chromatography utilized Sorbent Technologies 50-200 um Basic Activity II-II Alumina.

3.4.2. Synthetic Details

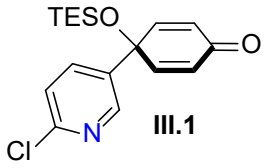

III.1

Synthesis of III.S1. A flame-dried 500 mL flask was charged with 5-bromo-2-chloropyridine (14.3 g, 74.3 mmol, 1.00 equiv.) and quinone monoketal (11.45 g, 74.3 mmol, 1.00 equiv.) and then dissolved in 250 mL THF. The resulting solution was then cooled to -78 °C for 1h, at which point *n*-BuLi (2.5 M in hexanes, 29.7 mL, 74.3 mmol, 1.00 equiv.) was added dropwise resulting in a transparent orange solution. The solution was allowed to stir for 1.5 h at which point H_2O (100 mL) was added, then allowed to warm to room temp. THF was then removed via rotary evaporation and the remaining aqueous phase was extracted with diethyl ether (3 x 100 mL). The combined organic

phases were washed with H_2O (3 x 100 mL), and brine (1 x 100 mL), and dried over sodium sulfate. The solvent was removed under reduced pressure to afford a yellow oil. Addition of hexanes this oil caused a white solid to precipitate which was collected via filtration and washed with additional hexanes. The resulting solid was then dissolved in acetone (25 mL) in a 500 mL RBF, followed by the addition of 10% AcOH/H_2O (100 mL), and then stirred for 1 h. The acetone was removed with under reduced pressure, and the remaining aqueous phase was extracted with ethyl acetate (3 x 100 mL). The combined organic phases were washed with H_2O (3 x 100 mL), and brine (1 x 100 mL), and dried over sodium sulfate. After removal of solvent, a tan solid emerged **III.S1** (8.71 g, 53%).

TES protection. Imidazole (5.21 g, 76.6 mmol, 2.00 equiv), and free alcohol **III.S1** (8.71 g, 38.3 mmol, 1.00 equiv.) were added to a 500 mL flame-dried RBF, then dissolved in 150 mL DMF. The resulting solution was heated to 40 °C at which point TESCl (9.74 mL, 57.5 mmol, 1.50 equiv.) was added dropwise. The reaction was monitored via ^{1}H NMR until all the starting material was consumed (typically 2 hours). Once complete, the reaction was flask was placed cooled to 0 °C, then neutrazlied with sodium bicarbonate. The resulting suspension was extracted EtOAc (3 x 100 mL). The combined organic phases were washed with 5% LiCl (5 x 100 mL), followed by H2O (1 x 100 mL), brine (1 x 100 mL), and then placed over sodium sulfate. Removal of solvent via rotary evaporation yielded a brown oil which, after chromatography (5% EtOAc/Hex), yielded TES protected **III.1** as a white solid (12.8 g, 96%). ^{1}H NMR (500 MHz, Chloroform-*d*) δ 8.52 (d, *J* = 2.7 Hz 1H), 7.62 (dd, *J* = 8.3, 2.7 Hz, 1H), 7.29 (d, *J* = 8.3 Hz, 1H), 6.79 (d, *J* = 10.1 Hz, 1H), 6.28 (d, *J* = 10.1 Hz, 1H), 0.97 (t, *J* = 7.9 Hz, 7H), 0.66 (q, *J* = 7.9 Hz, 4H).

^{13}C NMR (126 MHz, $CDCl_3$) δ 185.08, 151.39, 150.62, 147.81, 136.32, 135.17, 127.51, 124.17, 71.87, 6.99, 6.33. δ HRMS (TOF, ES+) (m/z): [M+H]+ calculated for $C_{17}H_{23}NO_2SiCl$, 336.1187; found, 336.1197. IR (neat): 3096.51, 3072.96, 3043.06, 2957.86, 2908.88, 2876.74, 1689.96, 1670.66, 1629.23, 1605.12, 1580.69, 1564.16, 1477.67, 1453.30, 1411.73, 1387.98, 1363.08, 1283.33, 1234.00, 1200.27, 1180.08, 1145.73, 1105.89, 1078.80, 1066.55, 1028.11, 1017.39, 969.22, 925.61, 886.59, 832.11, 790.11, 756.45. MP (75.0-76.4°C).

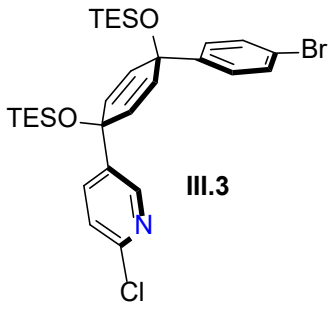

III.3

Synthesis of III.3. A flame-dried 500 mL flask was charged with 1,4-dibromobenzene (9.96 g, 42.2 mmol, 1.00 equiv.) 200 mL THF. The resulting solution was then cooled to -78 °C for 1h, at which point *n*-BuLi (2.5 M in hexanes, 16.9 mL, 42.2 mmol, 1.00 equiv.) was added dropwise resulting in a white suspension after stirring for 30 minutes. To this solution was added **III.1** (14.2 g, 42.2 mmol, 1.00 equiv) in 5 mL THF, resulting in a dark green solution. The solution was allowed to stir for 1h at which point H_2O (100 mL) was added, then allowed to warm to room temp. THF was then removed via rotary evaporation and the remaining aqueous phase was extracted with EtOAc (3 x 100 mL). The combined organic phases were washed with H_2O (3 x 100 mL), and brine (1 x 100 mL), and dried over sodium sulfate. After removal of solvent, a brown oil (**III.2**) was obtained (19.4 g, 94%) which was then TES protected as in the case of **III.1**. Chromatography (5%EtOAc/Hex) yielded **III.3** as a clear oil (17.9 g, 70%). ^{1}H NMR (500 MHz,

Chloroform-*d*) δ 8.31 (d, *J* = 2.6 Hz, 1H), 7.50 (dd, *J* = 8.4, 2.6 Hz, 1H), 7.41 (d, *J* = 8.5 Hz, 2H), 7.18 (d, *J* = 8.4 Hz, 3H), 1.03 – 0.84 (m, 18H), 0.63 (q, *J* = 7.9 Hz, 6H), 0.56 (q, *J* = 7.9 Hz, 6H). ^{13}C NMR (126 MHz, $CDCl_3$) δ 150.34, 147.81, 144.60, 140.44, 136.40, 132.16, 131.59, 130.75, 127.48, 123.63, 121.72, 70.86, 70.07, 7.04, 6.50, 6.45. δ HRMS (TOF, ES+) (m/z): [M+H]+ calculated for $C_{29}H_{42}NO_2Si_2ClBr$, 606.1626; found, 606.1621. IR (neat): 3096.68, 3072.82, 3043.31, 2956.72, 2909.34, 2876.05, 1690.07, 1670.93, 1629.39, 1605.14, 1580.68, 1564.01, 1477.74, 1453.33, 1411.77, 1388.07, 1363.20, 1283.47, 1234.09, 1200.28, 1180.21, 1145.77, 1105.84, 1079.16, 1028.02, 1017.17, 969.40, 925.69, 886.41, 832.28, 790.29, 756.50.

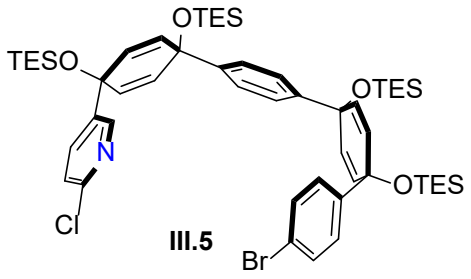

III.5

Synthesis of III.5. To a flame-dried 250 mL flask was added **III.3** (3.60 g, 6.00 mmol, 1.00 equiv.), which was then dissolved in 125 mL THF. The resulting solution was cooled to -78 °C for 1h, at which point *n*-BuLi (2.5 M in hexanes, 2.40 mL, 6.00 mmol, 1.00 equiv.) was added dropwise resulting in a bright red solution. After stirring for 10 minutes, bromo ketone[XX] (2.27 g, 6.00 mmol, 1.00 equiv), as a solution in 3 mL THF, was added resulting in a light orange solution. After stirring for 1 h, the reaction was quenched with H_2O (100 mL), then allowed to warm to room temp. The THF was then removed via rotary evaporation and the remaining aqueous phase was extracted with EtOAc (3 x 100 mL). The combined organic phases were washed with H_2O (3 x 100 mL), and brine (1 x

100 mL), and dried over sodium sulfate. After removal of solvent, a yellow oil was obtained (3.90 g, 72%) which was then TES protected as in the case of **III.1**. Chromatography (5%EtOAc/Hex) yielded **III.5** as a clear oil (3.70 g, 61%). ^{1}H NMR (500 MHz, Chloroform-*d*) δ 8.36 (d, *J* = 2.6 Hz, 1H), 7.45 (dd, *J* = 8.4, 2.6 Hz, 1H), 7.38 (d, *J* = 8.7 Hz, 2H), 7.28 – 7.25 (m, 4H), 7.17 (d, *J* = 8.5 Hz, 2H), 7.14 (d, 1H), 6.11 (d, *J* = 10.1 Hz, 2H), 6.01 (d, *J* = 10.2 Hz, 2H), 5.91 (m, 4H), 1.26 – 0.82 (m, 36H), 0.83 – 0.43 (m, 24H). ^{13}C NMR (126 MHz, $CDCl_3$) δ 150.28, 148.04, 145.47, 145.29, 144.75, 140.72, 136.47, 132.55, 131.81, 131.30, 130.54, 127.76, 126.09, 125.76, 123.51, 121.31, 71.38, 71.30, 70.98, 70.29, 7.18, 7.18, 7.15, 7.13, 6.61, 6.56, 6.51. δ HRMS (TOF, ES+) (m/z): [M+H]+ calculated for $C_{53}H_{80}NO_4Si_4ClBr$, 1020.4021; found, 1020.4036. IR (neat): 2952.93, 2909.24, 2874.43, 1579.78, 1560.83, 1479, 1454.10, 1406.87, 1378.10, 1357.68, 1238.08, 1189.24, 1104.84, 1069.29, 1008.55, 956.76, 880.03, 856.36, 825.58, 765.84. MP (86.9-88.0°C).

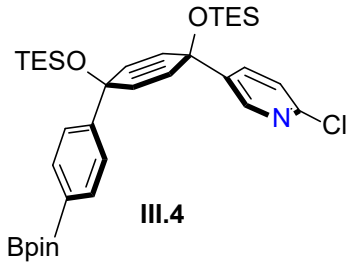

III.4

Synthesis of III.4. To a flame-dried 250 mL flask was added **III.3** (2.66 g, 4.38 mmol, 1.00 equiv.), which was then dissolved in 100 mL THF. The resulting solution was cooled to -78 °C for 1h, at which point *n*-BuLi (2.5 M in hexanes, 1.75 mL, 4.38 mmol, 1.00 equiv.) was added dropwise resulting in a bright red solution. The solution was allowed to stir for 10 minutes at which point 2-isopropoxy-4,4,5,5-tetramethyl-1,3,2-dioxaborolane (2.67 mL, 13.1 mmol, 3.00 equiv.) was quickly added, resulting in a bright yellow solution.

After stirring for 1 h, the reaction was quenched with H_2O (50 mL) and then brought to room temperature. The THF was then removed via rotary evaporation and the remaining aqueous phase was extracted with DCM (3 x 100 mL). The combined organic phases were washed with H_2O (3 x 100 mL), and brine (1 x 100 mL), and dried over sodium sulfate to give a bright yellow oil, which after chromatography (1% EtOAc/Hex), yielded **III.4** as a white solid (2.20 g, 77%). ^{1}H NMR (500 MHz, Chloroform-*d*) δ 8.35 (d, *J* = 2.6 Hz, 1H), 7.74 (d, *J* = 8.4 Hz, 2H), 7.45 (dd, *J* = 8.4, 2.6 Hz, 1H), 7.33 (d, *J* = 8.4 Hz, 2H), 7.16 (d, *J* = 8.4 Hz, 1H), 6.10 (d, *J* = 10.2 Hz, 2H), 5.89 (d, *J* = 10.1 Hz, 2H), 1.35 (s, 12H), 0.95 (t, *J* = 7.9 Hz, 9H), 0.89 (t, *J* = 7.9 Hz, 9H), 0.65 (q, *J* = 7.9 Hz, 6H), 0.54 (q, *J* = 7.9 Hz, 6H). ^{13}C NMR (126 MHz, $CDCl_3$) δ 150.22, 148.54, 148.03, 140.67, 136.54, 135.11, 132.50, 130.61, 125.15, 123.57, 83.97, 71.29, 70.31, 25.04, 7.13, 6.50. δ HRMS (TOF, ES+) (m/z): [M-Me]+ calculated for $C_{35}H_{54}BNO_4Si_2Cl$, 654.3372; found, 654.3373. IR (neat): 2956.22, 2910, 2875.23, 1671.62, 1629.67, 1607.50, 1581.03, 1560.65, 1454, 1399.37, 1390.67, 1361.49, 1322.25, 1284.20, 1272.46, 1235.06, 1191.25, 1100.05, 1145.72, 1081.81, 1008.47, 969.74, 956.94, 925.78, 856.66, 838.25. MP (108.4-109.6°C).

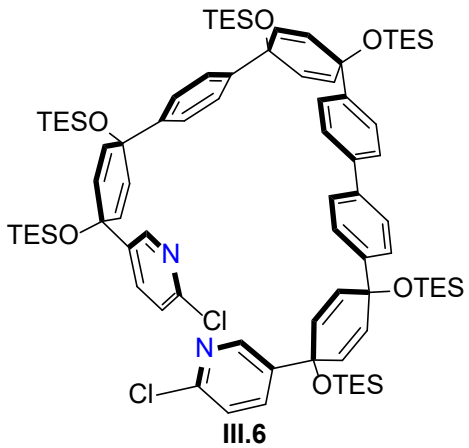

III.6

Synthesis of III.6. To a flame-dried 100 mL round bottom flask equipped with a stir bar was added **III.4** (1.35 g, 2.10 mmol, 1.20 equiv.), **III.5** (1.76 g, 1.72 mmol, 1.00 equiv.),

and $Pd(dppf)Cl_2$ (60.5 mg, 0.827 mmol, 0.04 equiv.). The flask was evacuated and back-filled with N_2 5 times, followed by addition of 1,4-dioxane (35 mL). This solution was then vigorously spared with N_2 for 2h at which point an aqueous solution of 2M K_3PO_4 (3.50 mL, 7.00 mmol, 3.01 equiv) was added, followed by heating of this solution to 80 °C taking the orange solution to a dark red within 15 minutes. The solution was allowed to stir for 12h, at which point the solution was allowed to cool to room temperature. After removal of the solvent via rotary evaporation, the resulting brown oil was extracted with DCM (3 x 75 mL), followed by washing of the combined organic phases with with H_2O (3 x 100 mL), brine (1 x 100 mL), and finally placed over sodium sulfate. After solvent removal, the resulting brown oil was chromatographed (5% EtOAc/Hex) to give **III.6** as a clear oil (1.64 g, 81%). ^{1}H NMR (500 MHz, Chloroform-*d*) δ 8.39 – 8.34 (m, 2H), 7.54 – 7.50 (m, 4H), 7.42 – 7.36 (m, 6H), 7.32 (d, *J* = 8.3 Hz, 2H), 7.25 (d, *J* = 9.3 Hz, 2H), 7.16 (d, *J* = 8.4 Hz, 1H), 7.10 (d, *J* = 8.4 Hz, 1H), 6.15-6.10 (m, 4H), 6.01 (s, 4H), 5.93 (d, *J* = 10.1 Hz, 2H), 5.87 (d, 10.2 Hz, 2H), 0.98 - 0.87 (m, 54H), 0.66 – 0.52 (m, 36H). ^{13}C NMR (126 MHz, $CDCl_3$) δ 150.26, 150.19, 148.02, 145.74, 145.40, 144.58, 144.49, 140.78, 140.73, 140.14, 139.45, 136.63, 136.54, 132.68, 132.59, 131.66, 131.56, 130.50, 127.16, 126.86, 126.40, 126.24, 126.15, 125.72, 123.62, 123.46, 71.50, 71.42, 71.11, 70.98, 70.32, 70.29, 7.23, 7.21, 7.14, 6.62, 6.53, 6.50. δ HRMS (TOF, ES+) (m/z): [M+H]+ calculated for $C_{82}H_{121}N_2O_6Si_6Cl_2$, 1467.7180; found, 1467.7217. IR (neat): 2953.17, 2909.27, 2874.46, 1579.90, 1560.79, 1479.09, 1454.11, 1406.76, 1357.77, 1237.94, 1189.38, 1104.91, 1069.24, 1008.68, 956.72, 880.25, 856.55, 825.85, 765.81. MP (72.5-74.0°C).

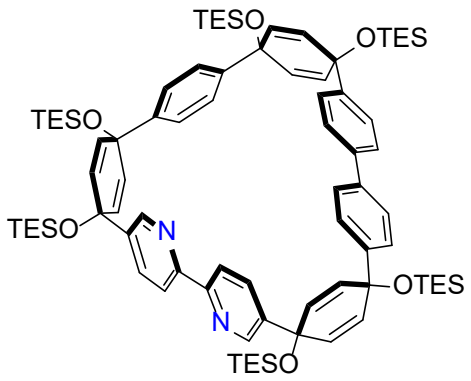

III.7

Synthesis of III.7. To a flame-dried 100 mL round bottom flask equipped with a stir bar was added $Ni(PPh_3)_2Br_2$ (0.464 g, 0.625 mmol, 1.50 equiv.), Mn (0.0686 g, 1.25 mmol, 3.00 equiv.) PPh_3 (0.328 g, 0.625 mmol, 3.00 equiv.), NEtI (0.160 g, 0.625 mmol, 1.50 equiv.). The flask was evacuated and back-filled with N_2 5 times, followed by the addition of N_2 sparged DMF (6.25 mL). The resulting suspension was sonicated until the solution turned from green to dark red (typically 5 minutes) at which point the suspension was stirred at 60°C for 1h. In a separate flame-dried pear-shaped flask was added **III.6** followed DMF (8.33 mL). This solution was then sparged with N_2 for 1h. The solution containing dichloride **III.6** in DMF was then added to the catalyst mixture dropwise over 2 hours via syringe pump, resulting in a dark brown suspension. Once all the solution had been added, the reaction was allowed to proceed for an additional hour. After 1h, the reaction was brought to room temperature at which point aqueous (18 w/w%) ammonia (30 mL) and EtOAc (25 mL) was added, followed by stirring for 30 minutes. The resulting clear solution was then filtered over celite, followed extraction of the aqueous phase with EtOAc (3 x 50 mL). The combined organic phases were then washed with 5% LiCl (5 x 50 mL) to remove the remaining DMF, followed by washing with H_2O (1 x 100 mL) and brine (1 x 100 mL) and then finally placed over sodium sulfate. The solvent was then removed

via rotary evaporation to afford a brown/yellow oil. Chromatography of the oil (1%EtOAc/Hex to remove PPh_3 then eluted with 5%EtOAc/Hex) yielded a clear oil which, after washing with a small amount of acetone, yielded **III.7** as a white solid (0.305 g, 57%). ^{1}H NMR (500 MHz, Chloroform-*d*) δ 8.78 (d, *J* = 2.4 Hz, 1H), 8.30 – 8.18 (m, 2H), 8.14 (d, *J* = 8.4 Hz, 1H), 7.61 (dd, *J* = 8.3, 2.4 Hz, 1H), 7.56 – 7.43 (m, 7H), 7.40 (d, *J* = 8.5 Hz, 2H), 7.35 (d, *J* = 8.5 Hz, 2H), 7.10 (d, *J* = 8.4 Hz, 2H), 6.16 (d, *J* = 10.1 Hz, 2H), 6.12 (d, *J* = 10.1 Hz, 2H), 6.05 (d, *J* = 10.1 Hz, 4H), 5.93 – 5.91 (m, 4H), 1.08 – 0.88 (m, 56H), 0.78 – 0.62 (m, 24H), 0.60 – 0.51 (m, 12H). ^{13}C NMR (126 MHz, $CDCl_3$) δ 155.01, 154.90, 147.62, 147.13, 146.26, 145.69, 145.40, 142.77, 141.67, 140.18, 139.62, 139.56, 135.04, 134.51, 132.97, 132.11, 131.96, 131.32, 131.18, 131.04, 126.99, 126.83, 126.69, 126.13, 126.05, 125.94, 120.36, 120.19, 72.46, 71.61, 71.38, 70.89, 70.68, 70.48, 7.27, 7.24, 7.23, 7.19, 7.17, 6.68, 6.67, 6.63, 6.55, 6.52. δ HRMS (TOF, ES+) (m/z): [M+H]+ calculated for $C_{82}H_{121}N_2O_6Si_6$, 1397.7823; found, 1397.7840. IR (neat): 2953.12, 2909.98, 2874.69, 1579.76, 1560.69, 1455.98, 1400.38, 1360.50, 1238.15, 1189.48, 1071.32, 1004.14, 957.35, 858.68, 820.54. MP (decomp. 262.2°C).

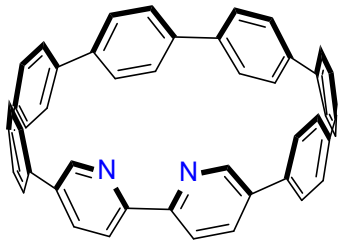

III.8

Synthesis of III.8. To a flame-dried 100 mL round bottom flask equipped with a stir bar was added **III.7** (0.360 g, 0.257 mmol, 1.00 equiv.), followed by THF (20 mL). To this solution was slowly added TBAF (1M in THF, 2.57 mmol, 2.58 mL, 10 equiv), resulting in

a tan suspension. After stirring for 2 hours, the THF removed via rotary evaporation, followed by addition of H_2O (20 mL) resulting in a white precipitate. The white solid was collected via filtration, washed with H_2O (50 mL), DCM (5 mL) and was then transferred to a flame-dried 100 mL RBF with stir bar. After addition of THF (20 mL), H_2SnCl_4 was added dropwise, turning the colorless solution to a bright orange over 20 minutes. This was then allowed to stir for 3h, at which point aqueous (18 w/w%) ammonia (5 mL) was added, quickly turning the solution from bright orange to bright yellow. The THF was removed via rotary evaporation, followed extraction of the resulting yellow/orange aqueous suspension with DCM (3 x 50 mL). The combined organic phases were washed with H_2O (3 x 50 mL), brine (1 x 50 mL) and then dried over sodium sulfate. After removal of DCM under reduced pressure, the resulting yellow solid was run through a short alumina column using DCM eluent, providing **III.8** as a yellow solid (0.111 g, 63%). ^{1}H NMR (500 MHz, Chloroform-*d*) δ 8.81 (d, *J* = 2.3 Hz, 2H), 8.13 (d, *J* = 8.4 Hz, 2H), 7.87 (dd, *J* = 8.5, 2.4 Hz, 2H), 7.65 – 7.38 (m, 24H). ^{13}C NMR (151 MHz, $CDCl_3$) δ 146.44, 138.93, 138.08, 137.69, 137.56, 137.55, 127.95, 127.74, 127.67, 127.61, 127.54, 121.19. δ HRMS (TOF, ES+) (m/z): [M+H]+ calculated for $C_{46}H_{31}N_2$, 611.2489; found, 611.2487. IR (neat): 3021.71, 2920.80, 2850.30, 1734.72, 1701.01, 1695.95, 1685.16, 1651.96, 1576.20, 1479.42, 1456.28, 1360.84, 1262.90, 1232.38, 1119.42, 1069.21, 999.13, 855.24, 818.47, 768.13. MP (decomp. 150°C).

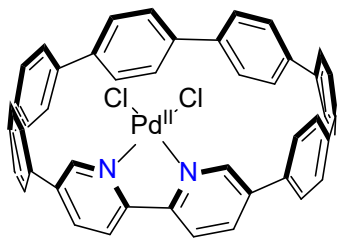

III.9

Synthesis of III.9. To a flame-dried 25 mL round bottom flask equipped with a stir bar was added **III.8** (20.0 mg, 0.0291 mmol, 1 equiv) and $PdCl_2$ (5.17 mg, 0.0291 mmol, 1 equiv), followed by dissolution in MeCN (10.00 mL). The resulting yellow suspension was stirred at room temperature for 5 h, at which point the solvent was removed via rotary evaporation resulting a bright orange solid. This solid was then washed with diethyl ether (5 x 15 ml) yielding **III.9** as a bright orange solid (22.9 mg, 99%). ^{1}H NMR (500 MHz, Methylene Chloride-d_2) δ 9.06 (d, J = 2.2 Hz, 2H), 8.24 (dd, J = 8.8, 2.2 Hz, 2H), 7.73 (d, J = 8.8 Hz, 2H), 7.71 – 7.53 (m, 24H). ^{13}C NMR (126 MHz, CD_2Cl2) δ 153.71, 151.95, 141.04, 138.94, 138.05, 137.76, 137.70, 137.10, 134.35, 132.40, 128.71, 128.08, 127.95, 123.90. IR (neat): 3021.28, 2918.11, 2849.79, 1616.96, 1576.06, 1566.20, 1560.62, 1554.46, 1478.80, 1460.28, 1456.75, 1437.16, 1388.03, 1365.31, 1323.08, 1297.64, 1259.30, 1241.92, 1204.93, 1144.66, 1070.14, 1042.84, 999.14, 815.74. MP (decomp. 170°C).

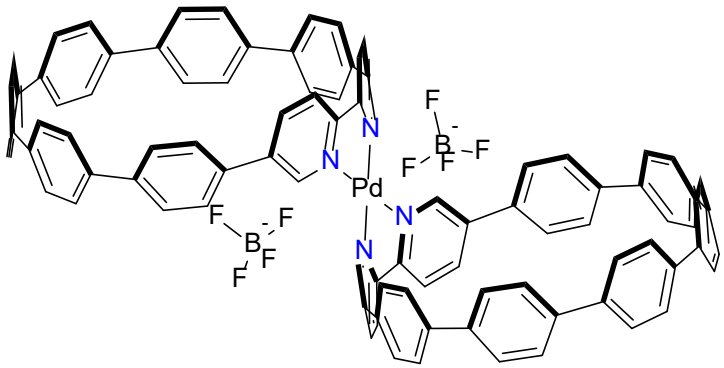

III.10

Synthesis of III.10. To a flame-dried 25 mL round bottom flask equipped with a stir bar was added **III.9** (5.00 mg, 0.00634 mmol, 1 equiv), $AgBF_4$ (2.50 mg, 0.0127 mmol, 2 equiv), **III.8** (4.36 mg, 0.00634 mmol, 1 equiv) and DCM (5.00 mL). The resulting bright orange solution was stirred for 5 h, at which the resulting dark red precipitate was collected

via filtration, followed by washing of the precipitate with H_2O (5.00 mL), diethyl ether (5.00 mL), and DCM (5.00 mL), yielding **III.10** as a dark red solid (9.51 mg, 99%). ^{1}H NMR (500 MHz, Acetone-d_6) δ 8.98 (d, J = 2.0 Hz, 4H), 8.86 (dd, J = 9.0, 2.0 Hz, 4H), 8.53 (d, J = 9.0 Hz, 4H), 7.85 (d, J = 8.9 Hz, 8H), 7.79 – 7.59 (m, 40H). ^{13}C NMR (126 MHz, Acetone) δ 155.10, 150.79, 141.51, 139.48, 139.23, 138.36, 137.87, 137.30, 132.33, 129.24, 128.73, 128.30, 128.25, 126.45. IR (neat): 2924.65, 2853.75, 1700.99, 1699.22, 1685.16, 1695.92, 1675.98, 1651.96, 1630.27, 1616.97, 1576.40, 1560.62, 1554.57, 1478.21, 1465.66, 1456.68, 1437.12, 1419.82, 1371.35, 1325.89, 1243.33, 1058.34, 828.34, 752.12.

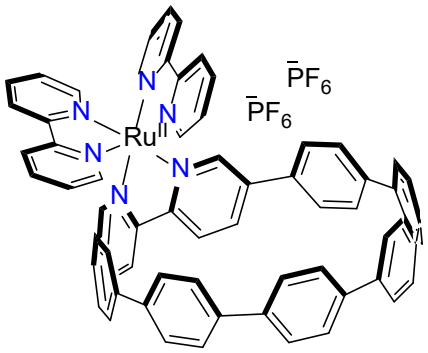

III.11

Synthesis of III.11. To a flame-dried 25 mL round bottom flask equipped with a stir bar was added **III.8** (10.0 mg, 0.0146 mmol, 1 equiv), $Ru(bipy)_2Cl_2$ (7.06 mg, 0.0146 mmol, 1 equiv) and EtOH (10.0 mL), followed by the addition of a reflux condenser. The purple-yellow suspension was then heated to reflux for 12h, gradually turning the reaction mixture to a bright orange solution. At 12h, the reaction flask was placed in an ice bath, followed addition of (saturated) NH_4PF_4 (aq) (5.00 mL) quickly resulting in the formation a dark red precipitate. The precipitate was then collected via filtration, washed with H_2O and diethyl ether to provide **III.11** as a dark red solid (15.9 mg, 83%). ^{1}H NMR (600 MHz, Acetone-d_6) δ 8.95 (t, J = 6.8 Hz, 2H), 8.77 – 8.74 (m, 3H), 8.50 – 8.39 (m, 5H), 8.29 (t, J = 7.9 Hz,

1H), 8.24 (t, J = 7.9 Hz, 2H), 8.18 (d, J = 5.6 Hz, 1H), 8.08 (d, J = 5.6 Hz, 1H), 7.84 – 7.50 (m, 28H), 7.24 – 7.11 (m, 2H), 6.46 (t, J = 6.6 Hz, 1H). ^{13}C NMR (151 MHz, Acetone) δ 158.49, 158.36, 158.05, 157.79, 155.80, 155.75, 153.66, 153.20, 153.15, 152.16, 150.65, 150.28, 140.87, 140.31, 139.34, 139.17, 139.07, 138.99, 138.92, 138.52, 138.37, 138.25, 137.98, 137.85, 137.45, 137.43, 136.51, 134.54, 134.52, 132.69, 132.61, 129.25, 129.00, 128.73, 128.60, 128.46, 128.43, 128.33, 128.28, 128.25, 128.21, 127.51, 126.90, 125.77, 125.73, 125.65, 125.08, 124.93, 29.84. δ HRMS (TOF, ES+) (m/z): [M-2·PF_6]+ calculated for $C_{66}H_{46}N_6Ru$, 1024.2827; found, 1024.2992. IR (neat): 3073.81, 3024.78, 2967.21, 2925.28, 1708.48, 1701.04, 1699.25, 1695.99, 1651.98, 1616.91, 1575.95, 1566.22, 1560.65, 1554.46, 1542.37, 1479.38, 1460.70, 1445.93, 1437.22, 1425.30, 13920, 1365.03, 1311.81, 1262.13, 1241.87, 1209.59, 1160.17, 1112.85, 1067.51, 1043.91, 999.64, 967.51, 838.03, 821.30, 763.12.

3.4.3. Photophysical Data

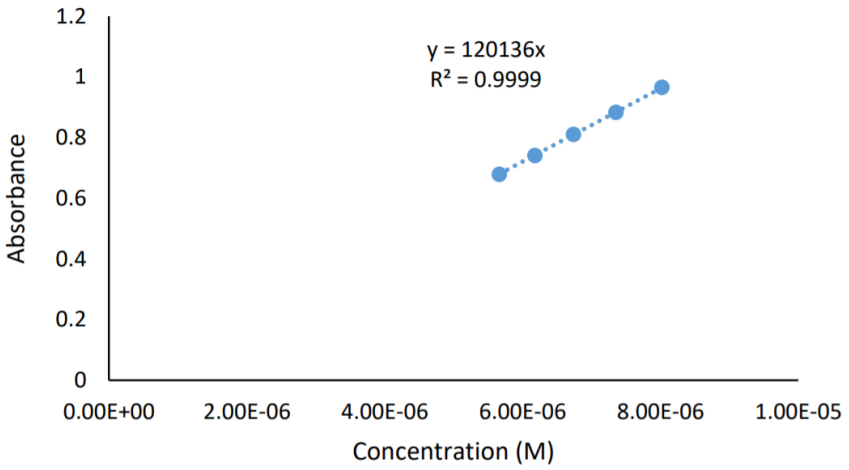

Figure 3.7. Extinction coefficient of **III.8** at 345 nm.

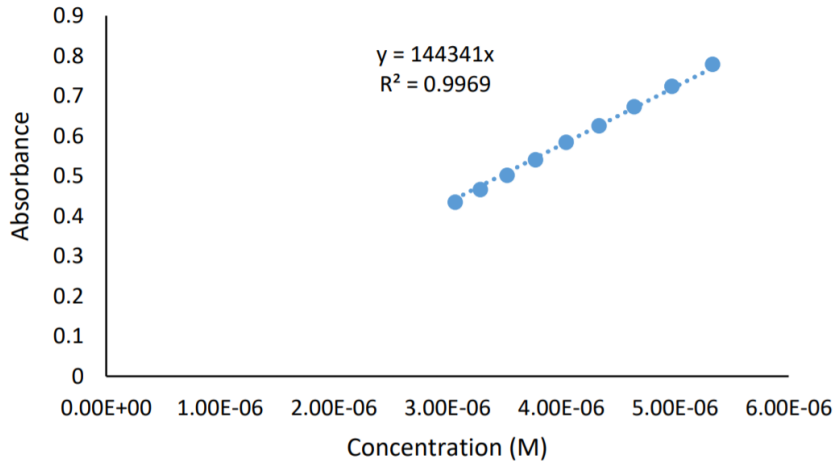

Figure 3.8. Extinction coefficient of **III.11** at 345 nm.

3.4.4. Computational Data

Calculations for **III.11** were carried out with Gaussian 09 package5 using B3LYP/6-31g* (for C, H, N) and LANL2DZ (Ru) level of theory. The geometry was first optimized in the gas phase. Once optimized, a single point calculation was carried out using the CPCM solvation model with acetonitrile as the solvent. All excited state calculations (TD-DFT) were performed on the fully optimized structures.

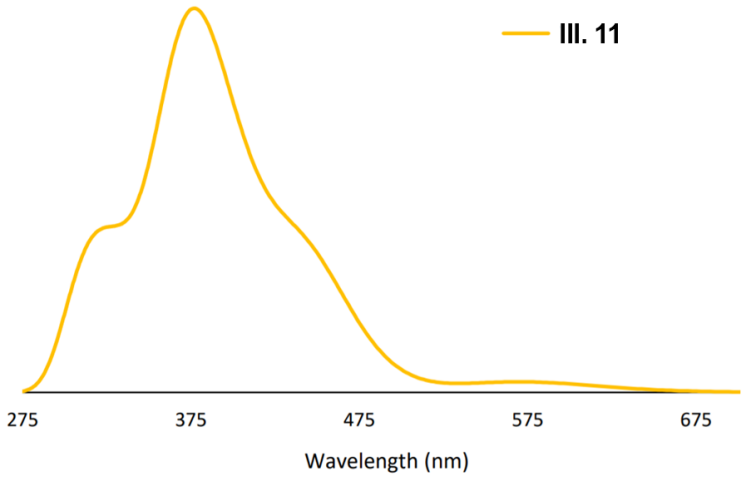

Figure 3.9. TD-DFT Absorbance of **III.11** (B3LYP/6-31g* (C, H, N) and LANL2DZ (Ru)).

3.4.5. Crystallographic Data

Crystallographic Data for **III.11**: $C_{76}H_{70}F_{12}N_6P_2Ru$, M = 1458.39, 0.19 x 0.16 x 0.01 mm, T = 173(2) K, Orthorhombic, space group $P_{ca}21$, a = 17.6487(16) Å, b = 20.6724(19) Å, c = 18.2635(14) Å, V = 6663.3(10) Å^3 , Z = 4, D_c = 1.454 Mg/m^3 , μ(Cu)= 3.071 mm^{-1}, F(000) = 3000, 2θmax = 118.78°, 22197 reflections, 8935 independent reflections [R_{int} = 0.1634], R1 = 0.1194, wR2 = 0.3092 and GOF = 1.019 for 8935 reflections (785 parameters) with I>2σ(I), R_1 = 0.1629, wR2 = 0.3449 and GOF = 1.031 for all reflections, Flack = 0.15(4), max/min residual electron density +1.649/-0.979 eÅ^{-3}.

Crystallographic Data for **III.10**: $C_{112}H_{102}B_2F_8N_4O_5Pd$, M = 1863.99, 0.14 x 0.06 x 0.02 mm, T = 173(2) K, Triclinic, space group P-1, a = 13.4593(3) Å, b = 24.9166(6) Å, c = 30.9993(8) Å, α = 79.836(2)°, β = 87.531(2)°, γ = 74.592(2)°, V = 9864.9(4) Å^3 , Z = 4, D_c = 1.255 Mg/m^3 , μ(Cu)= 2.093 mm^{-1}, F(000) = 3880, 2θmax = 99.62°, 68468 reflections, 20046 independent reflections [R_{int} = 0.0961], R1 = 0.0816, wR2 = 0.2149 and GOF = 1.071 for 20046 reflections (2172 parameters) with I>2σ(I), R1 = 0.1177, wR2 = 0.2354 and GOF = 1.100 for all reflections, max/min residual electron density +0.792/-0.926 eÅ^{-3}.

3.5. Bridge to Chapter IV

This chapter demonstrates that through the addition of an extra nitrogen atom, the cyclic framework of nanohoops can be transformed into a ligand that is capable of binding a wide-range of metal-centers. The synthesis of the key macrocyclic ligand, **III.8**, is achieved via a high-yielding Ni^0-mediated pyridyl chloride homocoupling reaction which allows for large quantities of the desired product to be available. With the ability to

coordinate a range of metals, the next chapter describes how these structures can be employed as ligands for metal-mediated reactions. Specifically, the ligand geometry has been designed such a coordinated metal is directed to interior of the macrocyclic pocket. Accordingly, when used in metal-mediated bond-forming reactions, the resulting product can be trapped as a rotaxane, which we then show can used to generate a new type of small-molecule fluorescent sensor.

CHAPTER IV

NANOHOOP ROTAXANES VIA ACTIVE METAL TEMPLATE SYNTHESES AND THEIR POTENTIAL IN SENSING APPLICATIONS

From Van Raden, J. M.; White, B. M.; Zakharov, L. N.; Jasti, R. *Angew. Chem. Int. Ed.* **2019**, *58*, 7341-7345. Further permissions related to the use of the material excerpted in this chapter should be directed to Wiley-VCH. This manuscript was written by myself with editorial assistance from Professor Ramesh Jasti and Dr. Brittany M. White. Experimental work in this chapter was performed by myself or Dr. Brittany M. White. Crystal structure analysis was done by Lev N. Zakharov.

The unique optoelectronic properties and smooth, rigid pores of macrocycles with radially oriented π systems render them fascinating candidates for the design of novel mechanically interlocked molecules with new properties. Two high-yielding strategies are used to prepare nanohoop [2]rotaxanes, which owing to the π-rich macrocycle are highly emissive. Then, metal coordination, an intrinsic property afforded by the resulting mechanical bond, can lead to molecular shuttling as well as modulate the observed fluorescence in both organic and aqueous conditions. Inspired by these findings, a self-immolative [2]rotaxane was then designed that self-destructs in the presence of an analyte, eliciting a strong fluorescent turn-on response, serving as proof-of-concept for a new type of molecular sensing material. More broadly, this work highlights the conceptual advantages of combining compact π-rich macrocyclic frameworks with mechanical bonds formed via active-template syntheses.

4.1. Introduction

Carbon-rich molecules with closed circuits of delocalized π electrons have been of longstanding interest owing to their unique optical, magnetic, and electronic properties.[1-6] Of this broad class of molecules, structures that have radially oriented π–π systems pointing inwards to the cavity of a macrocycle have recently emerged as a new class of strained, nonplanar aromatic molecules with unusual properties. Specifically, our laboratory and others have synthesized molecules referred to as carbon nanohoops because of their structural relationship to carbon nanotubes (**Figure 4.1a**).[7-14] These shape-persistent macrocycles can be prepared with varying size and atomic composition (**Figure 4.1b**),[15-29] which has unveiled their numerous size-dependent optoelectronic behavior and promising materials applications.[14] In particular, owing to the tunable and bright fluorescence,[9] biocompatibility,[23] and metal binding capabilities,[17, 21, 22] we have a growing interest in the development of these π-rich macrocycles for biological applications.

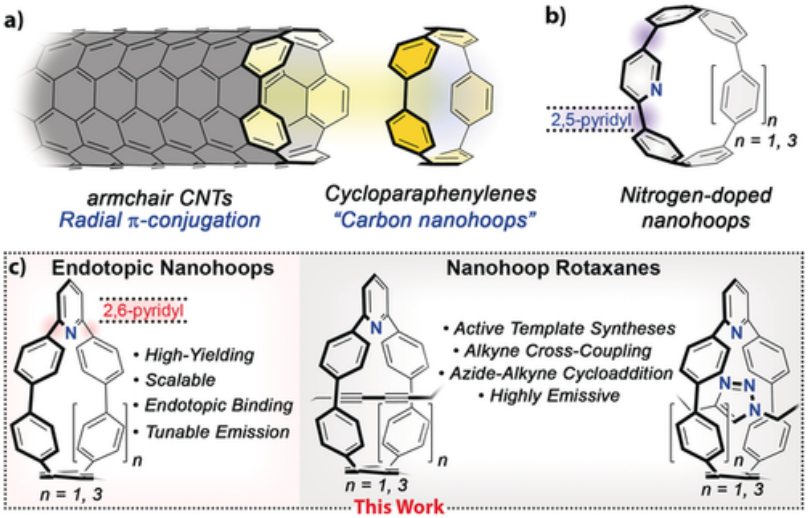

Figure 4.1. a) Structural relationship between armchair carbon nanotubes and cycloparaphenylenes (carbon nanohoops). b) Previously prepared 2,5-substituted pyridyl-embedded CPPs. c) Nanohoop macrocycles and rotaxanes in this work.

In the field of supramolecular chemistry, mechanically interlocked molecules (MIMs) such as catenanes, rotaxanes, and molecular knots have captured the imagination of chemists, highlighted by the recent Nobel Prize in 2016.[30-43]A particularly intriguing consequence of threading and/or weaving molecular components is that the resulting structures often possess highly selective molecular recognition sites that would be difficult to access using traditional covalent bonding, a feature that has contributed to a growing interest in employing these architectures as selective sensing platforms,[33,35] as well as new types of biological materials.[41, 44-46] In this regard, MIMs comprised of macrocycles with radial π-conjugation could provide new topological landscapes for a variety of applications owing to the exotic optical and electronic properties of structures possessing radial π-conjugation.[15-29]Only very recently have the first of these fascinating interlocked structures via passive template synthesis approaches have been reported.[47-49] Alternatively, the active-template method (AT)[31] could be a more powerful approach to these types of MIMs in that it does not rely on formation of a thermodynamically stable preorganized complex and therefore a wider array of structures are possible. Specifically, in the AT approach, a metal bound to the macrocyclic component catalyzes bond formation in the interior of the structure, which gives rise to the interlocked molecules. Herein, we report the syntheses of nanohoop macrocycles that, via an embedded 2,6-pyridyl moiety, participate in AT reactions, ultimately giving rise to a new class of highly compact, fluorescent [2]rotaxanes (**Figure 4.1c**). Moreover, we show that triazole-embedded nanohoop [2]rotaxanes coordinate metals in a reversible manner, which is accompanied by drastic changes in the emission of the macrocyclic fluorophore. Motivated by these findings, we then describe the design and preparation of a self-immolative type of rotaxane sensing platform, ultimately

highlighting key conceptual advantages of forming mechanical bonds with fluorescent carbon nanohoops via AT syntheses.

4.2. Results and Discussion

Inspired by the work of Leigh and Goldup,[31, 36] we initially considered leveraging the coordination ability of our previously reported bipyridyl-embedded nanohoops[32] in AT reactions to prepare mechanically interlocked nanohoop structures. However, in contrast to macrocycles typically used in AT rotaxane synthesis, a catalytic metal bound to these conformationally rigid nanohoops would direct bond formation to the exterior of the macrocycle.[32] Thus, our investigations began by first preparing a nanohoop ligand that would direct bond-formation to the interior of the macrocyclic cavity, which we envisioned occurring through the incorporation of a single 2,6-pyridine unit into the nanohoop backbone. Based on the well-established reductive aromatization approach to nanohoop molecules,[15-29] curved diboronate Suzuki–Miyaura cross-coupling partner **IV.1** (**Figure 4.2**) was first prepared.[24] With boronate **IV.1** in hand, we next explored macrocyclization conditions where under dilute (5 mm) Suzuki–Miyaura cross-coupling conditions with commercially available 2,6-dibromo pyridine, the desired macrocycle **IV.2** was isolated in excellent yield. With macrocycle **IV.2** in hand, a H_2SnCl_4-based aromatization was pursued, which after deprotection with tetrabutylammonium fluoride (TBAF), the target macrocycle **IV.3** was accessed in a 94 % yield. Under similar conditions, larger macrocycle **IV.4** (**Figure 4.2b**) was also synthetically accessible, as confirmed by X-ray crystallography (**Figure 4.2c**), albeit in slightly reduced yield. Importantly, in stark contrast to our previously reported pyridyl nanohoops, these macrocycles now have a coordination

moiety located on the interior of the macrocyclic cavity, as confirmed via X-ray crystallography (**Figure 4.2c**). Additionally, as a consequence of breaking molecular orbital symmetry,[29] it should be noted that both **IV.3** and **IV.4** were fluorescent, with **IV.3** emitting at λ_{max} of 509 nm (Φ=0.14) and **IV.4** at $\lambda_{max}$of 476 nm (Φ=0.62). Of note, the all *para*-substituted nanohoop with a single embedded pyridine is non-emissive;[16] a detailed investigation of the result of symmetry breaking on nanohoop fluorescence is disclosed in a separate study.[29]

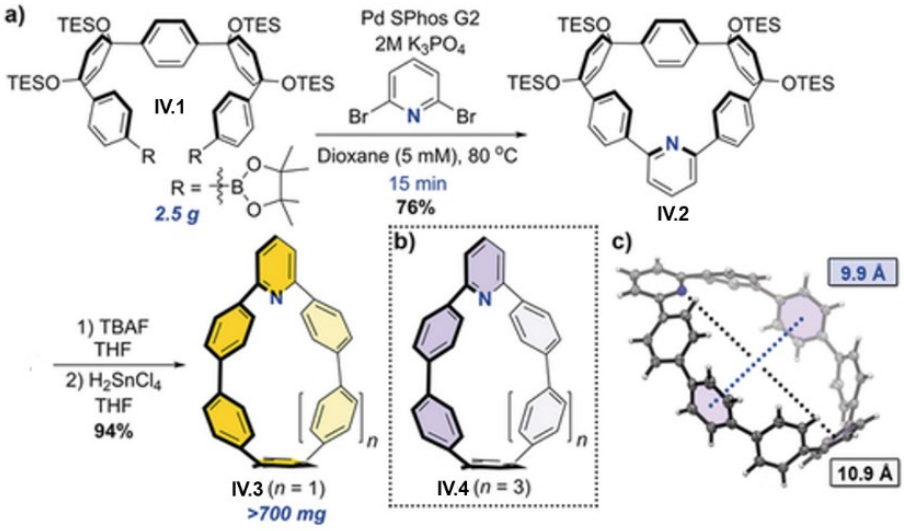

Figure 4.2. a) Synthetic route used to access ligand **IV.3** and **IV.4**. b) Structure of macrocycle **IV.4** and c) observed solid-state structure (ORTEP) of **IV.4**.

We next explored the potential of macrocycles **IV.3** and **IV.4** to participate in AT reactions. As a starting point (**Figure 4.3**), we first investigated the well-studied AT Cadiot–Chodkiewicz (AT-CC) reaction.[37, 38] While Glaser couplings have been shown to be quite successful in the preparation of rotaxanes, Cadiot–Chodkiewicz couplings allow for the preparation of unsymmetrical cross-coupled products and often tend to proceed under milder conditions. Based on the observed cavity size of macrocycle **IV.4** in the solid-

state (ca. 10 Å, **Figure 4.2c**), trityl-stoppered alkyne **IV.5** and trityl-stoppered bromo-alkyne **IV.6** were prepared by previously reported procedures.[39] After optimization, we found that when 1.2 equiv of alkyne **IV.5** and bromo-alkyne **IV.6** were subjected to the AT-CC conditions in **Figure 4.3**, the desired [2]rotaxane **IV.7** was isolated in 51 % yield. We next tested the ability of smaller macrocycle **IV.3** to participate in an AT-CC reaction, where it was found that the desired rotaxane **IV.8** formed with no loss in reaction efficiency. While small macrocycles have been explored in some cases,[36, 38] the rigid, shape-persistent nature of macrocycle **IV.3** results in a calculated cavity size of only 7.8 Å, rendering the formation of **IV.7** striking. Based on this result, we were curious whether rotaxanes could be prepared using simple, low-molecular-weight stopper groups, which would broaden the types of structures that could be accessed. Accordingly, it was found that under identical conditions, 3,5-di-*t*-butyl-stoppered rotaxane **IV.9** was readily formed, whereas unsubstituted benzene rings did not lead to rotaxane formation. Initial structural confirmation of each new [2]rotaxane was acquired by mass spectrometry. Furthermore, as is typical with MIMs, multiple upfield NMR shifts were observed in the thread component of each suspected [2]rotaxane, which further suggested a mechanically interlocked structure. For example, proton H_a (see **Figure 4.3a** for labels) of the encircled thread in [2]rotaxanes **IV.7a** and **IV.7b** is shifted significantly upfield by nearly 1.5 ppm and 2.0 ppm, respectively, relative to free thread.[40] Owing to the unusually small nature of macrocycle **IV.3**, we were particularly interested in the structural features of [2]rotaxanes **IV.7b** and **IV.7c**. Indeed, turning to single-crystal X-ray crystallography, the highly congested nature of these π-rich rotaxanes was revealed, where it was found that the cavity of macrocycle **IV.3** is an almost perfect fit for the diyne thread units of

both **IV.7b** and **IV.7c** (**Figure 4.3b, c**). For example, in the case of **IV.7b**, the observed distance between the central carbon atom of the threaded diyne component and the nitrogen of macrocycle **IV.3** was found to be 3.6 Å (**Figure 4.3b**). Additionally, no solvent molecules were observed in either structure, consistent with a tightly packed crystal structure overall. Given that conjugated macrocycles have recently emerged as strong candidates for new types of electronic materials, this result is particularly encouraging, as the ability to thread π-conjugated fragments in close contact could lead to new geometric designs for electron/hole transporting materials.

Owing to the wide range of commercially available azide- and alkyne-functionalized starting materials, we next pursued an active template Cu^{I}-catalyzed azide–alkyne cycloaddition (AT-CuAAC) reaction.[31] As a first pass, macrocycle **IV.4** was subjected to conditions (**Figure 4.4**) similar to those reported by Leigh et al.,[31] which provided the corresponding trityl-stoppered rotaxane **IV.9a** in excellent yield. However, when macrocycle **IV.3** was subjected to these conditions using 3,5-dimethyl ester substituted coupling partners (**Figure 4.4**, **IV.8c** and **IV.8b**), the desired rotaxane **IV.9b** was formed in 14 % yield. After screening various conditions, we found that the addition of acetic acid as well as elevated temperatures (100 °C via microwave irradiation) improved the yield considerably, with rotaxane **IV.9b** being isolated in 45 % yield (**Figure 4.4**, entry 2). While a more detailed investigation of the scope is ongoing, for our work presented herein, we viewed [2]rotaxane **IV.9b** as a particularly versatile intermediate. For example, motivated by our recent report on the biocompatibility of nanohoops[23] as well the emerging interest in using fluorescent rotaxane architectures in biological environments,[47-49] **IV.9b** was saponified to access

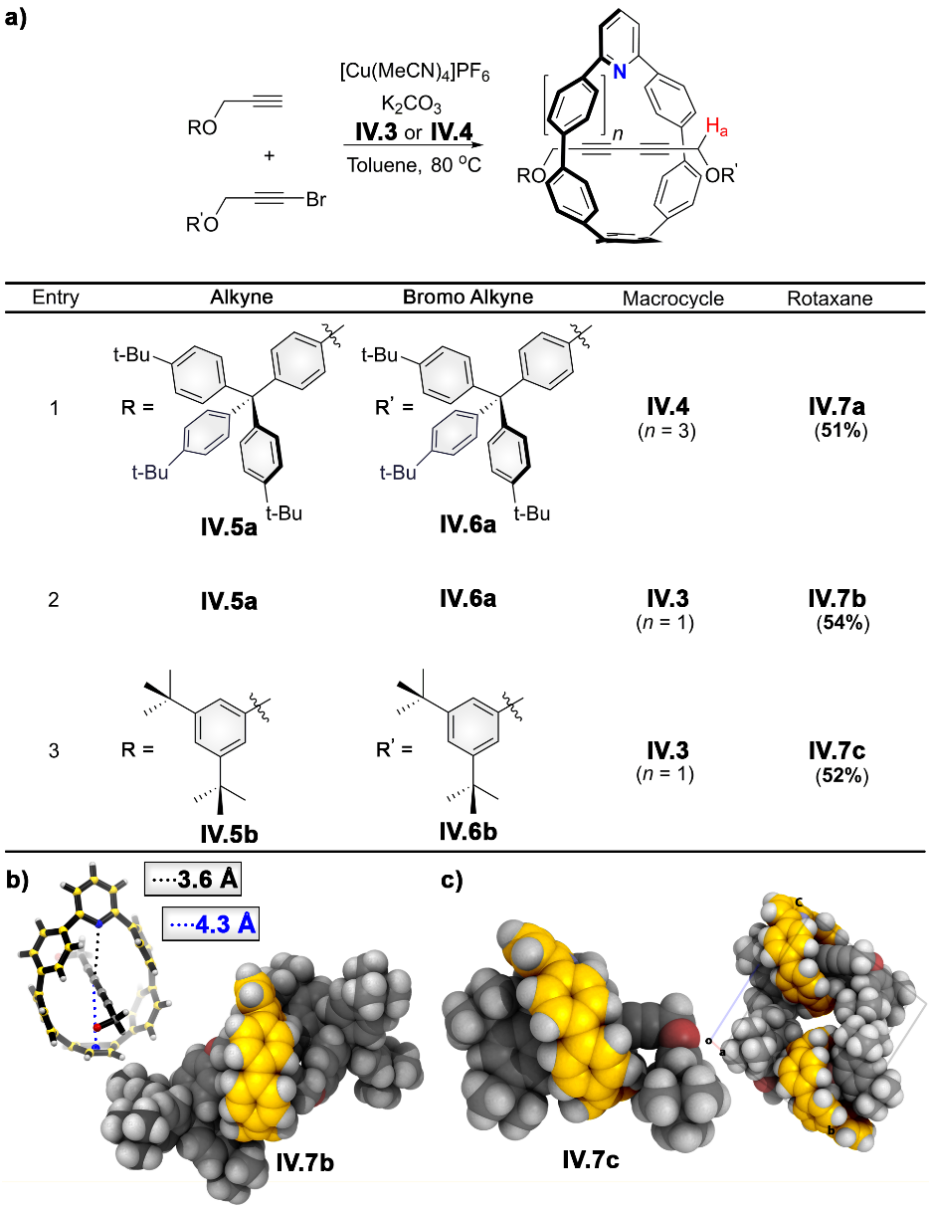

Figure 4.3. a) Synthesis of nanohoop [2]rotaxanes via AT-CC conditions; solid-state structures (space-filling) of b) [2]rotaxane **IV.7b** and c) **IV.7c**. Macrocycle **IV.3** has been colored yellow while each thread is colored in gray. The inset in (b) shows distances between selected points. For clarity, the trityl groups have been removed.

water-soluble [2]rotaxane **IV.9c** (**Figure 4.5a**), which retained the corresponding emission properties (Φ=0.07) in aqueous conditions. Additionally, apart from biological

systems, carboxylate functionalized [2]rotaxanes have also recently been incorporated into metal–organic frameworks,[50, 51] suggesting that this intermediate could act as a new π-rich building block for unusual types of coordination polymers. Ultimately, these results highlight the generality of both the AT-CC and AT-CuAAC reactions, a feature that is expected to provide a variety of new types of π-rich interlocked molecules and materials. Additionally, the narrow cavity of the nanohoops reduce the requirements of the stopper groups that can be employed, furthering the utility of these systems.

Mechanically interlocked molecules bearing nitrogen heteroatoms often engage in a wide range of unique co-ordination chemistry where, depending on the metal and resulting coordination geometry, features such as molecular shuttling, switching, and sensing can be enabled. Thus, we were curious if the congested binding pocket of triazole [2]rotaxanes such as **IV.9b** could still participate in metal coordination. To probe this, we next investigated the effects of metalation on **IV.9b** in both the solid state and solution through single-crystal X-ray crystallography, ^{1}H NMR titrations, and fluorescence spectroscopy. In the solid-state (**Figure 4.4**), without metal, the macrocycle of **IV.9b** resides over the propyl chain. In solution, a resonance at −1.43 ppm can be observed, indicating that the propyl chain experiences a particularly strong shielding effect, suggesting that the macrocycle resides over the propyl chain. On addition of Cu^{I}, this signal broadens, but never fully vanishes. Additionally, the appearance of multiple new resonances was observed which indicates the formation of a new species alongside metal-free **IV.9b**. To investigate this further, we then co-crystallized **IV.9b** with 1.0 equiv of $[Cu(MeCN)_4]PF_6$, which revealed that in the solid state, the macrocycle is now localized over the triazole unit with the Cu^{I} metal coordinated to both the triazole and macrocyclic nitrogen (**Figure 4.12**). A

similar shuttling effect was observed when **IV.9b** was titrated with $[Pd(MeCN)_4](BF_4)_2$. Notably, in presence of Pd^{II}, the observed signals in the ^1H NMR spectrum were noticeably sharper relative to that observed with $[Cu(MeCN)_4](PF_6)$, indicating a less dynamic system. Taken together, it can be concluded that, despite the sterically congested environment, triazole embedded rotaxanes bearing macrocycle **IV.3** bind metals such as Cu^I and Pd^{II}, with Pd^{II} acting as a stronger binding metal. From these initial studies, an additional key result was observed; as the amount of Pd^{II} increased, the fluorescence of **IV.9b** decreased. As can be seen in **Figure 4**, the addition of 1.0 equiv of $[Pd(MeCN)_4](BF_4)_2$ to **IV.9b** results in a non-emissive rotaxane, that is, Pd^{II}- **IV.9b**. Given that metalation with Pd^{II} effectively traps the fluorophore in a non-emissive state, we expected that demetalation should result in a turn-on response. To validate this, non-emissive Pd^{II}- **IV.9b** was treated with 1.0 equiv of ethylenediaminetetraacetic acid (EDTA), which quickly resulted in a pronounced 30-fold increase in emission (**Figure 4.5b**). Encouraged by this result, we were then curious if the emission of water-soluble rotaxane **IV.9c** (**Figure 4.5**) could be modulated in a similar fashion. Indeed, the emission of carboxylate rotaxane **IV.9c** was readily quenched (**Figure 4.12**) in aqueous media (PBS buffer) by the addition of 1.0 equiv of $[Pd(MeCN)_4](BF_4)_2$ to give Pd^{II}- **IV.9c**. Upon addition of EDTA to this aqueous solution, it was again found (**Figure 4.12**) that the emission quickly returned, albeit with reduced intensity (10-fold increase).

Inspired by the fluorescence quenching results with metals, we envisioned a perhaps more general sensing platform in which a suitable thread component could serve as both a stopper and fluorescence quencher. Analyte-induced bond cleavage of the thread could then perhaps release the quencher and lead to a turn-on fluorescence response.

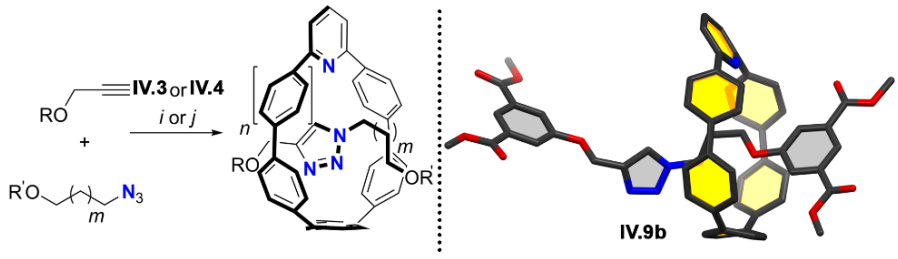

Entry	Alkyne	Azide	Macrocycle	Rotaxane
1	R = 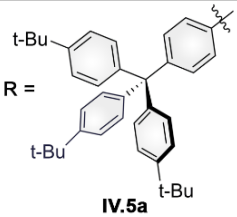 **IV.5a**	R' = 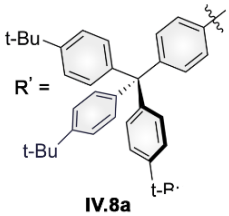 **IV.8a** (*m* = 2)	**IV.4** (*n* = 3)	**IV.9a** (**70%**)
2	R = 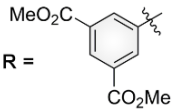 **IV.8c**	R' = 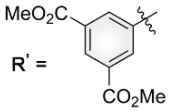 **IV.8b** (*m* = 1)	**IV.3** (*n* = 1)	**IV.9b** (**45%**)

Figure 4.4. AT-CuAAC conditions used to access triazole rotaxanes **IV.9a** and **IV.9b**. i=$[Cu(MeCN)_4]PF_6$ (0.95 equiv), CH_2Cl_2, rt, 24 h; j=AcOH (20.0 equiv), $[Cu(MeCN)_4]PF_6$(0.95 equiv), CH_2Cl_2, μW, 100 °C, 3 h. X-ray structure of **IV.9b** (top right) showing location of macrocycle **IV.3** (yellow) over triazole thread.

Encouraged by the ability of electron-deficient C_{60} to quench the emission of [10]CPP,[26] we hypothesized that macrocycle **IV.3** could temporarily be rendered non-emissive through the incorporation of a cleavable, mechanically bound electron-deficient stopper moiety. To investigate this concept, we prepared a 3,5-dinitro-functionalized rotaxane (**IV.9d**) bearing a fluoride-cleavable triisopropylsilyl (TIPS) stopper group (**Figure 4.5c**) via our AT-CC conditions (**Figure 4.7**) which we found to be non-emissive (**Figure 4.5d**). Importantly, treatment of rotaxane **IV.9d** with 1.0 equiv of tetra-*n*-butylammonium fluoride (TBAF) resulted in a nearly instantaneous dethreading event

which was accompanied by a dramatic 123-fold increase in emission intensity (**Figure 4.5d**), effectively serving as proof-of-concept for a highly responsive self-immolative rotaxane sensor. Additionally, through density functional theorem (DFT), it was found that the frontier molecular orbitals of **IV.9d** are redistributed relative to macrocycle **IV.3** (**Figure 4.5f**). Specifically, for macrocycle **IV.3** (**Figure 4.14**), both the highest-occupied molecular orbital (HOMO) and the lowest-unoccupied molecular orbital (LUMO) reside over the nanohoop backbone. In contrast, in the case of **IV.9d**, the HOMO is localized on the macrocyclic component and the LUMO is localized over the electron-deficient nitrobenzene stopper, consistent with a charge-transfer quenching mechanism. These results highlight the importance of electronic structure in the design of new non-emissive rotaxanes such as **IV.9d**, and we expect that through a computationally guided design approach, a wide range of new analyte-selective, turn-on scaffolds can be prepared. For example, the analyte recognition site (TIPS stopper) of **IV.9d** can likely be replaced by a range of small yet effective analyte-sensitive stopper groups such as boronates, amides, and esters, a key advantage of using a rigid macrocycle with small diameter. Moreover, we anticipate that this design can be applied to our larger macrocycle, **IV.4**, as a means to access different emission wavelength and higher quantum yield. Work is currently underway toward the preparation and application of these structures and will be reported in due course.

4.3. Conclusions

In conclusion, this work demonstrates that by embedding a 2,6-pyridine coordination motif into the backbone of a nanohoop macrocycle, a range of diverse

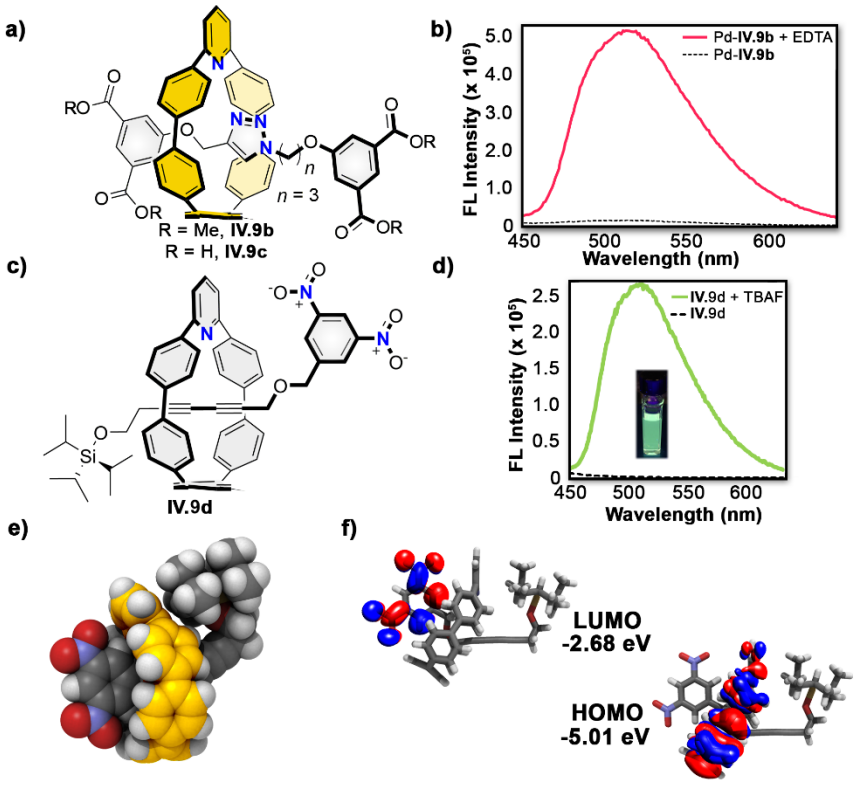

Figure 4.5. a) Structure of emissive triazole rotaxanes **IV.9b**, **IV.9c** and b) emission spectra: 8.6 μm, $CHCl_3$ (**IV.9b**) of metalated and demetalated rotaxane **IV.9b**. c) Structure of non-emissive diyne rotaxane **IV.9d**. d) Emission spectrum (8.6 μm, $CHCl_3$) of **IV.9d** before and after addition of 1.0 equivalent of TBAF. e) X-ray structure of [2]rotaxane **IV.9d** in space-filling representation and f) DFT calculated (B3LYP/6–31g) frontier molecular orbitals.

[2]rotaxanes are accessible via two different Cu^{I}-catalyzed active-metal template reactions. Based on fundamental metal coordination experiments with triazole-embedded [2]rotaxanes formed via AT-CuAAC reactions, we have found that two metals, Cu^{I} and Pd^{II}, effectively shuttle the nanohoop macrocycle along the length of a triazole-functionalized thread. A key result from these studies was the observation that in both

organic and aqueous conditions, metal binding is easily monitored by dramatic changes in fluorescence emission. Expanding on this finding, we then designed and prepared, via an AT-CC reaction, a metal-free, non-emissive nanohoop [2]rotaxane that has been stoppered with a fluorescence-quenching 3,5-dinitrobenzyl unit and fluoride-cleavable TIPS group. On bond cleavage, the quenching moiety is no longer in close proximity to the fluorophore, which results in a dramatic 123-fold increase in emission intensity, effectively serving as proof-of-concept for nanohoop rotaxane turn-on fluorescence sensors. Particularly noteworthy is that this self-immolative nanohoop [2]rotaxane was constructed in a modular fashion and therefore should be easily adaptable to other types of analytes and applications. More broadly, we expect that this active template synthetic strategy will provide efficient pathways for generating a wide array of very compact π-rich interlocked molecules as well as materials. Finally, owing to the highly tunable and rigid π-rich pores, catalytic metals bound to the interior of nanohoops represent an intriguing area of future exploration.

4.4. Experimental Sections

4.4.1. General Experimental Details

^{1}H NMR spectra were recorded at 500 MHz on a Varian VNMR spectrometer, 500 MHz on a Bruker, or 600 MHz on a Bruker. All ^{1}H NMR spectra are referenced to residual $CHCl_3$ (δ 7.26 ppm). All ^{13}C NMR spectra are referenced to residual $CHCl_3$ (δ 77.16 ppm). All reagents were obtained commercially. All glassware was flame-dried and cooled under an inert atmosphere of nitrogen unless otherwise noted. Moisture sensitive reactions were carried out under an inert atmosphere of nitrogen using standard syringe/septa technique. Silica column chromatography was conducted with Zeochem Zeoprep 60 Eco 40-63 uM

silica gel while alumina chromatography, where noted, utilized Sorbent Technologies 50-200 um Basic Activity II-II Alumina.

H_2SnCl_4, where noted, was prepared in the following manner: To a solution of $SnCl_2 \bullet {}_2H_2O$ (180.0 mg, 0.796 mmol, 1.00 equiv) in 10 mL THF was added conc. HCl (133.0 µL, 1.59 mmol, 2.0 equiv.). The resulting solution was then stirred for 15 minutes and used as needed. This procedure was scaled as needed.

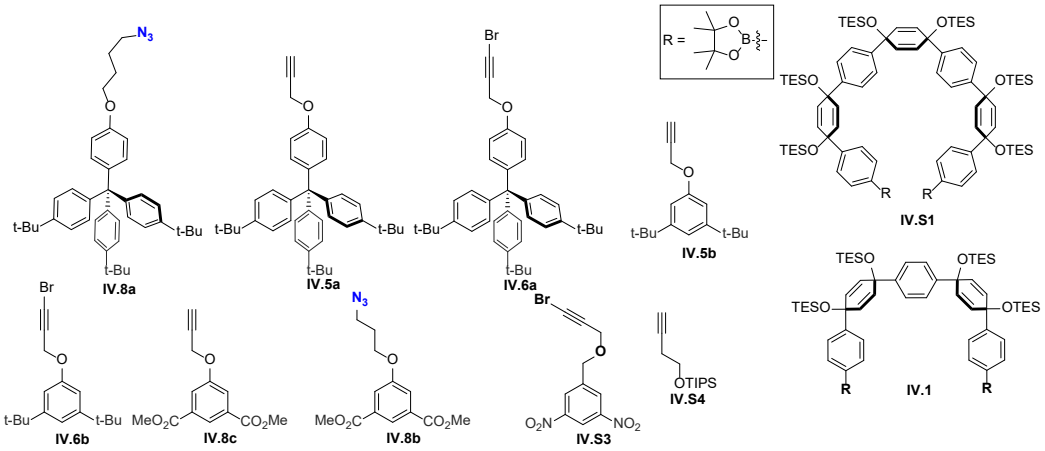

Figure 4.6. The compounds in this figure: **IV.1**,[24] **IV.S1**,[24] **IV.5a**,[31] **IV.8a**,[31] **IV.5b**,[39] **IV.8b**,[52] **IV.8c**[39] and **IV.S4**[52] were prepared via literature procedures. **IV.6b** and **IV.6a** were prepared by treating **IV.5b** and **IV.5a**, respectively, with NBS and AgNO3.[53]

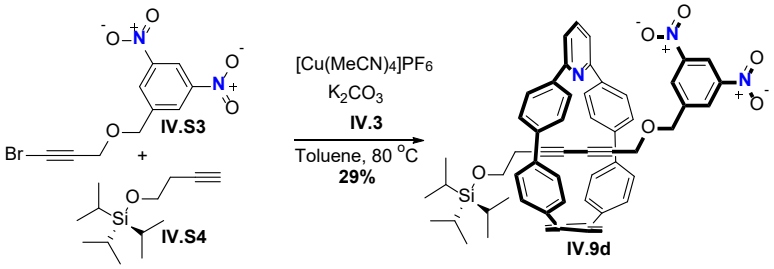

Figure 4.7. Synthesis of **IV.9d**.

4.4.2. Synthetic Details

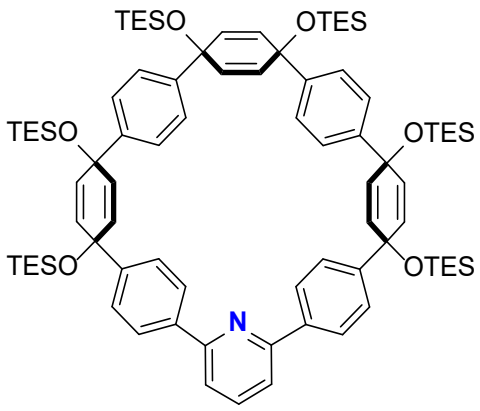

Synthesis of IV.S2. To a flame-dried 2 L round bottom flask equipped with a stir bar was added **IV.S1**[24] (2.10 g, 1.33 mmol, 1.00 equiv.), 2,6-dibromopyridine (0.330 g, 1.40 mmol, 1.05 equiv.), and Pd SPhos G2 (0.0958 g, 0.133 mmol, 0.10 equiv.). The flask was evacuated and back-filled with N_2 5 times, followed by addition of 1,4-dioxane (700 mL). This solution was then vigorously sparged with N_2 for 30 min at which point it was then placed into an 80 ºC oil bath for 30 min. At this point, an N_2 sparged aqueous solution of 2M K_3PO_4 (70.0 mL, 35.0 mmol, 26.3 equiv.) was added, quickly turning the solution to a bright yellow. The reaction was monitored until all starting material was consumed (typically 1h), at which point the solution was allowed to cool to room temperature. After removal of the solvent *via* rotary evaporation, the resulting yellow/brown oil was extracted with DCM (3 x 75 mL), followed by washing of the combined organic phases with H_2O (3 x 100 mL), brine (1 x 100 mL), and finally placed over sodium sulfate. Removal of the organic phase gave a yellow oil, which, on addition of acetone (5 mL), caused the precipitation of a white solid which was then collected *via* filtration to give **IV.S2** as a white solid (0.810 g, 45%). ^{1}H NMR (500 MHz, Chloroform-*d*) δ 8.05 (d, J = 8.4 Hz, 4H), 7.78 (t, J = 7.8 Hz, 1H), 7.67 (d, J = 7.8 Hz, 2H), 7.52 – 7.41 (m, 12H), 6.14 (s, 4H), 6.05 (d, J = 10.0 Hz, 4H), 5.90 (d, J = 10.1 Hz, 4H), 0.98 (m, 18H), 0.91 (m, 36H), 0.70 (m,

12H), 0.59 – 0.50 (m, 24H). ^{13}C NMR (126 MHz, Chloroform-*d*) δ 156.28, 147.25, 146.11, 145.75, 138.04, 132.67, 131.80, 131.22, 126.75, 126.12, 125.93, 118.06, 71.67, 70.97, 69.86, 7.29, 6.74, 6.67, 6.58. MS (MALDI-TOF) (m/z): [M]+ calculated for $C_{83}H_{121}NO_6Si_6$, 1395.780; found, 1395.820

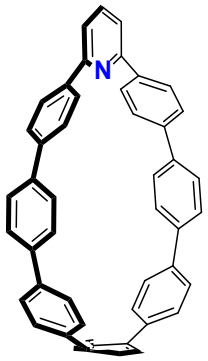

Synthesis of IV.4. To a flame-dried 100 mL round bottom flask equipped with a stir bar was added **IV.S2** (0.360 g, 0.257 mmol, 1.00 equiv.), followed by THF (20 mL). To this solution was slowly added TBAF (1M in THF, 2.57 mmol, 2.58 mL, 10.0 equiv.), resulting in a tan suspension. After stirring for 45 min, the THF was removed *via* rotary evaporation, followed by addition of H_2O (20 mL) resulting in a white precipitate. The white solid was collected via filtration, washed with H_2O (50 mL), DCM (5 mL) and was then transferred to a flame-dried 100 mL RBF with stir bar. After addition of THF (20 mL), H_2SnCl_4 (4.00 equiv.) was added dropwise, turning the colorless solution to a bright orange over 20 minutes. This was then allowed to stir for 45 min, at which point the reaction contents were neutralized with 1M NaOH, quickly turning the solution from bright orange to bright yellow. The THF was removed *via* rotary evaporation, followed extraction of the resulting yellow/orange aqueous suspension with DCM (3 x 50 mL). The combined organic phases were washed with H_2O (3 x 50 mL), brine (1 x 50 mL) and then dried over sodium sulfate. After removal of DCM under reduced pressure, the resulting yellow solid

was run through a short alumina plug using DCM as eluent, providing **IV.4** as a yellow/white solid (0.111 mg, 53%). ^{1}H NMR (500 MHz, Chloroform-*d*) δ 7.81 (t, *J* = 7.8 Hz, 1H), 7.68 (d, *J* = 8.2 Hz, 4H), 7.58 (d, *J* = 7.8 Hz, 2H), 7.56 – 7.46 (m, 16H), 7.36 (d, *J* = 8.4 Hz, 4H), 7.33 (d, *J* = 8.5 Hz, 4H). ^{13}C NMR (126 MHz, $CDCl_3$) δ 158.93, 141.60, 140.40, 139.41, 138.17, 138.08, 137.97, 137.86, 137.04, 129.30, 128.22, 128.05, 127.93, 127.91, 127.36, 127.06, 117.48. MS (MALDI-TOF) (m/z): [M+H]+ calculated for $C_{47}H_{32}N$, 610.251; found, 610.210.

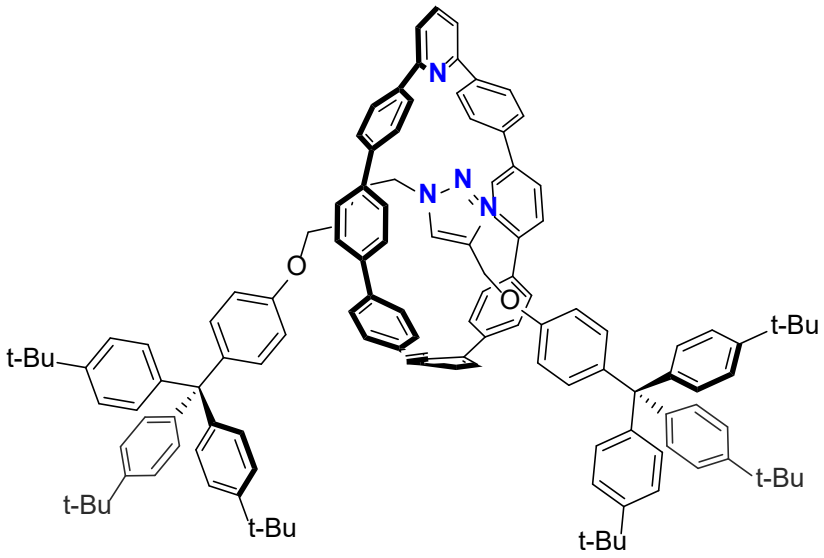

Synthesis of IV.9a. To a flame-dried 25 mL flask equipped with a stir bar was added ligand **IV.4** (11.7 mg, 0.0192 mmol, 1.00 equiv.), $Cu(MeCN)_4PF_6$ (6.4 mg, 0.0184 mmol, 0.96 equiv.), azide **IV.8a** (0.115 g, 0.192 mmol, 10.0 equiv.) and alkyne **IV.5a** (0.104 g, 0.192 mmol, 10.0 equiv.). The flask was then evacuated and refilled with N_2 5 times. A septum was then placed on the flask, followed by the addition of 5 mL DCM. The reaction was followed with TLC and allowed to stir until complete consumption of azide or alkyne. At this point, the reaction was quenched with an NH_3-EDTA (2 mL) and then allowed to

stir for 10 min. The layers were separated, followed by additional washing of the aqueous phase with DCM (2x 20 mL). The combined organic phases were washed with H_2O (3 x 20 mL), and brine (1 x 20 mL), and dried over sodium sulfate to give a bright yellow solid, which after chromatography (50% diethyl ether/hexanes, SiO_2), yielded the desired rotaxane **IV.9a** as a yellow solid/oil (23.5 mg, 70%).^{1}H NMR (500 MHz, Chloroform-*d*) δ 7.56 (t, *J* = 7.9 Hz, 1H), 7.50 – 7.28 (m, 30H), 7.24 – 7.08 (m, 26H), 6.97 (d, *J* = 8.8 Hz, 2H), 6.76 (d, *J* = 8.4 Hz, 2H), 5.73 (s, 1H), 4.74 (s, 2H), 1.92 (t, *J* = 6.7 Hz, 2H), 1.86 (d, *J* = 4.8 Hz, 2H), 1.32 (s, 27H), 1.29 (s, 27H), -0.17 – -0.21 (m, 2H), -0.51 – -0.65 (m, 2H). ^{13}C NMR (126 MHz, $CDCl_3$) δ 148.59, 148.50, 144.40, 144.24, 141.01, 140.55, 139.01, 136.89, 132.48, 131.88, 130.87, 130.84, 129.27, 128.17, 127.85, 127.53, 127.34, 127.17, 124.35, 124.26, 122.35, 117.49, 113.26, 63.27, 34.50, 34.46, 31.57, 31.54. MS (MALDI-TOF) (m/z): [M]+ calculated for $C_{128}H_{128}N_4O_2$, 1753.003; found, 1752.858.

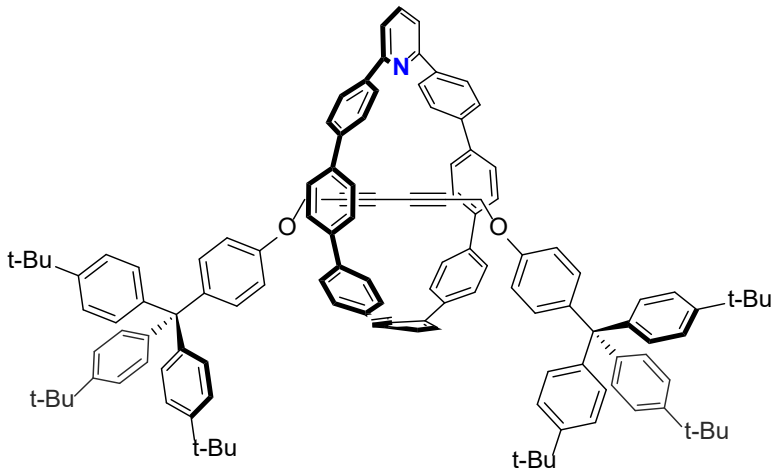

Synthesis of IV.7a. To a flame-dried 25 mL flask equipped with a stir bar was added ligand **IV.4** (17.8 mg, 0.0292 mmol, 1.00 equiv.), $Cu(MeCN)_4PF_6$ (10.4 mg, 0.0280 mmol, 0.96 equiv.), bromo alkyne **IV.6a** (0.0190 g, 0.0350 mmol, 1.2 equiv.), terminal alkyne **IV.5a** (0.0217 g, 0.0350 mmol, 1.2 equiv.), and potassium bicarbonate (20.1 mg, 0.146

mmol, 5.00 equiv.). The flask was then evacuated and refilled with N_2 5 times. A septum was then placed on the flask, followed by the addition of 5 mL toluene. The reaction was then heated to 80 °C and the reaction progress was followed with TLC. On completion, the reaction was quenched with an NH_3-EDTA (2 mL) solution and then allowed to stir for 10 min. The layers were separated, followed by additional washing of the aqueous phase with DCM (2x 20 mL). The combined organic phases were washed with H_2O (3 x 20 mL), and brine (1 x 20 mL), and dried over sodium sulfate to give a bright yellow solid/oil, which after chromatography (50% diethyl ether/hexanes), yielded the desired rotaxane **IV.7a** as a yellow solid (25.2 mg, 51%).^{1}H NMR (500 MHz, Chloroform-*d*) δ 7.77 (t, *J* = 7.8 Hz, 1H), 7.57 (d, *J* = 7.9 Hz, 4H), 7.54 (d, *J* = 7.8 Hz, 2H), 7.43 – 7.36 (m, 8H), 7.30 (d, *J* = 8.5 Hz, 16H), 7.27 (s, 4H), 7.21 (t, *J* = 8.5 Hz, 8H), 7.09 (d, *J* = 8.4 Hz, 12H), 6.78 (d, *J* = 8.7 Hz, 4H), 5.70 (d, *J* = 8.9 Hz, 4H), 3.56 (s, 4H), 1.33 (s, 54H). ^{13}C NMR (126 MHz, $CDCl_3$) δ 148.59, 148.50, 145.90, 144.40, 144.24, 141.01, 140.55, 139.01, 136.89, 132.48, 131.88, 130.87, 130.84, 129.27, 128.17, 127.85, 127.53, 127.34, 127.17, 124.35, 124.26, 117.49, 113.26, 63.27, 34.50, 34.46, 31.57, 31.54. MS (MALDI-TOF) (m/z): [M]+ calculated for $C_{127}H_{121}NO_2$, 1691.944; found, 1692.020.

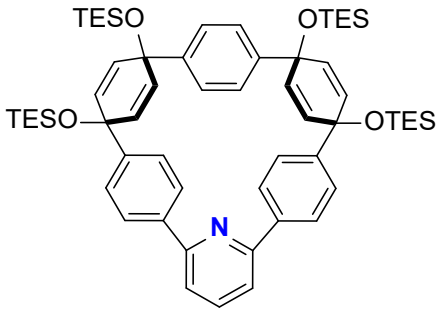

Synthesis of IV.2. To a 1 L round bottom flask equipped with a stir bar was added **IV.1**[24] (2.50 g, 2.16 mmol, 1.00 equiv.), 2,6-dibromopyridine (764.6 mg, 3.24 mmol, 1.50 equiv.), and Pd SPhos G2 (0.167 g, 0.216 mmol, 0.10 equiv.). The flask was evacuated and back-

filled with N_2 5 times, followed by addition of 1,4-dioxane (450 mL). This solution was then vigorously sparged with N_2 for 30 min at which point it was then placed into an 80 ºC oil bath for 30 min. At this point, an N_2 sparged aqueous solution of 2M K_3PO_4 (45.0 mL, 90.0 mmol, 42.0 equiv.) was added, quickly turning the solution to a bright yellow. The reaction was monitored until all starting material was consumed (~15 min), at which point the solution was allowed to cool to room temperature. After removal of the solvent *via* rotary evaporation, the resulting yellow/brown oil was extracted with DCM (3 x 100 mL), followed by washing of the combined organic phases with H_2O (3 x 100 mL), brine (1 x 100 mL), and finally placed over sodium sulfate. Removal of the organic phase gave a yellow oil, which, was then chromatographed (40% DCM/Hexanes, SiO_2) to give **IV.2** as a white solid (1.61 g, 76%). On larger scale reactions, the desired product **IV.2** can be isolated *via* the addition of acetone (5 mL) to the yellow oil obtained after workup, followed by sonication and collection of the solid *via* filtration to give **IV.2** as a white solid. ^{1}H NMR (500 MHz, Chloroform-*d*) δ 7.83 – 7.73 (m, 5H), 7.55 (d, *J* = 7.5 Hz, 2H), 7.50 (d, *J* = 7.6 Hz, 4H), 7.01 (s, 4H), 6.07 (d, *J* = 8.9 Hz, 4H), 5.74 (d, *J* = 8.8 Hz, 4H), 1.04 – 0.91 (m, 36H), 0.78 – 0.57 (m, 24H). ^{13}C NMR (126 MHz, $CDCl_3$) δ 157.96, 146.11, 144.80, 142.10, 137.94, 131.76, 131.56, 129.24, 125.75, 125.66, 116.16, 71.42, 71.28, 7.26, 7.19, 6.75, 6.57. HRMS (ESI-TOF) (m/z): [M]+ calculated for $C_{59}H_{83}NO_4Si_4$, 981.5400; found, 981.5406

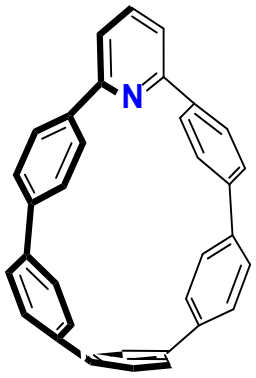

Synthesis of IV.3. To a flame-dried 100 mL round bottom flask equipped with a stir bar was added **IV.2** (1.60 g, 1.63 mmol, 1.00 equiv.), followed by THF (20 mL). To this solution was slowly added TBAF (1M in THF, 13.0 mmol, 13.0 mL, 8.00 equiv.), resulting in a tan suspension. After stirring for 1h, the THF was removed *via* rotary evaporation, followed by addition of H_2O (20 mL) resulting in a white precipitate. The white solid was collected *via* filtration, washed with H_2O (50 mL), DCM (15 mL) and was then transferred to a flame-dried 100 mL RBF with stir bar. After addition of THF (20 mL), H_2SnCl_4 (5 equiv.) was added dropwise, turning the colorless solution to a bright orange over 20 minutes. After stirring for 1h, the solution was neutralized with 1M NaOH, quickly turning the solution from bright orange to bright yellow. The THF was removed *via* rotary evaporation, followed extraction of the resulting yellow/orange aqueous suspension with DCM (3 x 100 mL). The combined organic phases were washed with H_2O (3 x 50 mL), brine (1 x 50 mL) and then dried over sodium sulfate. After removal of DCM under reduced pressure, the resulting yellow solid was run through a short alumina plug using DCM as eluent, providing **IV.3** as a yellow solid (0.701 g, 94%). ^{1}H NMR (500 MHz, Chloroform-*d*) δ 7.81 (t, *J* = 7.8 Hz, 1H), 7.68 (d, *J* = 8.2 Hz, 4H), 7.58 (d, *J* = 7.8 Hz, 2H), 7.56 – 7.46 (m, 16H), 7.36 (d, *J* = 8.4 Hz, 4H), 7.33 (d, *J* = 8.5 Hz, 4H). ^{13}C NMR (126 MHz, $CDCl_3$) δ 158.93, 141.60, 140.40, 139.41, 138.17, 138.08, 137.97, 137.86, 137.04,

129.30, 128.22, 128.05, 127.93, 127.91, 127.36, 127.06, 117.48. HRMS (ESI-TOF) (m/z): [M]+ calculated for $C_{35}H_{23}N$, 457.1831; found, 457.1843.

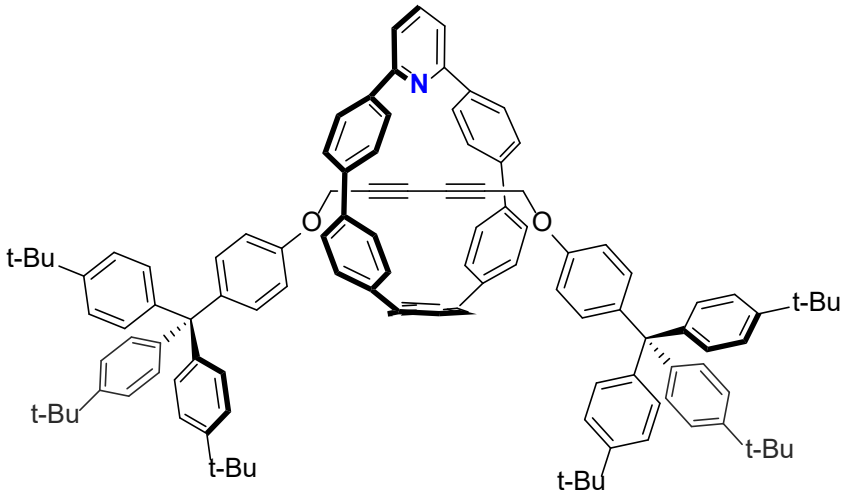

Synthesis of IV.7b. To a flame-dried 25 mL flask equipped with a stir bar was added ligand **IV.3** (22.2 mg, 0.0485 mmol, 1.00 equiv.), $Cu(MeCN)_4PF_6$ (17.0 mg, 0.0461 mmol, 0.95 equiv.), bromo alkyne **IV.6a** (36.5 mg, 0.0582 mmol, 1.2 equiv.), terminal alkyne **IV.5a** (31.4 mg, 0.0582 mmol, 1.2 equiv.), and potassium bicarbonate (33.5 mg, 0.243 mmol, 5.00 equiv.). The flask was then evacuated and refilled with N_2 5 times. A septum was then placed on the flask, followed by the addition of 5 mL toluene. The reaction was then heated to 80 ^oC and the reaction progress was followed with TLC. On completion, the reaction was quenched with an NH_3-EDTA (2 mL) solution and then allowed to stir for 10 min. The layers were separated, followed by additional washing of the aqueous phase with DCM (2x 20 mL). The combined organic phases were washed with H_2O (3 x 20 mL), and brine (1 x 20 mL), and dried over sodium sulfate to give a bright yellow solid/oil. This oil was then loaded onto SiO_2, eluted with 15% EtOAc/Hexanes to separate **IV.3** from **IV.7b**. Next, crude **IV.7b** was purified on SiO_2 (30%DCM/Hexanes) to give the desired rotaxane as a yellow solid (40.4 mg, 54%).^{1}H NMR (600 MHz, Chloroform-*d*) δ 7.57 (t, *J* = 7.7 Hz,

1H), 7.34 (s, 4H), 7.30 (d, J = 7.7 Hz, 2H), 7.25 – 7.21 (m, 16H), 7.18 (d, J = 1.1 Hz, 8H), 7.10 (d, J = 8.6 Hz, 12H), 7.05 (d, J = 8.8 Hz, 4H), 7.02 (d, J = 8.9 Hz, 4H), 3.22 (s, 4H), 1.30 (s, 54H). ^{13}C NMR (151 MHz, $CDCl_3$) δ 159.84, 155.40, 148.50, 144.20, 141.25, 140.58, 140.18, 137.88, 137.68, 136.43, 136.13, 132.13, 130.84, 129.99, 128.18, 128.15, 128.05, 127.86, 124.26, 116.51, 112.99, 73.54, 70.71, 63.24, 55.20, 34.45, 31.54, 29.86. HRMS (ESI-TOF) (m/z): [M]+ calculated for $C_{115}H_{113}NO_2$, 1539.8771; found, 1539.8601.

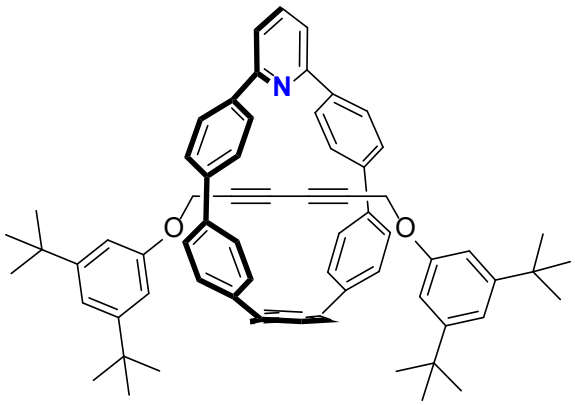

Synthesis of IV.7c. To a flame-dried 25 mL flask equipped with a stir bar was added ligand **IV.3** (22.2 mg, 0.0485 mmol, 1.00 equiv.), $Cu(MeCN)_4PF_6$ (17.0 mg, 0.0461 mmol, 0.95 equiv.), bromo alkyne **IV.6b** (36.5 mg, 0.0582 mmol, 1.2 equiv.), terminal alkyne **IV.5b** (31.4 mg, 0.0582 mmol, 1.2 equiv.), and potassium bicarbonate (33.5 mg, 0.243 mmol, 5.00 equiv.). The flask was then evacuated and refilled with N_2 5 times. A septum was then placed on the flask, followed by the addition of 5 mL toluene. The reaction was then heated to 80 ºC and the reaction progress was followed with TLC. On completion, the reaction was quenched with an NH_3-EDTA (2 mL) solution and then allowed to stir for 10 min. The layers were separated, followed by additional washing of the aqueous phase with DCM (2x 20 mL). The combined organic phases were washed with H_2O (3 x 20 mL), and

brine (1 x 20 mL), and dried over sodium sulfate to give a bright yellow solid/oil. This oil was then loaded onto SiO_2, eluted with 15% EtOAc/Hexanes to separate **IV.3** from **IV.7c**. Next, crude **IV.7c** was purified on SiO_2 (20%DCM/Hexanes) to give the desired rotaxane as a yellow solid (40.4 mg, 54%).^{1}H NMR (500 MHz, Chloroform-*d*) δ 7.73 (t, *J* = 7.5, 1H), 7.50 (s, 4H), 7.46 (d, *J* = 7.7, 2H), 7.33 – 7.28 (m, 8H), 7.20 (d, *J* = 7.9, 4H), 7.01 – 6.91 (m, 6H), 6.28 (s, 4H), 2.92 (s, 4H), 1.28 (s, 36H). ^{13}C NMR (126 MHz, $CDCl_3$) δ 159.93, 157.14, 152.10, 141.38, 141.14, 138.34, 137.78, 136.99, 136.46, 130.03, 128.60, 128.55, 128.23, 116.78, 115.17, 108.51, 74.33, 70.46, 55.00, 35.09, 31.63. HRMS (ESI-TOF) (m/z): [M]+ calculated for $C_{69}H_{69}NO_2$, 943.5328; found, 943.5315.

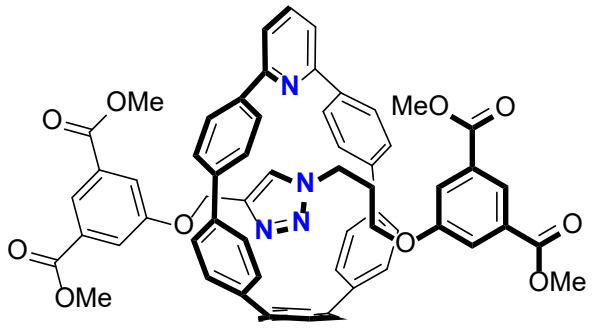

Synthesis of IV.9b. To a flame-dried 25 mL flask equipped with a stir bar was added ligand **IV.3** (30.1 mg, 0.0658 mmol, 1.00 equiv.), $Cu(MeCN)_4PF_6$ (23.3 mg, 0.0625 mmol, 0.95 equiv.), azide **IV.8b** (0.180 g, 0.658 mmol, 10.0 equiv.) and alkyne **IV.8c** (0.163 g, 0.658 mmol, 10.0 equiv.). The flask was then evacuated and refilled with N_2 5 times. A septum was then placed on the flask, followed by the addition of 10.0 mL DCM. The reaction was followed with TLC and allowed to stir until complete consumption of azide or alkyne. At this point, the reaction was quenched with an NH_3-EDTA (2 mL) and then allowed to stir for 10 min. The layers were separated, followed by additional washing of the aqueous phase with DCM (2x 20 mL). The combined organic phases were washed with H_2O (3 x 20 mL), and brine (1 x 20 mL), and dried over sodium sulfate to give a

bright yellow solid, which after chromatography (50% DCM/Hexanes to remove unreacted **IV.3**, then 0→50% EtOAc/hexanes to elute **IV.9b**, SiO_2), yielded the desired rotaxane **IV.9b** as a yellow oil (29.6 mg, 45%). ^{1}H NMR (500 MHz, Chloroform-*d*) δ 8.39 (s, 1H), 8.36 (s, 1H), 7.90 (s, 2H), 7.75 (t, *J* = 8.5 Hz, 1H), 7.64 (s, 2H), 7.60 (d, *J* = 9.0 Hz, 2H), 7.55 (s, 2H), 7.53 – 7.44 (m, 8H), 7.38 (d, *J* = 8.7 Hz, 4H), 7.21 (d, *J* = 8.4 Hz, 2H), 7.10 (d, *J* = 8.9 Hz, 2H), 7.01 (d, *J* = 9.5 Hz, 2H), 6.38 (s, 1H), 5.18 (s, 2H), 4.06 (s, 6H), 3.97 (s, 6H), 1.68 – 1.64 (m, 2H), 1.42 (t, *J* = 7.5 Hz, 2H), -1.40 (q, *J* = 8.5 Hz, 2H). ^{13}C NMR (126 MHz, $CDCl_3$) δ 166.48, 166.13, 159.96, 158.99, 158.60, 142.09, 141.51, 139.52, 137.92, 136.97, 135.85, 135.62, 132.28, 132.07, 130.32, 130.05, 129.97, 129.46, 128.62, 128.48, 127.87, 127.51, 126.58, 124.70, 123.80, 122.72, 122.19, 120.13, 119.37, 118.05, 64.08, 62.83, 52.77, 52.72, 44.96, 25.78.MS (ESI-TOF) (m/z): [M]+ calculated for $C_{61}H_{50}N_4O_{10}$, 998.3527; found, 998.3525.

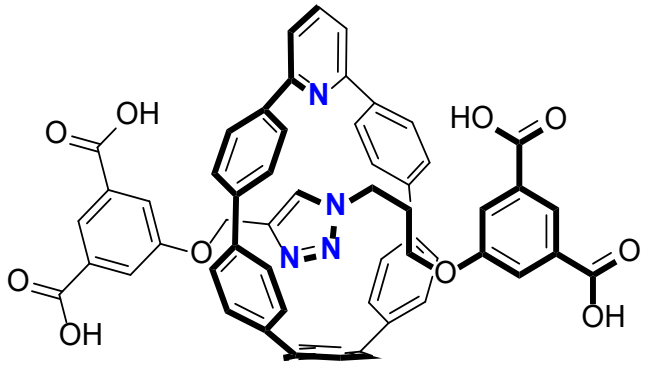

Synthesis of IV.9c. To a 50 mL flask equipped with a stir bar was added rotaxane **IV.9b** (20.2 mg, 0.0202 mmol, 1.00 equiv.) and NaOH (242.6 mg, 6.07 mmol, 300.0 equiv.) followed 20.0 mL of a 1:1 THF:H_2O solution. The resulting suspension was heated at 55 °C for 16h, at which point the THF was removed via rotary evaporation. The resulting bright green/yellow solution was then acidified with 1M HCl and extracted with EtOAc (3

x 25 mL). The combined organic phases were washed with H_2O (3 x 20 mL), and brine (1 x 20 mL), and dried over sodium sulfate to give **IV.9c** as a bright yellow/orange solid (40.4 mg, 99%). ^{1}H NMR (500 MHz, D_2O) δ 8.05 (s, 1H), 7.98 (s, 1H), 7.83 – 7.78 (m, 3H), 7.70 (d, J = 8.0 Hz, 4H), 7.66 (d, J = 8.5 Hz, 4H), 7.50 (d, J = 7.8 Hz, 2H), 7.44 (d, J = 8.9 Hz, 2H), 7.41 – 7.34 (m, 6H), 7.19 (d, J = 8.4 Hz, 2H), 7.09 (d, J = 8.9 Hz, 2H), 6.94 (d, J = 8.4 Hz, 2H), 6.53 (s, 1H), 5.35 (s, 2H), 1.71 (t, J = 7.0 Hz, 2H), 1.17 – 1.14 (m, 2H), -1.39 (q, J = 8.4 Hz, 2H). ^{13}C NMR (126 MHz, D_2O) δ 174.84, 173.98, 159.51, 157.81, 156.85, 141.98, 141.44, 138.75, 138.49, 138.32, 138.19, 136.63, 135.73, 135.40, 130.22, 129.81, 128.83, 128.58, 128.48, 128.29, 127.52, 127.43, 127.08, 125.25, 123.88, 122.99, 121.19, 118.70, 118.05, 117.64, 64.05, 61.80, 44.72, 24.54. HRMS (ESI-TOF) (m/z): [M]+ calculated for $C_{57}H_{42}N_4O_{10}$, 942.2901; found, 942.2942.

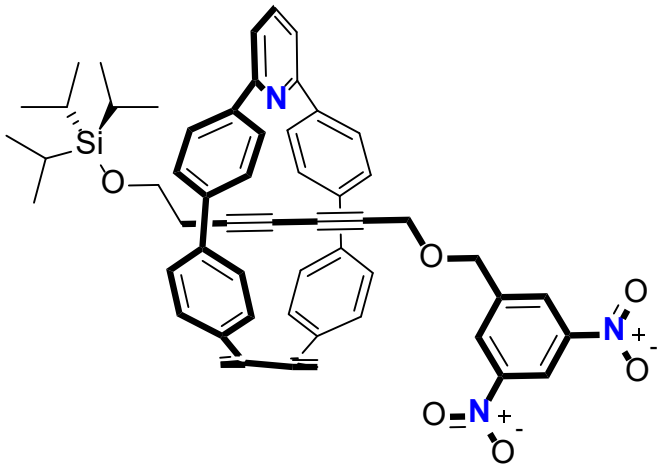

Synthesis of IV.9d. To a flame-dried 25 mL flask equipped with a stir bar was added ligand **IV.3** (35.2 mg, 0.0770 mmol, 1.00 equiv.), $Cu(MeCN)_4PF_6$ (27.2 mg, 0.0731 mmol, 0.95 equiv.), bromo alkyne **IV.S3** (72.8 mg, 0.231 mmol, 3.0 equiv.), terminal alkyne **IV.S4** (52.3 mg, 0.231mmol, 3.0 equiv.), and potassium bicarbonate (53.1 mg, 0.385 mmol, 5.00 equiv.). The flask was then evacuated and refilled with N_2 5 times. A septum

was then placed on the flask, followed by the addition of 8.0 mL toluene. The reaction was then heated to 80 ºC and the reaction progress was followed with TLC. On completion, the reaction was quenched with an NH_3-EDTA (2 mL) solution and then allowed to stir for 10 min. The layers were separated, followed by additional washing of the aqueous phase with DCM (2x 20 mL). The combined organic phases were washed with H_2O (3 x 20 mL), and brine (1 x 20 mL), and dried over sodium sulfate to give a bright yellow solid/oil. This oil was then loaded onto SiO_2, eluted with 50% DCM/Hexanes to separate **IV.3** from **IV.9d**. Next, crude **IV.9d** was purified via size exclusion chromatography to give the desired rotaxane as an orange foam/solid (20.1 mg, 29%).^{1}H NMR (500 MHz, Chloroform-*d*) δ 8.79 (s, 1H), 7.77 (t, *J* = 7.7 Hz, 1H),), 7.69 – 7.65 (m, 8H), 7.57 (s, 2H), 7.45 (d, *J* = 7.7 Hz, 2H), 7.41 (d, *J* = 8.4 Hz, 2H), 7.31 (d, *J* = 8.9 Hz, 2H), 7.19 (s, 2H), 7.10 (d, *J* = 8.4 Hz, 2H), 6.88 (d, *J* = 8.3 Hz, 2H), 6.80 (d, *J* = 8.9 Hz, 2H), 3.74 (t, *J* = 6.9 Hz, 2H), 2.42 (t, *J* = 6.9 Hz, 2H), 1.90 (s, 2H), 1.77 (s, 2H), 1.09 – 1.08 (m, 21H). ^{13}C NMR (126 MHz, $CDCl_3$) δ 159.92, 147.61, 144.06, 141.59, 139.64, 138.12, 137.31, 136.30, 136.17, 131.22, 131.15, 129.33, 129.06, 128.78, 128.06, 127.41, 127.15, 126.70, 126.55, 124.04, 117.29, 116.83, 83.64, 78.06, 72.76, 71.91, 67.20, 66.52, 61.77, 57.82, 25.18, 23.97, 18.16, 12.14. HRMS (ESI-TOF) (m/z): [M]+ calculated for $C_{58}H_{55}N_3O_6Si$, 917.3860; found, 917.3832.

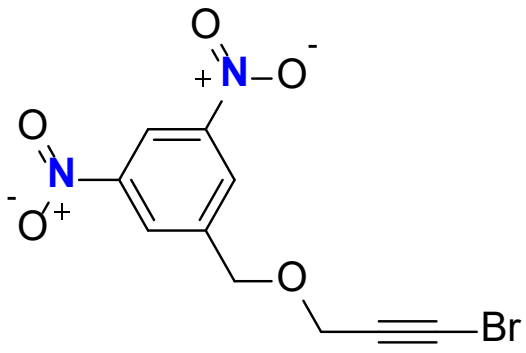

Synthesis of IV.S3. To a flame-dried 100 mL flask equipped with a stir bar was added 3,5-

dinitro benzyl alcohol (1.06 g, 0.00535 mol, 1.00 equiv.) and THF (20 mL). The resulting solution was then cooled at 0 ºC for 15 minutes, at which point NaH (0.158 mg, 0.00657 mol, 1.30 equiv.) was added, quickly resulting in a brown/purple suspension. After stirring for an additional 10 minutes at 0 ºC, propargyl bromide (0.956 g, 0.00803 mol, 1.50 equiv.) was added, followed by warming to room temperature. After stirring for 24 hours at room temperature, the reaction was quenched with H_2O (10 mL). The THF was then removed via rotary evaporation and the resulting aqueous suspension was extracted with EtOAc (3 x 50 mL). The combined organic phases were washed with H_2O (3 x 20 mL), and brine (1 x 20 mL), and dried over sodium sulfate to give a brown oil. This oil was then passed through a small alumina pad (eluted with 100% DCM) to give the corresponding crude terminal alkyne as a yellow oil (0.253 mg, 21%). This oil was then transferred to a 100 mL flask, followed by the addition of $AgNO_3$ (0.182 mg, 1.07 mmol, 1.00 equiv.), NBS (0.285 mg, 1.61 mmol, 1.50 equiv.), and 50 mL acetone. After stirring for 1h at room temperature, the solvent was removed and the resulting yellowish solid was loaded onto a small pad of SiO_2. At this point, the SiO_2 pad was flushed several times with 100% hexanes followed by 100% DCM to elute **IV.S3** as a yellow oil which crystallized on standing (0.317 mg, 94%). ^{1}H NMR (500 MHz, Chloroform-*d*) δ 8.97 (s, 1H), 8.56 (s, 2H), 4.80 (s, 2H), 4.37 (s, 2H). ^{13}C NMR (126 MHz, $CDCl_3$) δ 148.72, 142.59, 127.37, 118.19, 75.23, 69.57, 59.57, 48.20. HRMS (ESI-TOF) (m/z): [M]+ calculated for $C_{10}H_7N_2O_5Br$, 313.9538; found, 313.9673.

4.4.3. NMR Titrations

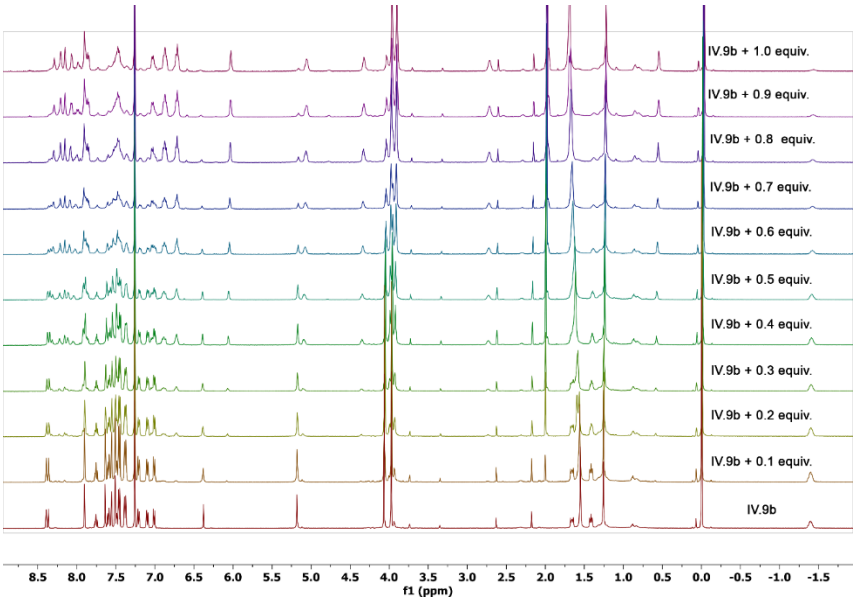

Figure 4.8. NMR Titration of IV.**9b** with $[Cu(MeCN)_4]PF_6$ from 0.0 to 1.0 equivalents. Conditions: 5.0 mM **IV.9b** ($CDCl_3$), 100 mM $[Cu(MeCN)_4]PF_6$ (Acetonitrile-d3), performed at 298K.

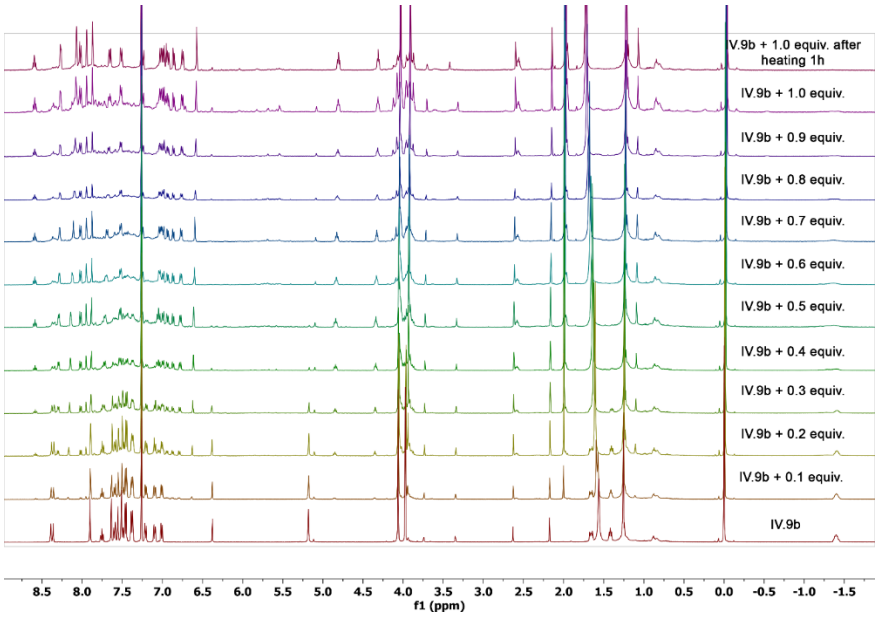

Figure 4.9. NMR Titration of **IV.9b** with $[Pd(MeCN)_4](BF_4)_2$ from 0.0 to 1.0 equivalents. Conditions: 5.1 mM **IV.9b** ($CDCl_3$), 100 mM $[Pd(MeCN)_4](BF_4)_2$ (Acetonitrile-d3), performed at 298K.

4.4.4. Photophysical Characterization

The quantum yields of **IV.3**, **IV.4**, **IV.7a-c** and **IV.9a-c** were determined as described by Jobin Yvon Horiba using anthracene (ethanol) and quinine sulfate (0.1M H_2SO_4) as standards while exciting at 325 nm. The fluorescence of **IV.4**, **IV.9a** and **IV.7a** were integrated from 415-600 nm, **IV.3**, **IV.7b-c**, **IV.9b** and **IV.9c** were integrated from 450-640 nm, anthracene was integrated from 360-480 nm and quinine sulfate was integrated from 400-600 nm. Compounds **IV.3**, **IV.4**, **IV.9a**, and **IV.7a-c** were measured in DCM while compound **IV.9b** was determined in MeCN and compound **IV.9c** was measured in PBS buffer.

For the metal titration experiments, compound **IV.9b** was measured in chloroform and **IV.9c** was measured in PBS buffer. Both compounds were prepared as 20.6 uM solutions, excited at 325 nm and the fluorescence for each measurement was integrated from 450-640 nm to determine relative intensity. Palladium stock solutions were prepared at 20 mM in MeCN and EDTA solutions were prepared in 6% NH_3OH at 20 mM. The quantum yields of **IV.3**, **IV.4**, **IV.7a-c** and **IV.9a-b** were determined as described by Jobin Yvon Horiba[XX] using anthracene (ethanol) and quinine sulfate (0.1M H_2SO_4) as standards while exciting at 325 nm. The fluorescence of **IV.4**, **IV.9a** and **IV.7a** were integrated from 415-600 nm, **IV.3**, **IV.7b-c**, **IV.9b** and **IV.9c** were integrated from 450-640 nm, anthracene was integrated from 360-480 nm and quinine sulfate was integrated from 400-600 nm. Compounds **IV.3**, **IV.4**, **IV.9a**, and **IV.7a-c** were measured in DCM while compound **IV.9b** was determined in MeCN and compound **IV.9c** was measured in PBS buffer.

For the fluoride titration experiments, a 206 μM stock solution of compound **IV.9d** was first prepared in chloroform. The emission spectra of an 8.6 uM concentration solution

was then measured. Next, 1.0 equivalent of TBAF was added to a vial containing 125.0 µL of a 206 µM solution of **IV.9d** in chloroform. The vial was then sonicated for 5 minutes, quickly turning light purple. The solution was then diluted to 8.6 µM and the emission was recorded.

Summary of Optical Properties

Compound	λ_{abs} (nm)	ε (M^{-1} cm^{-1})	λ_{em} (nm)	ϕ_F
IV.4	323	7.0×10^4	476	0.62
IV.9a	325	2.9×10^4	477	0.50
IV.7a	325	4.2×10^4	479	0.53
IV.3	322	3.5×10^4	509	0.14
IV.7b	322	5.0×10^4	515	0.15
IV.7c	322	7.0×10^4	513	0.13
IV.9b	318	3.2×10^4	511	0.10
IV.9c	327	3.3×10^4	516	0.07
IV.9d	326	2.6×10^4	--	--

Figure 4.10. Summary of photophysical properties of all relevant compounds

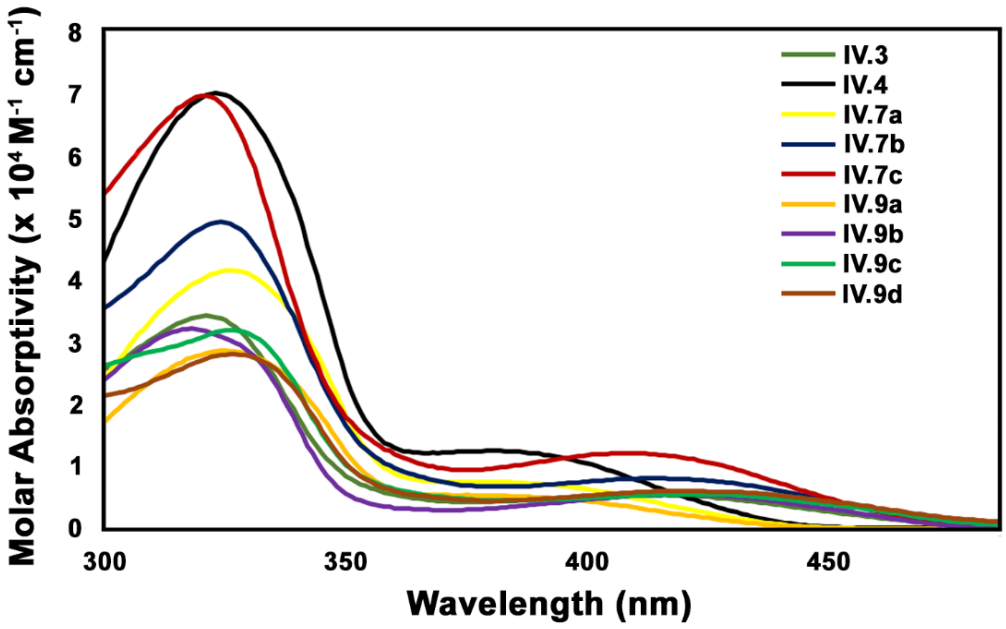

Figure 4.11. Absorption spectra of all relevant compounds in dichloromethane.

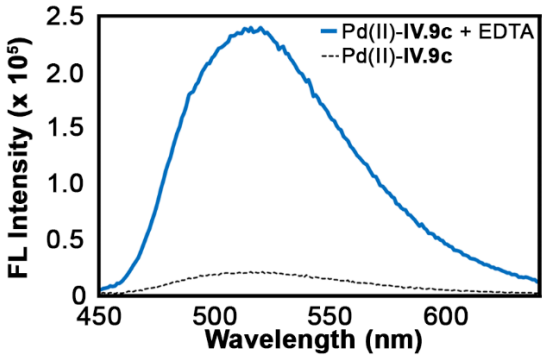

Figure 4.12. Emission spectrum of water soluble rotaxane **IV.9c** in the presence of 1.0 equivalent of Pd(II) (dotted trace) and demetallation of Pd(II)-**IV.9c** with 1.0 equivalent of EDTA (solid trace).

4.4.5. Crystallographic Data

Crystallographic Data for **IV.4**: $C_{49}H_{35}Cl_4N$, $C_{47}H_{31}N\cdot(CH_2Cl_2)_2$, M = 779.58, 0.22 x 0.18 x 0.12 mm, T = 173(2) K, Triclinic, space group *P*-1, a = 12.3367(8) Å, b = 15.3339(10) Å, c = 22.9899(15) Å, α = 98.146(3)°, β = 91.411(3)°, γ = 111.537(3)°, V = 3990.6(3) Å^3, Z = 4, D_c = 1.298 Mg/m^3, μ(Cu) = 2.963 mm^{-1}, F(000) = 1616, $2\theta_{max}$ = 133.65°, 55669 reflections, 14063 independent reflections [R_{int} = 0.0433], R1 = 0.0453, wR2 = 0.1229 and GOF = 1.036 for 14063 reflections (867 parameters) with I>2s(I), R1 = 0.0526, wR2 = 0.1268 and GOF = 1.036 for all reflections, max/min residual electron density +0.191/-0.195 eÅ^{-3}. CCDC# = 1851935

Crystallographic Data for **IV.7b**: $C_{115}H_{113}NH_2O_2$, M = 1541.06, 0.15 x 0.12 x 0.04 mm, T = 173(2) K, Triclinic, space group *P*-1, a = 11.8752(4) Å, b = 19.0169(6) Å, c = 21.4758(7) Å, α = 99.972(2)°, β = 100.647(2)°, γ = 103.394(2)°, V = 4516.9(3) Å^3, Z = 2, D_c = 1.133 Mg/m^3, μ(Cu) = 0.496 mm^{-1}, F(000) = 1652, 2θmax = 133.42°, 64826

reflections, 15906 independent reflections [R_{int} = 0.0531], R1 = 0.0593, wR2 = 0.1641 and GOF = 1.054 for 15906 reflections (1063 parameters) with I>2s(I), R1 = 0.0715, wR2 = 0.1764 and GOF = 1.061 for all reflections, max/min residual electron density +0.732/-0.426 eÅ^{-3}. CCDC# = 1851936

Crystallographic Data for **IV.7c**: $C_{69}H_{69}NO_2$, M = 944.25, 0.13 x 0.11 x 0.06 mm, T = 173(2) K, Triclinic, space group *P*-1, *a* = 9.6861(3) Å, *b* = 16.6342(5) Å, *c* = 17.4806(5) Å, α = 94.164(2)°, β = 93.992(2)°, γ = 99.564(2)°, *V* = 2760.43(14) Å^3, *Z* = 2, D_c = 1.136 Mg/m^3, μ(Cu) = 0.509 mm-1, F(000) = 1012, 2θmax = 133.29°, 41514 reflections, 9697 independent reflections [R_{int} = 0.0471], R1 = 0.0499, wR2 = 0.1374 and GOF = 1.041 for 9697 reflections (781 parameters) with I>2s(I), R1 = 0.0628, wR2 = 0.1485 and GOF = 1.041 for all reflections, max/min residual electron density +0.487/-0.205 eÅ^{-3}. CCDC# = 1854176

Crystallographic Data for **IV.9b**: $C_{65}H_{56}N_{10}O_{10}$, M = 1137.19, 0.15 x 0.12 x 0.08 mm, T = 173(2) K, Monoclinic, space group $P2_1/c$, *a* = 17.9478(5) Å, *b* = 24.3248(7) Å, *c* = 25.2984(7) Å, β = 95.194(1)°, *V* = 10999.3(5) Å^3, *Z* = 8, D_c = 1.373 Mg/m^3, μ(Cu) = 0.775 mm^{-1}, *F*(000) = 4768, 2θmax = 133.34°, 94936 reflections, 19445 independent reflections [R_{int} = 0.0563], R1 = 0.0577, wR2 = 0.1651 and GOF = 1.012 for 19445 reflections (1459 parameters) with I>2s(I), R1 = 0.0740, wR2 = 0.1849 and GOF = 1.012 for all reflections, max/min residual electron density +1.294/-0.354 eÅ^{-3}. CCDC# = 1897177

Crystallographic Data for **Cu(I)-IV.9b**: $C_{65}H_{60}Cl_6CuF_6N_4O_{12}P$, M = 1510.38, 0.15 x 0.10 x

0.02 mm, T = 173(2) K, Triclinic, space group *P*-1, a = 14.5355(11) Å, b = 14.7688(13) Å, c = 17.1644(13) Å, α = 81.085(6)°, β = 66.303(5)°, γ = 80.201(5)°, V = 3309.5(5) Å^3, Z = 2, D_c = 1.516 Mg/m^3, μ(Cu) = 3.626 mm^{-1}, F(000) = 1548, 2θmax = 101.26°, 21568 reflections, 6947 independent reflections [R_{int} = 0.0859], R1 = 0.0880, wR2 = 0.2294 and GOF = 1.027 for 6947 reflections (820 parameters) with I>2s(I), R1 = 0.1299, wR2 = 0.2529 and GOF = 1.027 for all reflections, max/min residual electron density +1.079/-0.723 eÅ^{-3}. CCDC# = 1897179

Crystallographic Data for **IV.9d**: $C_{58}H_{55}N_3O_6Si$, M = 918.14, 0.13 x 0.06 x 0.01 mm, T = 173(2) K, Monoclinic, space group $P2_1/c$, a = 16.0398(11) Å, b = 33.042(3) Å, c = 9.3543(7) Å, β = 99.334(6)°, V = 4892.1(7) Å^3, Z = 4, D_c = 1.247 Mg/m^3, μ(Cu) = 0.864 mm^{-1}, F(000) = 1944, 2θmax = 118.11°, 27770 reflections, 7040 independent reflections [R_{int} = 0.1036], R1 = 0.0610, wR2 = 0.1355 and GOF = 1.011 for 7040 reflections (631 parameters) with I>2σ(I), R1 = 0.1225, wR2 = 0.1631 and GOF = 1.011 for all reflections, max/min residual electron density +0.240/-0.259 eÅ^3. CCDC# = 1897178

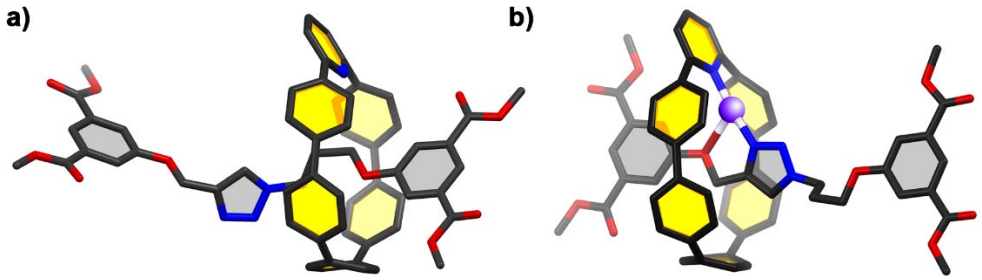

Figure 4.13. X-ray structures of (a) **IV.9b** and (b) **IV.Cu(I)-9b** showing locations of macrocycle **IV.3** over thread unit.

4.4.6. Computational Data

All calculations were carried out with the Gaussian 09 package[6] using B3LYP-6-31G level of theory. All excited state calculations (TD-DFT) were performed on the fully optimized structures. Energy calculations for **IV.9d** were acquired from the solid-state structure obtained via XRD.

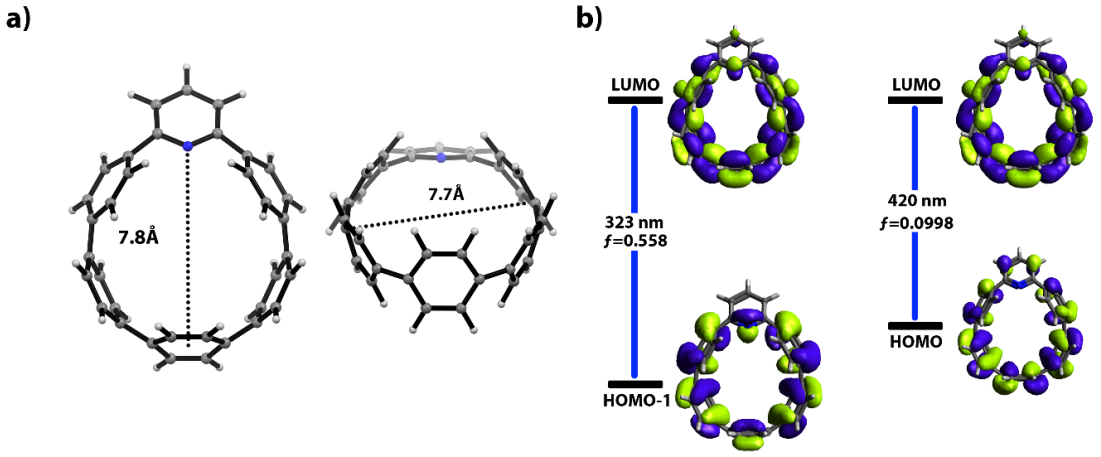

Figure 4.14. DFT (B3LYP/6-31G) minimized structure of ligand **IV.3** showing (a) cavity dimensions and (b) frontier molecular orbitals.

4.5. Bridge to Chapter V

In this chapter, we show that by embedding a 2,6-pyridine unit into a nanohoop framework, we can successfully generate a wide-range of nanohoop-based [2]rotaxanes through an active-metal template strategy. The resulting structures are highly emissive, which we then leverage toward in design of a self-immolating [2]rotaxane fluorescent sensor. Ultimately, through a supramolecular design strategy, we have shown that dative bonds can be combined with the unique properties of a nanohoop macrocycle to construct a new platform for sensing. While coordination chemistry is a powerful tool in the context

of supramolecular design, we became interested in how other types of non-covalent interactions could be applied to the nanohoop framework. In the next chapter, we show that by fluorinating cycloparaphenylenes, weak arene-perfluoroarene interactions can be used to assemble nanohoops into large solid-state nanotube-like structures.

CHAPTER V

PRECISION NANOTUBE MIMICS VIA SELF-ASSEMBLY OF PROGRAMMED CARBON NANOHOOPS

Adapted with permission from Leonhardt, E. J.; Van Raden, J. M.; Miller, D. J.; Zakharov, L. N.; Aleman, B. J.; Jasti, R. A Bottom-Up Approach to Solution-Processed, Atomically Precise Graphitic Cylinders on Graphite. *Nano Lett.* **2018**, *18*, 7991-7997. Additionally, this chapter includes unpublished work. The excerpt included was written by myself with assistance from Erik Leonhardt. The experimental work included from the published material was performed by myself with assistance from Erik Leonhart and David Miller. Lev N. Zakharov provided crystal structure analysis of the final products discussed in the experimental section. Professor Ramesh Jasti provided editorial assistance.

Extended carbon nanostructures, such as carbon nanotubes (CNTs), exhibit remarkable properties but are difficult to synthesize uniformly. Herein, we present a new class of carbon nanomaterials constructed via the bottom-up self-assembly of cylindrical, atomically precise small molecules. Guided by supramolecular design principles and circle packing theory, we have designed and synthesized a fluorinated nanohoop that, in the solid state, self-assembles into nanotube-like arrays with channel diameters of precisely 1.63 nm. A mild solution-casting technique is then used to construct vertical "forests" of these arrays on a highly ordered pyrolytic graphite (HOPG) surface through epitaxial growth. Furthermore, we show that a basic property of nanohoops, fluorescence, is readily transferred to the bulk phase, implying that the properties of these materials can

be directly altered via precise functionalization of their nanohoop building blocks. The strategy presented is expected to have broader applications in the development of new graphitic nanomaterials with π-rich cavities reminiscent of CNTs.

5.1. Introduction

Carbon nanotubes (CNTs) exhibit a wide range of unique properties depending on their precise atomic structure. The remarkable optical and electronic properties of CNTs are intimately connected to CNT chirality.(1) The scalable preparation of single-chirality CNTs, therefore, has been a longstanding goal in the field of nanoscience.[2-4] Similarly, the unique frictionless channels of CNTs exhibit fascinating mass transport behavior, but only when the channel diameters are smaller than 2 nm,[5,6] again highlighting the need for precise CNT structural control. In addition to chirality and diameter, the position and orientation of CNTs on substrates (for example, the vertical alignment of CNTs into surface-bound "forests")[7] is important for fully realizing potential applications such as membranes,[8] sensors,[9, 10] and electronics.[11] While much progress has been made in the synthesis and deposition of CNTs, a completely new approach to these types of cylindrical materials may open up new opportunities. Herein, we disclose a "bottom-up" synthesis strategy based on self-assembly of short fragments of CNTs (i.e., cycloparaphenylenes or carbon nanohoops, (**Figure 5.1a**) to produce vertically oriented "forests" of graphitic cylinders on surfaces with precise structural control.

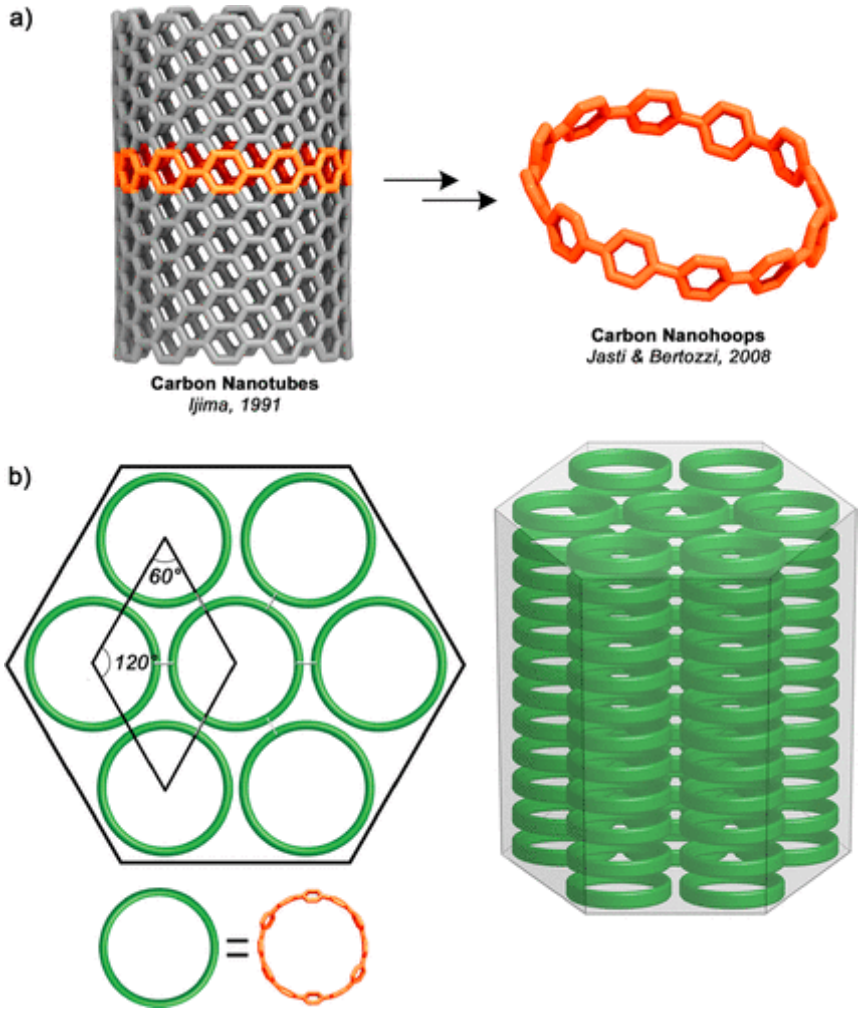

Figure 5.1. (a) Cartoon representation of a [12,12] armchair CNT and an X-ray crystal structure of its smallest cross-sectional fragment, [12]CPP (crystal structure data from ref [36]). (b) (Left) schematic depiction of hexagonal circle packing, in which the central circle in the lattice is symmetrically surrounded by six other circles. CPPs can be seen as geometrically equivalent to perfect circles. (Right) stacking sheets of hexagonally packed hollow circles resulting in the formation of channels with diameters defined by the constituent circles.

Inspired by the work of Smalley regarding the amplification of CNTs,[12] the

synthesis of cycloparaphenylenes (CPPs) aimed to provide ideal templates or building blocks for the uniform fabrication of CNTs.[13-15] Since their initial synthesis in 2008,[16] methods have been developed to synthesize these "carbon nanohoops" in various sizes[17-20] and with numerous functionalities.[21-23] More recently, "carbon nanobelts" have been synthesized by Itami and co-workers, again in hopes of accessing effective seed molecules for CNT growth.[24, 25] As a consequence of their curved geometries and cyclic conjugation, carbon nanohoops and nanobelts exhibit unique size-dependent electronic and photophysical properties.[24-27] Despite their fascinating circular geometries, CNT-like pores, and highly tunable properties, CPPs and related structures have only recently begun to be explored in the context of solid-state materials.[28-32] Seeking to expand on this, we envisioned the development of a new class of CPP-based carbon nanomaterials that would mimic the tubular structures of CNTs. Through the vertical self-assembly of CPPs, we speculated that it would be possible to construct arrays of noncovalent nanotubes with diameters that could be synthetically altered with atomic precision. Moreover, the properties of these materials could be fine-tuned via the bottom-up functionalization of nanohoop building blocks. In this work, we merge synthetic organic chemistry, supramolecular design, and fundamental circle packing theory to construct arrays of noncovalent nanotubes with uniform channel diameters of precisely 1.63 nm via the self-assembly of functionalized nanohoop building blocks. We then prepare vertically oriented "forests" of these structures on a highly ordered pyrolytic graphite (HOPG) surface through epitaxial growth using a simple solution-casting approach.

5.2. Results and Discussion

CPPs are unique among macrocyclic small molecules in that their full sp^2 hybridization and para connectivity gives rise to a circular geometry. Thus, we were curious to what extent CPPs could be treated as geometrically perfect circles, as this would allow for elementary circle packing concepts in our design.[33] Inspired by the dense arrangements found within CNT bundles,[34] we ultimately targeted a hexagonal circle packing motif, the densest arrangement for circles of identical diameters.[33] This packing requires each circle in the 2D lattice to be symmetrically surrounded by six other circles (**Figure 5.1b**). Stacking these hexagonal "sheets" vertically would then afford the desired CNT-like columns (**Figure 5.1b**). Translating all of this into practical molecular design necessitated a supramolecular strategy that would allow for both face-to-face (horizontal) and edge-to-edge (vertical) interactions between nanohoops. Unfunctionalized CPPs do not exhibit face-to-face arene–arene stacking, as is often observed in linear acene systems[35] and instead tend to adopt dense herringbone-like packing motifs with inaccessible pores as a result of the hoops "filling" one another.[27, 36] However, arene–perfluoroarene interactions have yet to be thoroughly explored as a self-assembly strategy in CPP systems and were viewed as an attractive alternative to induce the desired face-to-face arrangement. Arene–perfluoroarene interactions, which result from the favorable electronic interaction between electron-rich aryl rings and electron-deficient perfluorinated aryl rings,[37] have proven useful in supramolecular design due to their powerful and relatively predictable self-assembly capabilities.[38, 39] Conveniently, aryl C–H···F interactions are also known to be powerful guiding forces in systems containing fluorinated aryl moieties.[40] Therefore, we hypothesized that a drive to maximize C–H···F contacts would "lock" **V.1** into a vertical assembly.

Nanohoop **V.1** (**Figure 5.2a**) was designed to leverage the symmetry of the [12]CPP backbone to afford six arene–perfluoroarene interactions per hoop, where every interaction represents one of the six hoop-to-hoop contacts needed to achieve hexagonal packing. Additionally, we hypothesized that C–H···F interactions would align **V.1** into nanotube-like channels. Yamago and co-workers have recently found that incorporation of fluorines into a nanohoop backbone can indeed result in tubular solid-state structures via fluorine–hydrogen interactions.[41] The synthesis of (**Figure 5.2**) **V.1** relied on previously established synthetic routes toward the size-selective synthesis of [*n*]CPPs.[17, 19] Here, a new synthesis involved subjecting intermediates **V.3** and **V.7**, which can be easily accessed on a multigram scale, to a dilute Suzuki–Miyaura cross-coupling reaction, a common aryl–aryl bond forming reaction,[42] to afford macrocycle **V.8** in 22% yield (**Figure 5.2**). Next, the triethylsilyl (TES) groups on the macrocycle were removed with tetrabutylammonium fluoride (TBAF) in the presence of excess acetic acid to afford an intermediate alcohol-functionalized compound. Finally, the cyclohexadiene moieties of this macrocycle were converted to benzene rings via reductive aromatization under mild tin-mediated conditions to afford nanohoop **V.1** in a 40% yield over two steps (versus 4% in the original preparation) as an off-white powder. We attribute the initial low yield to difficulty in the reductive aromatization step, a problem that also plagued Yamago and co-workers when employing the same aromatization conditions to their syntheses of fluorinated cycloparaphenylenes.[41] Halogenated cycloparaphenylenes have been calculated to have higher strain energies than their all-hydrocarbon counterparts which could be contributing to the low yields.[43]

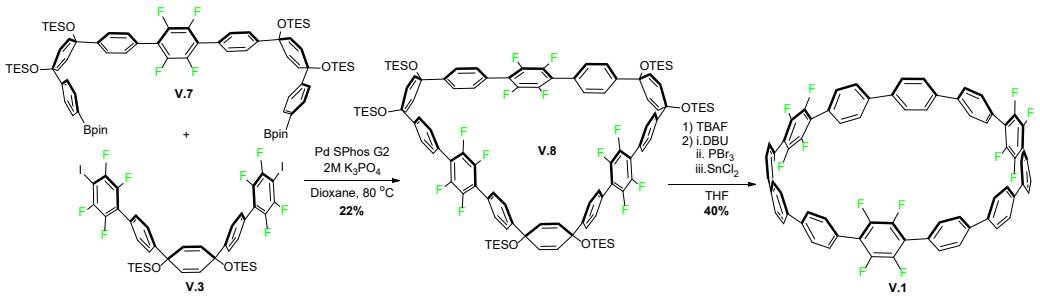

Figure 5.2. Synthesis of fluorinated nanohoop **V.1**.

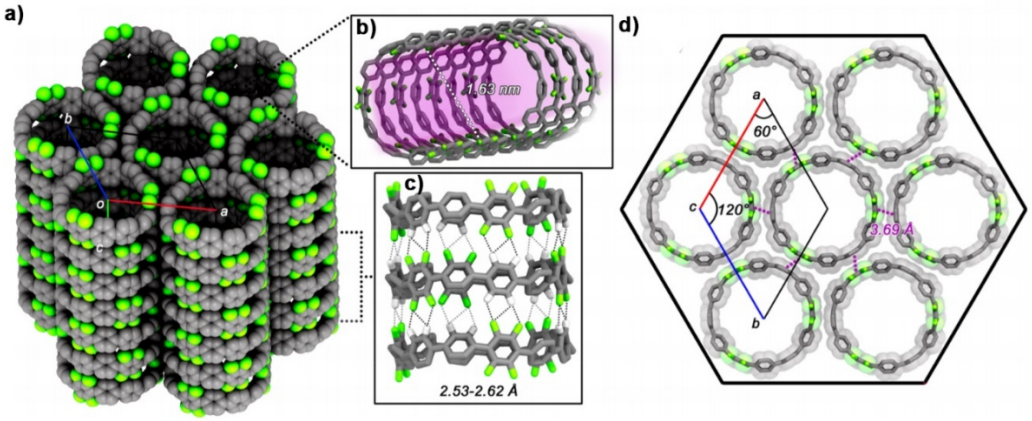

Figure 5.3. (a) X-ray crystal structure of nanohoop **V.1**, showing that the compound self-assembles into noncovalent nanotubes in the solid state. (b) Cross-section of a nanotube of **V.1**, highlighting the 1.63 nm diameter. (c) Aryl C–H···F interactions (dotted lines) that guide the vertical assembly of **V.1**, which range in distance from 2.53 to 2.62 Å. (d) Top-down view showing the hexagonal circle packing of **V.1**, which is guided by six arene–perfluoroarene interactions that measure at 3.69 Å (purple dotted lines) (chloroform solvent molecules omitted for clarity).

Nanohoop **V.1** was found to readily form colorless, needle-like crystals via slow evaporation from chloroform. X-ray diffraction of these crystals revealed

that **V.1** assembles into the desired nanotube-like structures, exhibiting a uniform array of 1.63 nm channels (**Figure 5.3a, c**). The vertical assembly of **V.1** appeared to be guided by a multitude of aryl C–H···F interactions (**Figure 5.3c**), resulting in perfectly linear columns. Thirty-six C–H···F interactions per hoop were found in the crystal packing of **V.1**, ranging from 2.53 to 2.62 Å.[41] The ability of the top and bottom "edges" of macrocycles with radially oriented π systems to take part in a large number of weak contacts has been observed previously[44] and highlights a potential advantage of using nanohoop-like structures to maximize vertical interactions in the construction of molecular crystalline systems. Upon closer inspection of this solid-state packing, we also observed six well-defined arene-perfluoroarene interactions per nanohoop with centroid-to-centroid distances of 3.69 Å (**Figure 5.3d**), well within the range of approximately 3.4–3.9 Å commonly observed in other studies.[38, 39] Importantly, these interactions result in an ideal 2D hexagonal circle packing motif, which is beautifully reflected in the symmetric, diamond-shaped unit cell of the lattice with vertices located at the centers of four nanohoops.

At the outset of this work, one of our primary goals was to mimic vertically oriented CNT "forests" through the vertical assembly of **V.1** on surfaces. Substrate-templated epitaxial growth has previously been shown to be an effective strategy for accessing well-oriented molecular assemblies.[45] Thus, we chose highly oriented pyrolytic graphite (HOPG) as a possible template, since HOPG has a lattice constant of a factor of 8 less than the horizontal lattice constants of 1 (a = 2.46 Å for HOPG vs a/b = 19.81 Å for 1). On the basis of this idea of lattice matching, we predicted that HOPG would serve as a suitable template for epitaxial growth of vertically aligned structures of **V.1**. We found that

drop-casting **V.1** from a chloroform solution onto a HOPG substrate at humid ambient conditions resulted in the rapid (~1–2 min) formation of numerous hexagonal and needle-like crystalline structures that were easily observable via optical microscopy (**Figure 5.4a**). Scanning electron microscopy (SEM) revealed that the hexagonal crystals were in fact nanowire-like pillars that form dense arrays on many regions of the substrate (**Figure 5.4b**). The structures displayed in **Figure 5.4b** range in size from 1 to 2 μm in both height and width, although various other morphologies, such as tall and thin pillars (5–10 μm in height and 0.2–0.5 μm in width) and short and wide structures (200–500 nm in height and 1–2 μm in width) were also found. The largest pillars and densest pillar populations were found along the chloroform drying rings that resulted from solution casting, an observation that could inform future optimization of this solution processing technique. Focused ion beam (FIB) microscopy of individual hexagonal pillars revealed that these structures do indeed exhibit six well-defined walls and a flat hexagonal top (**Figure 5.4c**). Satisfyingly, the hexagonal geometries of these pillars directly reflected the hexagonal molecular packing observed in the crystal structure of **V.1**, supporting the notion that the pillars we observed were composed of vertically aligned columns of **V.1**. These pillars were also successfully fabricated on multilayer graphene surfaces grown on copper foil. It is worth noting that deposition of the nonfluorinated analog ([12]CPP) onto an identical graphene–copper substrate produced no such structures, and instead affords flat plate-like structures consistent with the morphology of solution grown crystals of [12]CPP.

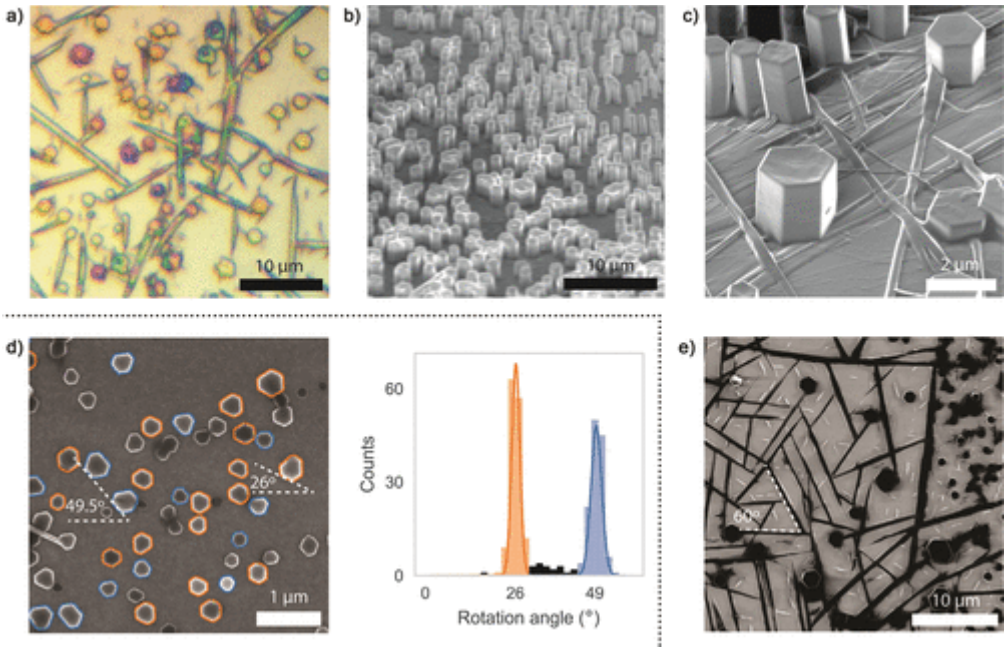

Figure 5.4. (a) Optical microscopy of hexagonal pillars and needle-like structures on HOPG surface. (b) Angled-SEM of an array of hexagonal pillars. Dense forests of hexagonal pillars are scattered across the sample with heights ranging from a few hundred nanometers to several microns. (c) Angled focused ion beam (FIB) microscopy of isolated hexagonal pillars. The flat hexagonal faces and top are readily apparent. (d) (Left) segment of a larger (25 µm × 16 µm) SEM image of short pillars showing growth templated by the substrate. The pillars are preferentially aligned in one of two angles, separated by ~23.5°. (Right) histogram of orientation angles in the full 25 µm × 16 µm image. A total of 290 hexagons are identified in the full image and nearly all of them are oriented in one of two angles. (e) FIB image of needle-like structures formed by **V.1**, which preferentially orient at 60° relative to one another on the HOPG surface.

Further inspection of the hexagonal pillars of **V.1** revealed preferential orientations on the HOPG surface, which is indicative of epitaxial growth on the graphite lattice. We

used a home-built image processing algorithm to identify hexagons and quantify their angles relative to an arbitrary normal. This allowed us to map regions of high pillar density and analyze the relative orientations of grouped pillars. Two distinct orientations for a given area emerged, averaging at 26.0° rotation and 49.5° rotation from an arbitrary normal, which were observed in relatively equal quantities (**Figure 5.4d**). We currently hypothesize that these populations represent two energetically favorable orientations that **V.1** can adopt on the HOPG surface. This notion is supported by a recent theoretical study implying that nanohoops should indeed exhibit energetically preferred orientations on graphene surfaces.[46] However, while our findings clearly indicate substrate-directed preferential orientation of the observed hexagonal pillars, further studies are required to elucidate the mechanisms behind the growth and orientation of nanohoop-based structures on graphite. Interestingly, we observe that the needle-like structures align to the graphite surface in multiples of 60° (**Figure 5.4e**), consistent with the 3-fold symmetry of the graphite lattice. This again supports the notion that the HOPG surface exhibits a heavy influence on the growth and orientation of the structures formed by **V.1**. Importantly, this well-templated growth offers the potential for deterministic growth of hexagonal wires.

While fluorination successfully oriented the nanohoops (**V.1**) into the desired CNT-like geometry, it was not clear the extent to which this self-assembly strategy could be regarded as a general strategy to CNT mimics. For example, we only examined the self-assembly of a single diameter nanohoop with a very specific fluorination pattern, raising the question of generality. We also recognized that in order for these materials to be considered genuine CNT mimics, these self-assembled systems would also have to exhibit some degree of CNT functionality. Accordingly, we then expanded this work by

demonstrating that these fluorinated, self-assembling nanohoops exhibit structural features and functions that have been previously observed in traditional CNTs, ultimately establishing fluorinated nanohoops as a new CNT-like precision nanomaterial. First, we describe the synthesis of two new fluorinated derivates—a reduced diameter [10]CPP analog and a [12]CPP derivative with a lesser degree of fluorination, both of which assemble into the desired CNT mimic structures. Next, we show that the [10]CPP analog is capable of linearly aligning C_{60} molecules as observed in CNT@C_{60} peapod structures. Neither of the above functionalities are observed in the respective non-fluorinated analogs, supporting our hypothesis that fluorination of the nanohoop backbone is an effective general strategy towards fabricating robust CNT solid-state mimics.

A primary aim was to determine if the supramolecular design strategy we had employed with nanohoop **V.1** was amenable to nanohoops of varying diameter and fluorination patterns. Additionally, we sought to develop a modular synthetic strategy where access to fluorinated structures of differing diameter and fluorination patterns could be quickly obtained via common intermediates. Ultimately, we aimed to synthesize (figure nanohoops **V.5** (a [10]CPP analog) and **V.6** (a [12]CPP analog), which each bear two symmetrically placed tetrafluorophenylene moieties. Critical to our investigation was the acquisition of single crystals of **V.5** and **V.6** suitable for x-ray diffraction in order to unambiguously determine the solid state packing of these materials and also to allow for the detailed analysis of arene-perfluoroarene and C—H---F interactions present in the solid-state arrangements.

With this in mind, we proceeded toward both **V.5** and **V.6** via the curved building blocks shown **Figure 5.5**. Importantly, each of these intermediates can be prepared on

multi-gram scale in excellent yield. Under dilute Suzuki-Miyaura cross-coupling conditions, triethylsilyl (TES) protected macrocycles **V.9** and **V.10** were synthesized in modest yields (**Figure 5.5**). Typically, after cleavage of the silyl protecting groups, the cyclohexadiene units can undergo reductive aromatization to give the final fully conjugated nanohoop, however, we found that treatment of macrocycles **V.9** and **V.10** with tetrabutylammonium fluoride (TBAF) consistently resulted in decomposition. We reasoned that the electron-withdrawing nature of the fluorinated aryl rings can promote a retro-addition reaction, ultimately resulting in a cyclohexadienone and an unstable anionic tetrafluoraryl ring. After screening various conditions, we found that the addition of excess acetic acid to the reaction mixture allowed for clean conversion to the desired free-alcohol functionalized macrocycles. However, as reported by both the Yamago group[41] and our previous work, initial attempts at reductive aromatization with H_2SnCl_4 lead to the desired products in low yield (15% and 12% for **V.5** and **V.6**, respectively). Through slight modification of the conditions reported by Yamago and coworkers,[41] we were able to improve the yield of both **V.5** (58% yield) and **V.6** (28% yield), providing ample material for our ongoing investigations.

As previously mentioned, nanohoop **V.1** self-assembles into perfectly linear nanotube-like arrays in the solid state, forming channels that are precisely 1.63 nm in diameter (**Figure 5.3**). The three-fold symmetry of the molecule allows for six arene-perfluoroarene interactions per hoop, each of which measure at 3.68 Å (**Figure 5.3**).[33] This results in an ideal hexagonal circle-packing motif, which is the densest theoretical packing possible for circles of identical diameter.[33] Vertical assembly in the solid-state architecture of **V.1** is guided by eighteen C—H---F interactions per hoop dimer (**Figure 5.3**), which

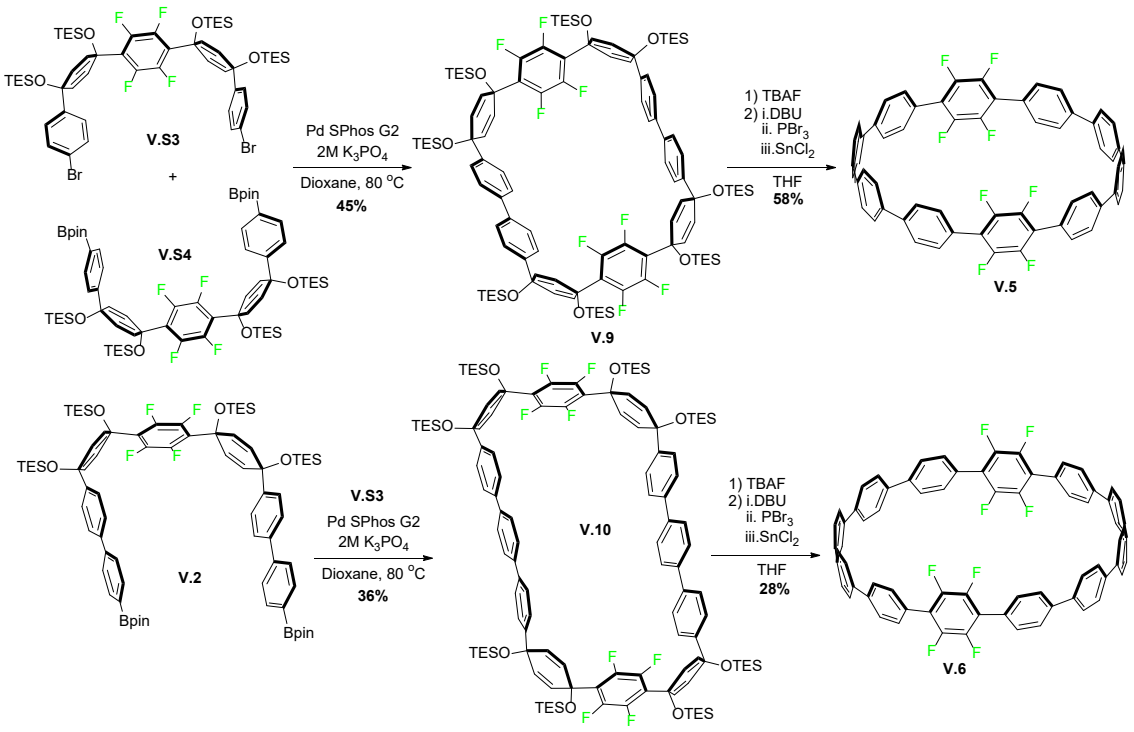

Figure 5.5. Synthetic routes towards nanohoops **V.5** and **V.6**.

range in distance from 2.53 – 2.62 Å.27 The readily apparent organofluorine interactions observed in the crystal packing of **V.1** provide an excellent reference point when analyzing the x-ray crystal structures of **V.5** and **V.6**.

Following the synthesis of nanohoop **V.5**, needle-like single-crystals suitable for X-ray crystallography were obtained by slow evaporation of a THF solution of fluorinated nanohoop **V.5**. The solid-state packing of **V.5** affords staggered nanotube-like columns (**Figure 5.6**) with channel diameters of precisely 1.38 nm. As was observed previously for **V.1**, the horizontal arrangement of **V.5** was found to be guided by arene-perfluoroarene interactions. Four of these interactions can be found in the crystal structure of **V.5**, all measuring at 3.78 Å (**Figure 5.6**) Likewise, the vertical alignment of **V.5** in the solid state is dictated by a multitude of C—H---F interactions, as was also the case with **V.1**. A total

of sixteen C—H---F interactions were observed, measuring between 2.53 – 2.85 Å (**Figure 5.6**). It should be stressed that the packing of **V.5** is significantly different than that of parent [10]CPP,[47] which adopts a herringbone-type motif—a common observation in the all-hydrocarbon parent nanohoops.

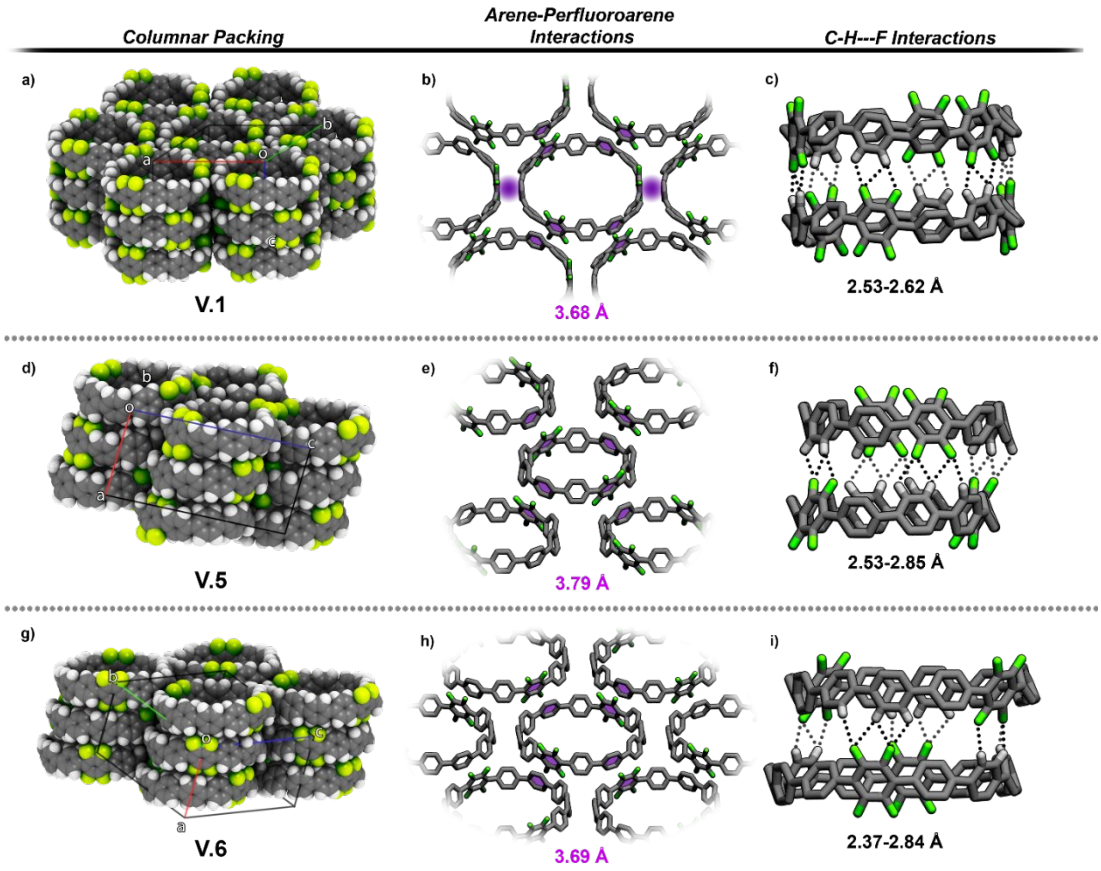

Figure 5.6. Columnar packing, arene-perfluoroarene interactions (highlighted in purple), and C—H---F interactions (dotted lines) observed in the crystal packings of nanohoops **V.1** (a-c), **V.5** (d-f), and **V.6** (g-i).

Pseudo-slow evaporation of **V.6** in dichloromethane (DCM), achieved via the reverse vapor diffusion of the DCM solvent into pentane, afforded needle-like crystals similar in appearance to those formed by **V.1** and **V.5**. Single-crystal XRD analysis

revealed that **V.6** also self-assembles into tubular arrays (**Figure 5.6**), again in stark contrast to the herringbone-like packing of the all-hydrocarbon analog of [12]CPP. Upon closer inspection of the crystal structure of **V.6**, we observed four aryl-perfluoro aryl distances measuring at 3.69 Å (**Figure 5.6**) and thirteen C—H---F interactions ranging between 2.48 and 2.84 Å (**Figure 5.6**). The solid-state packing of **V.6** in comparison to **V.1** results in linear channels (**Figure 5.6**) and an ideal hexagonal circle packing arrangement, the two-fold symmetry of **V.5** affords staggered columns and a pseudo-hexagonal horizontal assembly. Also, due to the inclusion of only two tetrafluorophenylene moieties, **V.5** exhibits two fewer arene-perfluoroarene interactions and twenty-three fewer C—H---F interactions than found in the crystal structure of **V.1** (**Figure 5.6**). Thus, we predict that organofluorine interactions may also allow for the further construction of tubular nanohoop-based assemblies with slightly varied morphologies but identical diameters.

However, it should be noted that the two-fold symmetry such as that found in **V.5** and **V.6** has been shown to result in non-tubular arrangements in fluorinated nanohoop systems. Indeed, Yamago and coworkers found that a two-fold symmetric fluorinated [6]CPP analog exhibits herringbone-like packing, presumably since this staggered arrangement allows for the maximization of solid-state C—H---F interactions.[41] Likewise, the same study by Yamago provided an example of a three-fold symmetric nanohoop (a [9]CPP analog) that assembles into tubular arrangements without the guidance of arene-perfluoroarene interactions, instead appearing to rely solely on C—H---F interactions. Therefore, we conclude that both nanohoop diameter and skeletal symmetry (i.e. the number of phenylene moieties present) are crucial factors to consider in the design of such

systems.

A notable application of CNT channels is the uptake and confinement of small molecule guests into 1D channels.[48, 49] Thus, we were curious if the nanotube-like channels formed by fluorinated nanohoops are accessible to guests. As an initial approach, we sought to leverage the size and shape complementarity of fluorinated nanohoop **V.5**, a [10]CPP derivative, with C_{60}. Indeed, macrocycles with radially oriented pi-conjugation,[50] in particular [10]CPP and its derivatives,[51, 52] have been shown to be strong hosts for C_{60} in both solution and the solid-state. Similar to the case of C_{60}@ [10]CPP, we found that the addition of C_{60} to fluorinated nanohoop **V.5** resulted in a decrease in the fluorescence intensity of fluorinated nanohoop **V.5** (**Figure 5.7**). From these fluorescence quenching data, we determined a binding constant (Ka) of $8.1 \pm 0.2 \times 10^5$ L^{-1} mol between fluorinated nanohoop **V.5** and C_{60} (**Figure 5.11**), a value that is lower than most binding constants reported [10]CPP hosts. For example, as compared to the parent [10]CPP host, the K_a is reduced (C_{60}@[10]CPP complex = $2.71 \pm 0.03 \times 10^6$ L^{-1} mol)[52] by nearly 30%. Despite this lowered affinity, the value is still relatively high amongst various fullerene hosts—a factor that allowed for a detailed investigation into the solid-state chemistry between nanohoop **V.5** and C_{60}. Dark red single-crystals of the C_{60}@**V.5** complex suitable for X-ray crystallography were grown via vapor diffusion of diethyl ether into a dilute THF/1,2-dichlorobenzene/toluene (1:1:1) solution of fluorinated nanohoop **V.5** and C_{60} (1:1). Interestingly, crystal structure analysis revealed cylindrical packing (**Figure 5.7**), but with the absence of perfluoroarene-arene interactions; however, numerous C—H---F interactions were found measuring from 2.54-2.87 Å (**Figure 5.13**). These interactions appear to be the driving force behind the linear arrangement of the C_{60}@**V.5** complex in the

solid-state, as the analogous all-hydrocarbon [10]CPP@C_{60} complex has been previously shown to adopt a staggered packing motif (**Figure 5.7**).34 The packing of **V.5**@C_{60} bears a striking aesthetic resemblance to CNT@C_{60} peapod structures, which have been shown to exhibit numerous exotic properties unique from bulk C_{60}. While not reported here, we expect that this arrangement can be adopted to align both endohedral and exohedrally functionalized fullerenes, a prospect that will likely result in new charge transport properties. Furthermore, given that the host-guest chemistry between nanohoops is just beginning to emerge, we anticipate that fluorinated nanohoops can potentially direct and pre-organize other guest molecules into columnar 1D arrays in a highly size-selective manner leading to new strategies for applications such as templated polymerizations and organic electronic materials.

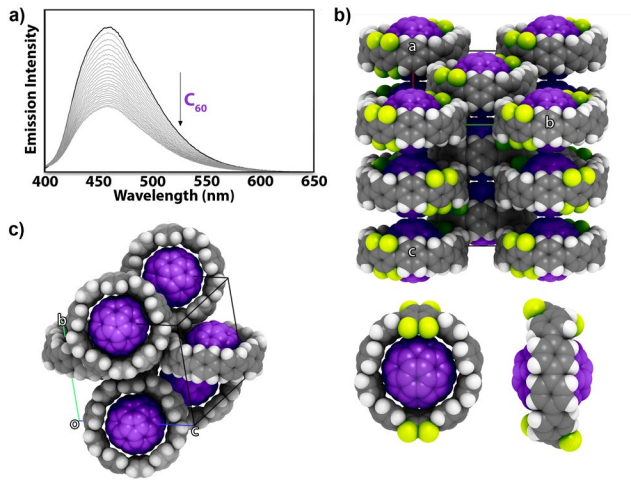

Figure 5.7. a) Observed emission response of nanohoop **V.5** to increasing quantities of C_{60}. b) Peapod-like crystal packing of the **V.5**@C_{60} complex (top) and views of a single host-guest complex (bottom); c) X-ray crystal structure of the [10]CPP@C_{60} complex in the solid-state. Fluorine atoms are colored in green, hydrogens in white, carbons in grey, and C_{60} has been colored purple.

5.3. Conclusions

In conclusion, we have presented a scalable, size-selective strategy for accessing functional CNT mimic systems. Two novel fluorinated nanohoops (**V.5** and **V.6**) were synthesized via a general route using common intermediates, and a new synthetic approach was developed to access previously reported nanohoop **V.1** on the gram scale. Through x-ray crystallographic analysis, it was determined that nanohoops **V.1**, **V.5**, and **V.6** all self-assemble into CNT mimic systems in the solid state via organofluorine interactions and boast uniform channel diameters defined by the diameters of their respective constituent nanohoops. Aside from the aesthetic similarities between CNTs and the mimic systems disclosed herein, CNT-like properties were also found to emerge as a result of tubular nanohoop alignment. Neither of these functionalities are observed in the analogous non-fluorinated nanohoop systems, implying that the arene-perfluoroarene and C—H---F interactions observed in the crystal structures of the CNT mimics are effective in maintaining a tubular architecture. The ability to fabricate these CNT mimics in a discrete, size-selective fashion is expected to benefit studies in nanofluidics and general nanoscale confinement, where access to atomically precise nanopores is difficult due to the inability to selectively produce CNTs or graphene nanopores. Furthermore, we believe the combined experimental and theoretical analysis of the CNT mimics presented may serve as an initial blueprint for the predictable design of other tubular systems based on the self-assembly of curved macrocycles, opening the door to a variety of new precision nanomaterials.

5.4. Experimental Sections

5.4.1. General Experimental Details

^{1}H NMR spectra were recorded at 500 MHz on Varian VNMR spectrometer, 500 MHz on a Bruker, or 600 MHz on Bruker. All 1H NMR spectra are referenced to TMS (δ 0.00 ppm), CH2Cl2 (δ 5.32 ppm), or (CH3)3CO (δ 2.05 ppm). All 13C NMR spectra are references to a residual CHCl3 (δ 77.16 ppm), CH2Cl2 (54.00 ppm), or (CH3)3CO (δ 29.84 ppm). All reagents were obtained commercially and used without further purification unless otherwise noted. All glassware was flame-dried and cooled under an inert atmosphere of nitrogen unless otherwise noted. Moisture sensitive reactions were carried out under an inert atmosphere of nitrogen using standard syringe/septa technique. Silica column chromatography was conducted with Zeochem Zeoprep 60 Eco 40-63 μM silica gel while alumina chromatography utilized Sorbent Technologies 50-200 um Basic Activity II-II Alumina.

SEM (Scanning Electron Microscopy), FIB (Focused Ion Beam), and EDS (Energy Dispersive X-Ray Spectroscopy) analysis were performed in an FEI Helios 600i FIB-SEM. The SEM images were taken with an accelerating voltage 5 kV while the Ga+ FIB was operated at 30 kV Angled SEM and FIB was performed at an angle of 52°. EDS data was acquired with a 5 kV electron beam.

Widefield fluorescent imaging was performed on a Nikon Eclipse Ti-U epifluorescence optical microscope with a 50x objective lens using a Nikon DAPI filterset (Excitation Filter at 375 nm, Dichroic Mirror at 415 nm, and a barrier filter at 460 nm).

Quantitative nanomechanical mapping was performed with a Bruker Dimension Icon atomic force microscope with an OTESPA-R3 probe (nominal spring constant 26 N/m) in PeakForce tapping mode. The force set-point was 60 nN, which was high enough

to indent both the hexagonal structures as well as the HOPG substrate. We use the known elastic modulus of HOPG (~18 GPa) to infer the modulus of the hexagons (~12 GPa). Raman spectroscopy was performed in a WiTec alpha300 confocal

Raman spectrometer with a 532 nm excitation laser and a 60x, 0.7 NA objective. Laser power was kept low to minimize damage to the hexagonal structures.

Measurements of the excitation and emission spectra were performed using a homebuilt fluorescence microscope with a 100x, 0.7 NA objective. A monochromator was used to select a 5 nm FWHM wavelength band from a Mercury/Xenon excitation source, which was then focused onto the sample with a spot-size comparable to a single hexagon. The S3 excitation power of all bands was measured after the objective and used to normalize the emission intensity. The emitted light was separated from the incident light using a 50:50 beamsplitter and spectra were acquired using an Ocean Optics Flame Spectrometer with an integration time of 1 second.

5.4.2. Sample Preparation for Surface Measurements.

Samples were prepared on either a freshly cleaved highly-ordered pyrolytic graphite (HOPG) substrate (SPI supplies HOPG Advanced Ceramics Brand Grade ZYH and Mikromasch HOPG Grade ZYA, both 12x12x2 mm) or on multi-layer graphene grown on Cu foil (Graphenen). A 1 mg/ml solution of 1 in chloroform was prepared and heated to roughly 45-50 °C, causing the solution to go from cloudy to clear. A small crystallizing dish was then filled halfway with deionized water and covered with a sheet of aluminium foil with small holes cut into it. The dish was then heated 85 °C on a hotplate. Next, the chosen substrate was carefully placed on the foil covering the dish so as to be centered and

level. The substrate was then flooded (approx. 0.05-0.1 mL) with the chloroform solution of 1 via dropcasting through a syringe filter (0.2 µm PTFE membrane). Subsequently, an appropriately-sized watch glass was quickly placed on top of the dish to induce a crude humid environment. The substrate was removed once the chloroform had completely evaporated (1-2 min.).

5.4.3. Synthetic Details

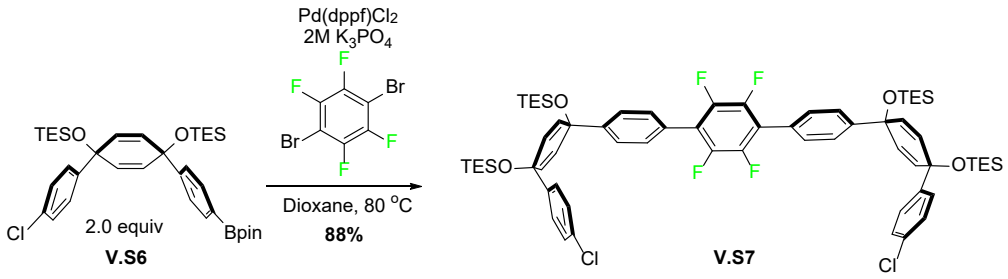

Figure 5.8. Synthesis of **V.S7** from **V.S6**.[19]

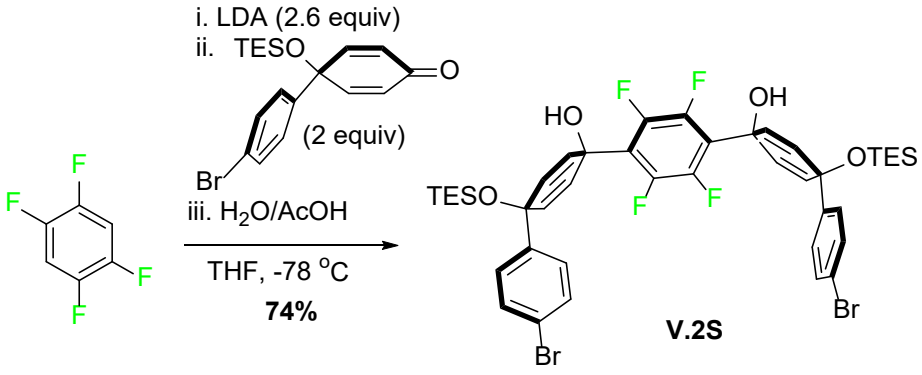

Figure 5.9. Synthesis of **V.S2**.

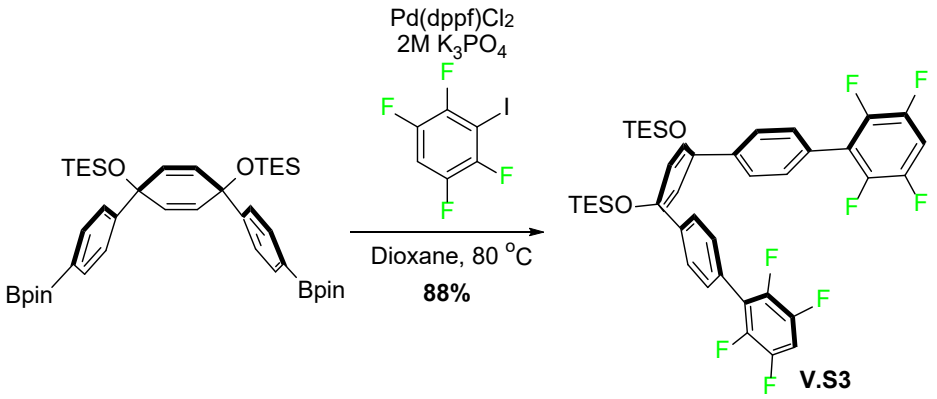

Figure 5.10. Synthesis of **V.S3**.

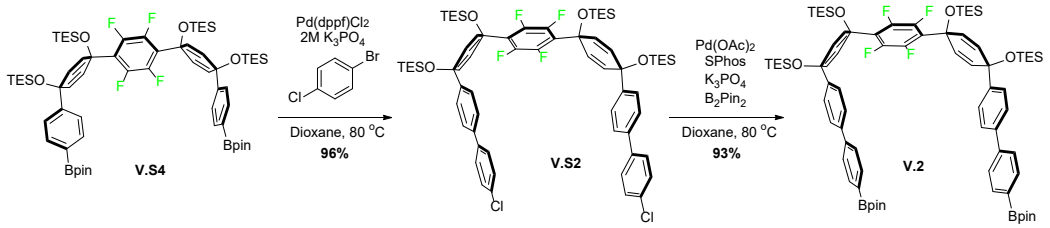

Figure 5.11. Synthesis of **V.2.**

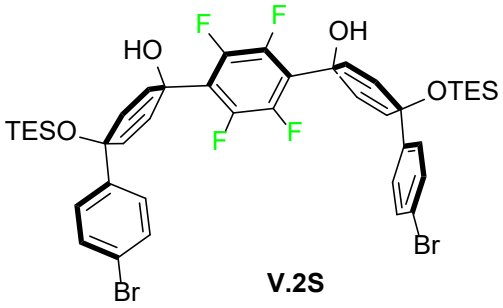

Synthesis of V.2S. To a flame-dried 100 mL flask containing THF (30 mL) was added diisopropylamine (0.774 mL, 5.49 mmol, 2.60 equiv). This flask was then cooled to 0 °C at which point *n*BuLi (2.5 M in hexanes, 1.94 mL, 4.85 mmol, 2.30 equiv.) was added dropwise. After stirring for 10 minutes at 0 °C, the flask was then was then cooled to -78 °C over 45 minutes. To this flask was then added 1,2,4,5-tetrafluorobenzene (neat) (240

uL, 2.11 mmol, 1.00 equiv) followed by bromo ketone[19] (as a solution in 3 mL THF) (2.0 g, 5.27 mmol, 2.5 equiv) resulting in a bright yellow solution that slowly became brown/orange over the course of 1 h. After 1 hour of stirring, the reaction was slowly quenched with a 20% acetic acid/methanol solution (5 mL), resulting in a colorless solution which was then brought to room temperature. The organic solvents were then removed via rotary evaporation and the remaining slightly yellow aqueous layer was extracted with ethyl acetate (3 x 75 mL). The combined organic phases were washed with H_2O (3 x 100 mL), and brine (1 x 100 mL), and dried over sodium sulfate. The solvent was removed under reduced pressure to afford a faint yellow oil. Chromatography (0 to 10% EtOAc/Hexanes) of this oil yielded **V.2S** as a colorless oil (1.41 g, 74%). ^{1}H NMR (500 MHz, Chloroform-*d*) δ 7.41 (d, *J* = 8.7 Hz, 4H), 7.21 (d, *J* = 8.5 Hz, 4H), 6.30 (d, *J* = 10.2 Hz, 4H), 6.01 (d, *J* = 10.1 Hz, 4H), 2.55 (s, 2H), 0.99 (t, *J* = 7.9 Hz, 18H), 0.69 (q, *J* = 7.9 Hz, 12H). ^{13}C NMR (126 MHz, $CDCl_3$) δ 143.96, 134.16, 131.48, 127.64, 127.41, 121.43, 71.06, 68.02, 7.18, 6.58. ^{19}F NMR (471 MHz, Chloroform-*d*) δ -138.00 (s). δ HRMS (TOF, ES+) (m/z): [M+2Na]+ calculated for $C_{42}H_{47}O_4Na_2Br_2F_4Si_2$, 951.1111; found, 951.1354.

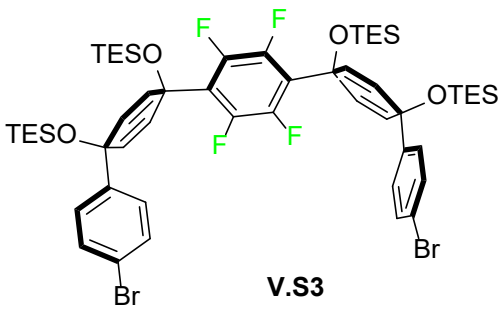

V.S3

Synthesis of V.S3. Imidazole (0.420 g, 6.16 mmol, 4.0 equiv), and **V.2S** (1.40 g, 1.54 mmol, 1.00 equiv.) were added to a 100 mL flame-dried RBF, then dissolved in 25 mL

DMF. The resulting solution was heated to 40 °C at which point chlorotriethylsilane (TESCl) (0.700 g, 4.63 mmol, 3.00 equiv.) was added dropwise. The reaction was monitored via ^{1}H NMR until all the starting material was consumed (typically 4 hours). Once complete, the reaction was neutralized with sodium bicarbonate followed by extraction of the resulting white suspension with EtOAc (3 x 75 mL). The combined organic phases were washed with 5% LiCl (5 x 100 mL), followed by H_2O (1 x 100 mL), brine (1 x 100 mL), and then placed over sodium sulfate. Removal of solvent via rotary evaporation yielded a yellow oil which was then triturated with MeOH followed by filtration and collection of the resulting white solid to give **V.S3** (1.52 g, 89%). ^{1}H NMR (500 MHz, Chloroform-*d*) δ 7.32 (d, *J* = 8.7 Hz, 4H), 7.13 (d, *J* = 8.7 Hz, 4H), 6.35 (d, *J* = 9.7 Hz, 4H), 5.95 (d, *J* = 10.2 Hz, 4H), 0.99 – 0.86 (m, 36H), 0.70 – 0.53 (m, 24H). ^{13}C NMR (126 MHz, $CDCl_3$) δ 144.58, 132.84, 131.32, 129.09, 127.32, 121.29, 71.15, 69.87, 7.17, 6.92, 6.53, 6.33. ^{19}F NMR (471 MHz, $CDCl_3$) δ -136.88 (s). δ LRMS (TOF, MALDI) (m/z): [M]+ calculated for $C_{54}H_{76}O_4Br_2F_4Si_4$, 1134.315; found, 1136.425.

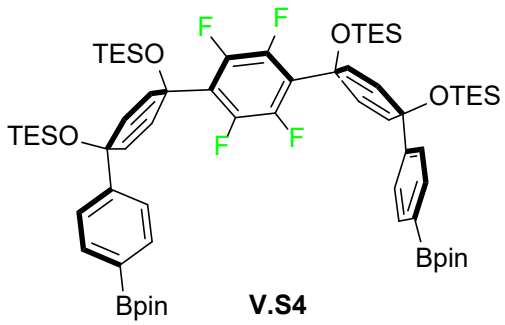

V.S4

Synthesis of V.S4. To a 100 mL flame-dried flask was added $Pd(OAc)_2$ (11.0 mg, 0.0484 mmol, 0.100 equiv), 2-dicyclohexylphosphino-2′,6′dimethoxybiphenyl (50.0 mg, 0.121 mmol, 0.250 equiv), bis(pinacolato)diboron (0.492 g, 1.94 mmol, 4.00 equiv.), **V.S3** (0.550 g, 0.484 mmol, 1.00 equiv.), and K_3PO_4 (0.520 g, 2.45 mmol, 5.00 equiv.). After the solids

were added, the flask was evacuated and backfilled with nitrogen 5 times. 1,4-dioxane (30 mL) was then added to the flask resulting in an orange solution, which was then placed into an 80 °C oil bath. After 3 h, the resulting black solution was brought to room temperature and the solvent was removed under reduced pressure. To this black solid was added H_2O (50 mL), followed by extracted with hexanes (3 x 75 mL). The combined organic phases were then washed with water (3 × 50 mL), brine (1 × 100 mL), and then dried over sodium sulfate. After removing the organic solvent via rotary evaporation, the resulting white solid was then washed with plenty of methanol, which after filtration, gave **V.S4** as a white solid (2.99 g, 92%). ^{1}H NMR (500 MHz, Chloroform-*d*) δ 7.66 (d, *J* = 8.4 Hz, 4H), 7.27 (d, *J* = 8.2 Hz, 4H), 6.34 (d, *J* = 10.1 Hz, 4H), 5.99 (d, *J* = 10.2 Hz, 4H), 1.30 (s, 24H), 0.98 – 0.88 (m, 36H), 0.68 – 0.56 (m, 24H). ^{13}C NMR (126 MHz, $CDCl_3$) δ 148.48, 134.84, 133.04, 128.90, 124.86, 83.78, 71.57, 69.96, 25.00, 7.19, 6.95, 6.59, 6.33. ^{19}F NMR (471 MHz, $CDCl_3$) δ -137.01 (s). δ HRMS (TOF, ES+) (m/z): [M+Na]+ calculated $C_{66}H_{100}O_8NaF_4Si_4B_2$, 1253.6515; found, 1253.6544.

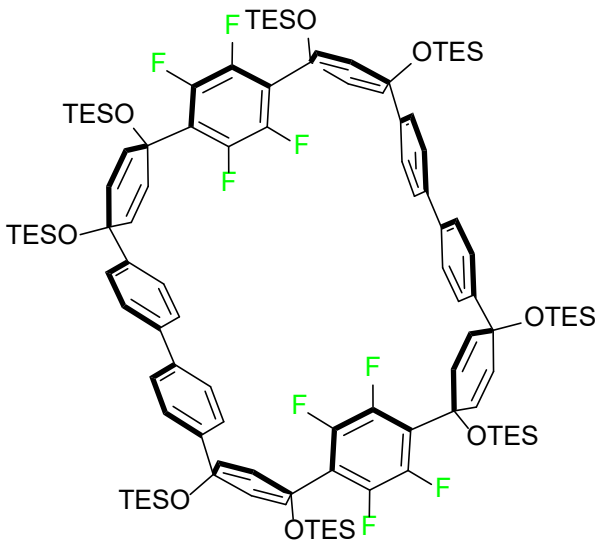

V.9

Synthesis of V.9. To a flame-dried 250 mL round bottom flask equipped with a stir bar was added **V.S3** (0.268 g, 2.36 mmol, 1.00 equiv.), **V.S4** (0.290 g, 2.36 mmol, 1.00 equiv.), and SPhos-Pd-G2 (16.9 mg, 0.0236 mmol, 0.100 equiv.). The flask was evacuated and back-filled with N_2 5 times, followed by addition of 1,4-dioxane (118 mL). This solution was then vigorously spared with N_2 for 2 h at which point the solution was placed into an oil bath at 80 ºC. At this point, an aqueous solution of 2M K_3PO_4 (11.8 mL, 23.6 mmol, 10.0 equiv) was added, quickly turning the colorless solution bright yellow. The solution was allowed to stir for 1h, at which point the solution was allowed to cool to room temperature followed by removal of the solvent via rotary evaporation. The resulting yellow/brown oil aqueous phase was extracted with hexanes (3 x 100 mL), followed by washing of the combined organic phases with H_2O (3 x 100 mL), brine (1 x 100 mL), and finally placed over sodium sulfate. After solvent removal, the brown oil was dissolved in hexanes and then filtered using a fritted funnel. The brown solids were washed with plenty of hexanes and the resulting yellow filtrate was concentrated to a yellow oil. The addition of acetone caused the precipitation of a white solid, which after collection via filtration and washing with acetone yielded **V.9** as a white solid (0.207 g, 45%). ^{1}H NMR (500 MHz, Chloroform-*d*) δ 7.15 (d, *J* = 8.4 Hz, 8H), 7.07 (d, *J* = 8.5 Hz, 8H), 6.37 (d, *J* = 10.2 Hz, 8H), 6.00 (d, *J* = 10.4 Hz, 8H), 1.01 – 0.81 (m, 72H), 0.76 – 0.53 (m, 48H). ^{13}C NMR (126 MHz, $CDCl_3$) δ 144.06, 139.70, 133.48, 129.01, 127.01, 125.52, 71.32, 70.16, 7.20, 6.93, 6.59, 6.30. ^{19}F NMR (471 MHz, $CDCl_3$) δ -136.43 (s). δ LRMS (TOF, MALDI) (m/z): [M]+ calculated for $C_{108}H_{152}O_8F_8Si_8$, 1952.951; found, 1954.126.

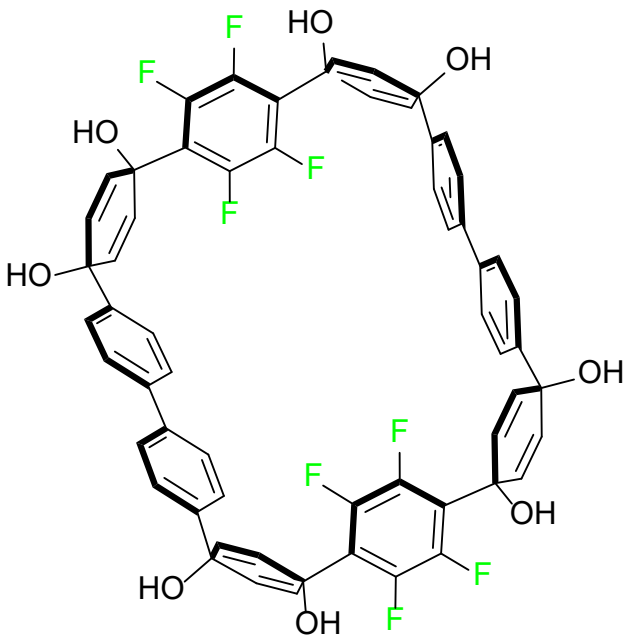

V.S5

Synthesis of V.S5. To a flame-dried 100 mL round bottom flask equipped with a stir bar was added **V.9** (0.180 g, 0.0922 mmol, 1.00 equiv.) followed by THF (20 mL). To this solution was then added glacial acetic acid (0.530 mL, 9.22 mmol, 100.0 equiv.), followed by tetrabutylammonium fluoride (1M in THF, 1.84 mL, 1.84 mmol, 20.0 equiv.) dropwise. The resulting colorless solution was then stirred for 18 h at which point H_2O (10 mL) was added, followed by removal of THF via rotary evaporation. The white solid was then filtered and washed with H_2O (30 mL) and DCM (3x 10 mL) to give **V.S5** (0.0901 g, 94%). ^{1}H NMR (500 MHz, DMSO-d_6) δ 7.47 (d, J = 8.5 Hz, 8H), 7.35 (d, J = 8.4 Hz, 8H), 6.20 (d, J = 9.9 Hz, 8H), 5.97 – 5.91 (m, 12H), 5.61 (s, 8H).^{19}F NMR (471 MHz, DMSO) δ -138.55 (s). Due to insolubility, ^{13}C NMR data could not be obtained. δ HRMS (TOF, ES+) (m/z): [M+Na]+ calculated for $C_{60}H_{40}F_8O_8Na$, 1063.2493; found, 1063.2474.

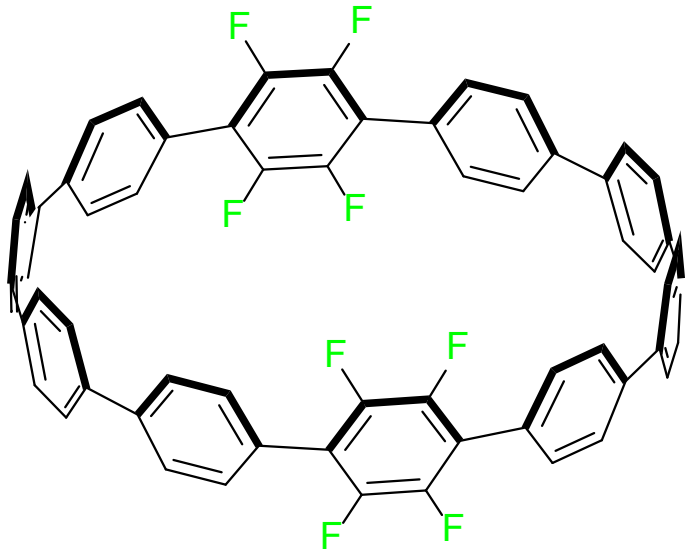

V.5

Synthesis of V.5. To a flame-dried 100 mL round bottom flask equipped with a stir bar was added **V.S5** (0.0901 g, 0.0866 mmol, 1.00 equiv.), followed by THF (40 mL). To this suspension was added H_2SnCl_4[2] (0.40 M in THF, 0.683 mmol, 1.73 mL, 5.00 equiv), resulting in a faint-yellow/white suspension which was stirred for 18h at 50 ºC. After cooling to room temperature, aqueous (18 w/w%) ammonia (10 mL) was added followed by filtration using a fritted funnel. The resulting faint blue filtrate was then collected in a round bottom flask which, after removal of THF via rotary evaporation, gave an off-white solid. This solid was then washed with a combination of hexanes, ethyl acetate, and ethanol to give **V.5** as a pristine white solid (15.3 mg, 16%). ^{1}H NMR (500 MHz, Chloroform-*d*) δ 7.71 – 7.45 (m, 32H). ^{19}F NMR (471 MHz, $CDCl_3$) δ -143.52 (s). Due to insolubility, ^{13}C NMR data could not be obtained. δ HRMS (TOF, ES+) (m/z): [M]+ calculated for $C_{60}H_{32}F_8$, 904.2376; found, 904.2380.

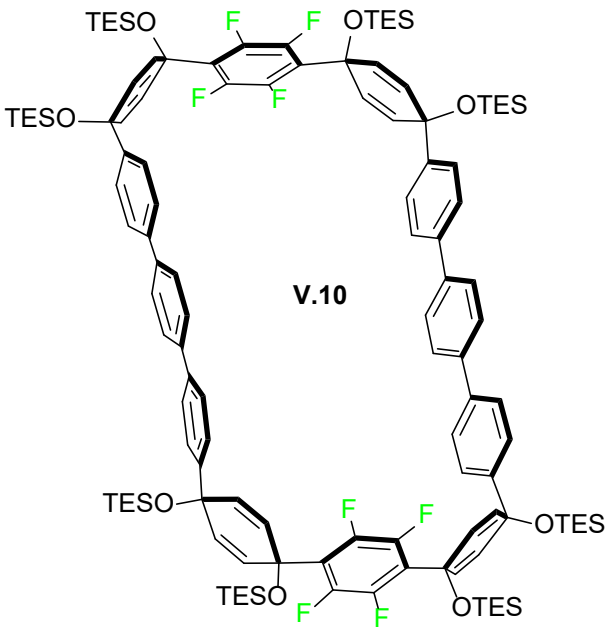

Synthesis of V.10. To a flame-dried 250 mL round bottom flask equipped with a stir bar was added **V.2** (0.334 g, 0.271 mmol, 1.00 equiv.), **V.S3** (0.325 g, 0.271 mmol, 1.00 equiv.), and SPhos-Pd-G2 (0.039 g, 0.0542 mmol, 0.200 equiv.). The flask was evacuated and back-filled with N_2 5 times, followed by addition of 1,4-dioxane (90 mL). This solution was then vigorously spared with N_2 for 1 h at which point the solution was placed into an oil bath at 80 °C. At this point, an aqueous solution of 2M K_3PO_4 (9.03 mL, 4.52 mmol, 17.0 equiv) was added. The solution was allowed to stir for 12 hr, after which the solution was brought to room temperature and the solvent was removed under reduced pressure. Water (50 mL) was added, followed by extraction with DCM (3 x 50 mL). The combined organic phases were washed with water (3 x 50 mL), brine (1 x 50 mL), and dried over sodium sulfate. The solvent was removed via rotary evaporation, and the resulting brown solid was purified via column chromatography (0-40% DCM/Hexanes) using basic alumina as the stationary phase. This afforded **V.10** as a white solid (0.199 g, 35%). ^{1}H NMR (500 MHz, Chloroform-*d*) δ 7.36 (d, *J* = 7.9 Hz, 8H), 7.28 (d, *J* = 7.7 Hz, 8H), 6.40

(d, J = 9.7 Hz, 8H), 5.99 (d, J = 9.3 Hz, 8H), 0.99 (t, J = 7.8 Hz, 36H), 0.94 (t, J = 8.0 Hz, 36H), 0.69 (q, J = 7.9 Hz, 24H), 0.61 (q, J = 7.8 Hz, 24H). ^{13}C NMR (126 MHz, Chloroform-*d*) δ 144.12, 139.60, 139.06, 133.18, 128.59, 127.09, 126.62, 125.66, 71.37, 69.95, 7.08, 6.80, 6.43, 6.20. ^{19}F NMR (471 MHz, Chloroform-*d*) δ -136.37 (s). δ HRMS (MALDI,TOF), m/z calculated for $C_{120}H_{160}F_8O_8Si_8$ (M)+ 2106.02, found 2106.02.

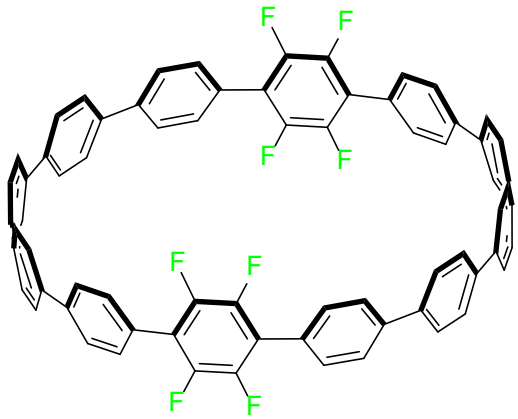

V.6

Synthesis of V.6. To a flame-dried 100 mL round bottom flask equipped with a stir bar was added **V.10** (0.036 g, 0.0171 mmol, 1.00 equiv.) followed by THF (10 mL). To this solution was then added glacial acetic acid (0.049 mL, 0.854 mmol, 50.0 equiv.), followed by tetrabutylammonium fluoride (1M in THF, 0.427 mL, 0. mmol, 25 equiv.) dropwise. The resulting colorless solution was then stirred for 18 h at which point H_2O (10 mL) was added, followed by removal of THF via rotary evaporation. The white solid was then filtered and washed with H_2O (30 mL) to afford the deprotected intermediate as a white solid. Without further purification, the intermediate was placed in a flame-dried 50 mL round bottom flask equipped with a stir bar followed by THF (8 mL). To the resulting cloudy-white solution was added 1,8-Diazabicyclo[5.4.0]undec-7-ene (0.020 mL, 0.137 mmol, 8 equiv), followed by PBr_3 (0.013 mL, 0.137 mmol, 8 equiv) dropwise, resulting in

an white precipitate. After ~5 min of stirring, anhydrous $SnCl_2$ (0.026 g, 0.137 mmol, 8 equiv.) was added as a solid, turning the solution yellow. After 1 h of stirring, the solution was quenched with 10% NaOH (5 mL) and THF was removed via rotary evaporation. To the resulting yellow suspension was added 125 mL of H_2O, followed by excessive extractions with DCM (6x50 mL). This was followed by washes with H_2O (3x50 mL) and brine (1x50 mL). The organic layer was then dried over sodium sulfate and filtered, followed by solvent removal via rotary evaporation. Purification via column chromatography (0-40% DCM/Hexanes) afforded **V.6** as an off-white solid (0.005 g, 28%). ^{1}H NMR (500 MHz, Chloroform-*d*) δ 7.70 – 7.63 (m, 30H), 7.57 (d, *J* = 8.4 Hz, 10H). ^{19}F NMR (471 MHz, Chloroform-*d*) δ -143.86 (s). Due to insolubility, ^{13}C NMR data could not be obtained. δ HRMS (MALDI,TOF), m/z calculated for $C_{72}H_{40}F_8$ (M)+ 1056.30, found 1056.30.

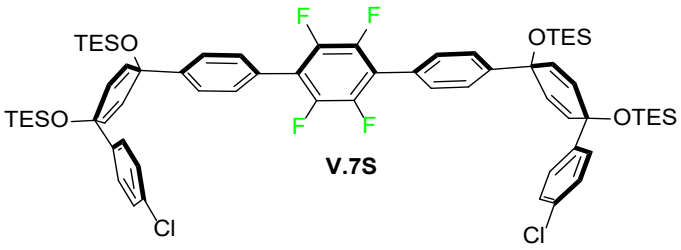

V.7S

Synthesis of V.7S. To a 250 mL flame-dried flask was added **V.S6**[19] (18.56 g, 28.0 mmol, 2 equiv), 1,4-dibromo-2,3,5,6-tetrafluorobenzene (4.27 g, 14.0 mmol, 1 equiv), and [1,1'bis(diphenylphosphino) ferrocenedichloropalladium (1.01 g, 1.39 mmol, 0.100 equiv). After the solids were added, the flask was evacuated and backfilled with nitrogen 3 times (it is recommended to keep evacuations to a minimum as 1-bromo-2,3,5,6-tetrafluorobenzene is quite volatile). The flask was then purged with N_2 for 20 min. 1,4-dioxane (100.0 mL) was then added to the flask, after which aqueous 2M K_3PO_4 (0.660

mL, 1.32 mmol, 5.5 equiv), sparged for 1 h prior to use, was added. The solution was then placed in an 80 °C oil bath and allowed to stir for 12 h. The next day, the reddish-black solution was allowed to come to room temperature before removing the solvent under reduced pressure. The resulting reddish-black sludge was dissolved in DCM and run through a plug of celite with a small pad of silica on top. This was followed by removal of DCM solvent from the eluent via rotary evaporation. The resulting yellow oil was washed with MeOH, causing the product to precipitate as a white solid. Vacuum filtration, followed by additional MeOH rinses, afforded V.**7S** as a white solid (14.70 g, 88%). ^{1}H NMR (500 MHz, Chloroform-*d*) δ 7.45 (dd, 8H), 7.32 (d, *J* = 8.5 Hz, 4H), 7.26 (d, 4H), 6.09 – 5.97 (dd, 8H), 0.97 (dt, *J* = 11.2, 7.9 Hz, 36H), 0.65 (dq, *J* = 21.6, 7.9 Hz, 24H). ^{13}C NMR (126 MHz, Chloroform-*d*) δ 146.81, 144.51, 133.13, 131.59, 131.45, 130.01, 128.30, 127.36, 126.40, 126.03, 71.38, 71.09, 7.03, 6.45. ^{19}F NMR (471 MHz, Chloroform-*d*) δ -144.35.

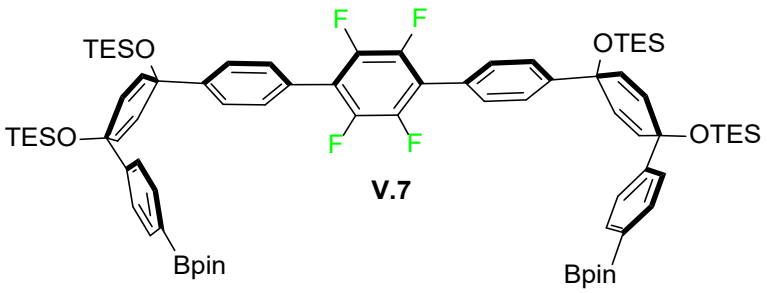

V.7

Synthesis of V.7. To a 100 mL flame-dried flask was added $Pd(OAc)_2$ (0.135 g, 0.602 mmol, 0.05 equiv), 2-dicyclohexylphosphino-2'6'dimethoxybiphenyl (0.618 g, 1.50 mmol, 0.125 equiv), bis(pinacolato)diboron (15.30 g, 60.2 mmol, 5 equiv), **V.7S** (14.45 g, 12.0 mmol, 1 equiv), and K_3PO_4 (5.91 g, 60.2 mmol, 5 equiv). After the solids were added, the flask was evacuated and backfilled with nitrogen 5 times. The flask was then purged with

N_2 for 20 min. 1,4-dioxane (100.0 mL) was then added to the flask and the solution was sparged for 20 min. before being placed in an 80 °C oil bath overnight. The next day, the black solution was brought to room temperature and the solvent was removed under reduced pressure. The resulting black sludge was dissolved in DCM and run through a plug of celite with a small pad of silica on top. After removing the DCM solvent from the eluent via rotary evaporation, the resulting dark-orange oil was washed with methanol, causing the product to precipitate as a white solid. Vacuum filtration afforded **V.7** as a white solid (15.54 g, 93%). ^{1}H NMR (500 MHz, Chloroform-*d*) δ 7.74 (d, *J* = 8.0 Hz, 4H), 7.45 (d, *J* = 8.4 Hz, 4H), 7.40 (d, *J* = 8.2 Hz, 8H), 6.05 (d, *J* = 10.1 Hz, 4H), 5.99 (d, *J* = 10.1 Hz, 4H), 1.33 (s, 24H), 0.94 (dt, *J* = 25.1, 7.9 Hz, 36H), 0.67 (q, *J* = 7.9 Hz, 12H), 0.57 (q, *J* = 7.9 Hz, 12H). ^{13}C NMR (126 MHz, Chloroform-*d*) δ 149.02, 147.00, 145.00, 143.15, 134.76, 131.58, 131.41, 129.95, 128.18, 126.25, 126.02, 125.93, 125.27, 83.76, 71.45, 24.88, 7.06, 7.04, 6.48, 6.44. ^{19}F NMR (471 MHz, Chloroform-*d*) δ -144.37. δ HRMS (TOF, ES+) (m/z): [M]+ calculated for $C_{78}H_{108}B_2O_8F_4NaSi_4$, 1405.7141; found, 1405.7163.

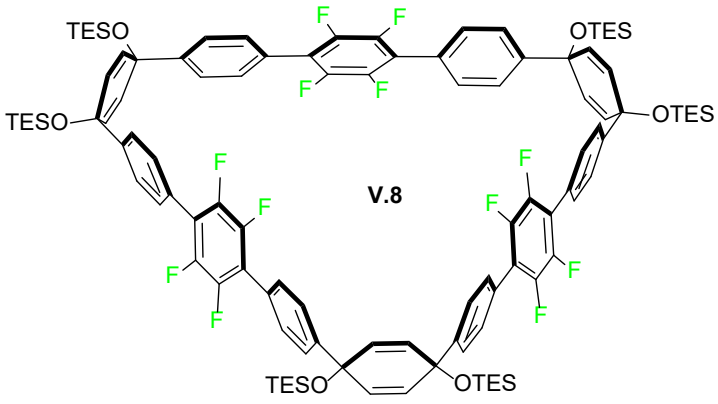

V.8

Synthesis of V.8. To a flame-dried 2000 mL round bottom flask equipped with a stir bar was added **V.S7** (14.44 g, 10.40 mmol, 1.00 equiv.), **V.3** (10.80 g, 10.40 mmol, 1.00

equiv.), and SPhos-Pd-G2 (1.50 g, 2.08 mmol, 0.200 equiv.). The flask was evacuated and back-filled with N_2 5 times, followed by 30 min. of purging with N_2. Next, 1,4-dioxane (1000 mL) was added to the flask via cannula to afford a 10 mM solution. This solution was then vigorously spared with N_2 for 2 h at which point the solution was placed into an oil bath at 80 °C. At this point, an aqueous solution of 2M K_3PO_4 (103.9 mL, 207.8 mmol, 20.0 equiv) was added. The solution was allowed to stir for 12 hr, after which the solution was brought to room temperature and the solvent was removed under reduced pressure. The resulting brown oil was dissolved in DCM and run through a plug of celite with a small pad of silica on top. The eluent was then dried via rotary evaporation to afford a sticky white solid. Purification via column chromatography (0-40% DCM/Hexanes) afforded **V.8** as a white solid (4.46 g, 22%) (alternatively, the crude material can be washed with hexanes to precipitate the product at a loss of yield). ^{1}H NMR (500 MHz, Chloroform-*d*) δ 7.53 (d, *J* = 8.2 Hz, 12H), 7.45 (d, *J* = 8.0 Hz, 12H), 6.10 (s, 12H), 0.99 (t, *J* = 7.9 Hz, 54H), 0.68 (q, *J* = 7.9 Hz, 36H). ^{13}C NMR (126 MHz, Chloroform-*d*) δ 146.97, 145.21, 143.05, 131.53, 130.02, 126.42, 126.09, 71.48, 7.05, 6.49. ^{19}F NMR (471 MHz, Chloroform-*d*) δ -144.38. MALDI TOF, m/z calculated for $C_{108}H_{126}F_{12}O_6Si_6$ (M)+ 1915.80, found 1915.96.

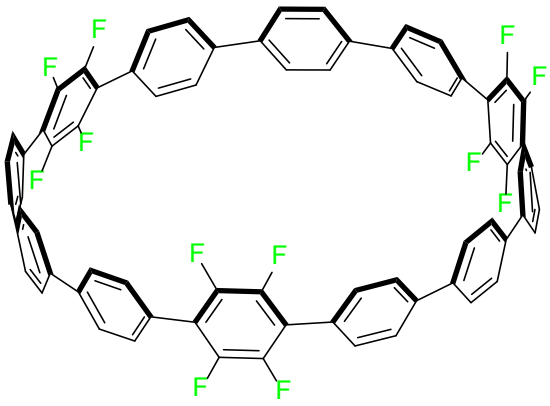

V.1

Synthesis of V.1. To a flame-dried 50 mL round bottom flask equipped with a stir bar was added **V.8** (0.174 g, 0.091 mmol, 1.00 equiv.) followed by THF (10 mL). To this solution was then added tetrabutylammonium fluoride (1M in THF, 2.27 mL, 2.27 mmol, 25.0 equiv.) dropwise. This solution was then stirred for 2 h at which point H_2O (10 mL) was added, followed by removal of THF via rotary evaporation. The resulting suspension was vacuum filtered, washed with water and allowed to fully dry. Without further purification, the crude white solid was placed in a flame-dried 250 mL round bottom flask equipped with a stir bar followed by THF (100 mL). The flask was then placed in an ice bath (0 °C) and allowed to cool for 30 min. After 30 min, 1,8-Diazabicyclo[5.4.0]undec-7-ene (0.027 mL, 0.292 mmol, 8 equiv) was added, followed by PBr_3 (0.044 mL, 0.292 mmol, 8 equiv) dropwise, resulting in a white precipitate. After ~5 min of stirring, anhydrous $SnCl_2$ (0.055 g, 0.292 mmol, 8 equiv.) was added as a solid, turning the solution yellow. After 1 h of stirring, a majority of the THF solvent was removed via rotary evaporation and the concentrated reaction mixture was poured directly onto a basic alumina plug. Flushing the plug with DCM caused only the product to elute. The eluent was dried under reduced pressure to afford **V.1** as an off-white solid (1.06 g, 40%). ^{1}H NMR (500 MHz, Chloroform-*d*) δ 7.69 (d, *J* = 6.2 Hz, 24H), 7.59 (d, *J* = 8.2 Hz, 12H). ^{19}F NMR (471 MHz, Chloroform-*d*) δ -143.82 (s). Due to insolubility, ^{13}C NMR data could not be obtained. MALDI TOF, m/z calculated for $C_{72}H_{36}F_{12}$ (M)+ 1128.2625, found 1128.0620.

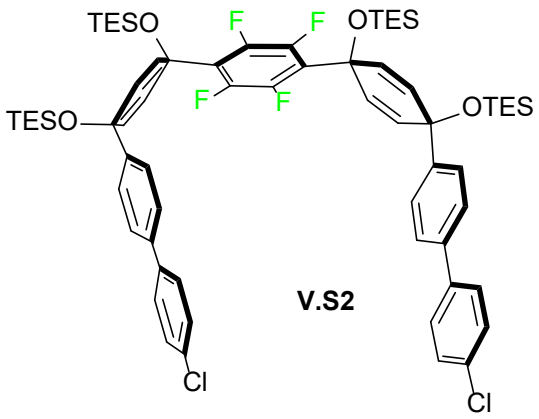

V.S2

Synthesis of V.S2. To a 100 mL flame-dried flask was added **V.S4** (0.296 g, 0.240 mmol, 1 equiv), 1-bromo-4-chlorobenzene (0.276 g, 1.44 mmol, 6 equiv), and [1, 1'bis(diphenylphosphino)ferrocenedichloropalladium (0.018 g, 0.024 mmol, 0.100 equiv). After the solids were added, the flask was evacuated and backfilled with nitrogen 5 times. 1,4-dioxane (10.0 mL) was then added to the flask and the solution was sparged with N_2 for 10 min. before aqueous 2M K_3PO_4 (0.660 mL, 1.32 mmol, 5.5 equiv), sparged with N_2 for 1 h prior to use, was added. The solution was then placed in an 80 °C oil bath and allowed to stir for 12 h. The next day, the reddish-black solution was allowed to come to room temperature before removing the solvent under reduced pressure. Next, H_2O (50 mL) was added, followed by extraction with hexanes (3 x 50 mL). The combined organic phases were then washed with water (3 x 50 mL), brine (1 x 75 mL), and dried over sodium sulfate. After removal of solvent via rotary evaporation, the resulting yellow oil was purified via column chromatography (2-5% EtOAc/Hexanes) to afford a **V.S4** as a clean, colorless oil that was pure via NMR. If desired, the oil can be washed with methanol to access the compound as a white solid (0.276 g, 96%). ^{1}H NMR (500 MHz, Chloroform-*d*) δ 7.40 – 7.35 (m, 8H), 7.31 (dd, J = 15.0, 8.0 Hz, 8H), 6.37 (d, J = 9.7 Hz, 4H), 6.01 (d, J = 9.7 Hz, 4H), 0.98 (t, J = 7.7 Hz, 19H), 0.91 (t, J = 8.9, 7.1 Hz, 19H), 0.67 (q, J = 7.9 Hz,

13H), 0.59 (q, J = 7.9 Hz, 13H). ^{13}C NMR (126 MHz, Chloroform-*d*) δ 144.74, 139.15, 138.72, 133.27, 133.02, 128.81, 128.77, 128.17, 126.69, 125.91, 71.21, 69.84, 7.06, 6.80, 6.44, 6.21. ^{19}F NMR (471 MHz, Chloroform-*d*) δ -136.83. δ HRMS (TOF, ES+) (m/z): [M+Na]+ calculated for $C_{66}H_{84}O_4NaF_4Si_4Cl_2$, 1221.4658; found, 1221.4629.

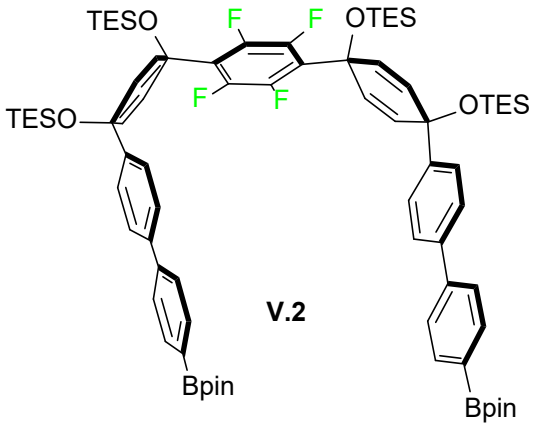

V.2

Synthesis of V.2. To a 100 mL flame-dried flask was added $Pd(OAc)_2$ (0.003 g, 0.029 mmol, 0.05 equiv), 2-dicyclohexylphosphino-2'6'dimethoxybiphenyl (0.015 g, 0.036 mmol, 0.125 equiv), bis(pinacolato)diboron (0.584 g, 2.30 mmol, 8 equiv), **V.S4** (0.353 g, 0.290 mmol, 1 equiv), and K_3PO_4 (0.228 g, 2.30 mmol, 8 equiv). After the solids were added, the flask was evacuated and backfilled with nitrogen 5 times. 1,4-dioxane (8.0 mL) was then added to the flask and the solution was sparged with N_2 for 10 minutes before being placed in an 80 °C oil bath overnight. The next day, the black solution was brought to room temperature and the solvent was removed under reduced pressure. To the resulting black solid was added H_2O (50 mL), followed by extraction with DCM (3 x 50 mL). The combined organic phases were then washed with water (3 x 50 mL), brine (1 x 100 mL), and then dried over sodium sulfate. After removing the solvent via rotary evaporation, the

resulting brown solid was washed with methanol, which after filtration afforded **V.2** as a white solid (0.374 g, 93%). ^{1}H NMR (500 MHz, Chloroform-*d*) δ 7.82 (d, *J* = 7.4 Hz, 4H), 7.52 (d, *J* = 7.4 Hz, 4H), 7.45 (d, *J* = 7.6 Hz, 4H), 7.33 (d, *J* = 7.9 Hz, 4H), 6.36 (d, *J* = 9.8 Hz, 4H), 6.01 (d, 8H), 1.35 (s, 24H), 0.98 (t, *J* = 7.9 Hz, 18H), 0.90 (t, *J* = 7.6 Hz, 18H), 0.67 (q, *J* = 7.9 Hz, 12H), 0.59 (q, *J* = 7.9 Hz, 12H). ^{13}C NMR (126 MHz, Chloroform-*d*) δ 144.66, 143.42, 139.71, 135.16, 133.07, 128.70, 126.93, 126.29, 125.79, 83.77, 71.25, 69.85, 24.88, 7.07, 6.80, 6.44, 6.19. ^{19}F NMR (471 MHz, Chloroform-*d*) δ -136.83 (s). δ HRMS (TOF, ES+) (m/z): [M+Na]+ calculated for $C_{78}H_{108}O_8NaB_2F_4Si_4$, 1405.7141; found, 1405.7137.

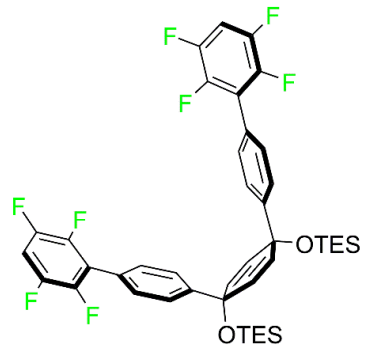

Synthesis of V.S3. To a 100 mL flame-dried flask was added diboronate[19] (0.224 g, 0.300 mmol, 1 equiv) and [1, 1'bis(diphenylphosphino)ferrocenedichloropalladium (0.022, 0.030 mmol, 0.100 equiv). After the solids were added, the flask was evacuated and backfilled with nitrogen 5 times. 1,4-dioxane (8.0 mL) was then added to the flask, followed by 1-bromo-2,3,5,6-tetrafluorobenzene (0.412 g, 1.80 mmol, 6 equiv), and the solution was sparged with N_2 for 10 minutes before 2M K_3PO_4 (0.825 mL, 1.65 mmol, 5.5 equiv), sparged for 1 h prior to use, was added. The solution was then placed in an 80 °C oil bath and allowed to stir overnight. The next day, the black solution was allowed to come to room temperature before removing the solvent under reduced pressure. Next, H_2O (50 mL)

was added, followed by extraction with hexanes (3 x 50 mL). The combined organic phases were then washed with water (3 x 50 mL), brine (1 x 75 mL), and dried over sodium sulfate. After removing the solvent via rotary evaporation, the crude, yellow-orange oil was purified via column chromatography (2-5% EtOAc/Hexanes) and **V.S3** was isolated as a pale-yellow oil (0.175 g, 74%). ^{1}H NMR (500 MHz, Chloroform-*d*) δ 7.47 (d, *J* = 7.7 Hz, 2H), 7.37 (d, *J* = 7.9 Hz, 2H), 7.04 (p, *J* = 8.4 Hz, 2H), 6.07 (s, 4H), 0.96 (t, *J* = 7.9 Hz, 18H), 0.64 (q, *J* = 7.8 Hz, 12H). ^{13}C NMR (126 MHz, Chloroform-*d*) δ 146.95, 131.58, 129.94, 126.12, 71.38, 7.03, 6.46. ^{19}F NMR (471 MHz, Chloroform-*d*) δ -139.24 (m, *J* = 22.4, 11.3 Hz), -143.81 (m, *J* = 21.1, 12.7, 7.4 Hz). δ HRMS (TOF, ES+) (m/z): [M+Na]+ calculated for $C_{42}H_{44}O_2NaF_8Si_2$, 811.2650; found, 811.2651.

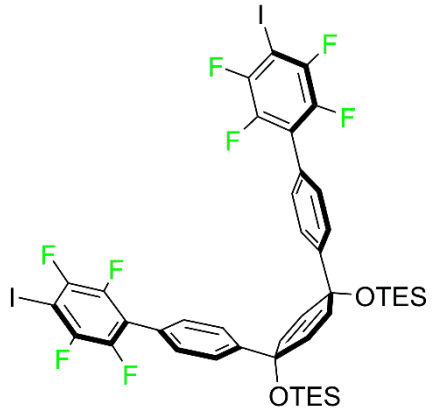

Synthesis of V.3. To a 250 mL flame-dried flask was added 20 mL THF and distilled diisopropylamine (0.093 mL, 0.666 mmol, 3 equiv). This solution was placed in a 0 °C ice bath and allowed to stir for 20 minutes before *n*-butyllithium (2.2 M in hexanes, 0.252 mL, 0.555 mmol, 2.5 equiv) was added dropwise. The solution was allowed to stir for 15 minutes before being transferred to a -78 °C dry ice bath, after which the solution was allowed to cool for 45 minutes. Next, **V.S3** (0.175 g, 0.222 mmol, 1 equiv), dissolved in minimal THF (approx. 2 mL), was added dropwise and the solution was allowed to stir for

10 minutes before I_2 (0.279 g, 1.11 mmol, 5 equiv.), dissolved in minimal THF (approx. 2 mL), was added quickly, turning the solution dark orange-brown. The solution was allowed to stir for 2 h before being quenched with concentrated $Na_2S_3O_3$ (approx. 100 mL), resulting in an off-white solution. The solution was brought under reduced pressure to remove THF and 50 mL of water was added, followed by a workup in EtOAc (3 x 50 mL). The combined organic phases were washed with water (3 x 50 mL), brine (1 x 50 mL), and dried over sodium sulfate. After removing the solvent via rotary evaporation, the crude yellow-brown oil was purified via column chromatography (10-25% DCM/Hexanes), resulting in a waxy clear oil. Washing with methanol then afforded **V.3** as a white powdery solid, which was collected via vacuum filtration (0.190 g, 82%). ^{1}H NMR (500 MHz, Chloroform-*d*) δ 7.47 (d, *J* = 8.2 Hz, 2H), 7.36 (d, *J* = 8.0 Hz, 2H), 6.07 (s, 4H), 0.95 (t, *J* = 7.9 Hz, 18H), 0.64 (q, *J* = 7.9 Hz, 12H). ^{13}C NMR (126 MHz, Chloroform-*d*) δ 147.16, 131.57, 129.87, 126.18, 71.38, 7.03, 6.46. ^{19}F NMR (471 MHz, Chloroform-*d*) δ -120.77 (m), -141.47 (m). δ HRMS (TOF, ES+) (m/z): [M]+ calculated for $C_{44}H_{41}O_2F_8Si_2I_2$, 1063.0607; found, 1063.0608.

5.4.4. Binding Affinity

Binding constants were determined via fluorescence quenching experiments as reported by the Yamago[53] groups. In a typical experiment, a solution of C_{60} in toluene (1.01×10^{-5} mol L^{-1}) was added to a solution of fluorinated nanohoop **V.5** in toluene (5.00×10^{-7} mol L^{-1}). The change in fluorescence emission intensity at 460 nm was then monitored for each addition.

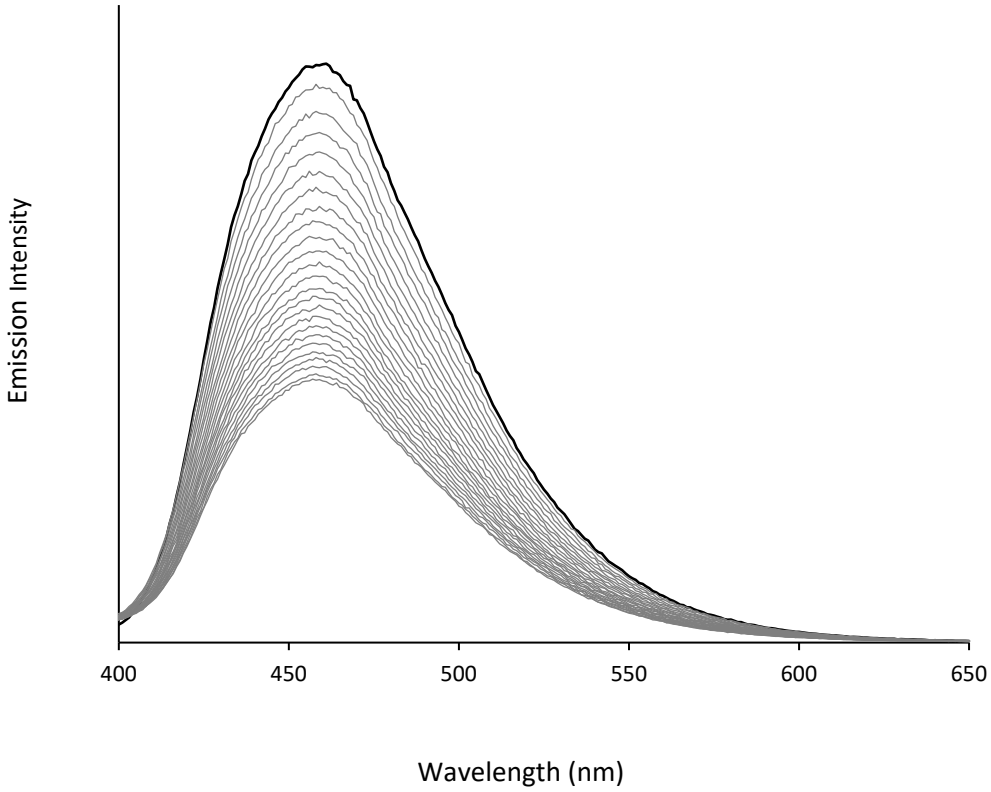

Figure 5.12. Change in emission intensity fluorinated nanohoop **V.5** with increasing concentration of C_{60}. The initial concentration of **V.5** was 5.00 X 10^{-7} mol L^{-1}, while the concentration of C_{60} was varied from 0.00 – 2.88 x 10^{-7} mol L^{-1}.

The Ka was then determined by fitting the data to following equation (1):

$$F/F_o=(1+ k_f/k_{sf} *K_a*[C_{60}])/(1+K_a*[C_{60}]) \quad (1)$$

Where F, F_o, k_f, k_s, K_a, $[C_{60}]$ is fluorescence intensity, fluorescence of fluorinated nanohoop **V.5** prior to the addition of C_{60}, a proportionality constant of the complex, a proportionality constant of the host, the binding constant of C_{60}, and the concentration of C_{60}, respectively. The data from **Figure 5.10** have been fit to equation 1 and are shown in **Figure 5.11**.

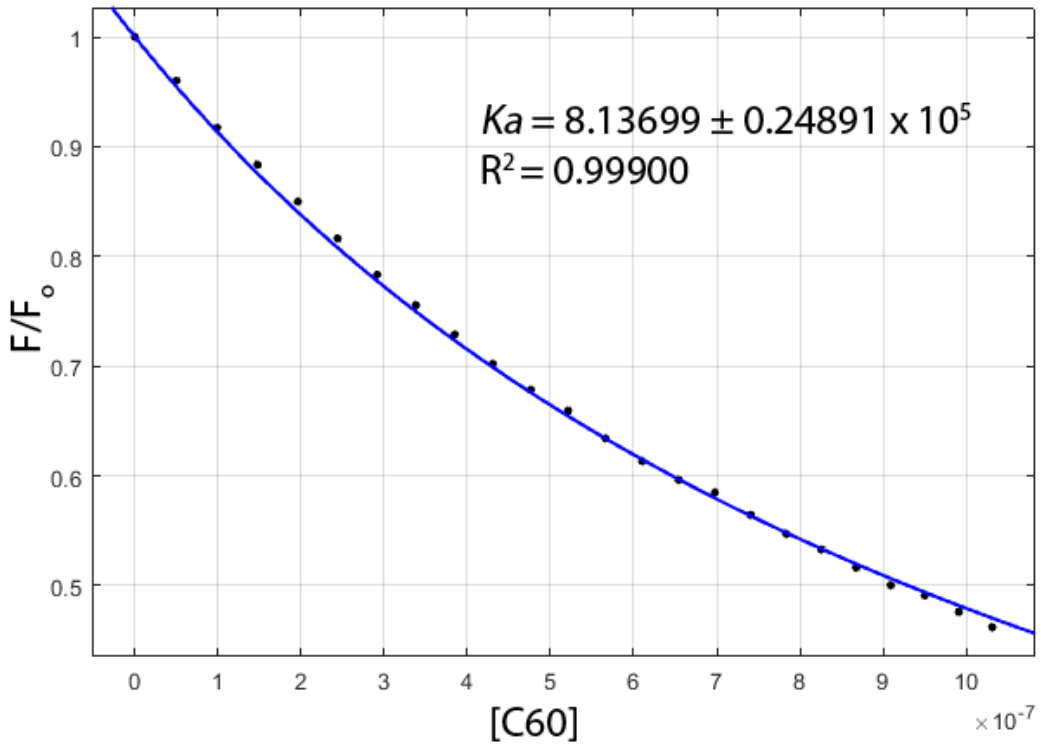

Figure 5.13. Correlation of [C_{60}] on the fluorescence intensity of fluorinated nanohoop **V.5** in toluene. The change in fluorescence at 460 nm (obtained from **Figure 5.10**) was fit to equation 1 to obtain the K_a.

5.4.5. Crystallographic Details

Crystallographic Data for **V.1**: $C_{77}H_{41}Cl_{15}F_{12}$, M = 1725.85, 0.13 x 0.02 x 0.02 mm, T = 173(2) K, Trigonal, space group *P*-3, a = 19.8149(6) Å, b = 19.8149(6) Å, c = 13.6041(6) Å, α = 90°, β = 90°, γ = 120°, V = 4625.8(3) Å^3, Z = 2, D_c = 1.239 Mg/m^3, μ(Cu) = 4.606 mm^{-1}, F(000) =1732,2θmax = 133.18°, 33778 reflections, 5443 independent reflections [R_{int} = 0.1426], R1 = 0.0829,wR2 = 0.2261 and GOF = 1.033 for 5443 reflections (313 parameters) with I>2(I), R1 = 0.1466, wR2 = 0.2475 and GOF = 1.033 for all reflections, max/min residual electron density +0.683/-0.594 eÅ^{-3}.

Crystallographic Data for **V.5**: $C_{84}H_{80}F_8O_6$, $C_{60}H_{32}F_8 \cdot 6(OC_4H_8)$, M = 1337.48, 0.12 x 0.08 x 0.05 mm, T = 173(2) K, Monolinic, space group $P2_1/c$, a = 13.4645(7) Å, b = 19.5258(12) Å, c = 26.8045(16) Å, β = 94.711(4)°, V = 7023.2(7) Å^3, Z = 4, D_c = 1.265 Mg/m^3, μ(Cu)= 0.764 mm^{-1}, F(000) = 2816, 2θmax = 98.79°, 26273 reflections, 7163 independent reflections [R_{int} = 0.0655], R1 = 0.0769, wR2 = 0.2115 and GOF = 1.021 for 7163 reflections (833 parameters) with I>2σ(I), R1 = 0.1071, wR2 = 0.2453 and GOF = 1.022 for all reflections, max/min residual electron density +0.559/-0.506 eÅ^{-3}.

Crystallographic Data for **V.6**: $C_{91}H_{84}Cl_8F_8$, $C_{72}H_{40}F_8 \cdot 4(CH_2Cl_2) \cdot 3(C_5H_{12})$, M = 1613.18, 0.15 x 0.08 x 0.03 mm, T = 173(2) K, Triclinic, space group *P*-1, a = 13.3910(4) Å, b = 20.0066(6) Å, c = 20.2292(6) Å, α = 119.204(2) °, β = 97.369(2) °, γ = 102.306(6) °, V = 4447.3(2) Å^3, Z = 2, D_c = 1.205 Mg/m^3, μ(Cu) = 2.795 mm^{-1}, F(000) = 1676, 2θmax = 133.39°, 61640 reflections, 15617 independent reflections [R_{int} = 0.0524], R1 = 0.0499, wR2 = 0.1240 and GOF = 1.045 for 15617 reflections (775 parameters) with I>2s(I), R1 = 0.0691, wR2 = 0.1313 and GOF = 1.045 for all reflections, max/min residual electron density +0.434/-0.404 eÅ^{-3}.

Crystallographic Data for **V.5**@C_{60}: $C_{150}H_{88}F_8O_4$, $C_{120}H_{32}F_8 \cdot 4(OC_4H_{10}) \cdot 2(C_7H_8)$, M = 2106.20, 0.12 x 0.06 x 0.02 mm, T = 173(2) K, Monolinic, space group $C2/c$, a = 25.1372(10) Å, b = 20.9252(9) Å, c = 19.7816(8) Å, β = 108.436(2)°, V = 9871.1(7) Å^3, Z = 4, D_c = 1.417 Mg/m^3, μ(Cu) = 0.759 mm^{-1}, F(000) = 4368, 2θmax = 133.13°, 39936 reflections, 8726 independent reflections [R_{int} = 0.0514], R1 = 0.0964, wR2 = 0.2870 and GOF = 1.030 for 8726 reflections (577 parameters) with I>2σ(I), R1 = 0.1143, wR2 =

0.3028 and GOF = 1.030 for all reflections, max/min residual electron density +1.271/-0.391 eÅ^{-3}.

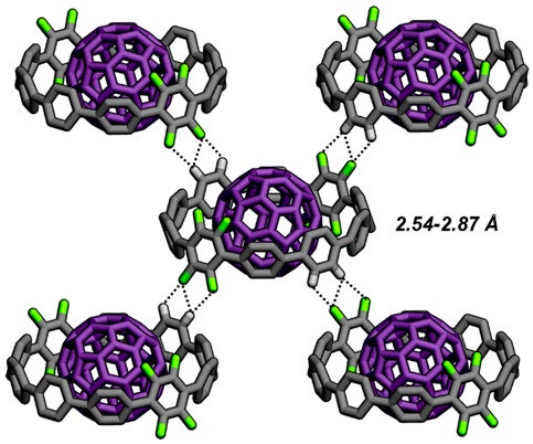

Figure 5.14. C—H---F interactions (dotted lines) observed in the crystal packing of **V.5**@C_{60}.

CONCLUDING REMARKS

In summary, the findings in this dissertation illustrate how heteroatoms such as nitrogen can be used a post-synthetic functional handle for nanohoop macrocycles. For example, through a combination of diameter changes and extent of *N*-alkylation, the electronic structure of can be fine-tuned. Additionally, by incorporating multiple nitrogen heteroatoms in the backbone of [8]CPP, initial investigations into nanohoop coordination complexes have been performed which highlight their potential as redox-active ligands or cylindrical building blocks metal organic frameworks. Since this initial report, the ability to use nanohoops as macrocyclic ligands has now been demonstrated via active metal template reactions. This result has lead to a variety of investigations into how these unique macrocycles can be employed as building blocks for new mechanically interlocked architectures. Ultimately, these reports provide a foundation for exploring how nanohoop

macrocycles can be combined with the principles of coordination chemistry to access a range of new molecular architectures with unusual properties.

REFERENCES CITED

Chapter I.

1. Böstrom, J.; Brown, D. G.; Young, R. J.; Këseru, G. M. Expanding the medicinal chemistry synthetic toolbox. *Nature Reviews Drug Discovery* **2018**, *17*, 709-727.
2. Erbas-Cakmak, S.; Leigh, D. A.; McTernan, C. T.; Nussbaumer, A. L. Artificial Molecular Machines. *Chem. Rev.*, **2015**, *115*, 10081-10206.
3. Lehn, J. M. Supramolecular Chemistry—Scope and Perspectives Molecules, Supermolecules, and Molecular Devices (Nobel Lecture). *Angew. Chem. Int. Ed.* **1988**, *27*, 89-112.
4. Cram, D. J. The Design of Molecular Hosts, Guests, and Their Complexes (Nobel Lecture). *Angew. Chem. Int. Ed.* **1988**, *27,* 1009-1020.
5. Pederson, C. J. The Discovery of Crown Ethers (Noble Lecture). *Angew. Chem. Int. Ed.* **1988**, *27*, 1021-1027.
6. De Volder, M.F.; Tawfick, S. H.; Baughman, A. J. Carbon nanotubes: present and future commercial applications. *Science* **2013**, *339*, 535–539.
7. Katsnelson, M. I. Graphene: carbon in two dimensions. *Mater. Today* **2007**, *10*, 20–27.
8. Novoselov, K. S.; Jiang, Z; Zhang, Y.; Morozov, S. V.; Stormer, H. L.; Zeitler, U.; Maan, J. C.; Boebinger, G. S.; Kim, P.; Geim, A. K. Room-Temperature Quantum Hall Effect in Graphene. *Science* **2007**, *315*, 1379.
9. Kroto, H. W.; Heath, J. R.; OQBrien, S. C.; Curl, R. F.; Smalley, R. E. C_{60}: Buckminsterfullerene. *Nature* **1985**, *318*, 162–163.

10. Segawa,Y.; Ito, H.; Itami, K. Structurally uniform and atomically precise carbon nanostructures. *Nat. Rev. Mater.* **2016**, *1*, 15002.

11. Narita, A.; Wang, X. Y.; Feng, X.; Mullen, K. New advances in nanographene chemistry. *Chem. Soc. Rev.* **2015**, *44*, 6616–6643.

12. Geim, A. K.; Novoselov, K. S. The rise of graphene. *Nat. Mater.* **2007** *6*, 183.

13. Majewski, M.; Stepien´, M. Bowls, Hoops, and Saddles: Synthetic Approaches to Curved Aromatic Molecules. *Angew. Chem. Int. Ed.* **2019**, *58*, 86 – 116.

14. Bols, P. S.; Anderson, H. A. Template-Directed Synthesis of Molecular Nanorings and Cages. *Acc. Chem. Res.* **2018**, *51*, 2083-2092.

15. Beves, J. E.; Blight, B. A.; Campbell, C. J.; Leigh, D. A.; Mcburney, R. T. Strategies and Tactics for the Metal-Directed Synthesis of Rotaxanes, Knots, Catenanes, and Higher Order Links. **2011**, *50*, 9260-9327.

16. Fielden, S. D. P.; Leigh, D. A.; Woltering, S. L. Molecular Knots. *Angew. Chem. Int. Ed.* **2017**, *56*, 11166 – 11194.

17. Dietrich-Buchecker, C.O.; Sauvage, J.P.; Kintzinger, J.P. Une nouvelle famille de molecules : les metallo-catenanes. **1983**, *24*, 5095-5098.

18. Wasserman, E. The Preparation of Interlocking Rings: A Catenane. *J. Am. Chem. Soc.* **1960**, *82*, 4433-4434.

19. Bäuerle, P.; Ammann, M.; Wilde, M.; Gçtz, G.; Rang, A.; Schalley, C. A.; Oligothiophene-Based Catenanes: Synthesis and Electronic Properties of a Novel Conjugated Topological Structure. *Angew. Chem. Int. Ed.* **2007**, *46*, 363 – 368.

20. Fan, Y.-Y.; Chen, D.; Huang, Z.; Zhu, J.; Tung, C.; Wu, L.; Cong, H. An isolable catenane consisting of two Möbius conjugatednanohoops. *Nat. Commun.* **2018**, *9*, 3037.

21. Aucagne, V.; Hanni, K. D.; Leigh, D. A.; Lusby, P. J.; Walker, D. B. Catalytic "Click" Rotaxanes: A Substoichiometric Metal-Template Pathway to Mechanically Interlocked Architectures. *J. Am. Chem. Soc.* **2006**, *128*, 2186 – 2187.

22. Denis, M.; Goldup, S. M. The active template approach to interlocked molecules. *Nat. Rev. Chem.* **2017**, *1*, 0061.

23. Movsisyan, L. D.; Franz, M.; Hampel, F.; Thomspon, A. L.; Tykwinski, R. R.; Anderson, H. A. Polyyne Rotaxanes: Stabilization by Encapsulation. *J. Am. Chem. Soc.* **2016**, *138*, 1366 – 1376.

24. Langton, M. J.; Matichak, J. D.; Thompson, A. L.; Anderson, H. L. Template-directed synthesis of π-conjugated porphyrin [2]rotaxanes and a [4]catenane based on a six-porphyrin nanoring. *Chem. Sci.* **2011**, *2*, 1897-1901.

25. Barran, P.E.; Cole, H.L.; Goldup, S.M.; Leigh, D. A.; McGonigal, P.R.; Symes, M.D.; Wu, J.; Zengerle, M. Active Metal Template Synthesis of a Molecular Trefoil Knot. *Angew. Chem. Int. Ed.*, **2011**, *50*, 12280-12284.

26. O'Sullivan, M.C.; Sprafke, J.K.; Kondratuk, D.V.; Rinfray, C.; Claridge, T.D.W.; Saywell, A.; Blunt, M.O.; O'Shea, J.N.; Beton, P.H.; Malfois, M.; Anderson, H.L. *Nature* **2011**, *469*, 72-75.

27. Hoffmann, M.; Wilson, C. J.; Odell, B.; Anderson, H. L. Template-Directed Synthesis of a π-Conjugated Porphyrin Nanoring. *Angew. Chem. Int. Ed.* **2007**, *46*, 3122-3125.

28. Hoffmann, H.; Kärnbratt, J.; Chang, M. H.; Herz, L. M.; Bo Albinsson, B.; Anderson, H. L. Enhanced π Conjugation around a Porphyrin[6] Nanoring. *Angew. Chem. Int. Ed.* **2008**, *47*, 4993-4996.

29. Peeks, M. D.; Claridge, T. D. W.; Anderson, H. L. Aromatic and antiaromatic ring currents in a molecular nanoring. *Nature* **2017**, *541*, 200-203.

30. Soya, T.; Kim, W.; Kim, D.; Osuka, A. Stable [48]-, [50]-, and [52]dodecaphyrins(1.1.0.1.1.0.1.1.0.1.1.0): the largest Hückel aromatic molecules. *Chem. Eur. J.* **2015**, *21*, 8341–8346.

31. Odell, B.; Reddington, M. V.; Slawin, A. M. Z.; Spencer, N.; Stoddart, J. F.; Williams, D. J. Cyclobis(paraquat-p-phenylene). A Tetracationic Multipurpose Receptor. *Angew. Chem. Int. Ed.***1988**, *27*, 1547-1550.

32. Dale, E. J.; Vermeulen, N. A.; Juríček, M.; Barnes, J. C.; Young, R. M.; Wasielewski, M. R.; Stoddart, J. F. Supramolecular explorations: Exhibiting the extent of extended cationic cyclophanes. *Acc. Chem. Res.* **2016**, *49*, 262-273.

33. Ashton, P. R.; Goodnew, T. T.; Kaifer, A. E.; Reddington, M. V.; Slawin, A. M. Z.; Spencer, N.; Stoddart, J. F.; Vincet, C.; Williams, D. J. A [2]Catenane Made to Order. *Angew. Chem. Int. Ed.* **1989**, *28*, 1396-1399.

34. Anelli, P. R.; Spencer, N.; Stoddart, J. F. A molecular shuttle. *J. Am. Chem. Soc.* **1991**, *113*, 5131-5133.

35. Ogoshi, T.; Kanai, S.; Fujinami, S.; Yamagishi, T.; Nakamoto, Y. para-Bridged Symmetrical Pillar[5]arenes: Their Lewis Acid Catalyzed Synthesis and Host–Guest Property. *J. Am. Chem. Soc.* **2008**, *130*, 5022-5023.

36. Ogoshi, T.; Takamichi, A.; Kitajima, K.; Fujinami, S.; Yamagishi, T.; Nakamoto, Y. Facile, Rapid, and High-Yield Synthesis of Pillar[5]arene from Commercially Available Reagents and Its X-ray Crystal Structure. *J. Org. Chem.* **2010**, *76*, 328-331.

37. Li, Y.; Flood, A. H. Pure C–H Hydrogen Bonding to Chloride Ions: A Preorganized and Rigid Macrocyclic Receptor. *Angew. Chem. Int. Ed.* **2008**, *47*, 2649-2652.

38. Liu, Y.; Zhao, W.; Chen, C. H.; Flood, A. H. Chloride capture using a C–H hydrogen-bonding cage. *Science* **2019**, *365*, 159-161.

39. Lee, S.; Chen, C. H.; Flood, A. H. A pentagonal cyanostar macrocycle with cyanostilbene CH donors binds anions and forms dialkylphosphate [3]rotaxanes. *Nat. Chem.* **2013**, *5*, 704-710.

40. Parekh, V. C.; Guha, P. C. *J. Indian Chem. Soc.* **1934**, *11*, 95.

41. Evans, P. J.; Darzi, E. R.; Jasti, R. Efficient Room-Temperature Synthesis of a Highly Strained Carbon Nanohoop Fragment of Buckminsterfullerene. *Nat. Chem.* **2014**, *6*, 404-408.

42. Jasti, R.; Bhattacharjee, J.; Neaton, J. B.; Bertozzi, C. R.; Synthesis, Characterization, and Theory of [9]-, [12]-, and [18]Cycloparaphenylene: Carbon Nanohoop Structures. *J. Am. Chem. Soc.*, **2008**, *130*, 17646–17647.

43. Darzi, E. R.; Jasti, R. The dynamic, size-dependent properties of [5]–[12]cycloparaphenylenes. *Chem. Soc. Rev.*, **2015**, *44*, 6401– 6410.

44. Segawa, Y.; Miyamoto, S.; Omachi, H.; Matsuura, S.; Šenel, P.; Sasamori, T.; Tokitoh, N.; Itami, K. Concise synthesis and crystal structure of [12]cycloparaphenylene. *Angew. Chem., Int. Ed.,* **2011**, *50*, 3244–3248.

45. Yamago, S.; Watanabe, Y.; Iwamoto, T. Synthesis of [8]Cycloparaphenylene from a Square Shaped Tetranuclear Platinum Complex. *Angew. Chem. Int. Ed.* **2010**, *49*, 757-759.

46. Kayahara, E.; Kouyama, T.; Kato, T.; Takaya, H.; Yasuda, N.; Yamago, S. Isolation and Characterization of the Cycloparaphenylene Radical Cation and Dication. *Angew. Chem. Int. Ed.* **2013**, *52*, 13722-13726.

47. Golder, M. R.; Wong, B. M.; Jasti, R. Photophysical and theoretical investigations of the [8]cycloparaphenylene radical cation and its charge-resonance dimer. *Chem. Sci.* **2013**, *11*, 4285-4291.

48. Toriumi, N.; Muranaka, A.; Kayahara, E.; Yamago, S.; Uchiyama, M. In-Plane Aromaticity in Cycloparaphenylene Dications: A Magnetic Circular Dichroism and Theoretical Study. *J. Am. Chem. Soc.* **2015**, *137*, 82-85.

49. Kayahara, E.; Sun, L.; Onishi, H.; Suzuki, K.; Fukushima, T.; Sawada, A.; Kaji, H.; Yamago, S. Gram-Scale Syntheses and Conductivities of [10]Cycloparaphenylene and Its Tetraalkoxy Derivatives. *J. Am. Chem. Soc.* **2017**, *139*, 18480 – 18483.

50. Iwamoto, T.; Watanabe, Y.; Sadahiro, T.; Haino, T.; Yamago, S. Size-selective encapsulation of C_{60} by [10]cycloparaphenylene: formation of the shortest fullerene-peapod. *Angew. Chem., Int. Ed.* **2011**, *50*, 8342−8344.

51. Kawase, T.; Tanaka, K.; Shiono, N.; Seirai, Y.; Oda, M. Onion-Type Complexation Based on Carbon Nanorings and a Buckminsterfullerene. *Angew. Chem. Int. Ed.* **2004**, *43*, 1722-1724.

52. Lee, S.; Chenard, E.; Gray, D.; Moore, J. S. Synthesis of Cycloparaphenyleneacetylene via Alkyne Metathesis: C70 Complexation and Copper-Free Triple Click Reaction. *J. Am. Chem. Soc.* **2016**, *138*, 13814-13817.

53. Huang, Q.; Zhuang, G.; Jia, H.; Qian, M.; Cui, S.; Yang, S.; Du, P. Photoconductive Curved-Nanographene/Fullerene Supramolecular Heterojunctions. *Angew. Chem. Int. Ed.* **2019**, *58*, 6244-6249.

54. Xu, Y.; von Delius, M. The Supramolecular Chemistry of Strained Carbon Nanohoops. *Angew. Chem. Int. Ed.* **2019**, *Accepted Article*

55. Xu, Y.; Kaur, R.; Wang, B.; Minameyer, M. B.; Gsanger, S.; Meyer, B.; Drewello, T.; Guldi, D. M.; von Delius, M. Concave–Convex π–π Template Approach Enables the Synthesis of [10]Cycloparaphenylene–Fullerene [2]Rotaxanes. *J. Am. Chem. Soc.* **2018**, *140*, 13413-13420.

Chapter II.

1. Izuhara, D.; Swager, T. M. Bispyridinium-phenylene-based copolymers: low band gap n-type alternating copolymers. *J. Mater. Chem.*, **2011**, *21*, 3579.

2. Anthony, J. E. Functionalized Acenes and Heteroacenes for Organic Electronics *Chem. Rev.,* **2006**, *106*, 5028–5048.

3. McQuade, D.T.; Pullen, A. E.; Swager, T.M., Conjugated polymer-based chemical sensors. *Chem. Rev.*, **2000**, *100*, 2537–2574.

4. Lewis, S. E. Cycloparaphenylenes and related nanohoops. *Chem. Soc. Rev.*, **2015**, *44*, 2221–2304.

5. Jasti, R.; Bhattacharjee, J.; Neaton, J. B.; Bertozzi, C. R.; Synthesis, Characterization, and Theory of [9]-, [12]-, and [18]Cycloparaphenylene: Carbon Nanohoop Structures. *J. Am. Chem. Soc.*, **2008**, *130*, 17646–17647.

6. Golder, M. R.; Jasti, R. Syntheses of the smallest carbon nanohoops and the emergence of unique physical phenomena. *Acc. Chem. Res.*, **2015**, *48*, 557– 566.

7. Omachi, H.; Segawa, Y.; Itami, K. Synthesis of cycloparaphenylenes and related carbon nanorings: a step toward the controlled synthesis of carbon nanotubes. *Acc. Chem. Res.*, **2012**, *45*, 1378–1389.

8. Darzi, E. R.; Jasti, R. The dynamic, size-dependent properties of [5]–[12]cycloparaphenylenes. *Chem. Soc. Rev.*, **2015**, *44*, 6401– 6410.

9. Darzi, E. R.; Hirst, E. S.; Weber, C. D.; Zakharov, L. N.; Lonergan, M. C.; Jasti, R. Synthesis, Properties, and Design Principles of Donor-Acceptor Nanohoops. *ACS Cent. Sci.*, **2015**, *1*, 335– 342.

10. Ball, M.; Fowler, B.; Li, P.; Joyce, L. A.; Li, F.; Liu, T.; Paley, D.; Zhong, Y.; Li, H.; Xiao, S.; Ng, F.; Steigerwald, M. L.; Nuckolls, C. Chiral Conjugated Corrals. *J. Am. Chem. Soc.*, **2015**, *137*, 9982–9987

11. Kuwabara, T.; Orii, J.; Segawa, Y.; Itami, K. Curved Oligophenylenes as Donors in Shape-Persistent Donor–Acceptor Macrocycles with Solvatofluorochromic Properties. *Angew. Chem., Int., Ed.*, **2015**, *54*, 9646–9649.

12. Paraknowitsch, J. P.; Thomas, A. Doping carbons beyond nitrogen: an overview of advanced heteroatom doped carbons with boron, sulphur and phosphorus for energy applications. *Energy Environ. Sci.*, **2013**, *6*, 2839–2855.

13. Cheng, M.; Yang, X.; Zhang, F.; Zhao, J.; Sun, L. Tuning the HOMO and LUMO Energy Levels of Organic Dyes with N-Carboxomethylpyridinium as Acceptor To Optimize the Efficiency of Dye-Sensitized Solar Cells. *J. Phys. Chem. C*, **2013**, *117*, 9076–9083

14. Matsui, K.; Segawa, Y.; Itami, K. Synthesis and Properties of Cycloparaphenylene-2,5-pyridylidene: A Nitrogen-Containing Carbon Nanoring. *Org. Lett.*, **2012**, *14*, 1888–1891

15. Segawa, Y.; Omachi, H.; Itami, K. Theoretical Studies on the Structures and Strain Energies of Cycloparaphenylenes. *Org. Lett.*, **2010**, *12*, 2262–2265

16. Evans, R. J.; Darzi, E. R.; Jasti, R. Efficient room-temperature synthesis of a highly strained carbon nanohoop fragment of buckminsterfullerene. *Nat. Chem.*, **2014**, *6*, 404–408.

17. Xia, J.; R. Synthesis, Characterization, and Crystal Structure of [6]Cycloparaphenylene. *Angew. Chem., Int. Ed.*, **2012**, *51*, 2474– 2476.

18. M. J. Frisch et al., Gaussian 09, Revision B.01, Wallingford, CT, **2009**

19. Méndez-Hernández, D. D.; Gillmore, J. G.; Montano, L. A.; Gust, D.; Moore, T. A.; Moore, A. L.; Mujica, V. Tuning ligand field strength with pendent Lewis acids: access to high spin iron hydrides. *J. Phys. Org. Chem.*, **2015**, *28*, 320–328.

20. Iwamoto, T.; Watanabe, Y.; Sakamoto, Y.; Suzuki, T.; Yamago, S. Selective and Random Syntheses of [n]Cycloparaphenylenes (n = 8–13) and Size Dependence of Their Electronic Properties. *J. Am. Chem. Soc.*, **2011**, *133*, 8354–8361.

21. Segawa, Y.; Fukazawa, A.; Matsuura, S.; Omachi, H.; Yamaguchi, S.; Irle, S.; Itami, K. Combined experimental and theoretical studies on the photophysical properties of cycloparaphenylenes. *Org. Biomol. Chem.*, **2012**, *10*, 5979.

22. Ball, M.; Nuckolls, C. Stepping into the Light: Conjugated Macrocycles with Donor–Acceptor Motifs. *ACS Cent. Sci.*, **2015**, *1*, 416–417.

23. Adamska, L.; Nayyar, I.; Chen, H.; Swan, A. K.; Oldani, N.; Fernandez-Alberti, S.; Golder, M. R.; Jasti, R.; Doorn, S. K.; Tretiak, S. Self-Trapping of Excitons, Violation of Condon Approximation, and Efficient Fluorescence in Conjugated Cycloparaphenylenes. *Nano Lett.*, **2014**, *14*, 6539–6546.

24. Segawa, Y.; Miyamoto, S.; Omachi, H.; Matsuura, S.; Šenel, P.; Sasamori, T.; Tokitoh, N.; Itami, K. Concise synthesis and crystal structure of [12]cycloparaphenylene. *Angew. Chem., Int. Ed.,* **2011**, *50*, 3244–3248.

25. Xia, J.; Bacon, J. W.; Jasti, R. Gram-scale synthesis and crystal structures of [8]- and [10]CPP, and the solid-state structure of C60@[10]CPP. *Chem. Sci.*, **2012**, *3*, 3018.

26. Kayahara, E.; Iwamoto, T.; Suzuki, T.; Yamago, S. Selective Synthesis of [6]-, [8]-, and [10]Cycloparaphenylenes. *Chem. Lett.*, **2013**, *42*, 621–623.

27. Kayahara, E.; Patel, V. K.; Xia, J.; Jasti, R.; Yamago, S. Selective and Gram-Scale Synthesis of [6]Cycloparaphenylene. *Synlett*, **2015**, *26*, 1615–1619.

Chapter III.

1. Jørgensen, C. K. Differences between the four halide ligands, and discussion remarks on trigonal-bipyramidal complexes, on oxidation states, and on diagonal elements of one-electron energy. *Coord. Chem. Rev.* **1966**, *1*, 164−178.

2. Lyaskovskyy, V.; de Bruin, B. Redox Non-Innocent Ligands: Versatile New Tools to Control Catalytic Reactions. *ACS Catal.* **2012**, *2*, 270−279.

3. Boyer, J. L.; Rochford, J.; Tsai, M.-K.; Muckerman, J. T.; Fujita, E. Ruthenium complexes with non-innocent ligands. *Coord. Chem. Rev.* **2010**, *254*, 309−330.

4. Chen, T. H.; Popov, I.; Kaveevivitchai, W.; Miljanic, O. S˙ˇ. Metal–Organic Frameworks: Rise of the Ligands. *Chem. Mater.* **2014**, *26*, 4322−4325.

5. Almeida Paz, F. A.; Klinowski, J.; Vilela, S. M. F.; Tome, J. P. C.; Cavaleiro, J. A. S.; Rocha, J.˙ Ligand design for functional metal–organic frameworks. *Chem. Soc. Rev.* **2012**, *41*, 1088−1110.

6. Pluth, M. D.; Bergman, R. G.; Raymond, K. N. Acid catalysis in basic solution: a supramolecular host promotes orthoformate hydrolysis. *Science* **2007**, *316*, 85−88.

7. Vermeulen, N. A.; Karagiaridi, O.; Sarjeant, A. A.; Stern, C. L.; Hupp, J. T.; Farha, O. K.; Stoddart, J. F. Aromatizing Olefin Metathesis by Ligand Isolation inside a Metal– Organic Framework. *J. Am. Chem. Soc.* **2013**, *135*, 14916−14919.

8. Stavila, V.; Talin, A. A.; Allendorf, M. D. MOF-based electronic and opto-electronic devices. *Chem. Soc. Rev.* **2014**, *43*, 5994−6010.

9. Kishi, N.; Li, Z.; Yoza, K.; Akita, M.; Yoshizawa, M. An M2L4 Molecular Capsule with an Anthracene Shell: Encapsulation of Large Guests up to 1 nm. *J. Am. Chem. Soc.* **2011**, *133*, 11438−11441.

10. Mal, P.; Breiner, B.; Rissanen, K.; Nitschke, J. R. White Phosphorus Is Air-Stable Within a Self-Assembled Tetrahedral Capsule. *Science* **2009**, *324*, 1697−1699.

11. Sun, L.; Campbell, M. G.; Dinca, M.˘Electrically Conductive Porous Metal-Organic Frameworks. *Angew. Chem., Int. Ed.* **2016**, *55*, 3566−3579.

12. Jasti, R.; Bhattacharjee, J.; Neaton, J. B.; Bertozzi, C. R. Synthesis, Characterization, and Theory of [9]-, [12]-, and [18]Cycloparaphenylene: Carbon Nanohoop Structures. *J. Am. Chem. Soc.* **2008**, *130*, 17646−17647.

13. Darzi, E. R.; Jasti, R. The dynamic, size-dependent properties of [5]–[12]cycloparaphenylenes. *Chem. Soc. Rev.* **2015**, *44*, 6401−6410.

14. Darzi, E. R.; Hirst, E. S.; Weber, C. D.; Zakharov, L. N.; Lonergan, M. C.; Jasti, R. Synthesis, properties, and design principles of donor-acceptor nanohoops. *ACS Cent. Sci.* **2015**, *1*, 335−342.

15. Patel, V. K.; Kayahara, E.; Yamago, S. Chem. - Eur. J. 2015, 21, 5742−5749

16. Kayahara, E.; Patel, V. K.; Yamago, S. Synthesis and Characterization of [5]Cycloparaphenylene. *J. Am. Chem. Soc.* **2014**, *136*, 2284−2287.

17. Darzi, E. R.; Sisto, T. J.; Jasti, R. Selective Syntheses of [7]–[12]Cycloparaphenylenes Using Orthogonal Suzuki–Miyaura Cross-Coupling Reactions. *J. Org. Chem.* **2012**, *77*, 6624−6628.

18. Iwamoto, T.; Watanabe, Y.; Sadahiro, T.; Haino, T.; Yamago, S. Size-selective encapsulation of C_{60} by [10]cycloparaphenylene: formation of the shortest fullerene-peapod. *Angew. Chem., Int. Ed.* **2011**, *50*, 8342−8344.

19. Xia, J.; Bacon, J. W.; Jasti, R. Gram-scale synthesis and crystal structures of [8]- and [10]CPP, and the solid-state structure of C_{60}@[10]CPP. *Chem. Sci.* **2012**, *3*, 3018−2021.

20. Iwamoto, T.; Slanina, Z.; Mizorogi, N.; Guo, J.; Akasaka, T.; Nagase, S.; Takaya, H.; Yasuda, N.; Kato, T.; Yamago, S. Partial Charge Transfer in Shortest Possible Metallofullerene Peapod, La@C82⊂[11]Cycloparaphenylene. *Chem. - Eur. J.* **2014**, *20*, 14403−14409.

21. Ueno, H.; Nishihara, T.; Segawa, Y.; Itami, K. Cycloparaphenylene-based ionic donor-acceptor supramolecule: isolation and characterization of Li^{+}@C60⊂[10]CPP. *Angew. Chem., Int. Ed.* **2015**, *54*, 3707−3711.

22. Ball, M.; Nuckolls, C. Stepping into the Light: Conjugated Macrocycles with Donor–Acceptor Motifs. *ACS Cent. Sci.* **2015**, *1*, 416−417.

23. Neuhaus, P.; Cnossen, A.; Gong, J. Q.; Herz, L. M.; Anderson, H. L. A Molecular Nanotube with Three-Dimensional π-Conjugation. *Angew. Chem., Int. Ed.* **2015**, *54*, 7344−7348.

24. Ball, M.; Fowler, B.; Li, P.; Joyce, L. A.; Li, F.; Liu, T.; Paley, D.; Zhong, Y.; Li, H.; Xiao, S.; Ng, F.; Steigerwald, M. L.; Nuckolls, C. Chiral Conjugated Corrals. *J. Am. Chem. Soc.* **2015**, *137*, 9982−9987

25. Ball, M.; Zhong, Y.; Fowler, B.; Zhang, B.; Li, P.; Etkin, G.; Paley, D. W.; Decatur, J.; Dalsania, A. K.; Li, H.; Xiao, S.; Ng, F.; Steigerwald, M. L.; Nuckolls, C. Rigid, Conjugated Macrocycles for High Performance Organic Photodetectors. *J. Am. Chem. Soc.* **2016**, *138*, 12861−12867

26. Kayahara, E.; Patel, V. K.; Mercier, A.; Kü ndig, E. P.; Yamago, S. Regioselective Synthesis and Characterization of Multinuclear Convex-bounded Ruthenium-[n]Cycloparaphenylene (n = 5 and 6) Complexes. *Angew. Chem., Int. Ed.* **2016**, *55*, 302−306.

27. Kubota, N.; Segawa, Y.; Itami, K. η^6-Cycloparaphenylene Transition Metal Complexes: Synthesis, Structure, Photophysical Properties, and Application to the Selective Monofunctionalization of Cycloparaphenylenes. *J. Am. Chem. Soc.* **2015**, *137*, 1356−1361.

28. Matsui, K.; Segawa, Y.; Itami, K. Synthesis and Properties of Cycloparaphenylene-2,5-pyridylidene: A Nitrogen-Containing Carbon Nanoring. *Org. Lett.* **2012**, *14*, 1888−1891.

29. Dick, G. R.; Woerly, E. M.; Burke, M. D. A General Solution for the 2-Pyridyl Problem. *Angew. Chem., Int. Ed.* **2012**, *51*, 2667−2672.

30. Cox, P. A.; Leach, A. G.; Campbell, A. D.; Lloyd-Jones, G. C. Protodeboronation of Heteroaromatic, Vinyl, and Cyclopropyl Boronic Acids: pH–Rate Profiles, Autocatalysis, and Disproportionation. *J. Am. Chem. Soc.* **2016**, *138*, 9145−9157.

31. Colon, I.; Kelsey, D. R. Coupling of aryl chlorides by nickel and reducing metals. *J. Org. Chem.* **1986**, *51*, 2627−2637.

32. Iyoda, M.; Otsuka, H.; Sato, K.; Nisato, N.; Oda, M. Homocoupling of Aryl Halides Using Nickel(II) Complex and Zinc in the Presence of Et4NI. An Efficient Method for the Synthesis of Biaryls and Bipyridines. *Bull. Chem. Soc. Jpn.* **1990**, *63*, 80−87.

33. Lewis, J. E. M.; Bordoli, R. J.; Denis, M.; Fletcher, C. J.; Galli, M.; Neal, E. A.; Rochette, E. M.; Goldup, S. M. High yielding synthesis of 2,2′-bipyridine macrocycles, versatile intermediates in the synthesis of rotaxanes. *Chem. Sci.* **2016**, *7*, 3154−3161.

34. Colquhoun, H. M.; Zhu, Z.; Dudman, C. C.; O'Mahoney, C. A.; Williams, D. J.; Drew, M. G. B. Synthesis of Strained Macrocyclic Biaryls for Enthalpy-Driven Ring-Opening Polymerization. *Macromolecules* **2005**, *38*, 10413−10420.

35. Milani, B.; Anzilutti, A.; Vicentini, L.; Sessanta o Santi, A.; Zangrando, E.; Geremia, S.; Mestroni, G. Palladium Complexes Containing Large Fused Aromatic N−N Ligands as Efficient Catalysts for the CO/Styrene Copolymerization. *Organometallics* **1997**, *16*, 5064−5075.

36. Prier, C. K.; Rankic, D. A.; MacMillan, D. W. C. Visible Light Photoredox Catalysis with Transition Metal Complexes: Applications in Organic Synthesis. *Chem. Rev.* **2013**, *113*, 5322−5363.

Chapter IV.

1. De Volder, M.F.; Tawfick, S. H.; Baughman, A. J. Carbon nanotubes: present and future commercial applications. *Science* **2013**, *339*, 535–539.

2. Katsnelson, M. I. Graphene: carbon in two dimensions. *Mater. Today* **2007**, *10*, 20–27.

3. Novoselov, K. S.; Jiang, Z; Zhang, Y.; Morozov, S. V.; Stormer, H. L.; Zeitler, U.; Maan, J. C.; Boebinger, G. S.; Kim, P.; Geim, A. K. Room-Temperature Quantum Hall Effect in Graphene. *Science* **2007**, *315*, 1379.

4. Kroto, H. W.; Heath, J. R.; OQBrien, S. C.; Curl, R. F.; Smalley, R. E. C_{60}: Buckminsterfullerene. *Nature* **1985**, *318*, 162–163.

5. Segawa,Y.; Ito, H.; Itami, K. Structurally uniform and atomically precise carbon nanostructures. *Nat. Rev. Mater.* **2016**, *1*, 15002.

6. Narita, A.; Wang, X. Y.; Feng, X.; Mullen, K. New advances in nanographene chemistry. *Chem. Soc. Rev.* **2015**, *44*, 6616–6643.

7. Jasti, R.; Bhattacharjee, J.; Neaton, J. B.; Bertozzi, C. R. Synthesis, Characterization, and Theory of [9]-, [12]-, and [18]Cycloparaphenylene: Carbon Nanohoop Structures. *J. Am. Chem. Soc.* **2008**, *130*, 17646–17647.

8. Golder, M. R.; Jasti, R. Selective Synthesis of Strained [7]Cycloparaphenylene: An Orange-Emitting Fluorophore. *Acc. Chem. Res.* **2015**, *48*, 557–566.

9. Darzi, E.R.; Jasti, R. The dynamic, size-dependent properties of [5]–[12]cycloparaphenylenes. *Chem. Soc. Rev.* **2015**, *44*, 6401 – 6410.

10. Lewis, S. E. Cycloparaphenylenes and related nanohoops. *Chem. Soc. Rev.* **2015**, *44*, 2221 – 2304.

11. Majewski, M.; Stepien´, M. Bowls, Hoops, and Saddles: Synthetic Approaches to Curved Aromatic Molecules. *Angew. Chem. Int. Ed.* **2019**, *58*, 86 – 116.

12. Povie, G.; Segawa, Y.; Nishihara, T.; Miyauchi, Y.; Itami, K. Synthesis of a carbon nanobelt. *Science* **2017**, *356*, 172 – 175.

13. Iwamoto, T.; Watanabe, Y.; Sakamoto, Y.; Suzuki, T.; Yamago, S. Selective and Random Syntheses of [n]Cycloparaphenylenes (n = 8–13) and Size Dependence of Their Electronic Properties. *J. Am. Chem. Soc.* **2011**, *133*, 8354 – 8361.

14. Lin, J. B.; Darzi, E. D.; Jasti, R.; Yavuz, I.; Houk, K. N. Solid-State Order and Charge Mobility in [5]- to [12]Cycloparaphenylenes. *J. Am. Chem. Soc.* **2019**, *141*, 952 – 960.

15. Darzi, E. D.; Hirst, E. S.; Weber, C. D.; Zakharov, L. N.; Lonergan, R. Jasti, M. C. Synthesis, Properties, and Design Principles of Donor-Acceptor Nanohoops. *ACS Cent. Sci.* **2015**, *1*, 335 – 342.

16. Van Raden, J. M.; Darzi, E. D.; Zakharov, L. N.; Jasti, R. Synthesis and characterization of a highly strained donor–acceptor nanohoop. *Org. Biomol. Chem.* **2016**, *14*, 5721 – 5727.

17. Van Raden, J. M.; Louie, S.; Zakharov, L. N.; Jasti, R. . 2,2'-Bipyridyl-embedded Cycloparaphenylenes as a General Strategy to Investigate Nanohoop-based Coordination Complexes. *J. Am. Chem. Soc.* **2017**, *139*, 2936 – 2939.

18. Hashimoto, S.; Kayahara, E.; Mizuhata, Y.; Tokitoh, N.; Takeuchi, F. Ozawa, K.; Yamago, S. Synthesis and Physical Properties of Polyfluorinated Cycloparaphenylenes. *Org. Lett.* **2018**, *20*, 5973 – 5976.

19. Leonhardt, E. J.; Van Raden, J. M.; Miller, D. J.; Zakharov, L. N.; Aleman, B. J.; Jasti, R. A Bottom-Up Approach to Solution-Processed, Atomically Precise Graphitic Cylinders on Graphite. *Nano Lett.* **2018**, *18*, 7991 – 7997.

20. Schaub, T. A.; Margraf, J. T.; Zakharov, L. N.; Reuter, K.; Jasti, R. Strain-Promoted Reactivity of Alkyne-Containing Cycloparaphenylenes. *Angew. Chem. Int. Ed.* **2018**, *57*, 16348 – 16353.

21. Kayahara, E.; Patel, V. K.; Mercier, A.; Kundig, E. P.; Yamago, S. Regioselective Synthesis and Characterization of Multinuclear Convex-bounded Ruthenium-[n]Cycloparaphenylene (n = 5 and 6) Complexes. *Angew. Chem. Int. Ed.* **2016**, *55*, 302 – 306.

22. Kubota, N.; Segawa, Y.; Itami, K. η^6-Cycloparaphenylene Transition Metal Complexes: Synthesis, Structure, Photophysical Properties, and Application to the Selective Monofunctionalization of Cycloparaphenylenes. *J. Am. Chem. Soc.* **2015**, *137*, 1356 – 1361.

23. White, B. M.; Zhao, Y.; Kawashima, T. E.; Branchaud, B. P.; Pluth, M. D.; Jasti, R. Expanding the Chemical Space of Biocompatible Fluorophores: Nanohoops in Cells. *ACS Cent. Sci.* **2018**, *4*, 1173 – 1178.

24. Patel, V. K.; Kayahara, E.S.; Yamago, S. Practical Synthesis for [n]Cycloparaphenylenes (n = 5, 7-12) by H2SnCl4-Mediated Aromatization of 1,4-Dihydroxylcyclo-2,5-diene Precursors. *Chem. Eur. J.* **2015**, *21*, 5742 – 5749.

25. Adamska, L.; Nayyar, L.; Chen, H.; Swan, A. K.; Oldani, N.; Fernandex-Alberti, S.; Golder, M. R.; Jasti, R.; Doorn, S. K.; Tretiak, S. Self-Trapping of Excitons, Violation of Condon Approximation, and Efficient Fluorescence in Conjugated Cycloparaphenylenes. *Nano Lett.* **2014**, *14*, 6539 – 6546.

26. Iwamoto, T.; Watanabe, Y.; Sadahiro, T.; Haino, T.; Yamago, S. Size-selective encapsulation of C60 by [10]cycloparaphenylene: formation of the shortest fullerene-peapod. *Angew. Chem. Int. Ed.* **2011**, *50*, 8342 – 8344.

27. Ball, M.; Zhong, Y.; Fowler, B.; Zhang, B.; Li, P.; Etkin, G.; Paley, D. W.; Decatur, J.; Dalsania, A. K.; Li, H.; Xiao, S.; Ng, F.; Steigerwald, M. L.; Nuckolls, C. Macrocyclization in the Design of Organic n-Type Electronic Materials. *J. Am. Chem. Soc.* **2016**, *138*, 12861 – 12867.

28. Kayahara, E.; Sun, L.; Onishi, H.; Suzuki, K.; Fukushima, T.; Sawada, A.; Kaji, H.; Yamago, S. Gram-Scale Syntheses and Conductivities of [10]Cycloparaphenylene and Its Tetraalkoxy Derivatives. *J. Am. Chem. Soc.* **2017**, *139*, 18480 – 18483.

29. Lovell, T.; Colwell, C.; Zakharov, L. N.; Jasti, R. Symmetry breaking and the turn-on fluorescence of small, highly strained carbon nanohoops. *Chem. Sci.* **2019**, *10*, 3786 – 3790.

30. Bruns, C. J.; Stoddart, J. F.; The Nature of the Mechanical Bond: From Molecules to Machines, Wiley-VCH, Weinheim, **2016**.

31. Aucagne, V.; Hanni, K. D.; Leigh, D. A.; Lusby, P. J.; Walker, D. B. Catalytic "Click" Rotaxanes: A Substoichiometric Metal-Template Pathway to Mechanically Interlocked Architectures. *J. Am. Chem. Soc.* **2006**, *128*, 2186 – 2187.

32. Denis, M.; Goldup, S. M. The active template approach to interlocked molecules. *Nat. Rev. Chem.* **2017**, *1*, 0061.

33. Denis, M.; Lei, Q.; Turner, P.; Jolliffe, K. A.; Goldup, S. M. A Fluorescent Ditopic Rotaxane Ion-Pair Host. *Angew. Chem. Int. Ed.* **2018**, *57*, 5315 – 5319.

34. Denis, M.; Pancholi, J.; Jobe, K.; Watkinson, M.; Goldup, S. M. Chelating Rotaxane Ligands as Fluorescent Sensors for Metal Ions. *Angew. Chem. Int. Ed.* **2018**, *57*, 5310 – 5314.

35. Langton, J. M.; Beer, P. D. Rotaxane and Catenane Host Structures for Sensing Charged Guest Species. *Acc. Chem. Res.* **2014**, *47*, 1935 – 1949.

36. Lahlali, H.; Jobe, K.; Watkinson, M.; Goldup, S. M. Macrocycle Size Matters: "Small" Functionalized Rotaxanes in Excellent Yield Using the CuAAC Active Template Approach. *Angew. Chem. Int. Ed.* **2011**, *50*, 4151 – 4155.

37. Berna, J.; Goldup, S. M.; Lee, A.-L.; Leigh, D. A.; Symes, M. D.; Teobaldi, G.; Zerbetto, F. Cadiot–Chodkiewicz Active Template Synthesis of Rotaxanes and Switchable Molecular Shuttles with Weak Intercomponent Interactions. *Angew. Chem. Int. Ed.* **2008**, *47*, 4392 – 4396.

38. Movsisyan, L. D.; Franz, M.; Hampel, F.; Thomspon, A. L.; Tykwinski, R. R.; Anderson, H. A. Polyyne Rotaxanes: Stabilization by Encapsulation. *J. Am. Chem. Soc.* **2016**, *138*, 1366 – 1376.

39. Neal, E. A.; Goldup, S. M. A Kinetic Self-Sorting Approach to Heterocircuit [3]Rotaxanes. *Angew. Chem. Int. Ed.* **2016**, *55*, 12488 – 12493.

40. Crowley, J. D.; Goldup, S. M.; Gowans, N. D. Leigh, D. A.; Ronaldson, V. E.; Slawin, A. M. An Unusual Nickel−Copper-Mediated Alkyne Homocoupling Reaction for the Active-Template Synthesis of [2]Rotaxanes. *J. Am. Chem. Soc.* **2010**, *132*, 6243 – 6248.

41. Baumes, J. M.; Gassensmith, J. J.; Giblin, J.; Lee, J.-J.; White, A. G.; Culligan, W. J.;. Leevy, W. M; Kuno, M.; Smith, B. D. Storable, thermally activated, near-infrared chemiluminescent dyes and dye-stained microparticles for optical imaging. *Nat. Chem.* **2010**, *2*, 1025 – 1030.

42. Sagara, Y.; Karman, M.; Verde-Sesto, E.; Matsuo, K.; Kim, Y.; Tamaoki, N.; Weder, C. J. Rotaxanes as Mechanochromic Fluorescent Force Transducers in Polymers. *J. Am. Chem. Soc.* **2018**, *140*, 1584 – 1587.

43. Fielden, S. D. P.; Leigh, D. A.; Woltering, S. L. Molecular Knots. *Angew. Chem. Int. Ed.* **2017**, *56*, 11166 – 11194.

44. Ambrogio, M. W.; Thomas, C. R.; Zhao, Y.-L.; Zink, J. I.; Stoddart, J. F. Mechanized Silica Nanoparticles: A New Frontier in Theranostic Nanomedicine. *Acc. Chem. Res.* **2011**, *44*, 903 – 913.

45. Barat, R.; Legigan, T.; Tranoy-Opalinski, I.; Renoux, B.; Peraudeau, E.; Clarhaut, J.; Poinot, P.; Fernandes, A. E.; Aucagne, V.; Leigh, D. A.; Papot, S. A mechanically interlocked molecular system programmed for the delivery of an anticancer drug. *Chem. Sci.* **2015**, *6*, 2608 – 2613.

46. Pairault, N. ; Barat, R.; Tranoy-Opalinski, I.; Renoux, B.; Thomas, M.; Papot, S. C. R.; *Chim.* **2016**, *19*, 103 – 112.

47. Xu, Y.; Kaur, R.; Wang, B.; Minameyer, M. B.; Gsanger, S.; Meyer, B.; Drewello, T.; Guldi, D. M.; von Delius, M. Concave–Convex π–π Template Approach Enables the Synthesis of [10]Cycloparaphenylene–Fullerene [2]Rotaxanes. *J. Am. Chem. Soc.* **2018**, *140*, 13413 – 13420.

48. Fan, Y.-Y.; Chen, D.; Huang, Z.; Zhu, J.; Tung, C.; Wu, L.; Cong, H. An isolable catenane consisting of two Möbius conjugatednanohoops. *Nat. Commun.* **2018**, *9*, 3037.

49. Bauerle, P.; Ammann, M.; Wilde, M.; Gçtz, G.; Rang, A.; Schalley, C. A.; Oligothiophene-Based Catenanes: Synthesis and Electronic Properties of a Novel Conjugated Topological Structure. *Angew. Chem. Int. Ed.* **2007**, *46*, 363 – 368.

50. Vukotic, V. N.; Harris, K. J.; Zhu, K.; Schurko, R. W.; Loeb, S. K. Metal-organic frameworks with dynamic interlocked components. *Nat. Chem.* **2012**, *4*, 456 – 460.

51. Vukotic, V. N.; Loeb, S. K. Coordination polymers containing rotaxane linkers. *Chem. Soc. Rev.* **2012**, *41*, 5896 – 5906.

52. Nejrotti, S.; Cerai, G. P.; Oppedisano, A.; Maranzana, A.; Occhiato, E. G.; Scarpi, D.; Deagostino, A.; Prandi, A Gold(I)-Catalyzed Oxidative Rearrangement of Heterocycle-Derived 1,3-Enynes Provides an Efficient and Selective Route to Divinyl Ketones. C. *Eur. J. Org. Chem.* **2017**, *41*, 6228-6238.

53. Boden, C. D. J.; Pattenden, G.; Ye, T. Palladium-catalysed hydrostannylations of 1-bromoalkynes. A practical synthesis of (E)-1-stannylalk-1-enes. *J. Chem. Perkin Trans. 1*, **1996**, *0*, 2417-2419.

Chapter V.

1. Jariwala, D.; Sangwan, V. K.; Lauhon, L. J.; Marks, T. J.; Hersam, M. C. Carbon nanomaterials for electronics, optoelectronics, photovoltaics, and sensing. *Chem. Soc. Rev.* **2013**, *42*, 2824−2860.

2. Wang, H.; Wang, B.; Quek, X.-Y.; Wei, L.; Zhao, J.; Li, L.-J.; Chan-Park, M. B.; Yang, Y.; Chen, Y. CMPs as Scaffolds for Constructing Porous Catalytic Frameworks: A Built-in Heterogeneous Catalyst with High Activity and Selectivity Based on Nanoporous Metalloporphyrin Polymers. *J. Am. Chem. Soc.* **2010**, *132*, 16747−16749.

3. He, M.; Chernov, A. I.; Fedotov, P. V.; Obraztsova, E. D.; Rikkinen, E.; Zhu, Z.; Sainio, J.; Jiang, H.; Nasibulin, A. G.; Kauppinen, E. I.; Niemela, M.; Krause, A. O. I. Selective growth of SWNTs on partially reduced monometallic cobalt catalyst. *Chem. Commun.* **2011**, *47*, 1219−1221.

4. Sanchez-Valencia, J. R.; Dienel, T.; Gröning, O.; Shorubalko, I.; Mueller, A.; Jansen, M.; Amsharov, K.; Ruffieux, P.; Fasel, R. Controlled synthesis of single-chirality carbon nanotubes. *Nature* **2014**, *512*, 61−64.

5. Holt, J. K.; Park, H. G.; Wang, Y.; Stadermann, M.; Artyukhin, A. B.; Grigoropoulos, C. P.; Noy, A.; Bakajin, O. Fast mass transport through sub-2-nanometer carbon nanotubes. *Science* **2006**, *312*, 1034−1037.

6. Tunuguntla, R. H.; Allen, F. I.; Kim, K.; Belliveau, A.; Noy, A. Synthesis, lipid membrane incorporation, and ion permeability testing of carbon nanotube porins. *Nat. Nanotechnol.* **2016**, *11*, 639−644.

7. Hata, K.; Futaba, D. N.; Mizuno, K.; Namai, T.; Yumura, M.; Iijima, S. Water-assisted highly efficient synthesis of impurity-free single-walled carbon nanotubes. *Science* **2004**, *306*, 1362−1364.

8. Fornasiero, F.; Park, H. G.; Holt, J. K.; Stadermann, M.; Grigoropoulos, C. P.; Noy, A.; Bakajin, O. Ion exclusion by sub-2-nm carbon nanotube pores. *Proc. Natl. Acad. Sci. U. S. A.* **2008**, *105*, 17250−17255.

9. Qu, L.; Vaia, R. A.; Dai, L. Multilevel, Multicomponent Microarchitectures of Vertically-Aligned Carbon Nanotubes for Diverse Applications. *ACS Nano* **2011**, *5*, 994−1002.

10. Bsoul, A.; Sultan Mohamed Ali, M.; Nojeh, A.; Takahata, K. Piezoresistive strain sensing using carbon nanotube forests suspended by Parylene-C membranes. *Appl. Phys. Lett.* **2012**, *100*, 213510.

11. Miyake, T.; Yoshino, S.; Yamada, T.; Hata, K.; Nishizawa, M. Self-Regulating Enzyme−Nanotube Ensemble Films and Their Application as Flexible Electrodes for Biofuel Cells. *J. Am. Chem. Soc.* **2011**, *133*, 5129−5134.

12. Smalley, R. E.; Li, Y.; Moore, V. C.; Price, B. K.; Colorado, R.; Schmidt, H. K.; Hauge, R. H.; Barron, A. R.; Tour, J. M. Single Wall Carbon Nanotube Amplification: En Route to a Type-Specific Growth Mechanism. *J. Am. Chem. Soc.* **2006**, *128*, 15824−15829.

13. Xia, J.; Golder, M. R.; Foster, M. E.; Wong, B. M.; Jasti, R. Synthesis, Characterization, and Computational Studies of Cycloparaphenylene Dimers. *J. Am. Chem. Soc.* **2012**, *134*, 19709−19715.

14. Sisto, T. J.; Tian, X.; Jasti, R. Synthesis of Tetraphenyl-Substituted [12]Cycloparaphenylene: Toward a Rationally Designed Ultrashort Carbon Nanotube. *J. Org. Chem.* **2012**, *77*, 5857− 5860.

15. Omachi, H.; Nakayama, T.; Takahashi, E.; Segawa, Y.; Itami, K. Initiation of carbon nanotube growth by well-defined carbon nanorings. *Nat. Chem.* **2013**, *5*, 572−576.

16. Jasti, R.; Bhattacharjee, J.; Neaton, J. B.; Bertozzi, C. R. Synthesis, Characterization, and Theory of [9]-, [12]-, and [18]Cycloparaphenylene: Carbon Nanohoop Structures. *J. Am. Chem. Soc.* **2008**, *130*, 17646−17647.

17. Darzi, E. R.; Sisto, T. J.; Jasti, R. Selective Syntheses of [7]–[12]Cycloparaphenylenes Using Orthogonal Suzuki–Miyaura Cross-Coupling Reactions. *J. Org. Chem.* **2012**, *77*, 6624− 6628.

18. Xia, J.; Jasti, R. *Angew. Chem., Int. Ed.* **2012**, *51*, 2474−2476.

19. Patel, V. K.; Kayahara, E.; Yamago, S. *Chem. - Eur. J.* **2015**, *21*, 5742−5749.

20. Evans, P. J.; Darzi, E. R.; Jasti, R. Efficient room-temperature synthesis of a highly strained carbon nanohoop fragment of buckminsterfullerene. *Nat. Chem.* **2014**, *6*, 404−408.

21. Tran-Van, A.-F.; Huxol, E.; Basler, J. M.; Neuburger, M.; Adjizian, J.-J.; Ewels, C. P.; Wegner, H. A. A Strain Induced Change of Mechanism from a [2 + 2 + 2] to a [2 + 1 + 2 + 1] Cycloaddition Reaction. *Org. Lett.* **2014**, *16*, 1594− 1597.

22. Van Raden, J. M.; Louie, S.; Zakharov, L. N.; Jasti, R. 2,2'-Bipyridyl-embedded Cycloparaphenylenes as a General Strategy to Investigate Nanohoop-based Coordination Complexes. *J. Am. Chem. Soc.* **2017**, *139*, 2936−2939.

23. White, B. M.; Zhao, Y.; Kawashima, T. E.; Branchaud, B. P.; Pluth, M. D.; Jasti, R. Expanding the Chemical Space of Biocompatible Fluorophores. *ACS Cent. Sci.* **2018**, *4*, 1173−1178.

24. Povie, G.; Segawa, Y.; Nishihara, T.; Miyauchi, Y.; Itami, K. Synthesis of a carbon nanobelt. *Science* **2017**, *356*, 172−175.

25. Povie, G.; Segawa, Y.; Nishihara, T.; Miyauchi, Y.; Itami, K. Synthesis and Size-Dependent Properties of [12], [16], and [24]Carbon Nanobelts. *J. Am. Chem. Soc.* **2018**, *140*, 10054−100059.

26. Fujitsuka, M.; Cho, D. W.; Iwamoto, T.; Yamago, S.; Majima, T. Phys. Size-dependent fluorescence properties of [n]cycloparaphenylenes (n = 8–13), hoop-shaped π-conjugated molecules. *Chem. Chem. Phys.* **2012**, *14*, 14585−14588.

27. Darzi, E. R.; Jasti, R. The dynamic, size-dependent properties of [5]–[12]cycloparaphenylenes. *Chem. Soc. Rev.* **2015**, *44*, 6401−6410.

28. Sakamoto, H.; Fujimori, T.; Li, X.; Kaneko, K.; Kan, K.; Ozaki, N.; Hijikata, Y.; Irle, S.; Itami, K. Cycloparaphenylene as a molecular porous carbon solid with uniform pores exhibiting adsorption-induced softness. *Chem. Sci.* **2016**, *7*, 4204−4210.

29. Kayahara, E.; Sun, L.; Onishi, H.; Suzuki, K.; Fukushima, T.; Sawada, A.; Kaji, H.; Yamago, S. Gram-Scale Syntheses and Conductivities of [10]Cycloparaphenylene and Its Tetraalkoxy Derivatives. *J. Am. Chem. Soc.* **2017**, *139*, 18480− 18483.

30. Ozaki, N.; Sakamoto, H.; Nishihara, T.; Fujimori, T.; Hijikata, Y.; Kimura, R.; Irle, S.; Itami, K. Electrically Activated Conductivity and White Light Emission of a Hydrocarbon Nanoring–Iodine Assembly. *Angew. Chem., Int. Ed.* **2017**, *56*, 11196−11202.

31. Mori, T.; Tanaka, H.; Dalui, A.; Mitoma, N.; Suzuki, K.; Matsumoto, M.; Aggarwal, N.; Patnaik, A.; Acharya, S.; Shrestha, L. K.; Sakamoto, H.; Itami, K.; Ariga, K. Carbon Nanosheets by Morphology-Retained Carbonization of Two-Dimensional Assembled Anisotropic Carbon Nanorings. *Angew. Chem., Int. Ed.* **2018**, *57*, 9679−9683.

32. Ball, M.; Zhong, Y.; Fowler, B.; Zhang, B.; Li, P.; Etkin, G.; Paley, D. W.; Decatur, J.; Dalsania, A. K.; Li, H.; Xiao, S.; Ng, F.; Steigerwald, M. L.; Nuckolls, C. Rigid, Conjugated Macrocycles for High Performance Organic Photodetectors. *J. Am. Chem. Soc.* **2016**, *138*, 12861− 12867.

33. Bezdek, A.; Kuperberg, W. Maximum density space packing with congruent circular cylinders of infinite length. *Mathematika* **1990**, *37*, 74−80.

34. Peigney, A.; Laurent, C.; Flahaut, E.; Bacsa, R. R.; Rousset, A. Specific Surface Area of Carbon Nanotubes and Bundles of Carbon Nanotubes. *Carbon* **2001**, *39*, 507−514.

35. Anthony, J. E.; Brooks, J. S.; Eaton, D. L.; Parkin, S. R. Functionalized Pentacene: Improved Electronic Properties from Control of Solid-State Order. *J. Am. Chem. Soc.* **2001**, *123*, 9482−9483.

36. Segawa, Y.; Miyamoto, S.; Omachi, H.; Matsuura, S.; Šenel, P.; Sasamori, T.; Tokitoh, N.; Itami, K. Concise Synthesis and Crystal Structure of [12]Cycloparaphenylene. *Angew. Chem., Int. Ed.* **2011**, *50*, 3244−3248.

37. Patrick, C. R.; Prosser, G. S. A Molecular Complex of Benzene and Hexafluorobenzene. *Nature* **1960**, *187*, 1021.

38. Coates, G. W.; Dunn, A. R.; Henling, L. M.; Dougherty, D. A.; Grubbs, R. H. Phenyl–Perfluorophenyl Stacking Interactions: A New Strategy for Supermolecule Construction. *Angew. Chem., Int. Ed.* **1997**, *36*, 248−251.

39. Kissel, P.; Murray, D. J.; Wulftange, W. J.; Catalano, V. J.; King, B. T. A nanoporous two-dimensional polymer by single-crystal-to-single-crystal photopolymerization. *Nat. Chem.* **2014**, *6*, 774−778.

40. Thalladi, V. R.; Weiss, H.-C.; Blaser, D.; Boese, R.; Nangia, A.; Desiraju, G. R. C−H···F Interactions in the Crystal Structures of Some Fluorobenzenes. *J. Am. Chem. Soc.* **1998**, *120*, 8702−8710.

41. Hashimoto, S.; Kayahara, E.; Mizuhata, Y.; Tokitoh, N.; Takeuchi, K.; Ozawa, F.; Yamago, S. Synthesis and Physical Properties of Polyfluorinated Cycloparaphenylenes. *Org. Lett.* **2018**, *20*, 5973−5976.

42. Suzuki, A. Cross-Coupling Reactions Of Organoboranes: An Easy Way To Construct C-C Bonds (Nobel Lecture). *Angew. Chem., Int. Ed.* **2011**, *50*, 6722−6737.

43. Rio, J.; Erbahar, D.; Rayson, M.; Briddon, P.; Ewels, C. P. Cyclotetrahalo-*p*-phenylenes: simulations of halogen substituted cycloparaphenylenes and their interaction with C_{60}. *Phys. Chem. Chem. Phys.* **2016**, *18*, 23257−23263.

44. Li, P.; Zakharov, L. N.; Jasti, R. A Molecular Propeller with Three Nanohoop Blades: Synthesis, Characterization, and Solid-State Packing. *Angew. Chem., Int. Ed.* **2017**, *56*, 5237−5241.

45. Falcaro, P.; Okada, K.; Hara, T.; Ikigaki, K.; Tokudome, Y.; Thornton, A. W.; Hill, A. J.; Williams, T.; Doonan, C.; Takahashi, M. Centimetre-scale micropore alignment in oriented polycrystalline metal-organic framework films via heteroepitaxial growth. *Nat. Mater.* **2017**, *16*, 342−348.

46. Perez-Guardiola, A.; Pe´ rez-Jime´ nez, A. J.; Sancho-García, J. C.´ *Mol. Syst. Des. Eng.* **2017**, *2*, 253.

47. Xia, J.; Bacon, J. W.; Jasti, R. Gram-scale synthesis and crystal structures of [8]- and [10]CPP, and the solid-state structure of C_{60}@[10]CPP. *Chem. Sci.* **2012**, *3*, 3018−2021.

48. Koga, K.; Gao, G. T.; Tanaka, H.; Zeng, X. C. Formation of Ordered Ice Nanotubes Inside Carbon Nanotubes. *Nature* **2001**, *412*, 802−805.

49. Hornbaker, D. J.; Kahng, S.-J.; Misra, S.; Smith, B. W.; John-son, A. T.; Mele, E. J.; Luzzi, D. E.; Yazdani, A. Mapping the One-Dimensional Electronic States of Nanotube Peapod Structures. *Science.* **2002**, *295*, 828−831.

50. Sato, S.; Yamasaki, T.; Isobe, H. Solid-State Structures of Pea-pod Bearings Composed of Finite Single-Wall Carbon Nanotube and Fullerene Molecules. *Proc. Natl. Acad. Sci.*, **2014**, *111*, 8374−8379.

51. Xu, Y.; Wang, B.; Kaur, R.; Minameyer, M. B.; Bothe, M.; Drewello, T.; Guldi, D. M.; von Delius, M. A Supramolecular [10]CPP Junction Enables Efficient Electron Transfer in ModularPorphyrin–[10]CPPFullerene Complexes. *Angew. Chem. Int. Ed.* **2018**, *57*, 11549−11553.

52. Xu, Y.; Kaur, R.; Wang, B.; Minameyer, M. B.; Gsaenger, S.; Meyer, B.; Drewello, T.; Guldi, D. M.; von Delius, M. Concave-Convex π-πTemplate Approach Enables the Synthesis of [10]Cy-cloparaphenylene-Fullerene [2]Rotaxanes. *J. Am. Chem. Soc.* **2018**, *140*, 13413−13420.

53. Iwamoto, T.; Watanabe, Y.; Sadahiro, T.; Haino, T.; Yamago, S. Size-Selective Encapsulation of C_{60} by [10]Cycloparaphenylene: Formation of the Shortest Fullerene Peapod. *Angew. Chem. Int. Ed.* **2011**, *50*, 8342−8344.